TECHNISCHE UNIVERSITÄT WIEN
Vienna University of Technology

PhD Thesis

Scale-Dependent Investigation of Tribology Related Surface Interactions in Biological Media

Submitted in satisfaction of the requirements for the degree

Doctor of technical sciences (Ph.D.)

Of the TU Wien, Faculty of Mechanical and Industrial Engineering

---

Dissertation

Skalenabhängige tribologische Untersuchungen von Oberflächenwechselwirkungen in biologischen Geweben

ausgeführt zum Zwecke der Erlangung des akademischen Grads

Doktor der technischen Wissenschaften (Dr. techn.)

eingereicht an der TU Wien, Fakultät der für Machinenwesen und Betriebswissenschaften

Author**: Hakan Göçerler, M.Sc.**

Mat.Nr.: 0526993

under the supervision of

Univ.Prof. Dipl.-Ing. Dr. Carsten Gachot

Head of the Tribology Research Unit

Institute of Engineering Design and Product Development, E 307

Vienna, July 2023

Composition of graduation committee:

Chairman and Secretary:

Univ.Prof. Dipl.-Ing. Dr.-Ing. Michael Weigand   TU Wien

Supervisor:

Univ.Prof. Dipl.-Ing. Dr.-Ing. Carsten Gachot   TU Wien

Reviewer 1:

Prof. Dipl.-Ing.in Dr.in techn. Ille C. Gebeshuber   TU Wien

Reviewer 2:

Prof. Dr. Haytam Kasem   Azrieli College of Engineering

Affidavit

I declare in lieu of oath that I wrote this thesis and performed the associated research myself, using only literature cited in this volume. If text passages from sources are used literally, they are marked as such. I confirm that this work is original and has not been submitted elsewhere for any examination, nor is it currently under consideration for a thesis elsewhere. I confirm that going to press of this thesis needs the confirmation of the examination committee. I acknowledge that the submitted work will be checked electronically-technically using suitable and state-of-the-art means (plagiarism detection software). On the one hand, this ensures that the submitted work was prepared according to the high-quality standards within the applicable rules to ensure good scientific practice "Code of Conduct" at the TU Wien. On the other hand, a comparison with other student theses avoids violations of my personal copyright.

Vienna, September 2023   Hakan Göçerler

Acknowledgements

I wish to express my heartfelt gratitude to the individuals who have played pivotal roles in shaping my academic and professional journey, each of whom has contributed significantly to my growth and development.

To begin, my sincere appreciation goes to all my teachers, from my early education through university, for imparting their knowledge and wisdom. Special mention must be made of the esteemed professors at Dokuz Eylül University, particularly Erol Uyar, Aytaç Gören, Levent Çetin, and Çınar Yeni, who provided me with a solid educational foundation.

My indebtedness extends to Numan Durakbaşa, whose guidance and mentorship not only opened the doors to the fascinating realm of tribology but also facilitated my transition to a tribologist. Furthermore, I am grateful to Friedrich Franek and Andreas Pauschitz for their instrumental role in establishing Vienna as a global hub for tribology. Professors Wilfried Bartz and Herbert Störi, along with project managers Thomas Wopelka and Martin Jech, deserve special acknowledgment for their creation of WEMESURF Marie Curie Research Training Network and their unwavering support. I would also like to express my gratitude to Alessandro Podesta, Marco Indrieri, Simone Bovio, Lasma Gailite, Varun Yvas, Ajay Singh from University of Milano, along with many other collaborators from various universities, research centres, and companies who have enriched my professional journey.

My experience at Philips Applied Technologies was transformative, and I extend my thanks to Steve Franklin and Kees Hendriks for imparting invaluable lessons in professionalism within a global corporation.

Most of my career in tribology has been dedicated to my work at AC2T research GmbH. I wish to extend my thanks to all my colleagues, particularly Josef Brenner, Michael Adler, Ivana Toth, and Christian Tomastik, whose collaboration has yielded fruitful results. Some of these colleagues have become like family, and I am truly thankful to Adina Neacşu, Lazslo Katona, and Peter Somkuti for both their scientific contributions and emotional support. I would like to extend my appreciation to Ille Gebeshuber for reshaping my outlook on the world. Embracing and learning from nature has not only guided me academically but has also had a significant impact on my personal growth.

I would be remiss not to mention my colleagues from Donau Universitat Krems Christoph Bauer, Stefan Nehrer, and Thomas Klestil and from the tribology group at TU Wien, including Stefan

Eder, Philipp Grützmacher, Simon Medina, Azhaarudeen Anifa Mohamed Faruck and Chia-Jui Hsu. Finally, I owe a debt of gratitude to my supervisor, Carsten Gachot, for making it possible to pursue my research in an academic setting conducive to doctoral studies.

Last but certainly not least, I wish to thank Halime and Metin Göcerler, who have exemplified the boundless possibilities that love, and dedication can achieve. As Friedrich Nietzsche said, "In family life, love is the oil that eases friction, the cement that binds closer together, and the music that brings harmony." Thanks to you two, I never felt lack of love in any dimension.

In conclusion, I am deeply appreciative of the collective efforts and unwavering support of these individuals, without whom my academic and professional journey would not have been possible. Their contributions have been instrumental in shaping the researcher and person I have become today.

Abstract

This thesis explores the multifaceted applications of biotribology, aiming to enhance tribometer capabilities across various scales. The primary focus is understanding lubrication mechanisms inherent to dermatological, ophthalmological, and orthopaedic tissues. Additionally, the research aims to provide innovative solutions to improve tissue well-being and extend the operational life of artificial systems designed to optimise those tissues' contact dynamics. An essential motivation lies in the challenges posed by real-world contexts that deviate from the original tribological investigations, prompting iterative enhancements in tribometer design and methodology.

Starting with biotribological interactions involving human skin, this work examines how the skin interacts with diverse consumer products and medical devices. To avoid variations due to anatomy, demographics, and lifestyle, the study focused on the skin's natural oil distribution on the stratum corneum using atomic force microscopy. Elasticity variations due to dermis and other layers of epidermis were bypassed, and the tribological behaviour of the oil and keratin layer could be observed separately.

Shifting to the ophthalmic domain, the dynamic interplay between the cornea and eyelid was examined. This investigation emphasizes lubrication and friction while uncovering limitations in current tribometric methods that struggle to capture the complexities of tear-film interactions. A microtribometer was adapted to work with cell culture samples submerged in various solutions. Also, various eyedrops were tested to observe improvements in lubrication properties as a solution to dry eye disease.

Finally, this work also investigates articular joints using cartilage-on-cartilage systems. An SRV tribometer was adapted to conduct tests using synovial fluid at body temperature. The vital role of water in the lubrication scenario of knee joints is highlighted, along with exploring the effects of pro- and anti-inflammatory agents on tribological interactions. A significant point is the evaluation of transplanting healthy knee tissue, exploring how grafted cartilage orientation impacts the corresponding tribology.

Zusammenfassung

Diese Arbeit erforscht die vielfältigen Anwendungen der Biotribologie mit dem Ziel, die Funktionalität von Tribometern auf verschiedenen Skalen zu verbessern. Der Schwerpunkt liegt auf dem Verständnis der Schmiermechanismen, die in dermatologischem, ophthalmologischem und orthopädischem Gewebe auftreten. Zusätzlich zielt die Forschung darauf ab, innovative Lösungen zur Verbesserung des Gewebezustands zu liefern und die Betriebsdauer künstlicher Systeme zu verlängern, die entwickelt wurden, um die Kontaktmechanik dieser Gewebe zu optimieren. Eine wesentliche Motivation besteht in den Herausforderungen aus realen Kontexten, die von tribologischen Untersuchungen abweichen, was zu iterativen Verbesserungen im Design und der Methodik von Tribometern führt.

Beginnend mit biotribologischen Interaktionen, die die menschliche Haut betreffen, untersucht diese Arbeit, wie die Haut mit verschiedenen Konsumprodukten und medizinischen Geräten interagiert. Um Variationen aufgrund von Anatomie, Demografie und Lebensstil zu vermeiden, konzentriert sich die Studie auf die Untersuchung der Verteilung des Hautfetts auf der Hornschicht mithilfe der Rasterkraftmikroskopie. So wurden Elastizitätsunterschiede aufgrund der Dermis und anderer Epidermisschichten umgangen, sodass das tribologische Verhalten von Hautfett und Keratinschicht separat beobachtet werden konnte.

Im ophthalmologischen Bereich untersucht diese Arbeit das dynamische Zusammenspiel zwischen der Hornhaut und dem Augenlid. Die Untersuchung legt den Schwerpunkt auf Schmierung und Reibung und deckt dabei Einschränkungen in gängigen tribometrischen Methoden auf, die Schwierigkeiten haben, die Komplexität der Tränenfilminteraktionen zu erfassen. Ein Mikrotribometer wurde angepasst, um mit Zellkultur-Proben in verschiedenen Lösungen zu arbeiten. Auch verschiedene Augentropfen wurden getestet, um Verbesserungen der Schmiereigenschaften als Lösung für das Trockene-Augen-Syndrom zu beobachten.

Schließlich untersucht die Arbeit auch Gelenke in Form von Knorpel-auf-Knorpel-Systemen. Ein Schwing-Reib-Verschleiß Tribometer wurde angepasst, um Tests mit Gelenksflüssigkeit bei Körpertemperatur durchzuführen. Die wichtige Rolle von Wasser bei der Schmierung von Kniegelenken wird hervorgehoben, ebenso wie die Erforschung der Auswirkungen von entzündungsfördernden und -hemmenden Mitteln auf tribologische Wechselwirkungen. Ein wichtiger Punkt ist die Bewertung der Transplantation von gesundem Kniegewebe, wobei erforscht wird, wie die orientierte transplantierte Knorpelstruktur die entsprechende Tribologie beeinflusst.

Table of Contents

Dedicated to Halime and Metin Göçerler

Chapter 1 Introduction

This thesis endeavors to undertake an exploration into diverse applications of biotribological principles across a spectrum of scales. The main idea is to either modify or design additional features for tribometers available on the market, not only in order to understand real-life lubrication mechanisms of tissues, but also offer solutions to improve either health of the tissue, or the life cycle of artificial systems used to improve contact conditions for those tissues. The necessity to use tribometers in settings they weren't originally intended for has prompted improvements in the tribometers utilized in this work. The focus was on three main tissues: skin, eye and synovial joints. These tissues were examined at three different scales, nano-, micro-, and macro-scale, to observe the effect of different contact conditions.

1.1 Dermatological studies (Paper I and Book Chapter I)

Our initial point of emphasis was directed toward the integumentary system, specifically the skin, which is recognized as the body's largest organ., covering ~ 2 m^2, it is an important interface with the outside world [1]. Skin has biotribological ineractions with a wide range of materials, as well as medical, cosmetic and technological products. Different types of detergents, and soaps, shaving products like creams or blades, cosmetic products, technological products like watches, cellphone screens or a steering wheel, different types of clothing, UV light, polluted air, insects, are some examples of items and phenomena that are interacting with the skin in daily life. Besides, there are various medical devices that are in contact with the skin, fortunately not on a daily basis, but the interaction parameters can be vital for us. Different bandages (to protect scars or to limit some certain type of movement), operation tools like a scalpel (most operations begin with a permanent damage on skin with a cut), vaccines, prescription glasses could be listed as the less commonly used but important applications of biotribology on skin. The variety of interactions and counterbodies are the reasons of the continuous scientific studies on tribology of human skin as a major research topic over the years. The observation that the characteristics of skin exhibit variations dependent upon factors such as anatomical location, age, gender, skin typology, pigmentation, vascularization, and lifestyle choices underscores the imperative of discerning the principal unit within each individual's skin structure for the purposes of meaningful comparative analysis [2]. Consequently, our inquiry prompted an exploration into the microstructural

composition of the skin. From a structural perspective, the human skin manifests as a composite assembly comprising three primary layers, namely the epidermis, dermis, and hypodermis [3]. Each of these layers represents a intricate multiscale structure in its own right, which can be further partitioned into discrete components.

As part of a research project between Philips Applied Technologies and the Interdisciplinary Center for Nanostructured Materials and Interfaces of the University of Milano, which concerned the interaction between a shaver and the skin, the focus was chosen to be the most outer layer of the skin: the epidermis.

The avascular epidermal layer can be dissected into two primary constituents: the living epidermis, which encompasses vital keratinocytes, and the stratum corneum (SC), stratum consisting of flattened, deceased corneocytes [4]. Typically, the epidermis is shielded by an acidic hydrolipid film, serving to regulate the skin's microbiota, prevent the colonization of pathogenic organisms, and act as a barrier against invading microorganisms [5]. The hydrolipid film is constituted by a composite blend of aqueous and sebaceous components, deriving from the eccrine and sebaceous glands, respectively. The translocation of these constituents towards the epidermal surface culminates in their emulsification, forming a protective layer that envelops the (SC). The SC's structural configuration can be likened to a brick-and-mortar model, where corneocytes are embedded within lamellar epidermal lipids, effectively serving as a robust defense mechanism against excessive water loss [6]. A thorough literature research was conducted to identify the vital parameters within nature focusing specifically on humans. The information gathered was collected in Paper I, **"Skin as an Interface: Understanding the Synergy of Dermatology, Biomimetics and Tribology"**. In the framework of the project, the oil distrubution on SC was studied using atomic force microscopy. The main idea was to understand the tribological parameters for the shaving machine application in dry conditions. The results have been published as part of the Book Chapter I, **"Bridging Nano- and Microtribology in Mechanical and Biomolecular Layers"** in **"Scanning Microscopy in Nanoscience and Nanotechnology Vol. 3"** by Bharat Bhushan. The chapter compares industrial and biological applications of coatings in different scales, and considers SC as a hard coating for the human body.

1.2 Ophthalmological studies (Paper II and Book Chapter I)

The second tissue of interest was the human eye. The human eye is a sophisticated and highly complex organ that provides the ability to process visual detail. In the eyes, light is converted

into electro-chemical impulses that are sent to the brain for processing [7]. This delicate organ is protected with two layers of tissues. The first line of defence is the eyelid, a thin fold of skin. Apart from protection, the eyelid is also responsible for the spread of the tear film on the surface of the eye [8]. Right behind the eyelid there is the cornea. The top layer of the cornea, an epithelial layer, is the one exposed to the surroundings when the eyelid is open. The primary function of the cornea lies in its ability to refract or bend incoming light. It assumes a pivotal role in focusing most of the incident light upon entering the eye. However, due to its position as the eye's outermost layer and its susceptibility to potential harm, the preservation of its integrity becomes of paramount importance [8]. The cornea is primarily constituted of proteins and cellular components, but notably, it lacks the presence of blood vessels, a characteristic that distinguishes it from most bodily tissues. This absence of blood vessels serves a critical purpose, as the introduction of blood vessels into the cornea could induce clouding, impairing its ability to effectively refract light and potentially compromising visual acuity. Given the absence of blood vessels for nutrient supply, the cornea relies on the provision of nutrients from tears and the aqueous humor present in the anterior chamber [9]. The epithelial layer within the cornea absorbs essential nutrients and oxygen from tears and subsequently distributes them throughout the corneal structure. This not only sustains the cornea's metabolic needs but also serves as a protective barrier, preventing the ingress of foreign matter into the eye. As the term implies in Greek "Epi" meaning, "on, upon," and "Theli" meaning "tissue. This particular tissue type serves as an external layer enveloping connective tissue, consequently assuming the foremost position in encountering mechanochemical interactions associated with tribological processes across various applications.

The interface between the cornea and the eyelid undergoes a substantial volume of mechanical activity, involving approximately 10,000 to 20,000 blinks per day. These blinks exert varying contact pressures within the range of Pascals to a few kiloPascals, accompanied by sliding speeds spanning from approximately 10 μm/s to 100 mm/s [10]. Remarkably, despite the rigorous conditions imposed on the eye by these mechanical actions, it maintains its structural integrity and sustains clear vision, primarily attributed to the role of the tear film. Among its multifarious functions, the tear film serves to lubricate the corneal surface, facilitate the removal of proteinaceous waste materials from the eye, and offer safeguard against wind-induced abrasion, as well as the infiltration of airborne debris and contaminants. However, its most pivotal function lies in effecting a complete separation between the

surfaces of the eyelid and the cornea during each blink, thereby mitigating the shear stresses that would otherwise induce cellular damage [11].

In the context of the ocular environment, distinct from the integumentary system (skin), wear is not a predominant consideration. Nevertheless, within this specialized milieu, both lubrication and friction assume paramount importance. The principal challenge in characterizing the material properties of ophthalmic biomaterials, such as contact lenses, lies in the formidable complexity inherent to the accurate replication of the intricate interplay between tear composition, ocular tissues, and variables like the load and velocity of the eyelid—the predominant dynamic interface within the ocular system. Most tribological testing devices, designed to operate under minimal loads, are ill-suited to replicate the high-speed dynamics associated with eyelid movement [12]. For individuals who employ contact lenses, either for therapeutic or cosmetic purposes, the eye experiences additional perturbations due to the mechanical influence of the eyelid and the presence of a foreign body, compounded by the requisite use of hygiene-related solutions to maintain ocular health. In the context of this thesis, a test system was devised to facilitate the utilization of a variety of contact lenses as a part of probing instruments. The system can operate in sub-mN force range so that cellular lines would not be completely damaged during the tests. Results were published within the Book Chapter 1 **"Bridging Nano- and Microtribology in Mechanical and Biomolecular Layers"** in **"Scanning Microscopy in Nanoscience and Nanotechnology Vol. 3"** as the corneal cell lines would represent non-mechanical, biomolecular layer.

This test design also took the interest of Croma Pharma GmbH, a pharmaceutical company that would like to introduce a solution not only for moisturizing the cornea, and creating a hygenic environment for the eye, but also to treat dry eye syndrome (DES). DES represents a multifaceted ocular surface disorder delineated by the disruption of tear film homeostasis and its concomitant instability [13]. Over time, this condition renders the eye susceptible to external stimuli and triggers inflammatory responses. This complication with the tear film, led to research on possible solutions, which could create an artificial layer on the cornea. Such solutions would be beneficial not only for DES but also many other diseases, such as glaucoma and retinopathy, that require prolonged treatment times [14]. Tribological properties of four different solutions were compared in the updated test system and these results were published in Paper II, **"A simple cornea model for the tribological performance**

assessment of the lubricating eye drops" in the Journal of Industrial Lubrication and Tribology.

1.3 Orthopedical studies (Papers III-V)

The final focus of the thesis lies on the cartilage-on-cartilage (CoC) systems. Cartilage represents a resilient and pliable fibrous tissue with diverse manifestations and multifaceted functions distributed across the human anatomy [15]. Within the human body, three distinct types of cartilage exist: hyaline, elastic, and fibrocartilage. Fibrocartilage, exemplified by anatomical structures such as the meniscus and spinal vertebrae disks, is characterized by its dense fibrous composition, rendering it the most robust albeit least flexible among the three variants. Its primary role resides in stabilizing bodily components and absorbing mechanical impacts. Conversely, elastic cartilage, found in locations such as the external ear and larynx, stands as the most adaptable cartilaginous subtype [16]. It provides structural support to anatomical regions necessitating pliability and mobility in their function. Remarkably, elastic cartilage exhibits a remarkable capacity to revert to its original configuration even when subjected to substantial mechanical loads. Lastly, hyaline cartilage, which prevails as the most prevalent cartilage type in the human body, envelops joint surfaces and caps the extremities of bones. Noteworthy for its slick and sleek texture, hyaline cartilage facilitates the seamless articulation of bones within joints, balancing suppleness with adequate structural strength to preserve joint integrity [17]. Hyaline cartilages that are part of articular joints are generally referred to as articular cartilage. They are situated within joint structures, exhibits a dual characteristic of low friction and high wear resistance, thereby facilitating weight-bearing and weight distribution. Nevertheless, a notable drawback associated with hyaline cartilage resides in its limited regenerative potential, primarily attributable to the absence of vascular, lymphatic, and neural networks, consequently constraining its intrinsic healing and reparative capabilities [18]. In this context, the preservation and well-being of articular cartilage emerge as pivotal factors in safeguarding joint health.

In our studies, we initially tried to understand how the system functions in the framework of tribology, without any health problems. A (CoC) experimental system was created that works in a hygienic, closed environment at body temperature. The design details of this system and initial observation on CoC system was published in Paper III, **"The dominance of water on lubrication properties of articular joints"**. The publication focused on lubrication regimes in the knee joint, and explored how water in synovial fluid improves tribological performance. This system would also allow us to introduce pro- and anti-inflammatory agents into solutions

in which the CoC experimental system is fully submerged in. Pro-inflammatory agents share similarities with the pathological conditions associated with osteoarthritis, which is the prevailing form of arthritis [19]. 80% of adults older than 55 experience various levels of this condition [20]. Because of osteoarthritis, the degradation of cartilaginous tissue within joints can ensue, ultimately precipitating discomfort and inflammation within the affected joint. These adverse outcomes result from the diminishing capacity of the cartilage to provide adequate cushioning and lubrication. Together with the University for Continuing Education Krems (DUK), we presented the results in Paper IV, **"Biotribological Tests of Osteochondral Grafts after Treatment with Pro-Inflammatory Cytokines"**.

Following these studies, we introduced the next step, in which the cartilage tissue is damaged, but the joint does not require a total joint replacement. One of the techniques used to fix cartilage damage is the Osteochondral Autograft Transfer (OATS) [21]. In this surgical procedure, clinicians harvest a cartilaginous plug from a non-load-bearing anatomical region of the patient's knee and subsequently graft it into the compromised region of the knee joint. As the hyaline cartilage is directly derived from the patient, the acceptance rate of the transplanted part is high and there is a relatively short recovery (four to eight months) [22]. The technique is cost-effective, and long-term durability is good. During our discussions with the colleagues at DUK, a question on the orientation of the cartilage matrix arose. The articular cartilage within the knee experiences loading in a consistent direction of walk, and it has been postulated that the orientation of the grafted osteochondral components could potentially exert an influence on the tribological characteristics of the joint. We developed a test matrix to compare the test pieces that are aligned with the loading direction in the knee, and the ones that have 90° degrees rotation to the loading axis. The results were published in Paper V, **"Effect of Osteochondral Graft O2rientation in a Biotribological Test System"**.

All the above-mentioned studies on CoC systems were done using bovine cartilage. Our final application was on human cartilage (as we developed the system gradually for this application), using hydrogels as a protective layer over the cartilage tissue [23]. This study is also published in **"Gelatin methacryloyl as environment for chondrocytes and cell delivery to superficial cartilage defects"** but was not included in the framework of this thesis as it appears in the thesis of the study's first author.

Chapter 2 Fundamental Principles and Research Endeavors

2.1 Tribological concepts

Tribology is life.

While this assertion may initially appear somewhat hyperbolic, I trust that as we delve further into this introduction, its clarity will become evident. The term was coined in 1966 by a British mechanical engineer, late Sir Peter Jost, deriving from the Greek root τριβ- of the verb τρίβω, tribo, "I rub" in classic Greek, and the suffix -logy from -λογία, -logia "study of", "knowledge of" [24]. The basic definition of tribology would be 'the study of friction, wear and lubrication, and design of bearings, science of interacting surfaces in relative motion' but we inadvertently introduce a greater influx of foreign terminology to individuals already lacking familiarity with foundational concepts, such as those pertaining to friction and wear [25]. Even though I will be explaining and studying these terms within this thesis, it is useful to focus on the term "interacting surfaces in relative motion". When we wake up and put our slippers on, the contact between our slippers and the floor is tribology; then we brush our teeth while a mostly polymer material is in relative motion to the teeth; we shave and it's a metal in relative motion to our skin; washing our face is skin against skin in relative motion with a non-abrasive lubricant. We then go to our work and not only are car tires on the road tribology, but thousands of pieces are in relative motion such as the engine piston-rings, and hopefully functioning brakes when we need to stop the car occasionally. We need to navigate on our screen with a mouse at work - it's the relative motion of a polymer on our table; and on lunch break there is a relative motion between the food and our teeth. Almost everywhere we look in life we would observe objects in contact that have relative motion, as life is rarely static. Even the systems that do not move according to our perception, have interactions at molecular levels as the molecules vibrate against each other.

Focusing on numbers may give us a better idea about the importance of tribology. One of the first credible studies on the impact of tribology was performed by a committee led by Sir Peter Jost for the British government in the 1960s. The committee suggested that nearly 500 million pounds could be saved through better tribological practices [26]. A simple inflation algorithm converts this number to almost 10 billion pounds for today's economic value. It is

not a secret that the industrial revolution had a pivoting role on global energy consumption. This consumption is estimated to be around 400 exajoules annually and almost 10% of this consumption is due to the friction and wear observed in moving parts of transportation vehicles. But if we look at the bigger picture, global level calculations show that 23% (119 EJ) of the total annual energy consumption worldwide originates from tribological contacts [27]. If we consider that the emissions are directly related to the energy used, tribology is responsible for 8,120 MtCO2/year carbon emission. Reduction of this value is directly proportional to our life quality, with climate change leading to multiple ecological issues.

To further investigate how tribology is life, we would like to focus on the term "bio-tribology", introduced by Dowson in 1970 [28], meaning to investigate the interface behavior and mechanisms related to biological systems. But first, as promised, it would be more sensible to explain the terms "friction" and "wear" as the terminology has been used to identify tribology within this text twice already.

2.1.1 Friction

Friction constitutes the counterforce impeding or opposing the relative motion between two interacting surfaces, and it emanates from intricate molecular and mechanical interplays transpiring within these surfaces [29]. The manifestation of friction is contingent upon the specific properties of the materials involved, the geometrical configurations, and the surface characteristics of the contacting entities, in addition to the prevailing operational circumstances and environmental context.

It might be considered a negative image for friction to resemble tug of war, In the realm of engineering and process optimization, it is generally deemed advantageous to mitigate friction to enhance the efficiency of a component or process. However, it is often more precise to employ the term "optimize" rather than "minimize." We need friction in many applications, such as brakes in cars, or we need air resistance so that a plane can stay in the air. Anyhow this game of tug of war, we will never lose. The friction force will only be equal to the force applied to initiate relative motion until we reach the limit of static friction [30].

We can understand from the previous sentence that there are various forms of friction. Friction can be static, kinetic, sliding, rolling, fluid, dry, lubricated or skin friction [31]. Suppose a force F is applied on a rope by a group of people as in Figure 2.1, which is balanced by the equal and opposite force of static friction f_s applied by the group of people on the other side of the rope. As force F increases, the force of static friction f_s also increases until f_s reaches a

certain maximum value just before one of the groups pulling the other from their position towards the direction of F. When the value of applied force F is greater than the maximum force of static friction $(f_s)_{max}$, $F > (f_s)_{max}$, then the losing group of people starts moving in the direction of the people winning the tug of war. The frictional forces acting on surfaces in relative motion are called the force of kinetic friction. The other types of friction, except from the skin friction, are self-explanatory by their names, and we will not go in detail in this section. Skin friction on the other hand, has no direct relation to skin: the largest organ of our body [32].
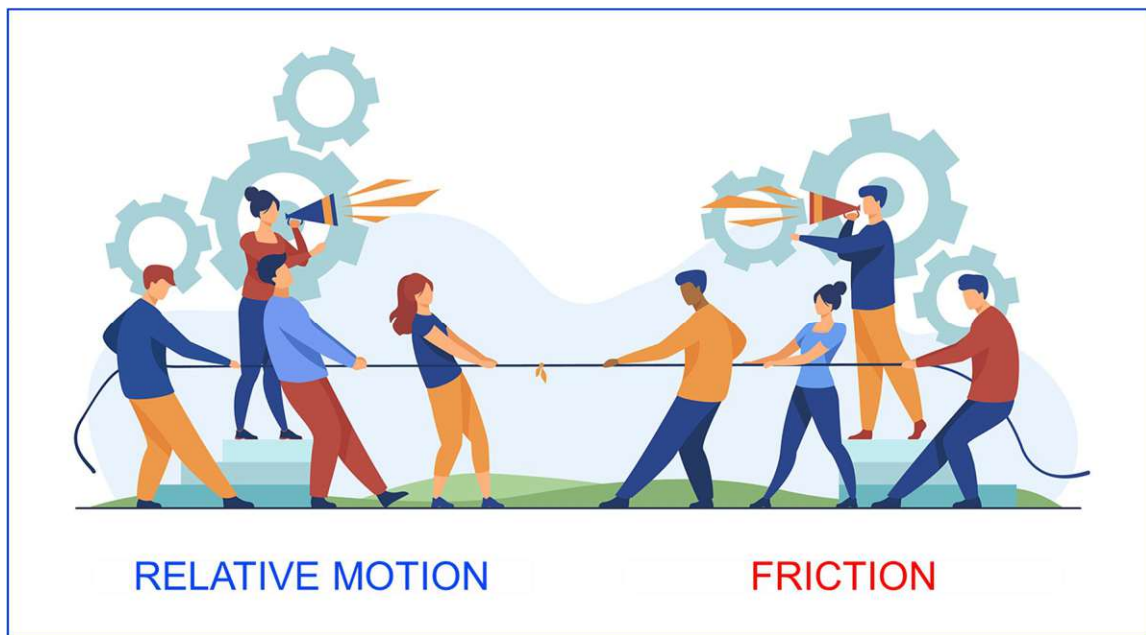

Fig. 2.1 Illustration of friction working against the relation motion.

This category of friction pertains to the resistance encountered between a fluid and the surface of a solid object in motion within it, or between a fluid in motion and the boundary surface encompassing it. This fluid medium may include air, and the term "skin friction" is specifically indicative of the component of drag experienced by an aircraft or the hydrodynamic resistance encountered by a ship, arising from the interaction between the air or water and their respective surfaces. It is essential to note that within the context of this thesis, I do not consider skin friction as previously defined; rather, our focus remains directed towards the examination of friction as it pertains to the skin as a bodily organ. Friction does not exist as an aberrant force in the realm of physical phenomena. Leonardo da Vinci was the first to study the laws of sliding friction (Figure 2.2) and describe them with his first statement of the laws, dating from 1493 [33]. Guillaume Amontons stated them in the

formulation of empirical laws of sliding friction in 1699 [34]. The laws of friction may be stated as follows:

1   The frictional force exhibits a direct proportionality to the normal load applied.

2   The frictional force remains unaffected by variations in the apparent contact area, but only relying on real contact area.

In addition to these principles, a third law, frequently ascribed to Coulomb (1785), posits:

3   The frictional force is unaffected by changes in the relative sliding velocity.

These three laws of friction summarize most empirical observations except in some important cases.
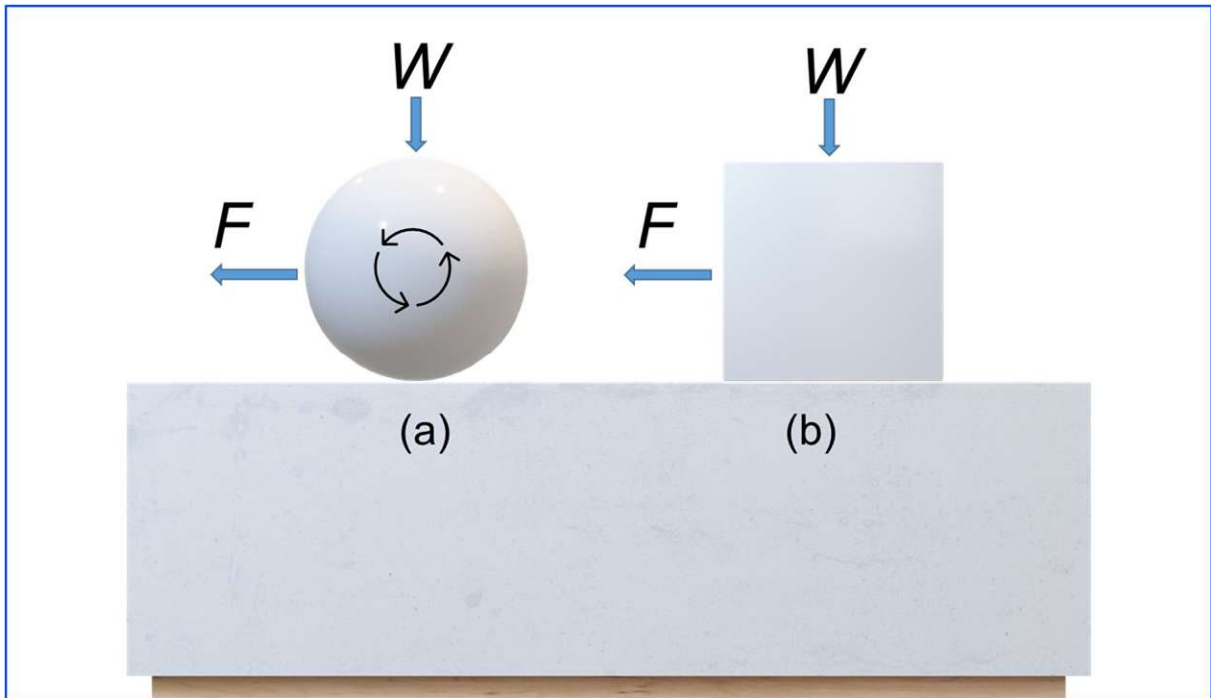

Fig. 2.2 Friction force in (a) rolling and (b) sliding.

The first law may be expressed as;

$$F = \mu \cdot W \tag{1}$$

Here in Equation 1, the proportion between the normal load and the friction force is μ, the coefficient of friction [35]. This term will be used often in this thesis, to refer to the friction phenomenon, independent from the normal load applied on the system. While the First Law is generally adhered to by most metals and a broad array of other materials, it is notable that polymers and materials characterized by an exceptionally low elastic modulus frequently deviate from this adherence.

When considering the third law of friction, two distinct variations of the friction coefficient become apparent. It is of significance to note that the force necessary to initiate the sliding motion typically exceeds that needed for maintaining sliding, leading to the conclusion that the coefficient of static friction (μ_s) exceeds the coefficient of kinetic friction (μ_k). However, once sliding is initiated, it is often observed that μ_k remains relatively constant across a broad spectrum of sliding velocities for many systems. [36].

2.1.2 Wear

Wear is a phenomenon characterized by the gradual erosion of material from the surface of a solid, induced by mechanical stresses arising from the interaction and relative motion between a solid component and a counterpart, which can be in the form of a solid, liquid, or gas [37]. Observable indications of wear encompass the detachment of minute particulate matter, the transference of material from one frictional body to another, and alterations in the material composition and structural integrity within the tribologically stressed zones of one or both interacting surfaces. The specific nature of the tribological load and the material constituents involved are instrumental in delineating distinct wear processes, including pitting, deformation, mechanical wear, frictional wear, and welding wear. Moreover, the mechanisms underlying these wear processes serve as crucial diagnostic criteria for wear characterization. Four main types of wear mechanisms (Figure 2.3) often mentioned in tribological research are surface fatigue, abrasion, adhesion, and corrosion [37].
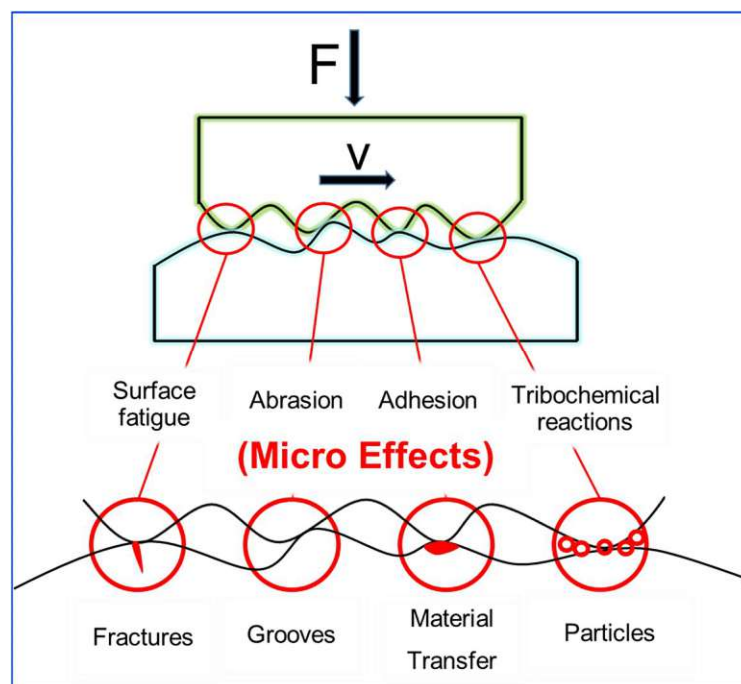

Fig. 2.3 Main types of wear mechanisms illustrated with basic appearances.

2.1.2.1 Adhesive wear:

Adhesive wear, alternatively referred to as adhesive friction or adhesive transfer, denotes a form of wear manifesting when two surfaces in relative motion adhere to each other momentarily and subsequently disengage, resulting in the transference of material from one surface to the other. This phenomenon of adhesive wear arises within localized frictional domains when the atomic forces operative between materials at contacting surfaces, subjected to pressures, exceed the intrinsic material properties inherent to each respective surface [38].

2.1.2.2 Abrasive Wear:

In a general context, abrasive wear can be defined as the process involving the abrasion, scraping, ploughing, or cutting of a material surface, which includes oxides, coatings, and substrates. This abrasive action is executed by particles, edges, or other entities possessing sufficient hardness to induce greater damage to the target material than to themselves [39]. In accordance with the definition established by ASTM International, abrasive wear is typified by the deterioration of a solid surface induced by the interaction with rigid particles subjected to compressive forces and concurrent sliding motion [40].

The abrasive wear mechanism is contingent upon the specific characteristics of the contact involved, and it manifests itself through two discernible modes: two-body wear and three-body wear [41]. Two-body wear transpires when rigid particles come into direct contact with a surface, engaging in abrasion that leads to the removal of material from the substrate. Conversely, three-body wear occurs when particles experience unimpeded mobility, allowing them to roll and glide freely across the surface, contributing to the abrasive process.

2.1.2.3 Corrosive wear:

Corrosive wear in general refers to tribochemical reactions between the two counteracting bodies and the interfacial medium [42]. An indirect wear mechanism manifests when a sliding surface is subjected to a corrosive environment, where the continuous sliding motion continually removes the protective corrosion product. Consequently, this exposes the fresh surface to additional corrosive deterioration. Corrosion wear can be characterized as an accelerated manifestation of the corrosion process due to its prompt removal of corrosive products and the passive protective layer, in contrast to static surfaces [43].

2.1.2.4 Surface fatigue:

Surface fatigue arises from the initiation, growth, and propagation of cracks [44]. This phenomenon represents a fundamental manifestation of material fatigue, wherein the material's surface experiences progressive degradation because of cyclic loading. We need to address a special case here, which is the fretting wear [45]. Fretting wear represents a distinctive variant of sliding wear, characterized by its occurrence when the relative displacement between the sliding surfaces is of exceedingly minute amplitude, typically falling below 100 μm. This recurring sub-micrometric relative motion is often induced by factors such as vibration or the elastic deformation of the contacting bodies subjected to applied loads. Such fretting-induced motion can culminate in the initiation of fatigue cracks within the material [46].

It should be stated that wear often cannot be prevented. We can minimize wear, but we won't be able to completely prevent it. In many cases we need to develop strategies to optimize friction and reduce wear. One of the main strategies would be to lubricate the surface, but we need to discuss the mechanisms and related concepts of lubrication, to understand a tribological system.

2.2 Roughness:

Surface roughness is of vital importance for many fundamental topics related to tribology such as friction, wear, thermal and electrical transfer, tolerances of contact joints, positional accuracy, additive deposition [47], lubricant wettability [48], material properties like fatigue strength [49], and of course lubrication regimes [50].

The complete characterization of real surface geometry proves challenging, as it cannot be adequately encapsulated using a finite set of parameters. The precision of the surface geometry description is intricately linked to the quantity of parameters employed. Hence, the introduction of novel parameters for surface evaluation finds justification. While existing literature has expounded upon the definitions and mathematical formulations for approximately 59 roughness parameters [51], this thesis will concentrate on a select subset of parameters sufficient to engage in discourse concerning a wide spectrum of contact scenarios and lubrication regimes.

Surface roughness parameters conventionally fall into three distinct categories, each delineated by its functional attributes: amplitude parameters, spacing parameters, and hybrid parameters [52]. Most used parameters are amplitude parameters, both 2D and 3D versions.
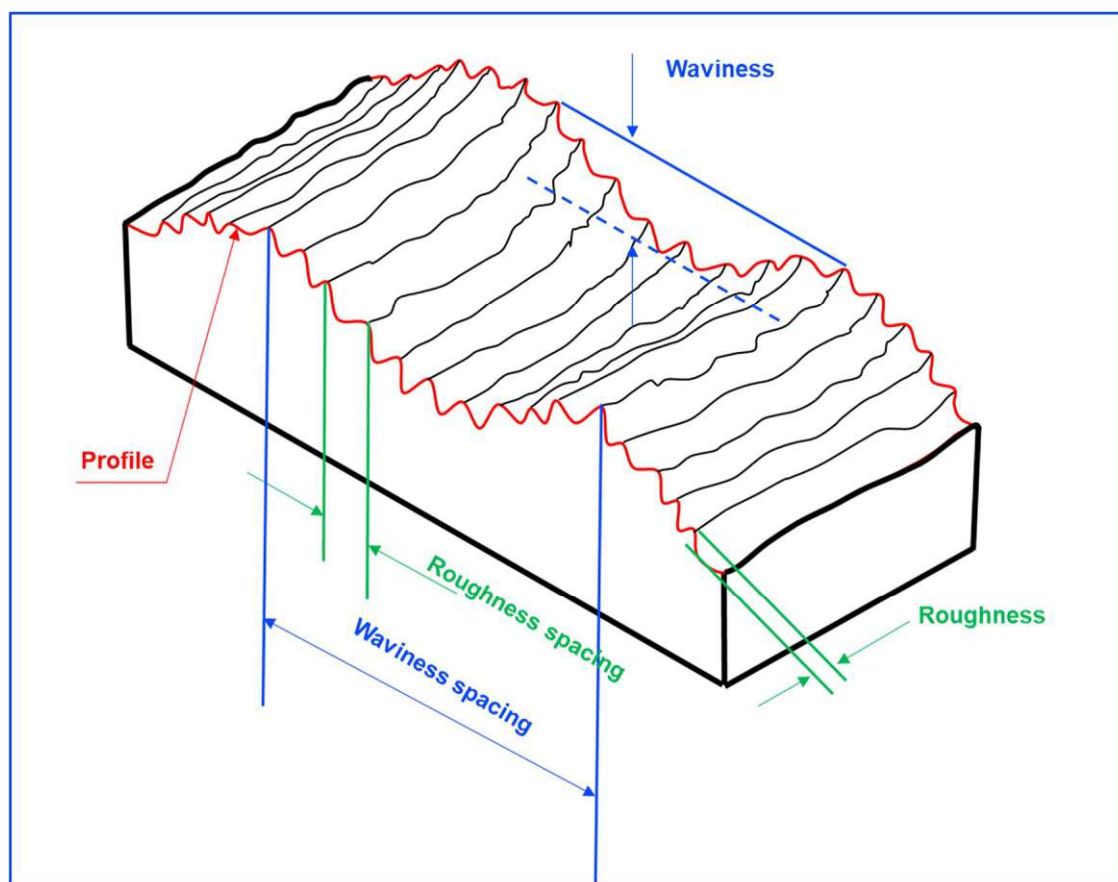
Fig. 2.4 Main definitions in surface characterization with physical appearances.

Surface roughness parameters conventionally fall into three distinct categories, each delineated by its functional attributes: amplitude parameters, spacing parameters, and hybrid parameters [52]. Most used parameters are amplitude parameters, both 2D and 3D versions. Conventionally, surface texture parameters were defined based on profile curves [53] (curves indicated by the intersection of surfaces). The 2D measurement is the profile method, but it is also known as line roughness measurement. The surface profile (Figure 2.4) is generally measured with stylus probe measurement instruments. ISO and other sets of international standards are designated for roughness measurements. Let's have a look at the main line roughness parameters as they are defined in ISO 4287 [54].

2.2.1 Maximum height (R_z):

The parameter denoted as "R_z" in profile analysis is defined as the combined magnitude of the maximum peak elevation and the maximum valley depression occurring within a specified reference length, as illustrated in Figure 2.5. Herein, "R_p" signifies the measurement of the highest peak amplitude within the profile, while "R_v" designates the quantification of the

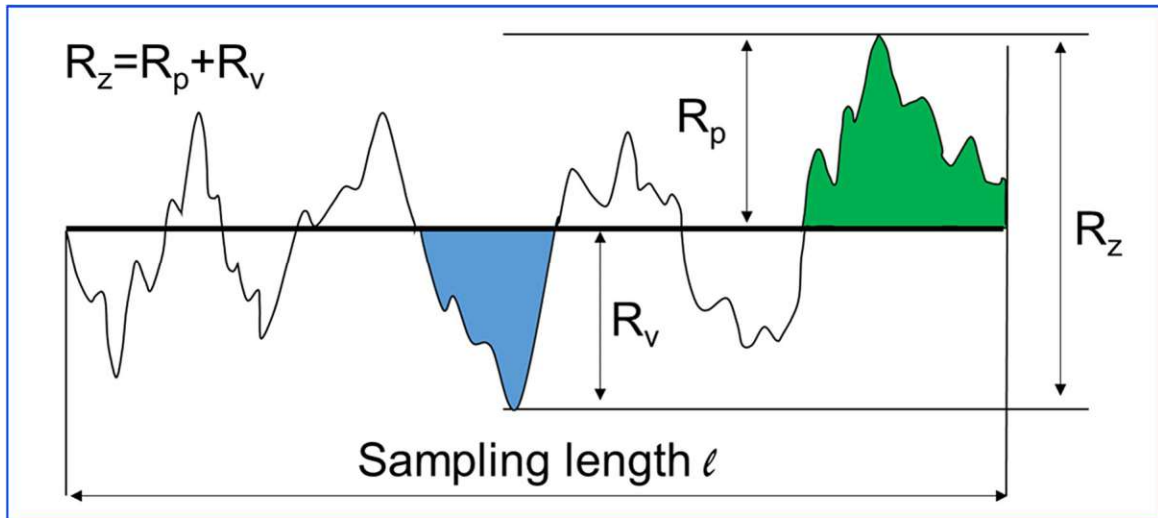deepest valley depth within the profile, both of which are assessed over the prescribed sampling length.

Fig. 2.5 Representation of the maximum peak height (R_p) and minimum valley depth (R_v) of a profile, forming the maximum height (R_z).

Even though the maximum height gives an idea about the contact zone, it can be influenced by measurement inconsistencies due to the profilometer limitations; it should be used with caution.

2.2.2 Arithmetic average height (R_a):

The arithmetic mean height parameter is widely employed in the realm of general quality control (Figure 2.6). Its popularity stems from its capacity to yield stable outcomes, as it is relatively impervious to the effects of surface imperfections, contaminants, and measurement noise. This parameter is formally defined as the arithmetic average of the absolute ordinate $Z(x)$ over the specified sampling length.
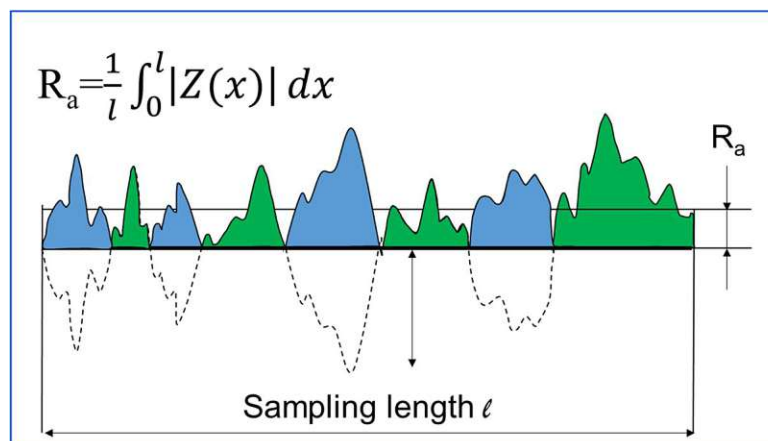

Fig. 2.6 Visualization of the calculation for arithmetic average height of a profile.

It can be easily observed that a surface with different extremities may end up with similar average values. The limitation of R_a is described also in the literature to identify functionality of the surface too [55], so we focus also on other parameters.

2.2.3 Root mean square deviation (R_q)

This parameter is alternatively referred to as the Root Mean Square (RMS) for Z(x). It serves as a metric for assessing surface roughness by characterizing the standard deviation of the distribution of surface heights, thus holding significance in the statistical description of surface topography, as depicted in Figure 2.7. Notably, this parameter exhibits heightened sensitivity in comparison to the arithmetic mean height (R_a) when it comes to discerning substantial deviations from the mean reference line. The mathematical definition and digital computation of this parameter are articulated as follows:
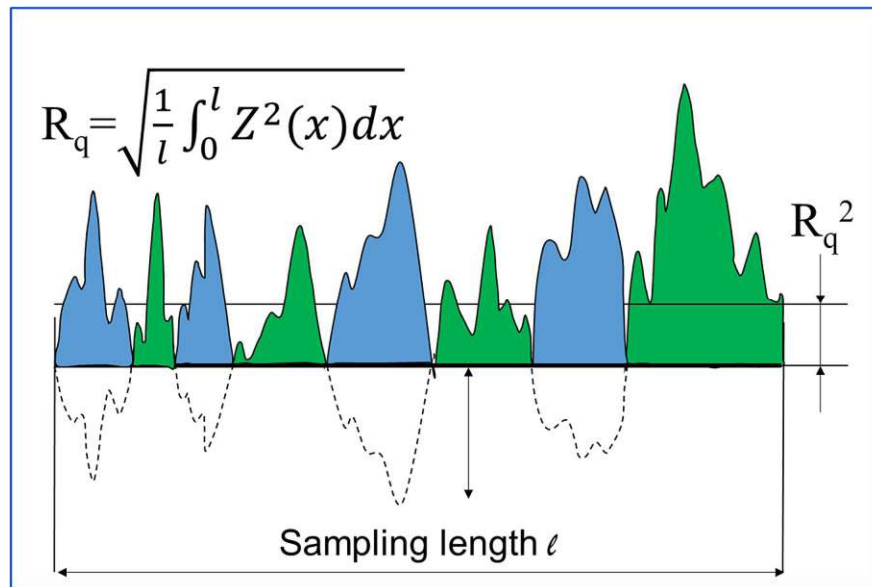

Fig. 2.7 Visualization of the calculation for root mean square deviation of a profile.

2.2.4 Skewness (R_{sk})

The skewness of a profile, as depicted in Figure 2.8, is computed as the third central moment of the probability density function associated with the amplitude of the profile, assessed across a specified length. It serves as a quantitative measure for assessing the symmetry exhibited by the profile with respect to the mean reference line. This parameter is particularly responsive to the presence of occasional extreme valleys or peaks in the profile, thereby aiding in the characterization of its asymmetry.
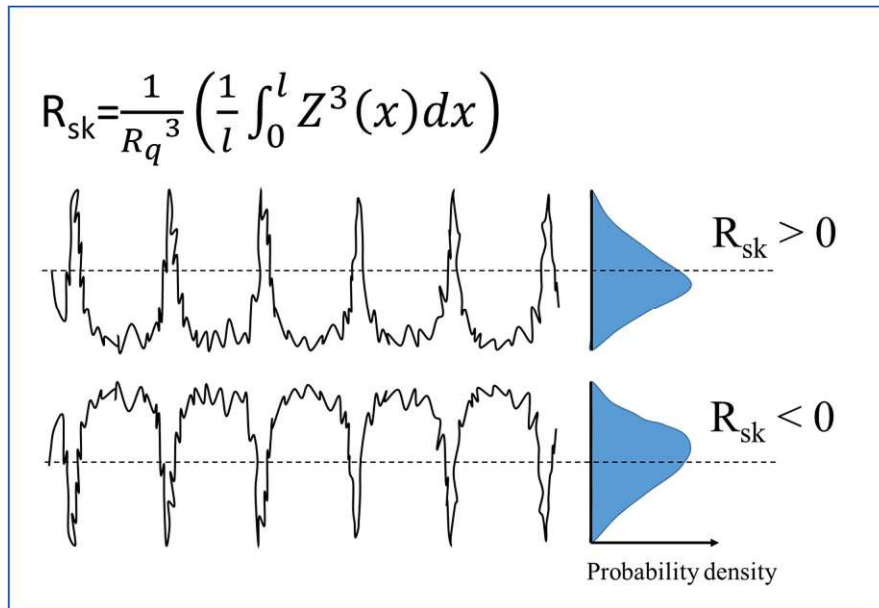
$$R_{sk} = \frac{1}{R_q{}^3} \left(\frac{1}{l} \int_0^l Z^3(x)\, dx \right)$$

$R_{sk} > 0$

$R_{sk} < 0$

Probability density

Fig. 2.8 Visualization of the skewness value for the profile and its mathematical definition.

$R_{sk}=0$: Symmetric against the mean line (normal distribution)

$R_{sk}>0$: Bulk material beneath the mean line (positive skewness)

$R_{sk}<0$: Bulk material above the mean line (negative skewness)

2.2.5 Kurtosis (R_{ku})

The kurtosis coefficient, as exemplified in Figure 2.9, constitutes the fourth central moment of the probability density function pertaining to profile amplitudes, assessed across a defined evaluation span. It serves as a quantifier of the concentration or dispersion within the probability density function associated with the profile. When the kurtosis coefficient, denoted as R_{ku}, assumes values less than 3, it characterizes the distribution curve as platykurtoic, signifying a probability density function with relatively fewer instances of pronounced peaks and deep valleys. Conversely, when R_{ku} exceeds 3, the distribution curve is classified as leptokurtoic, indicating a probability density function with a higher frequency of prominent peaks and shallow valleys.

This parameter's significance extends to the analysis of contact mechanics, as it pertains to the tip morphology of surface features, thereby offering insights into the extent of contact between two interacting objects.
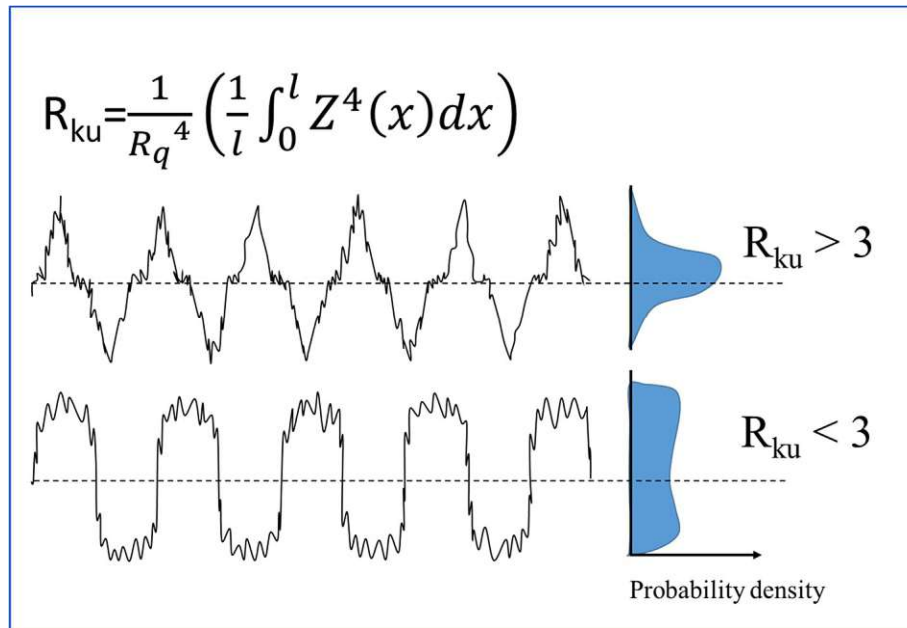
$$R_{ku} = \frac{1}{R_q{}^4}\left(\frac{1}{l}\int_0^l Z^4(x)\,dx\right)$$

Fig. 2.9 Visualization of the kurtosis value for the profile and its mathematical definition.

These discussed basic parameters describe the surface topography reasonably well. Many surfaces may have similar maximum height, arithmetic average height, or root mean square deviation, but we can identify the surface better with the help of skewness and kurtosis. Still all these discussions are based on a single line, although it can be applied to multiple lines on a surface. On the other hand, we can also look at the 3D versions of these parameters and their applications on the entire surface area of interest.
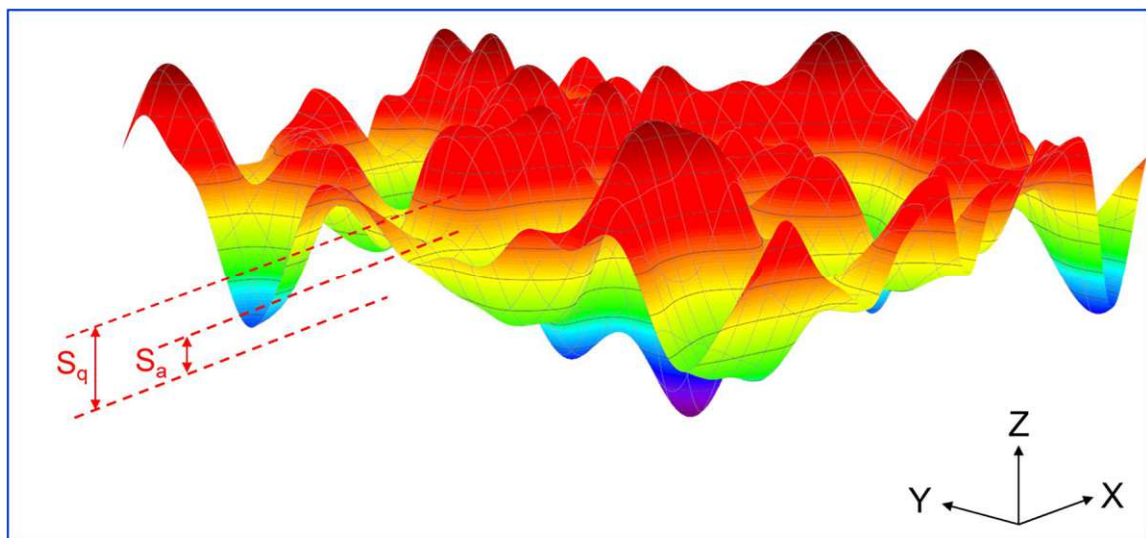

Fig. 2.10 Visualization of the arithmetic and squared mean height of a random 3D surface.

Areal roughness parameters are listed in ISO 25178 [53] but the ones we defined for profile parameters can simply be expanded or derived in a similar manner. S_p represents the

maximum peak height, S_v represents the maximum valley depth and eventually S_z would be the maximum height within the sampling area.

According to the ISO 25178, the average arithmetic mean height of the area (S_a) and squared mean height of the area (S_q) area (Figure 2.10) calculated as follows;

$$S_a = \frac{1}{A} \iint_A |Z(x,y)| \, dxdy \, , \, S_q = \sqrt{\frac{1}{A} \iint_A Z^2(x,y) dxdy} \qquad (2), (3)$$
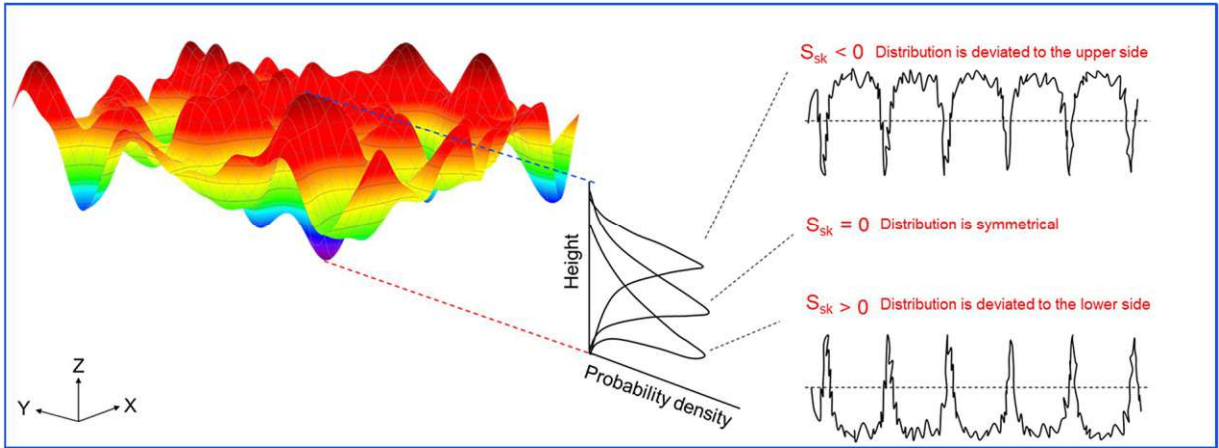
Fig. 2.11 Visualization of skewness parameter of a random 3D surface.

Also, skewness parameter, $S_{sk,}$ in three dimensions calculated as;

$$S_{sk} = \frac{1}{S_q{}^3} \left(\frac{1}{A} \iint_A Z^3(x,y) \, dxdy \right) \qquad (4)$$
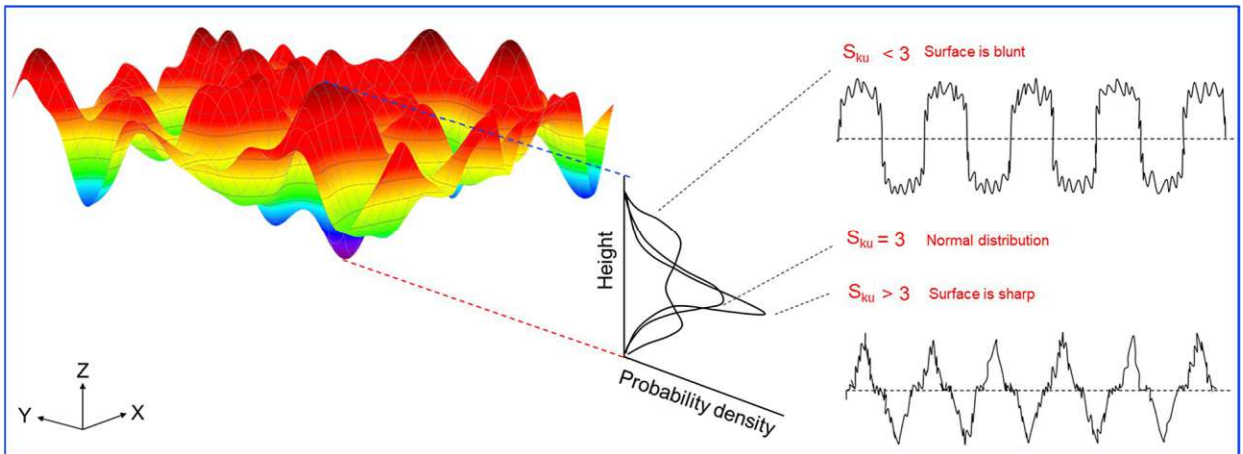

Fig. 2.12 Visualization of the kurtosis parameter of a random 3D surface.

Similarly, kurtosis parameter, $S_{ku,}$ in areal calculation defined as;

$$S_{ku} = \frac{1}{S_q{}^4} \left(\frac{1}{A} \iint_A Z^4(x,y) \, dxdy \right) \qquad (5)$$

19

Basically, we would be integrating the same values from the profile parameters in both x and y directions along the area, A (Figure 2.11 and Figure 2.12).

A cut-off length, denoted as λ_c or sampling length, is employed to mitigate the impact of extended spacing errors, such as waviness and form error, on the acquired profile measurements. Meanwhile, the evaluation length (L) signifies the span over which roughness is assessed or the distance traversed for roughness measurement, conventionally established at 5 times the value of λ_c. ISO 4288 [56] would lead us to the right cut-off length or sampling length to have the right parameters and isolate roughness from other spacing errors (Table 1).

Recommended Cut-off				
Periodic Profiles	Non-periodic profiles		Cut-off	Sampling/Evaluation length
Spacing distance [mm]	R_z [µm]	R_a [µm]	λ_c [mm]	L_c/L [mm]
> 0.0013-0.04	up to 0.1	up to 0.02	0.08	0.08/0.4
> 0.04-0.13	> 0.1-0.5	> 0.02-0.1	0.25	0.25/1.25
> 0.13-0.4	> 0.5-10	> 0.1-2	0.8	0.8/4
> 0.4-1.3	> 10-50	> 2-10	2.5	2.5/12.5
> 1.3-4	> 50	> 10	8	8.0/40.0

Table 1 Cut-off length or sampling length to have the right parameters and isolate roughness from other spacing errors.

2.3 Stribeck Curve:

To gain a comprehensive comprehension of the mechanisms governing lubricant functionality, it is imperative to explore the diverse operational regimes within which these lubricants operate [57]. In the present discourse, I endeavor to elucidate the transitions in frictional mechanisms encountered as one traverses distinct lubrication regimes, commencing from the initiation of motion, proceeding through lubrication at minimal surface speeds, and culminating in the attainment of complete surface separation facilitated by the emergence of a fully developed fluid film.

It is possible to base our observation on the film thickness derived from the Reynolds equation and the composite roughness parameter.

The lubrication regime is defined by the lambda ratio (λ), which is the ratio is the minimum film thickness (h_{min}) in relation to the composite surface roughness, where R_{a1} and R_{a2} are the roughness values for each surface respectively [58]:

$$\lambda = \frac{h_{min}}{\sqrt{R_{a1}^2 + R_{a2}^2}} \tag{6}$$

the root mean square deviation [59], or areal RMS [60,61] may also be used instead of the arithmetic average height. The λ value may be used for the x-axis of the Stribeck curve against the coefficient of friction. At lambda ratio (λ) values less than 1, it is traditionally posited that interactions among surface asperities become increasingly prominent, elevating the significance of shear characteristics within the films residing on solid surfaces, whether these films are formed through adsorption or chemical reactions [58]. This operational range is commonly denoted as the boundary lubrication regime. Within the realm of boundary lubrication, the intrinsic properties of the bulk lubricant, such as its density and viscosity, diminish in importance compared to the chemical attributes of the lubricant itself and the surface properties of the contacting surfaces. When the thickness of the lubricating film and the surface roughness are commensurate in scale, falling within the range of $1 < \lambda < 5$, the tractional behavior becomes contingent upon the bulk properties of the lubricant. However, it becomes imperative to consider the localized conditions arising from asperity interactions at the contact interfaces [62]. As lubrication conditions transition into a state characterized by the coexistence of both full film lubrication and intermittent asperity contact, this operational domain is categorized as the mixed lubrication regime. As operational speeds decrease and specific loads elevate significantly, the maintenance of complete film lubrication becomes challenging. In such circumstances, notwithstanding the concurrent existence of micro elasto-hydrodynamic lubrication (EHL), mechanical interchanges between opposing surface irregularities endure. Within this operational domain, the lubricating film provides only partial isolation between the surfaces in contact [63]. When mixed lubrication prevails, the applied contact load is distributed between the interplaying surface irregularities and the lubricant film.

In cases where the lambda ratio significantly exceeds unity, indicating the presence of a notably thick lubricating film, the traction or frictional force experienced becomes primarily contingent upon the bulk rheological characteristics of the lubricant. This dependence is observed under suitable operating conditions encompassing factors such as load, temperature, and shear rate. In this context, the influence of surface roughness becomes negligible. This

operational condition is formally acknowledged as full film lubrication, often referred to as hydrodynamic lubrication [64]. Full film lubrication represents the most preferable lubrication regime. Within this context, the contacting surfaces maintain a significant degree of separation, resulting in the frictional resistance to their relative tangential motion being predominantly contingent upon the viscosity of the lubricating medium. Additionally, given the theoretical absence of direct surface contact, the propensity for wear is minimal.
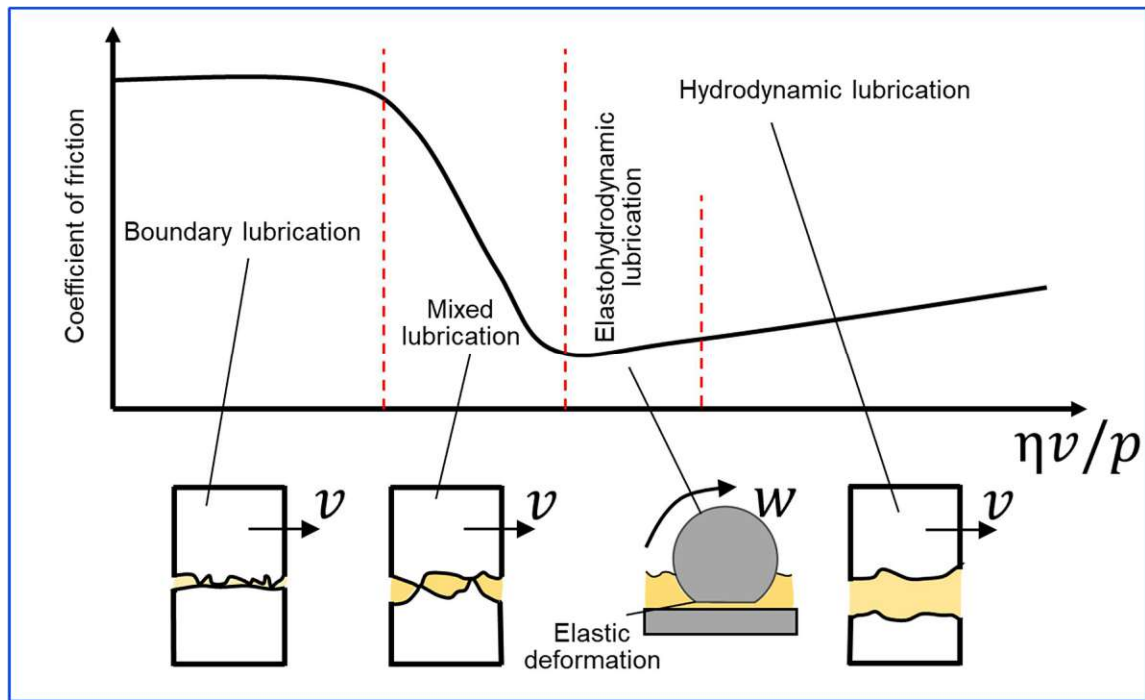

Fig. 2.13 Stribeck curve and visualization of the lubrication regimes.

Subsequently, following an analysis of Stribeck's findings, Gumbel and Hersey discerned that the friction curves exhibited a uniform pattern when plotted as a function of a parameter that encompasses various relevant factors; viscosity (η), speed (v) and load/pressure (p) [65]:

$$H = \frac{\eta \cdot v}{p} \tag{7}$$

This value is called the bearing parameter or the Hersey number (*H*), and it identifies also for the x-axis of the Stribeck curve against the coefficient of friction as it can be seen in Figure 2.13. For this calculation for $\lambda < 1.2$, the lubrication is in boundary lubrication, and for $1.2 < \lambda < 3$ it is in mixed lubrication. If the λ value is higher than 3, then it is hydrodynamic lubrication [59].

2.4 Lubrication

Lubrication is a practice employed to effectively isolate the surfaces of interacting frictional components, either completely or partially, through the judicious introduction of an intermediary medium, commonly referred to as a lubricant. This technique serves several essential purposes, including the management of heat within the contact region, the regulation of contamination levels, the mitigation of tribochemical effects, the facilitation of energy transfer, and the absorption of mechanical shocks. However, its principal objective lies in the minimization of both frictional forces and wear-related phenomena [66].

Lubricants, which encompass a diverse range of substances, are most frequently encountered in liquid form, including mineral oils, synthetic oils, and water, among gaseous forms. Nevertheless, solid lubricants are also utilized, particularly in dry sliding bearings, where materials like polytetrafluoroethylene, graphite, or molybdenum disulfide are employed. In some instances, grease finds application in components such as ball bearings, sliding bearings, and occasionally, gears. Furthermore, gases, such as air, are harnessed in gas-lubricated bearings [67].

The seminal contributions of Petrov (1883), Tower (1885), and Reynolds (1886) established the fundamental principles of lubrication theory. This theoretical framework continues to serve as the primary analytical tool for the calculation and design of machine components that undergo relative motion [68]. The characterization of frictional interactions occurring between nominally lubricated sliding surfaces frequently necessitates the evaluation of parameters such as lubricant film thickness. A method for achieving this involves the computation of film thickness and the distribution of contact pressure through the solution of the Reynolds equation [69]. In Equation (8), p is fluid film pressure, x and y are the bearing width and length coordinates, z is fluid film thickness coordinate, h is fluid film thickness, μ is fluid viscosity, ρ is fluid density, u, v, and w are the bounding body velocities in x, y, z respectively, a and b are subscripts denoting the top and bottom bounding bodies respectively.

$$\frac{\partial}{\partial x}\left(\frac{\rho h^3}{12\mu}\frac{\partial p}{\partial x}\right) + \frac{\partial}{\partial y}\left(\frac{\rho h^3}{12\mu}\frac{\partial p}{\partial y}\right) = \frac{\partial}{\partial x}\left(\frac{\rho h(u_a + u_b)}{2}\right) + \frac{\partial}{\partial y}\left(\frac{\rho h(v_a + v_b)}{2}\right) + \rho(w_a + w_b) - \rho u_a\frac{\partial h}{\partial x} - \rho v_a\frac{\partial h}{\partial y} + h\frac{\partial p}{\partial t} \qquad (8)$$

It should be noted that several assumptions were made in the derivation of the Reynolds equation [70]:

1. Negligible Body Forces: The mass of the lubricant film is considered negligible, leading to the insignificance of gravitational and inertial forces.

2. Constant Pressure: Pressure remains uniform throughout the lubricant film, implying a quasi-steady-state condition.

3. No-Slip Boundary: At the interfaces of interest, there is no relative motion between the lubricant and the solid surfaces.

4. Laminar Flow: Flow within the lubricant film is characterized by laminar behavior, rather than turbulent flow.

5. Negligible Inertia and Surface Tension: Inertia and surface tension forces exhibit minimal impact relative to viscous forces, owing to the low mass and negligible acceleration of the lubricant film.

6. Shear Stress and Viscosity Gradients: Significant variations in shear stress and viscosity gradients primarily occur within the lubricant film itself.

7. Newtonian Lubricant: The lubricant behaves according to the principles of Newtonian fluid dynamics.

8. Constant Viscosity: Viscosity of the lubricant remains constant across the entirety of the lubricant film.

9. Parallel or Slightly Inclined Surfaces: The surfaces in contact are either parallel or positioned at a slight angle relative to each other, facilitating the assessment of their relative motion and interaction.

The first six assumptions are almost always valid, but the 7th and 8th assumptions can be modified for non-Newtonian lubricants too.

2.5 Biotribology

After introducing the basic parameters and definitions in tribology, finally we can start focusing on the main topic of this thesis. The term "biotribology," encompassing the study of "all facets of tribology pertaining to biological systems," was introduced relatively recently, approximately four decades ago [71]. Nevertheless, investigations into the principles of friction, lubrication, and wear concerning biological tissues have a historical precedent extending much further back in time. As early as the nineteenth century, luminaries such as Young (1809) and Poiseuille (1840) delved into the flow characteristics of blood, a crucial endeavor with contemporary implications for the design of artificial organs [72]. Reynolds, in his pioneering work, drew parallels between the lubrication mechanisms operating within articulated joints and those in mechanical machine elements. In the concluding statement of

his seminal paper, Reynolds underscored the fundamental importance of hydrodynamic lubrication, noting that it is "as indispensable to the mechanics of living organisms as the lubricating function of the journal bearing is to mechanical devices" [73]. Biotribology has emerged as a dynamically evolving field, occupying a prominent position within the broader domain of tribological research over the past four decades. While the spectrum of topics encompassed by biotribology has considerably expanded during this period, it remains intriguing to discern fundamental similarities in the mechanisms governing lubrication, friction, and wear across diverse tissues engaged in disparate physiological functions (Figure 2.14).
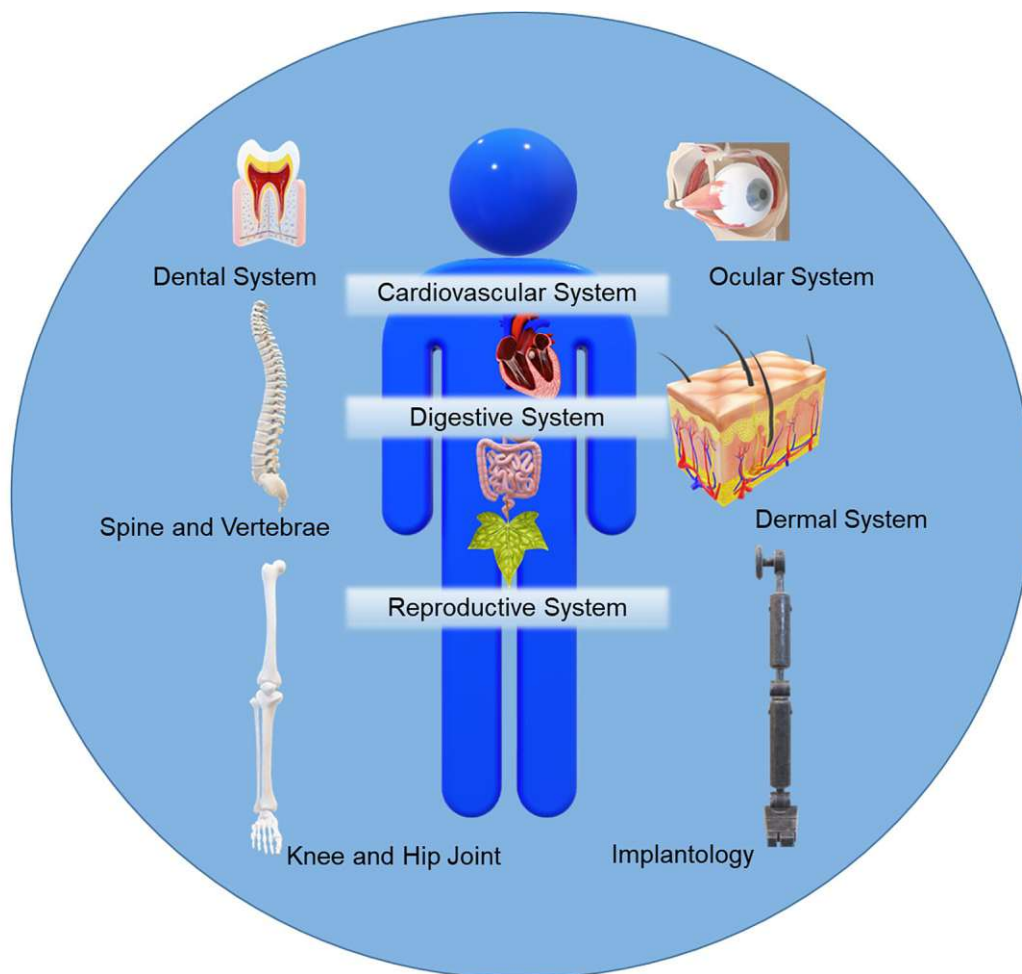

Figure 2.14 General aspects of biotribology with respect to different zones of the human body.

In general, applications related to biotribology are investigated in two main categories: lifestyle and healthcare [74]. In lifestyle applications we have, e.g., electric shavers, ironing machines, toothbrushes, cellphones, make up tools, piercings, glasses. On the other hand, in healthcare systems, applications include catheters, sleeping CPAP masks, contact lenses,

ultrasound, probes and gels, implants (dental, hearing, artificial joints). Some applications like contact lenses or glasses were also commonly used in both applications for medical purposes and fashion statements. If we talk about the global impact in a monetary way, the market for medical devices alone keeps increasing and reached about \$456.9 billion in 2019 [75].

Chapter 3 Methodology and Materials

3.1 Atomic Force Microscopy (AFM)

The atomic force microscope (AFM), alternatively referred to as a scanning force microscope, belongs to the category of microscopes categorized as scanning probe microscopes [76]. What sets AFM apart from other members within this family is its exceptional versatility. In contrast to conventional microscopes, which rely on the collection of radiation transmitted through or reflected from the specimen [77], the AFM operates on a fundamentally distinct principle. In the latter case, the ultimate resolution is constrained by diffraction limitations and is contingent upon the wavelength of the radiation employed. This is the reason that the maximal light microscopy resolution is approximately 200 nm. To achieve higher resolution images of biological samples, we may turn to electron microscopes (EM) that use high-energy electrons [77]. Even though there are many advances in the development of new EM models, we still need to create a full or partial vacuum environment and it is challenging to preserve the native structure of the sample.
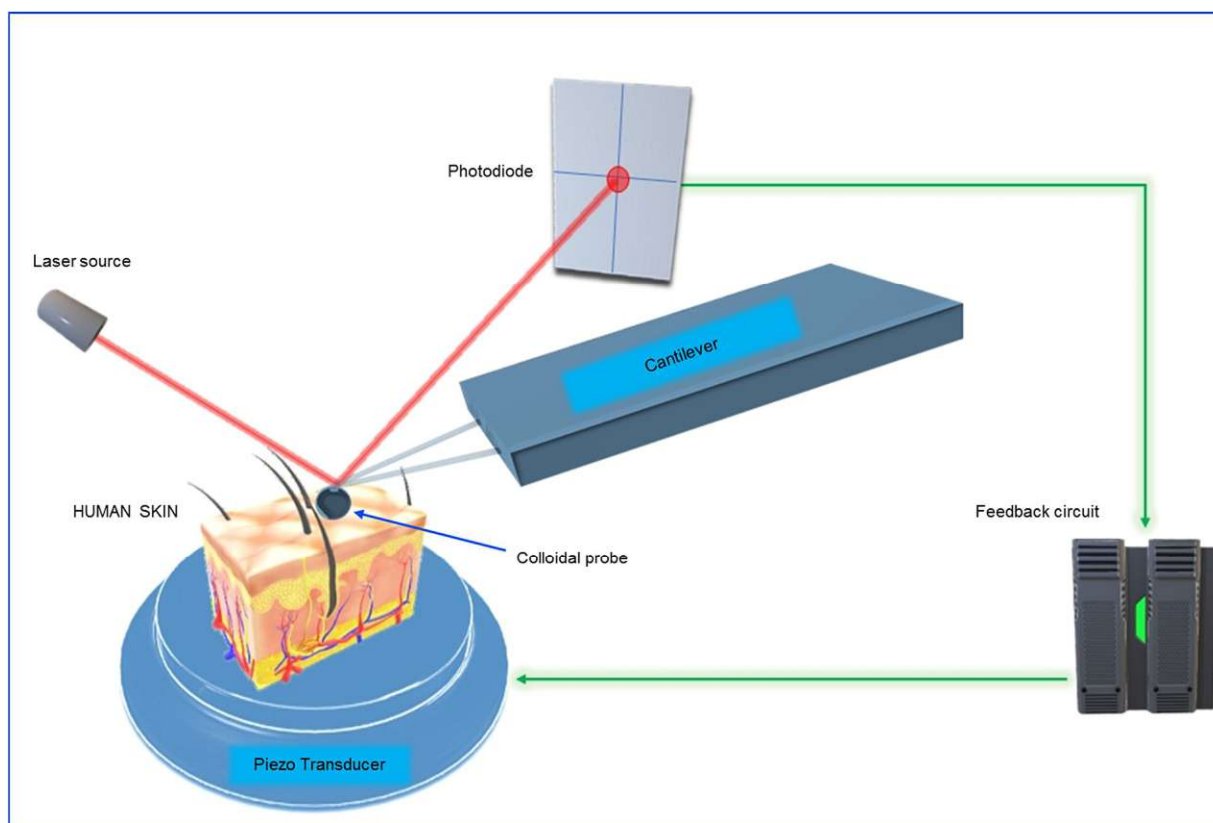

Fig. 3.1 Schematic diagram of an AFM tip-cantilever assembly processing a sample surface.

On the other hand, SPM images are recorded with the changes in the magnitude of interaction between the probes and the samples. In this case the resolution of SPM is defined by the sharpness of the probes [78]. This allows us to go to the atomic level in resolution and operate in gaseous and liquid environments. Eventually, the natural and physiological condition of the biological material can be observed. Figure 3.1 is a schematic illustrating the principle of the AFM. The AFM is like a stylus profilometer by means of construction, and it consists of a tip at the end of a cantilever beam.

The standard cantilever probe is designed to be sensitive enough to perceive forces in the range of piconewtons. This tip is subjected to interaction forces as it scans across the sample. These forces deflect the cantilever beam, and these deflections are correlated with the surface topography [79]. A laser source is directed on the back side of the cantilever and the reflection of the laser falls on the photodiode. This photodiode converts the tip deflection into a voltage signal. The deflection signal is passed to feedback circuitry controlling the vertical position of the probe, to hold the tip deflection constant as it scans over a sample (when the force is constant). The amount of vertical adjustment corresponds to the relative height of the surface [76].

Hysteresis can be corrected using linear position sensors (i.e., strain gauges) to adjust the drive voltage and counter piezo hysteresis during a scan [80]. AFM head and additional piezo stacks may increase the size range of samples that can be tested. This adjustment allows us to image even small tissue sections. For biological applications, the AFM scanner is typically positioned on the stage of an inverted epifluorescence or confocal microscope [81]. This allows not only the topographical AFM images to be registered with specific fluorescently labeled structures but also, as we will discuss in 3.1.1, production of self-adjusted tips for different needs of biological research. The tip design is the part with which the users may have control over the interaction between the surface and the probe, and the choice of geometry is an important part of the contact mechanics discussion during the analysis of the results [82]. Even though tip sharpness was mentioned to be important for image resolution, extremely sharp tips can be disruptive to the biological sample. In addition to that, a strong and stable adhesion force is essential for uninterrupted scanning over a sample with varying phases of materials, as it is in most cases of biomedical research [83].

3.1.1 Colloidal probe designed for skin measurements

Operating an AFM presents unique challenges, particularly in the context of environments that are arduous to replicate experimentally. Human tissue surfaces, often characterized by substantial compliance, exhibit responsiveness to mechanical stimuli. Additionally, the lubrication conditions within these environments tend to display a degree of variability [84]. Considering these conditions there would be three main concerning points that need to be adressed for the probe design [85]:

 ➢ Establishing well-defined geometry to enhance the precision of contact mechanics models.

 ➢ Augmenting lateral force sensitivity for improved measurement accuracy.

 ➢ Enhancing the adhesive interaction between the probing instrument and the skin tissue.
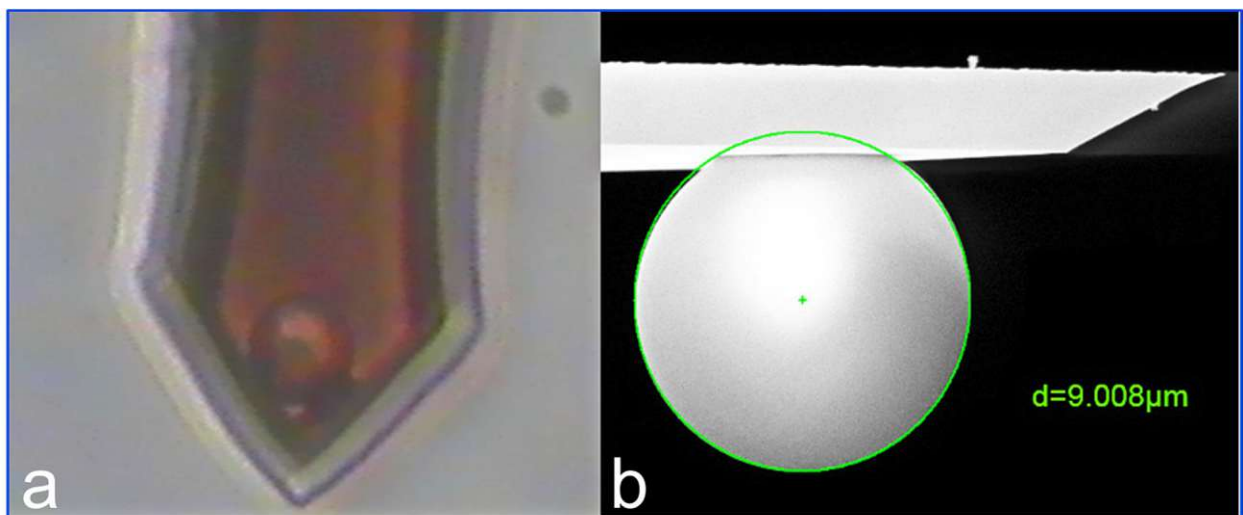

Fig. 3.2 Images of the colloidal probe a) with confocal microscope attached to AFM during the approach of the cantilever b) with scanning electron microscopy [84].

When we focus on the deformation observed when an AFM tip is in contact with sample surface, the basic model would be established on Hertz's theories on contact mechanics [86]. But his theory assumes that the surface being deformed is homogeneous and neglects the adhesive interaction between probe and the surface. Two major models that are based on the Hertz model, JKR (Johnson, Kendall and Roberts, 1971) and DMT (Derjaguin, Müller and Toporov, 1975) investigate the adhesive contact in more detail [87]. The JKR model is best suited to compliant samples, strong adhesive forces, and large tip radii; on the other hand, DMT is more suitable for stiff materials, weak adhesion forces and sharper tips [88]. In this

case, our biological system would fit more in the direction of JKR model as the sample is compliant, the choice of large tip radius of 9.008 μm (Figure 3.2) and eventually strong adhesive forces.

For the material of the colloidal probe, borosilicate glass microspheres were selected. The main reasons for the selection are that; these spheres have a roundness value larger than 90%, they have the lowest density among other glasses with 2.2 g/cc, and they have a very low thermal expansion coefficient of $32 \times 10^{-7} /°C$ [89]. This thermal expansion value is very important for the production method of the colloidal probe. Traditional methods include epoxy and adhesive application on the cantilever for the attachment [90]. This application may create contamination on the surface and change the adhesive interaction between the probe and the surface. We applied a novel method that uses the cantilever-moving approach and borosilicate glass microspheres were carefully grabbed like fishing, by the capillary adhesion between the cantilever and the spheres. A critical point here is the microspheres should be on a glass substrate that is sputtered with gold so that the cohesion between the glass substrate and the spheres is avoided. Then the cantilevers with attached spheres are placed in the oven and the temperature is gradually increased (100 °C/h) to 780 °C and the spheres would covalently bind to the cantilevers. In this point, the low thermal expansion coefficient of borosilicate glass is a defining parameter. Each probe was checked with SEM and the statistical method of AFM reverse imaging [90].

It is imperative to acknowledge that, despite the meticulous avoidance of contamination arising from epoxy or adhesive usage, there remains a potential for material transfer from the biological specimen onto the probing instrument. Consequently, a cleaning regimen becomes necessary at specified intervals during the testing process. In this context, the probe underwent a rigorous cleaning procedure, encompassing ultraviolet treatment and a series of sonications: 15 minutes in acetone, succeeded by 15 minutes in distilled water, repeated twice. Following these rigorous cleaning measures, the probe remained structurally intact, with no discernible abnormalities in its functionality, and the anticipated adhesion forces were duly observed in the force curve analysis conducted via AFM [91].

3.1.2 Skin samples for the AFM tests

The depiction of skin in Figure 3.1 portrays a generalized three-dimensional representation encompassing its three primary layers: the epidermis, dermis, and hypodermis. In our study utilizing AFM, our focus centers primarily on the epidermal layer. It is important to note,

however, that the epidermis itself comprises multiple sublayers, as delineated in Figure 3.3. Specifically, the outermost layer known as the stratum corneum plays a pivotal role in interfacing with the external environment [92]. The primary function of the stratum corneum is to regulate the evaporation of water from the skin, while concurrently serving as a protective barrier against mechanical abrasions, foreign substances, and microbial agents. Additionally, it constitutes the initial defense mechanism against ultraviolet light, effectively screening out over 80 percent of incident ultraviolet B irradiation [93].

A comprehensive grasp of the structural composition and functional attributes of the stratum corneum is essential for the optimization of its protective capabilities. Fundamentally, the process involves the transformation of living keratinocytes into non-living corneocytes, wherein the cell membrane is supplanted by a stratum of ceramides that establish covalent linkages with an encompassing framework of structural proteins [94]. This intricate configuration envelops the cells within the stratum corneum, contributing significantly to the skin's barrier function. Moreover, cells within the stratum corneum feature a dense keratin network, a protein renowned for its role in preserving skin hydration by mitigating water evaporation [95]. Furthermore, these cells possess the capacity to absorb water, further fortifying their role in maintaining skin hydration.

It is noteworthy that keratin, as a ubiquitous biological polymer, constitutes a predominant component of epidermal appendages in mammals, avians, and reptiles. These appendages encompass structures such as nails, hair, the outermost skin layer, feathers, beaks, horns, hooves, whale baleen, claws, and scales [96]. Notably, these examples underscore the robustness of these animal components, a quality that is attributable, in part, to the high stiffness characteristics inherent to keratin.

In addition to the keratin-based barrier, the stratum corneum also features a multifaceted amalgamation of lipids. These lipids are excreted by the sebaceous glands associated with mammalian hair follicles, subsequently forming a fluidic film that overlays the skin's surface [97–99]. This lipidic film encompasses various constituents, including triglycerides, diglycerides, free fatty acids, wax esters, squalene, and cholesterol [100]. It is important to note that delineating the distribution of this lipid layer, analyzing its mechanical characteristics, and ultimately discerning the tribological behavior of human skin in this context present noteworthy challenges.

Skin samples have been provided by Dr. Cilurzo from the University of Milano Department of pharmacy. The samples were obtained after an esthetic surgery following the standards introduces by Blank and McAuliffe [101].
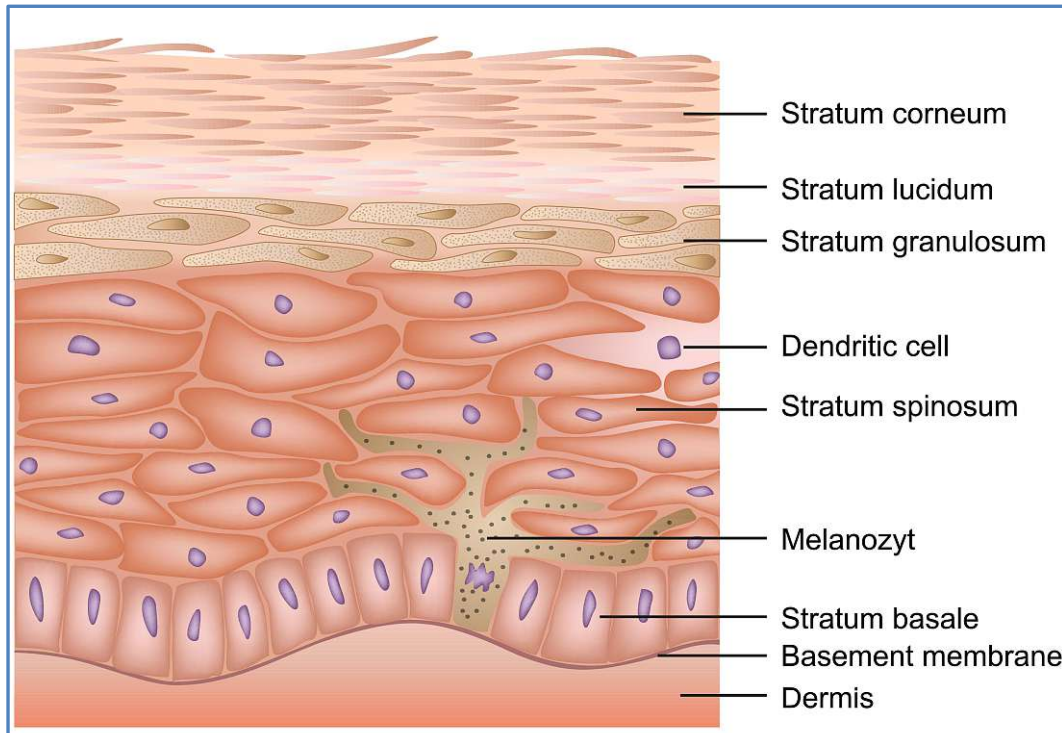

Fig. 3.3 Structure of epidermis and specifically the top layer, stratum corneum.

Full-thickness skin samples were hermetically sealed within evacuated plastic containers and promptly frozen at a temperature of -20°C within a 24-hour timeframe after their removal. For the subsequent preparations, the skin samples were methodically thawed to room temperature, and meticulous removal of any surplus adipose tissue was undertaken. The skin was then sectioned into square segments, followed by immersion in 60°C water for one minute to facilitate the gentle separation of the epidermal layer from the remaining tissue, allowing it to subsequently air-dry.

Upon receipt of the skin samples at the Center for Interdisciplinary Microsystems, Nano- and Molecular Systems (CIMaINa), they were further divided into appropriately sized fragments amenable for AFM investigations and subjected to storage at a sub-zero temperature of -40°C. Prior to commencing the measurements, each skin fragment underwent a thawing process, initially in a refrigerator set at -4°C for a duration of 2-3 hours, followed by a subsequent thawing period at room temperature for 4 hours. It is noteworthy that no supplementary procedures, such as nitrogen fluxing or cleansing with distilled water, were implemented before conducting the measurements.

The first challenge was to identify the side of the samples that is facing the direction of the environment (and not the side facing the stratum lucidum or stratum granulosum) as the two sides of the samples will represent significantly different morphologies [102]. A sample is cut in half, and one part is reversed upside down. In this case we assure that we are looking at both sides, and it is the same location skin sample.
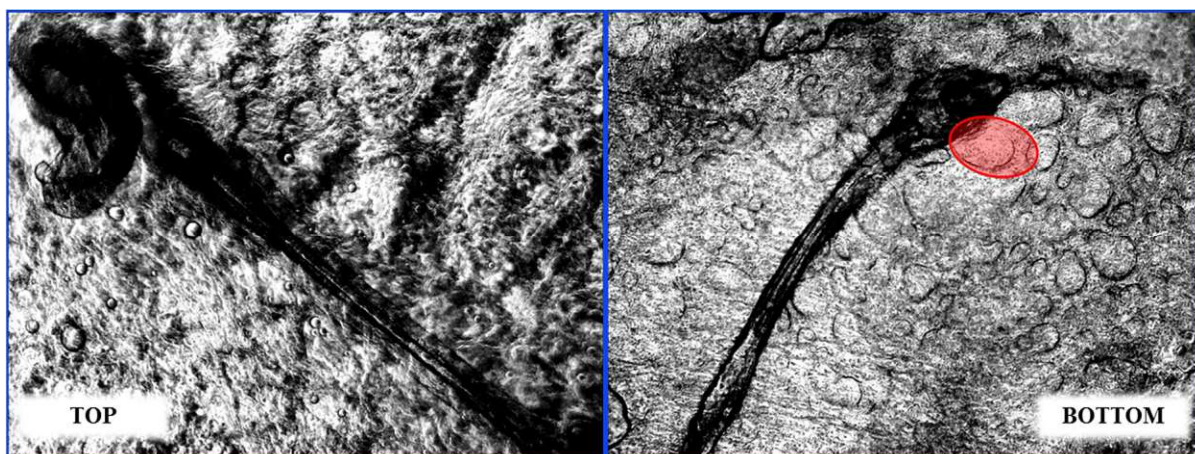

Fig. 3.4 Optical microscope image of top and bottom sides of the skin sample (highlighted granular images captured on bottom side)

Images taken with optical (confocal) microscope, attached on the AFM, with 10x magnification shows different morphologies of the two different sides (Figure 3.4). One side shows the flaky structure of keratin layers expected to be observed on the top side of the stratum corneum and, on the other side, we may observe a granular structure expected from the side lying on the stratum granulosum. Then the AFM images related to both sides were captured. The side capture on the top side of the sample has a similar layered structure with keratin flakes that was observed with optical microscopy and the bottom side with granular sites (Figure 3.5). Investigations on topography of the stratum corneum have been conducted using a regular rectangular tip with Nanoscope V Bioscope 2 AFM (Veeco Instruments).
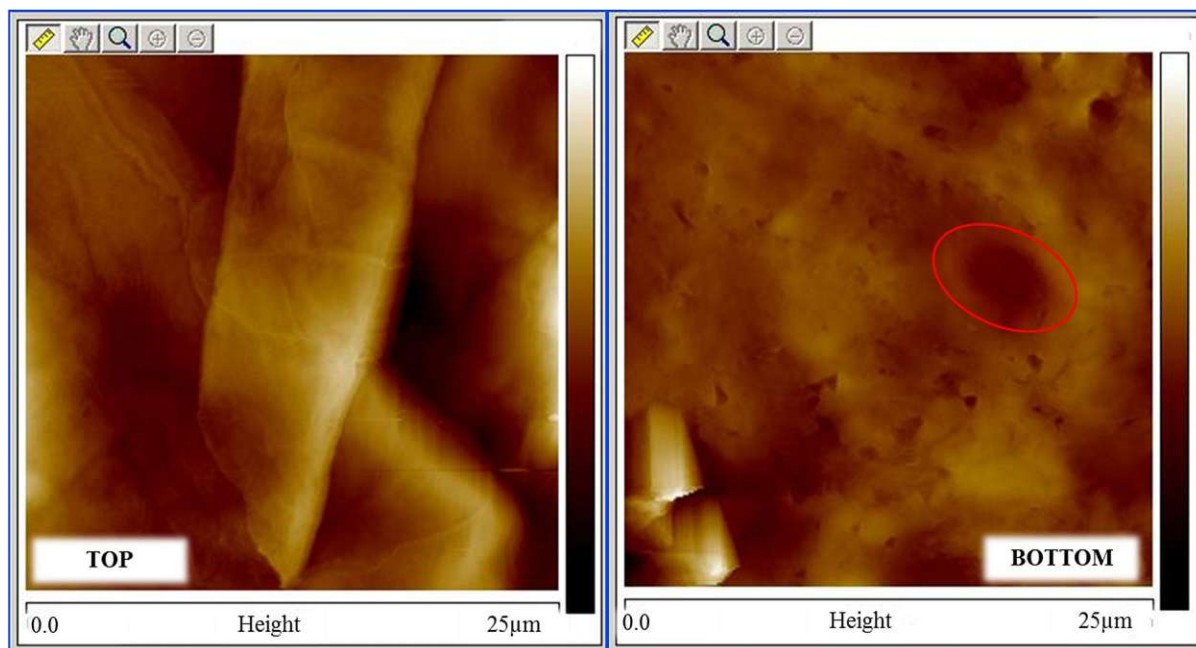
Fig. 3.5 AFM height maps of top and bottom images of the skin sample (highlighted granular images captured on bottom side).

3.2 Micro-Tribotester (MTT)

Within the framework of this thesis, we have used two different types of micro-tribotesters (MTT). The first one is the Tetra Basalt® - Must (Figure 3.6). This MTT is a modular system designed to measure surface interactions at a wide range of loads with high precision.

3.2.1 Tetra Basalt® - Must

Interchangeable modules for the movement of the specimen, let us use the reciprocating and pin-on-disc modes. The normal load may vary between 1 μN – 10 N. The value of the load can be adjusted with the selection of spring constant values and spring formations (Figure 3.6). As the measurements will be conducted on the corneal cell cultures, the lowest spring constant cantilever available using stainless steel was produced. Our primary objectives encompassed the assessment of various lens designs and materials, the cultivation of a foundational comprehension of damage mechanisms, the mitigation of epithelial injury, and the elucidation of factors that impact the interplay among the eye, contact lens, and eyelid. Furthermore, the devised system holds applicability in conjunction with cell cultures derived from diverse human tissues, such as vascular endothelium for applications pertaining to cardiovascular research, or columnar endothelium for studies focused on intestinal applications.

The fundamental operational unit within the Tetra Basalt® system, which is essential for the measurement of both normal and tangential forces, comprises a 2D-micro force transducer. This force transducer is constructed with a cantilever, designed according to a parallel spring system, along with two mirrors firmly affixed to the mobile segment of the cantilever, positioned directly in front of the fiber optic sensors (FOS), and is further supported by a mechanical framework, as illustrated in Figure 3.6. The fiber optic sensors serve the dual purpose of quantifying the deflection of the force transducer and facilitating the precise positioning of the piezo drives.
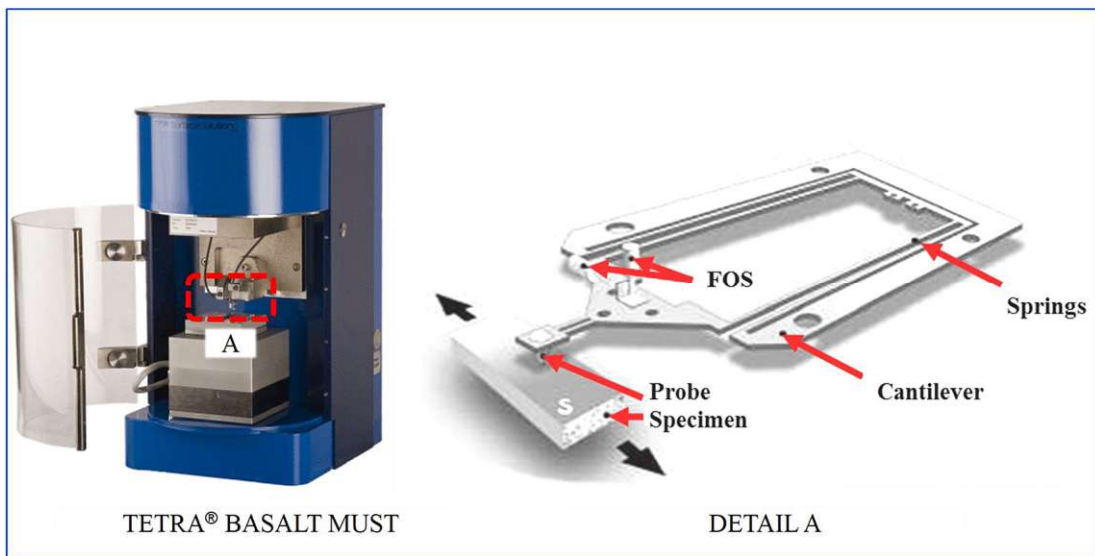

Fig. 3.6 General view of Tetra Basalt® - Must and detail of the selection A with the cantilever and fiber optic sensor set-up.

Within the terminal section of the fiber optic sensors (FOS), clusters of glass fibers are intricately amalgamated and meticulously fashioned to achieve an optical flat configuration. The transmission of light emanates from a bundle of light conductors and is subsequently redirected via a mirror, facilitated by an additional bundle of light conductors. Following this optical journey, the light is transformed into electrical signals through the agency of opto-electronic transducers, as delineated in Figure 3.7.

The determination of the sensing rate characteristic, denoted as $U_y = f(y)$, is primarily governed by optical principles and adheres to the photometric distance law. Notably, this sensor possesses the capacity for operation within two distinct measurement ranges. In specific intervals within these ranges, the alteration in intensity exhibits a linear relationship.

In the initial measurement range (as depicted in Figure 3.7, denoted as area 1 or the near range), a notable feature is the rapid elevation of the characteristic in response to a relatively

minor alteration in distance. Conversely, in the subsequent measurement range (Figure 3.7, area 2 or the far range), the span of measurement is broader, accompanied by a commensurately gentler ascent of the characteristic. The zenith point of this characteristic is referred to as the optical peak. It is pertinent to mention that the manufacturer undertakes the calibration of the Fiber Optic Sensor (FOS), and the calibration values for the standardized sensor characteristic are provided alongside the tribometer.
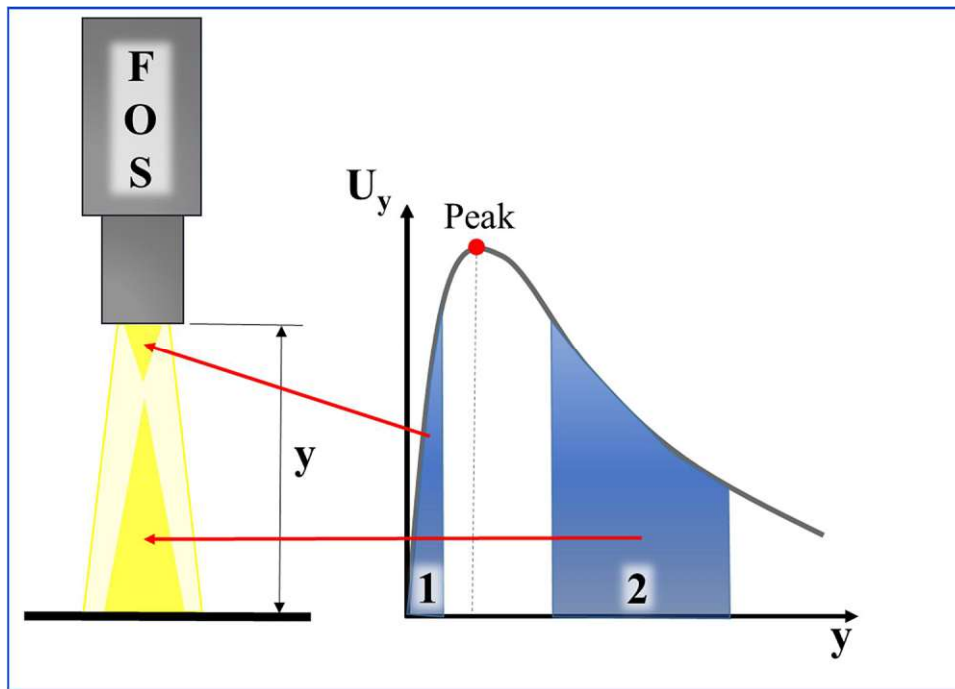

Fig. 3.7 Characteristic calibration line of fiber optic sensor.

3.2.1.1 Designed specimen holder for Testing Contact Lenses on Cell Lines

The main challenge for the probe design was that we aimed not to alter the shape of the delivered contact lens. The design is formed to hold the entire contact lens while creating a defined contact geometry. On the other hand, this probe should be attached to a very sensitive cantilever that can detect sub-millinewton forces but also work submerged in the buffer solutions to keep the cell lines in healthy conditions during the tribological tests.

The first step in designing the probe involved the meticulous selection of an appropriate cantilever. The scope of applications primarily revolved around pseudostratified variants of epithelial cell lines that were cultured to emulate various organ types within the human body. It is noteworthy that documented values for normal forces in this context have been as modest as 200 μN [103,104]. For the present study, we employed cantilever No 91555, sourced from TETRA Gesellschaft für Sensorik, Robotik und Automation mbH (Tetra GmbH, now an

integral component of Avatera medical GmbH). This cantilever is characterized by its specific spring constants $k_n = 16$ and $k_t = 7$, with a maximum normal load of 4 mN (with 4 μN resolution), and a maximum tangential force of 3.5 mN (with 3.5 μN resolution), was selected.
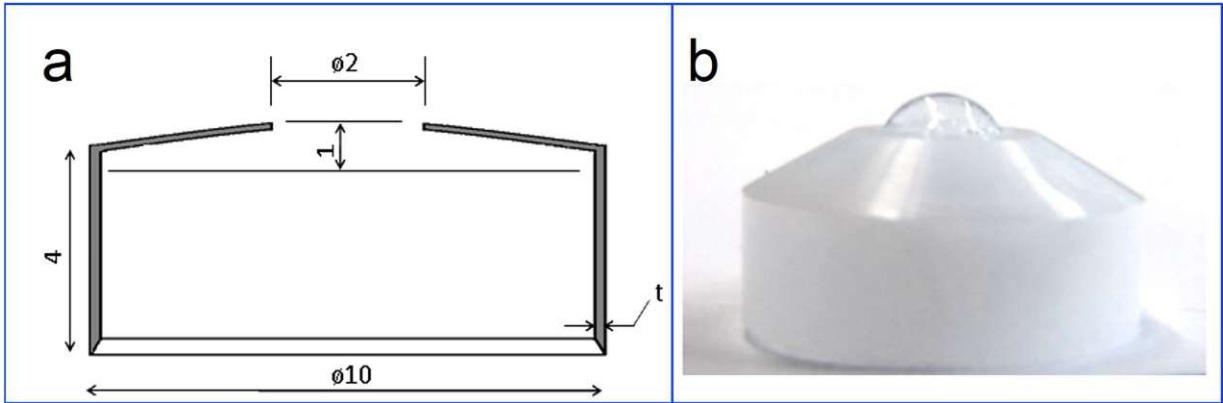

Fig. 3.8 a) Technical drawing of hardened plastic cover b) Real life image of hardened plastic cover and passing form of hydrogel contact lens.

The second step was to build a cover for the probe tip. This cover (Figure 3.8 a) was built with stainless steel as it was also used as a mold for the compliant silicon rubber that would mimic the eyeball and support the contact lens (Figure 3.8 b) and this mold would be put on another mold with half spheres with variable diameter half spheres on it to have a defined contact geometry (Figure 3.9)
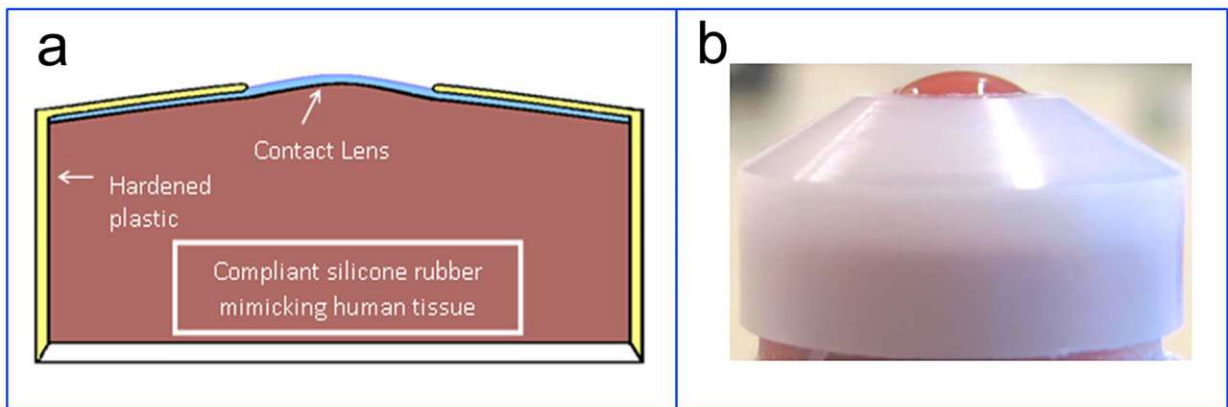

Fig. 3.9 a) Simulation of the final assembly b) Real life image of the final assembly.

The probe needs an extension to have the adequate height to be completely immersed in the biological solutions. This would also help us to eliminate the strong meniscus force that could have played a critical role at such small loads [105]. It also should be rigid to avoid self-bending and eventually cause the crosstalk effect on the cantilever during the test [106]. The probe has no

glue in its design, the lens is held in place by the contact around the edges, between the mold and the cover. Thus, contamination is minimized, and cleaning of the probe is possible for each test. The final appearance of the probe immersed into the biological solution can be seen in Figure 3.10.
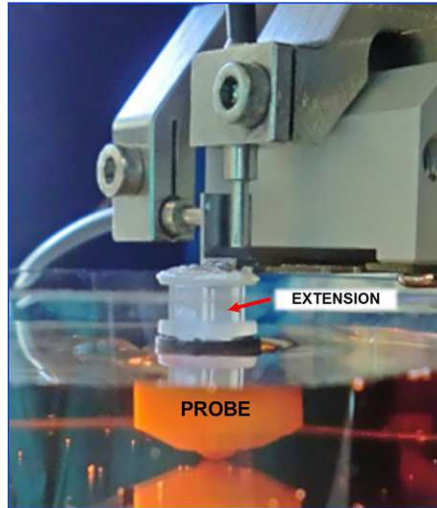

Fig. 3.10 Image of probe designed for the micro-tribometer with the extension for the probe.

3.2.1.2 Working in liquid environment and tare values

When we discuss large meniscus forces, we need to define what we mean by large. First of all, it needs to be underlined that tribotester was not designed to conduct experiments in liquid environments. In many cases, these meniscus forces are small enough to be neglected in ambient air conditions. We can observe that there is a pulling force of nearly 1 mN on the probe, where the desired force is 0.3 mN (Figure 3.11).
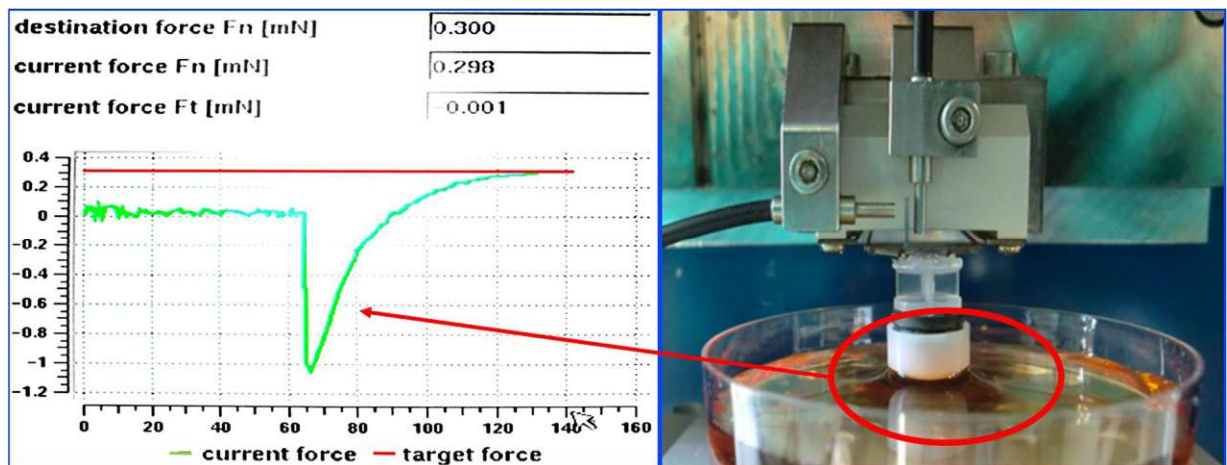

Fig. 3.11 Meniscus force recorded during the approach of the probe (screen captured /non-recordable data) with the meniscus formation highlighted in red.

In this unique application in solution, with less than a millinewton normal loads applied on the samples made of cellular lines, we cannot neglect this meniscus force [107]. To mitigate this complication, the tare function is usually applied. One may zero any load on the sample before the test is started, and this meniscus force would not affect the tests. We noticed, however, that the system of Tetra Basalt® - Must tribotester is designed to record loads only when the cantilever is pushed upwards. In this case the tare function does not recognize - 1 mN of meniscus force and we had to instead apply target force of 1.3 mN, instead of the desired 0.3 mN, which lead to total removal of cellular cultures. Following communication with the company Tetra GmbH, the software was updated accordingly, and the tare function recognized loads applied in a downward direction. This update solved the problem and tests managed to be conducted without the removal of entire cell culture.

3.2.1.3 Cell cultures and polymeric coatings used for micro-tribotester

Culturing cellular lines is a time consuming, sensitive, and costly procedure [108]. So before moving towards the tests with cellular lines, it would be a logical choice to test the stability of the tribotester with the new cantilever and probe on a biomaterial that mimics epithelial tissue. While the use of Dacron™ (a version of polyethyleneterephthalate) [109] and polytetrafluoroethylene (ePTFE) [110] is not possible due to their textured and non-transparent nature, we turned to multiple materials like Mylar™ (a film version of polyethylene terephthalate), Teflon-AF™ (a spun cast production and a copolymer of perfluoro 2,2 dimethyl-1,3-dioxole and tetrafluoroethylene) [111], poly-(amidoamine) hydrogels [112] and CarboSil® TSPCU that were used for applications related to cell culturing in the literature. Among the candidate materials considered, CarboSil® TSPCU (Figure 3.12) emerged as a noteworthy selection due to its tensile strength comparable to conventional polycarbonate urethanes, coupled with enhanced biostability attributed to its silicone component [113]. This material demonstrates versatility across diverse fabrication methodologies, rendering it adaptable to produce various medical devices of varying geometries. Its utility extends to an extensive array of medical applications, encompassing cardiovascular and neural electrostimulation, continuous glucose monitoring, drug-eluting systems, and orthopedic implants.

We conducted our repeatability tests with different scan rates (0.25-0.5-1.0 mm/s), normal load varied between 0.2 mN – 2 mN, and on three different versions of CarboSil®: 80A, 90A, and 55D.

For the cell cultures, Corning® culture dishes were used. These dishes are optically clear, made from polystyrene and tissue culture treated for optimum cell attachment. Also, Secureslip™ glass coverslips were used, and these coverslips were affixed to a thin transparent silicon base in order to secure the coverslip to culture vessels to prevent movement and cell damage during cultivation and assay procedures.

Two types of cell lines were chosen for our tests. The first one was the primary cell lines of fibroblasts with Biosafety Level 1. These cell lines were HT-1080 - muscle cells derived from the uterus of a mouse [114]. These cell lines represented good adherence and clear cell loading without stripping (Figure 3.13)
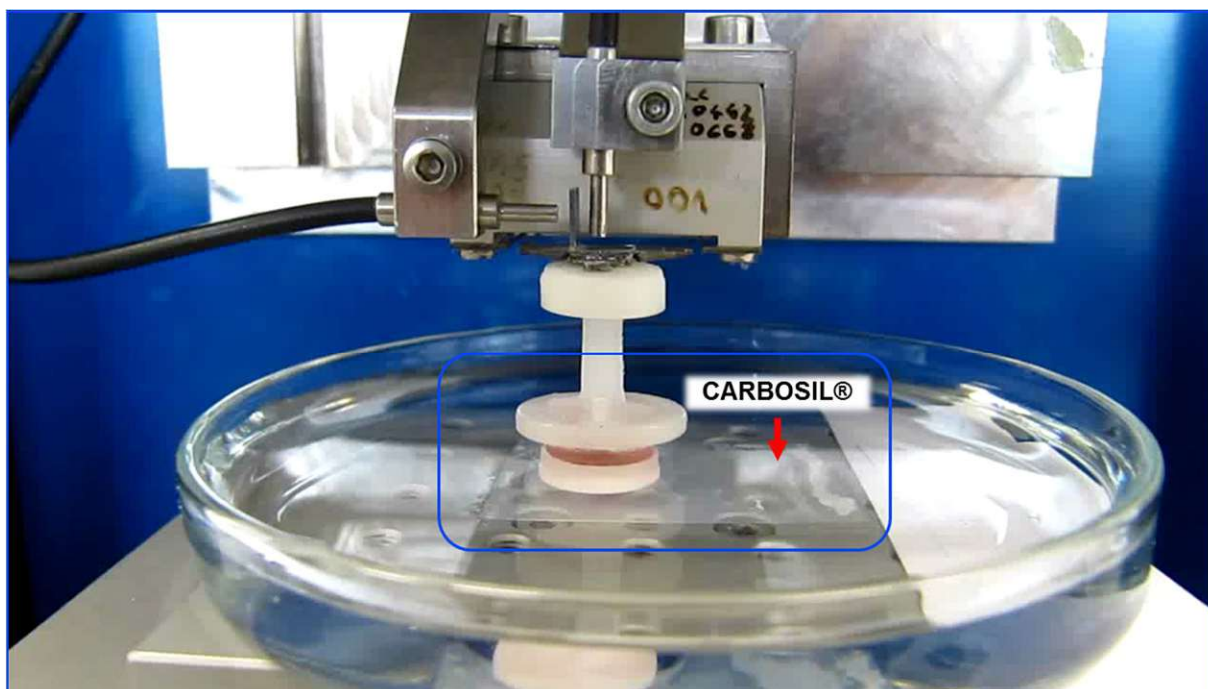

Fig. 3.12 Image captured during test on CarboSil® (Endothelium biomimic) in buffer solution (distilled water).

The second selected cell lines were human corneal epithelium cell lines. They had Biosafety level 2 (immortalized by DNA modification) consideration, and they were cell line CRL-11515 provided by ATCC [117]. Unfortunately, the culture of these cell lines was unsuccessful as they had poor adherence on to the culture dishes [118] It was decided to buy a 3D-tissue construct model of 4 cm2 human corneal epithelium (CCE 10-HCE-028) from SkinEthic™ for future studies.
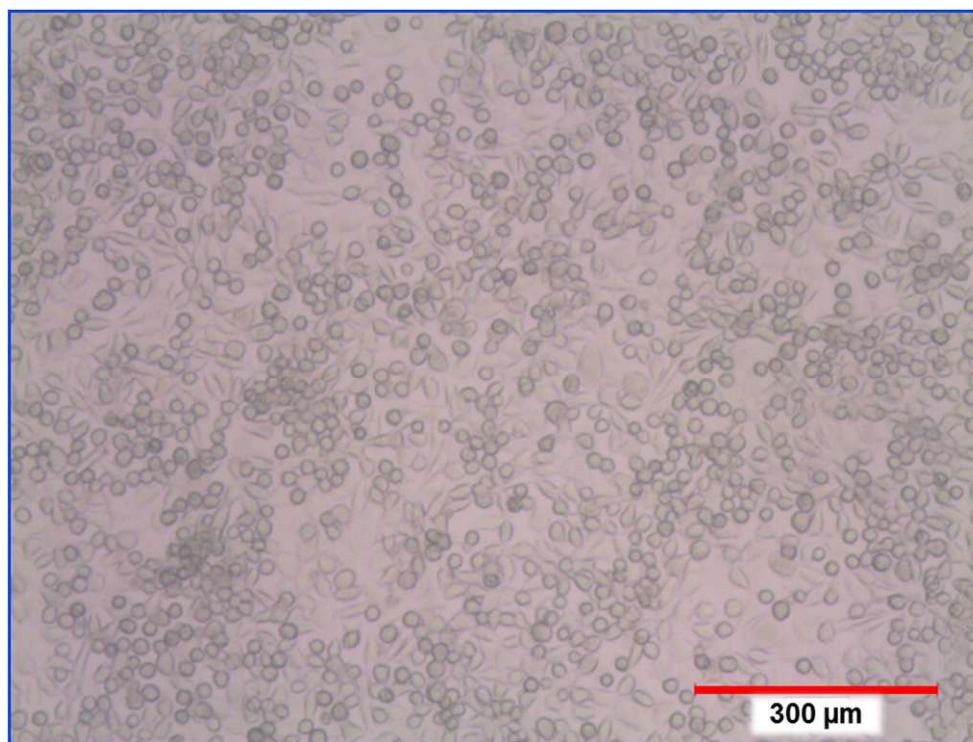
Fig. 3.13 Cultured HT 1080 muscle cells under optical microscope with a scale of 300 µm.

The probe and extension were checked for the cell culture insert height provided by SkinEthic[TM] and the speed for cell culture tests was reduced to 0.1 mm/s to reduce the inertial effect of the large probe. And finally, we use a now commercially available Acuvue Oasys with Hydraclear Plus (Senofilcon A) as the contact lens to test.

3.2.2 Tetra Basalt® - N2

The second modular concept used for this project is the Tetra BASALT®-N2 Surface Tester (Figure 3.14) that allows individual configuration according to customer requirements. Modules and sensors were selected according to the loading conditions and movement of the eye-eyelid system, based on literature survey [115–127]. Tribometrical assessments are conducted on a large variety of samples in order to find suitable geometries and materials under different operating conditions. Similar tribometer installations were used in ocular biotribology [115,117,119,125,127].
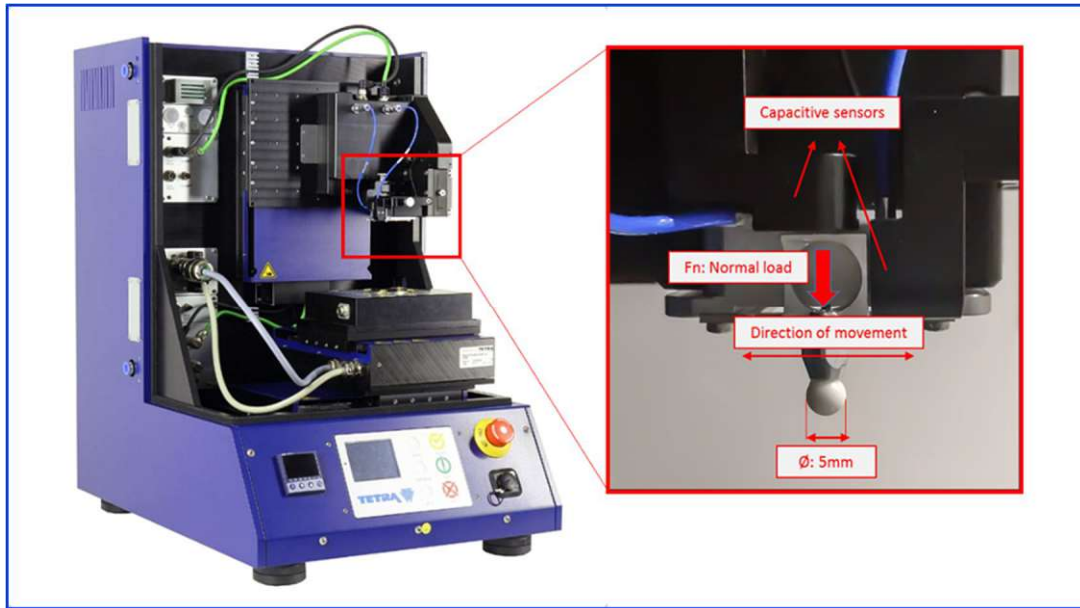
Fig. 3.14 View of the tribometer BASALT®-N2 Surface Tester (left) and details of the capacitive sensor and ceramic probe attached on the spring of the tribometer (right).

Selected modules used for this project, were able to vary normal load between 500 µN to 1 N using three different force modules together with translational load evaluated via capacitive sensors [128]. Following the initial tests, the high load sensor (200 mN-1000 mN) was decided to be outside the necessary load range. Reciprocating motion with a frequency between 0.1 Hz and 5 Hz and a stroke between 1 mm and 10 mm was possible (Figure 3.15).
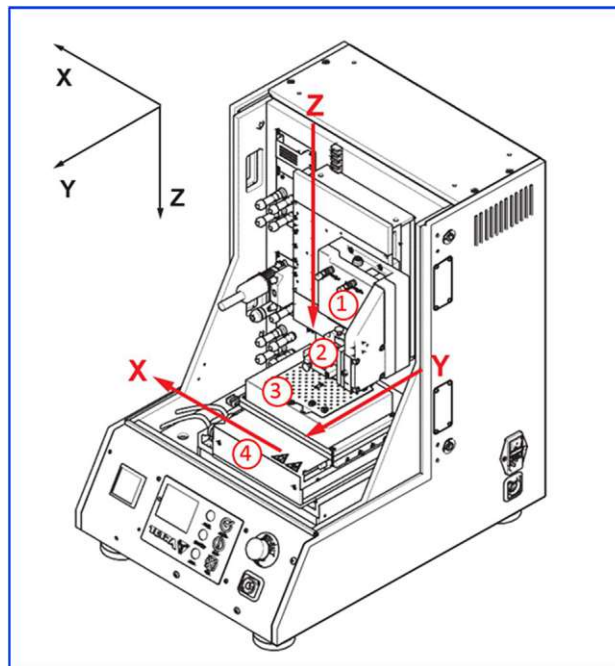

Fig. 3.15 Axis movement description of instrument module (1), sensor (2), specimen holder (3) and experimental module (4).

The instrumental module (Figure 3.15 no. 1) was not only responsible for the Z-axis movement and hence the normal load adjustment but also for the definition of the load range of the tribometer. Capacitive sensors and the spring (Figure 3.15 no. 2, detail in Figure 3.14 right) were attached to the instrumental module. The location of the sample was adjusted by the specimen holder (Figure 3.15 no. 3, Y-axis) and the experimental module (Figure 3.15 no. 4, X-axis). Frequency and stroke were also determined by the movement of either specimen holder or experimental module.

Our partner Croma-Pharma GmbH developed an eye-drop liquid (Lacrimera®) containing a thiolated chitosan [129–133] that succeeds in reconstructing a physiological tear film. The thiol (SH)-group mediated adherence of the effective hydrophilic biopolymer prevents leaching or ablation from the cornea and provides a long-term relief for patients with dry eye or Sicca syndrome, respectively [134,135]. In addition to clinical studies in human, a comparative experimental study was necessary, allowing the assessment of the tribological performance of these eye-drop liquids, i.e., benchmarking of their lubricating capabilities in terms of friction and wear protection as well as durability.

According to tribological interpretation of the ocular system consisting of eyelid and cornea, the effect of an eye-drop liquid can be attributed to two main mechanisms. First, the physical mechanism based on the formation of a polymer film on the cornea resulting in retention of water; this principle may be assigned to eye-drops containing sodium Hyaluronate (Na-HA), e.g., commercialized in Hylo-Comod® [136]. As such film is readily removed by blinking of the eye, low interaction, i.e., physically dominated adhesion to the outermost corneal epithelial cells can be concluded. Second, the chemical-physical mechanism characterized by additional chemical bonding of the polymer to corneal epithelial cells, i.e., binding of thiolated chitosan contained in Lacrimera® [137]. The formed film is covalently fixed on the corneal surface and hence cannot be easily removed by blinking. The resulting extended durability requires less frequent re-lubrication, i.e., application of eye-drop liquid, compared to products whose effect is (mainly) based on a physical mechanism.

3.2.2.1 Sample preparation for the eye-drop tests

In the context of this investigation, a primary focus was directed toward the tribological assessment of ocular solutions, achieved through the establishment of a tribological system designed to replicate the interactions occurring between the cornea and the eyelid wiper. Accordingly, the main objectives were to develop a simple model and experimental procedure

to assess the friction, wear, and durability of films formed from eye-drop liquids, and benchmarking of Lacrimera® [138].

Initially, chromium alum crosslinked gelatin of different rigidity (soft, medium, hard) was plated on polyurethane until it was decided to use glutaraldehyde crosslinked gelatin only as a substrate for mucin layers [139]. The experimental framework for conducting tribological measurements encompassed the utilization of plastic petri dishes of varying dimensions (ranging from 35 mm to 85 mm in diameter), fabricated from high-quality platinum-grade materials. The receptacles in question were filled with stabilized gelatin, crosslinked with glutaraldehyde, meticulously stratified into layers of varying thickness, ranging from 0.5 mm (distinguished by higher hardness) to 3 mm (distinguished by lower hardness), as visually represented in Figure 3.16. It is worth noting that the gelatin surfaces were coated with a mucin layer derived from porcine stomach Type III, characterized by a sialic acid content falling within the range of 0.5-1.5 %. Following the application of the mucin layer, the gelatin plate underwent a comprehensive washing procedure with water for injection, subsequently followed by the evaluation of mucin layer integrity via alcian-blue staining.
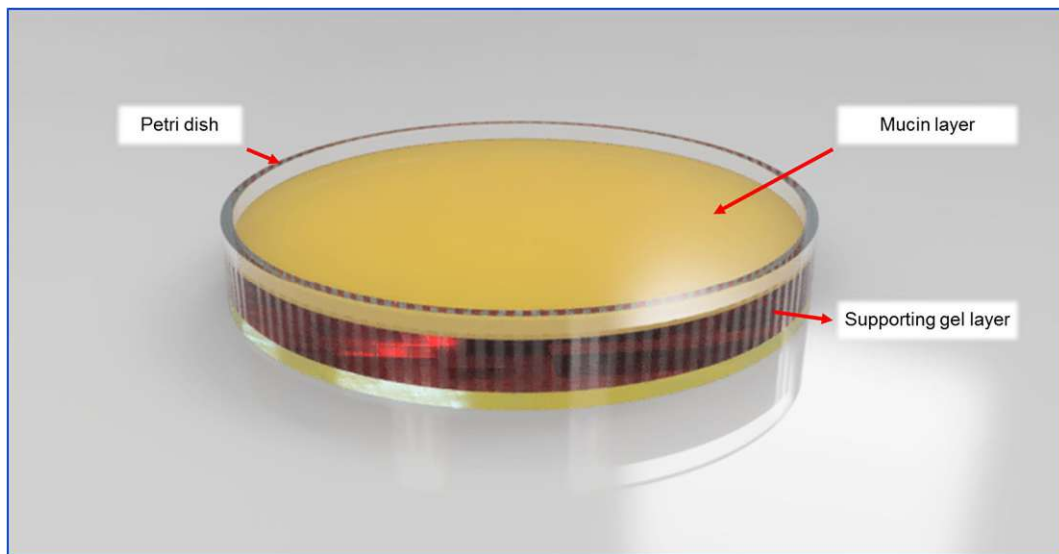

Fig. 3.16 Sample configuration, supporting gel layer in petri dish and mucin layer.

As counter bodies, aluminum oxide ceramic balls with a diameter of 5 mm, a specific weight of 3.95 g/cm3, and a hardness of HRA 70 were selected (www.kugelpompel.at). Roughness values are given as $R_z = 0.382$ µm and $R_a = 0.043$ µm. These ceramic balls were used as counter bodies for all documented measurements, as the inert properties of aluminum oxide towards biological systems were beneficial [140]. For each sample a new ball was applied. Prior to tribometrical experiments, the balls were cleaned by rinsing with ethanol. An approach to

use a gelatin-coated ball was not realized, because of possible inconsistencies, which may occur due to the detachment of the gelatin coating during the experiment. This may cause a third body effect in the contact zone, thereby creating uncertainties in the system. As material transfer happened within the first cycles of the test, it was concluded that the contact situation on a molecular level consists of gelatin-gelatin or mucin-mucin contact, respectively.

The tribological evaluations encompassed the application of four distinct lubricants: physiological saline solution (0.9 % NaCl w/w), chitosan-hydrochloride (1 mg/mL) in a physiologically buffered solution referred to as "Placebo," commercially available eye drops, specifically Lacrimera® (Croma-Pharma GmbH) and HyloComod® (Ursapharm GmbH). The "Placebo" formulation consisted of non-derivatized chitosan [141], and was buffered in a manner identical to Lacrimera®. In preparation for testing, each gelatin plate underwent preconditioning through immersion in a physiological sodium chloride solution. Subsequently, two drops of each lubricant were applied to their respective test zones, followed by a 5-minute incubation period. These tests were conducted under standard room temperature conditions, with humidity levels maintained at 45 %.
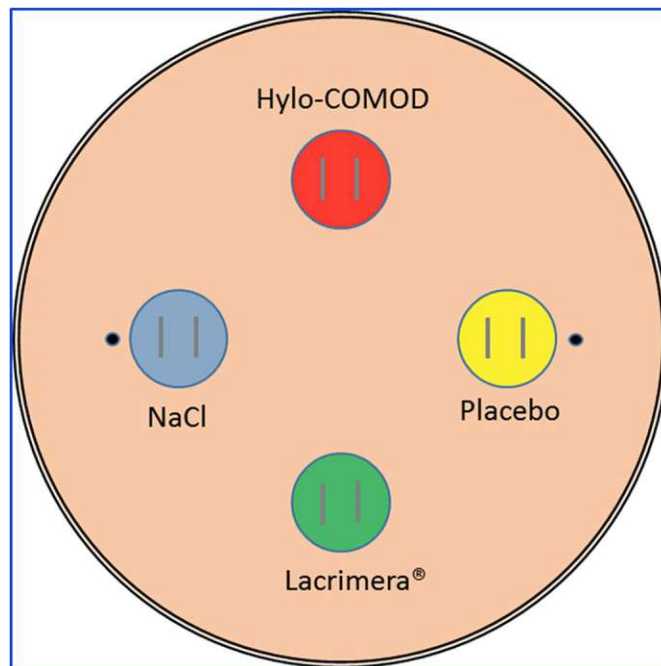

Fig. 3.17 Schematic presentation of a gelatin plate with locations of applied solutions and performed tests (strokes).

The experiments were carried out in a sequential fashion, wherein each gelatin plate commenced testing with one lubricant and proceeded in a counterclockwise manner to the next lubricant (Figure 3.17). This rotational procedure was employed to mitigate the potential

influence of drying on each tested solution. The results reported herein are the arithmetic means derived from four repetitions conducted for each sample. Notably, the computed average coefficients of friction values, determined by averaging the data points obtained from four tests per cycle, exhibited consistent ranking patterns for both soft and hard substrates.

3.2.2.2 Determination of Young's modulus for hardness discussion

The determination of Young's modulus (E) holds paramount significance in the assessment of contact conditions within tribological tests. To ascertain the Young's modulus of the gelatin hydrogel substrates specifically crafted for the designated tribological system (Figure 3.18), macro-indentation tests were conducted [142]. In such tests, a probe of precisely defined geometry indents the surface, while concurrently measuring the requisite force via a spring mechanism. Notably, the tribometer was employed as the indenter, utilizing a vertical displacement approach rather than lateral movement. An alumina oxide ceramic sphere, bearing the same specifications as those employed in the tribological investigations, was employed as the indenter. The selection of the indentation mode was contingent upon the pre-established criteria of penetration depth and indentation speed. To safeguard the preservation of the elastic characteristics of the gel samples and preclude any potential disruption of the mucin layer, a maximum penetration depth of 0.5 mm was deliberately opted for [143]. The indentation speed was maintained at 0.01 mm/s to mitigate abrupt alterations attributable to the viscoelastic behavior of the gels.
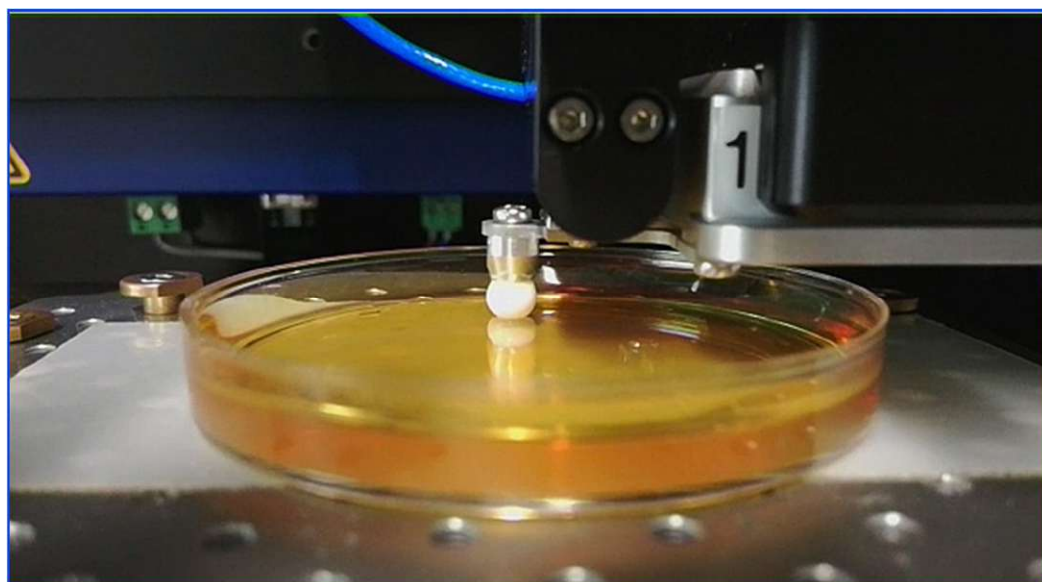

Fig. 3.18 Real life image of the test system with the ceramic probe and gelatin hydrogel samples.

The micro-tribotester registered the spring deflection during the approach phase, and this calibrated instrumentation subsequently converted these measurements into values representing the normal load. In Figure 3.15, denoted by black dots, are the designated locations for the indentation tests, with each plate subjected to testing at each location. The Young's modulus was determined through a fitting procedure that involved comparing the indentation force versus indentation depth data from the plates to an overlaid theoretical force derived from the Hertz model, as presented in equation (12) [144] (Figure 3.19, dashed lines):

$$F = \frac{4}{3} \cdot \frac{E}{(1 - \upsilon^2)} \cdot \delta^{3/2} \cdot R^{1/2} \tag{12}$$

where F is the force applied by the indenter, E is Young's modulus, υ is Poisson's ratio, δ is the indentation depth and R is the radius of the tip.

The modulus of elasticity for the soft and hard gel samples was computed through an iterative process, commencing with initial values of 18 kPa and 36 kPa, respectively, as stipulated by Equation 1. It is noteworthy that the calculated values were in accordance with previously reported values documented in the literature [145–149].
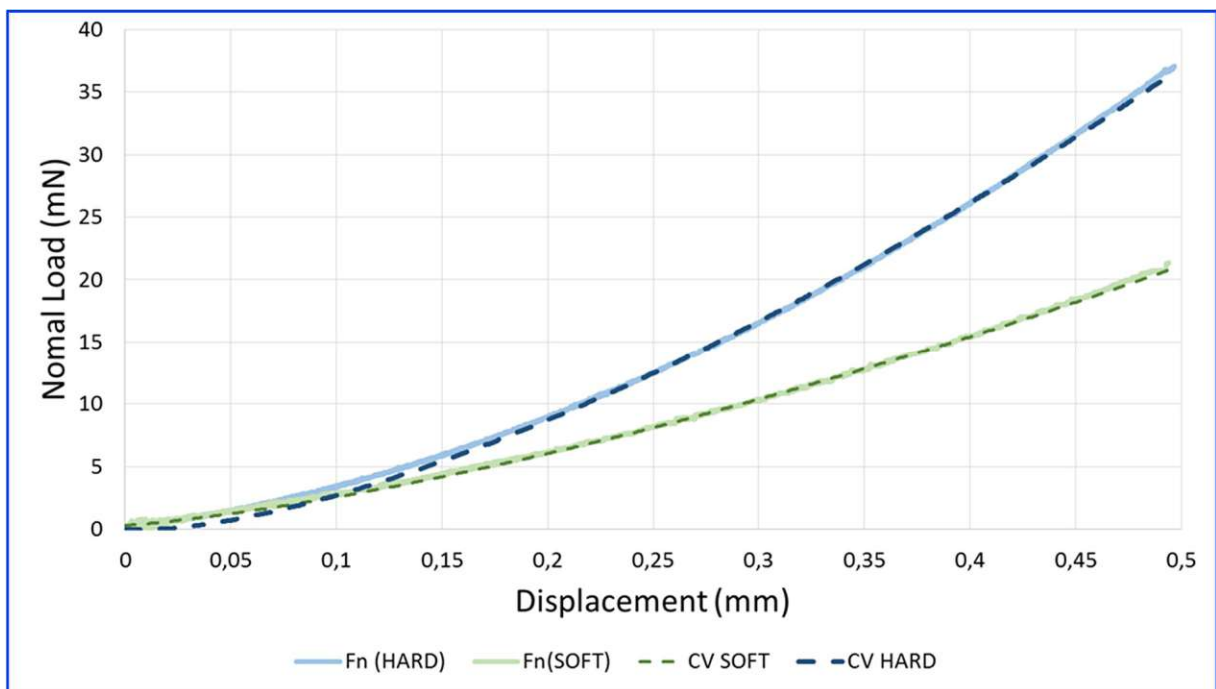

Fig. 3.19 Force as function of displacement for soft (continuous light green) and hard (continuous light blue line) gelatin gels vs. calculated value (CV) by iteration for each material (in dashed lines).

3.3 SRV Tribometer

The SRV® tribometer, initially designed for mechanical-dynamic testing, primarily within the realm of mixed friction scenarios, adheres to the design principles delineated by DIN 50322 standards. This multifaceted tribometer is proficient in assessing the frictional and wear properties of lubricants and materials in accordance with prescribed protocols [150]. Its modular design allows us to simulate in-situ conditions of real-life mechanical systems by means of translational and rotational motion.

The main parts of the SRV® (Figure 3.20) are the oscillation drive, the test chamber, the device for applying normal load with a geared motor, and the load cell [151]. There is a PID control system for the temperature adjustment to heat the specimens to in-situ values. The possibility to choose manual or PC control allows series of measurements without direct presence of an operator.
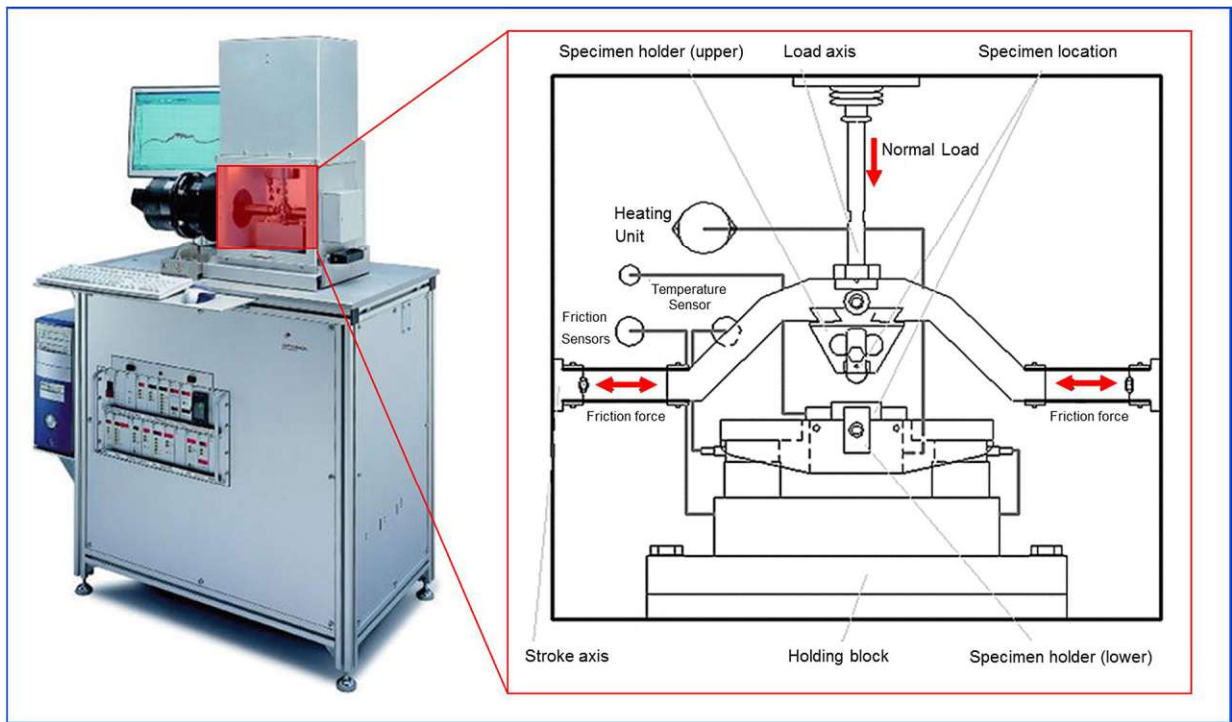

Fig. 3.20 General view of SRV® tribometer and the diagrammatic view of the test chamber (highlighted in red) designed for oscillation tests.

The system is capable of recording most used tribological parameters such as the coefficient of friction, stress condition, electrical resistance between specimens, wear amount, time resolved, and wear. In the test chamber (Figure 3.20, highlighted with red), friction force is calculated via two piezo force measuring elements, one for the friction force and another one for normal load, that are located under the block on which the specimens are placed. In the

traditional test system, specimens are held by the basic specimen holder and an exchangeable counter specimen holder, but both holders are redesigned for biotribological tests, and the details of the design will be given in section 3.3.1. The oscillatory movement is carried out by ensuring a solid connection of the counter specimen holder and the oscillation drive via the drive rod.

The SRV® tribometer has two loading modules that allow us to operate with the normal load of 1-2500 N and 0.5-200 N and oscillation frequency of 1-511 Hz and 0.01- 10 Hz respectively. We used the second force module because of the natural loading conditions of the knee joint [152]. There are three temperature ranges that allow working at temperatures ranging between -35 °C and 900 °C. We used the standard range as the internal body temperature of the bovine is 39 °C [153]. Finally, the stroke can be arranged between 0.01 mm to 5 mm.

3.3.1 Designed specimen holder for cartilage-on –cartilage tests

As it is mentioned in previous section, The SRV® tribometer has standard specimen holders for both test body and the counter body. But to evaluate in-situ working conditions for the knee joints, there was a need to design specimen holders for cartilage samples. Lower specimen holders also should include a housing for test lubricants (in our case distilled water, calf serum, bovine synovial fluid, and addition of pro-/anti-inflammatory agents) and the entire test system should be isolated from the environment.

The upper specimen holder consists of three main parts. The first part, indicated in Figure 3.21 as (1), is the attachment to the main body of the SRV® tribometer as shown in Figure 3.1. The part that is identified as (2) in Figure 3.21 is the fitting to one side of the industrial bulk that will exclude the tribosystem from the environment for hygienic purposes and to eliminate contamination. And finally, part (3) is where the cartilage samples will be placed. Details of the cartilage sample selection and production will be described in Section 3.3.2.

When we focus on the lower specimen holder, the design becomes complicated with 5 main parts (Figure 3.22). The first part to focus on here would be the (1) voluminizer. After the initial calculations with the distilled water, it is observed that the amount of lubricant to fill the entire bulk around the system would not be possible with a single donor bovine. An average bovine has 40 ml of synovial fluid [154] in the leg, and considering the multiple tests needed to observe repeatability of the test condition, we would have only 6-8 ml per test.
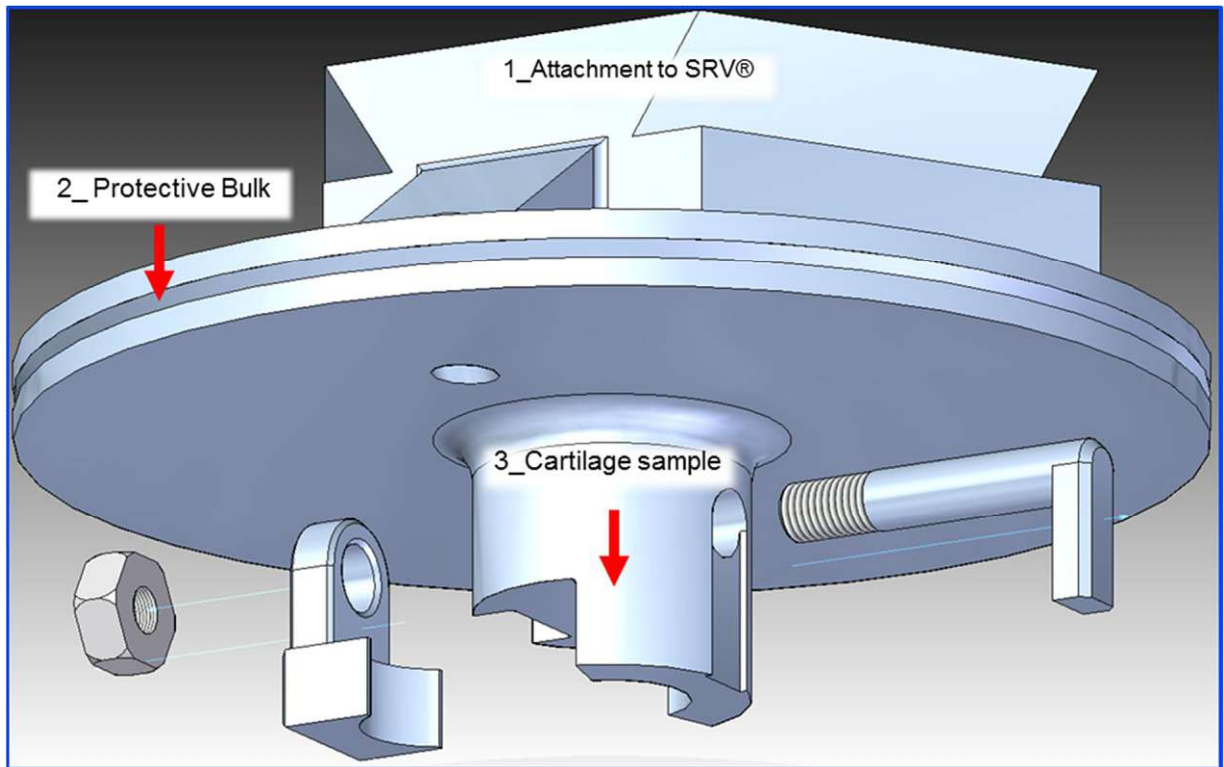
Fig. 3.21 Schematic view of the upper specimen holder.

Another issue with the lubricant directly filled in the bulk, would be that the elasticity of the bulk material may interfere with the results during the oscillating motion. As the entire system apart from the bulk material is made of stainless steel (biological grade), we would not have this problem of elasticity with the designed voluminizer.

Here it is also necessary to underline one more material that would stop the leakage between the voluminizer and the attachment to the SRV® (Figure 3.23, part (3)). An O-ring was placed between the part (1) and part (3) so that the solution would not move to the part (5). The outlet for the lubricant would be used only after the test, in order to analyze changes in the lubricant. The natural flow of the lubricant after the test was assured by the inclined surface of part (1) and part (3). Inclined and conic contact in the pairing surfaces was also desired as synovial fluid is very adhesive [155] and separating the surfaces from each other was challenging if both surfaces were parallel to the load axis. The inlet for pro/anti-inflammatory additives is on the upper specimen holder, which we may see in Figure 3.23 that shows the final assembly of the test system.
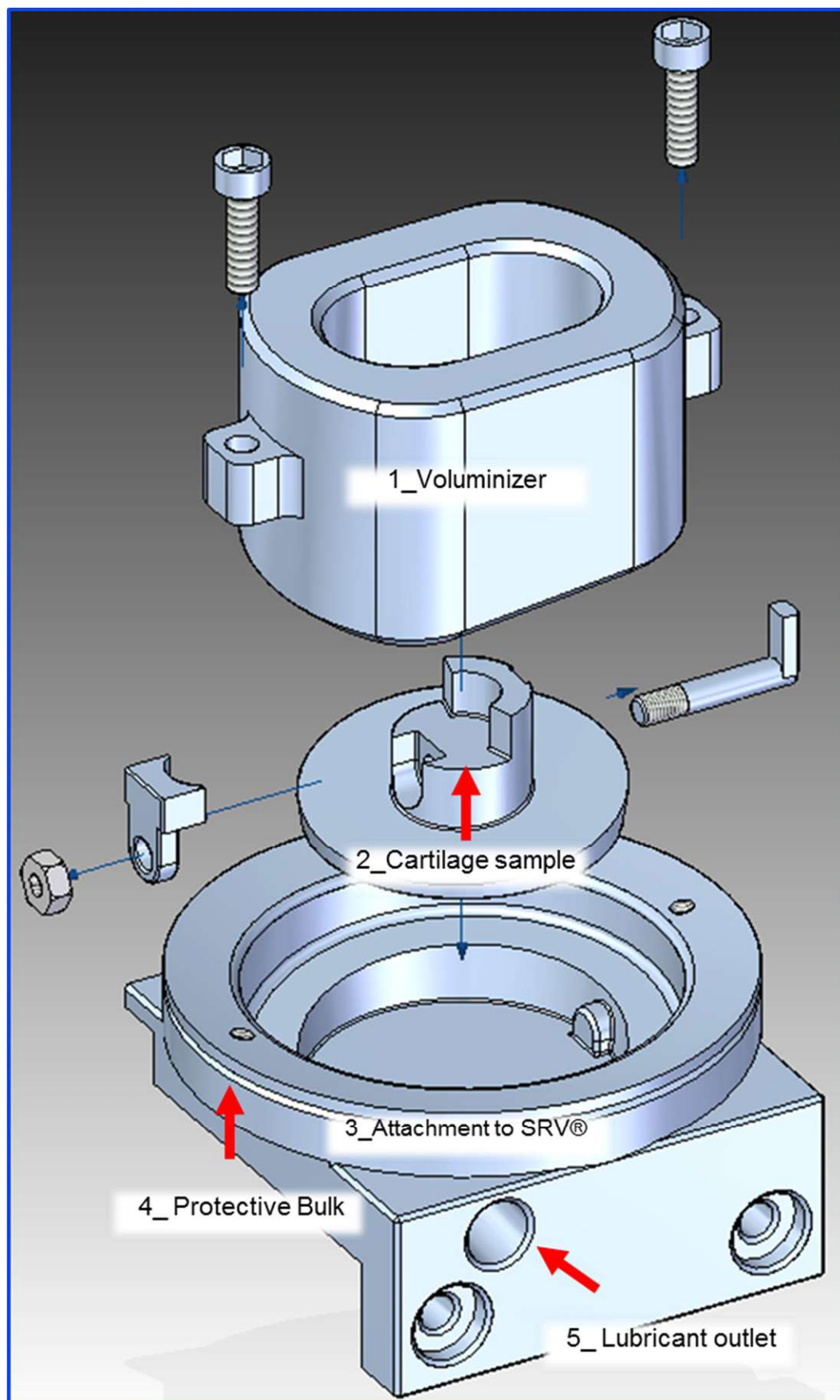
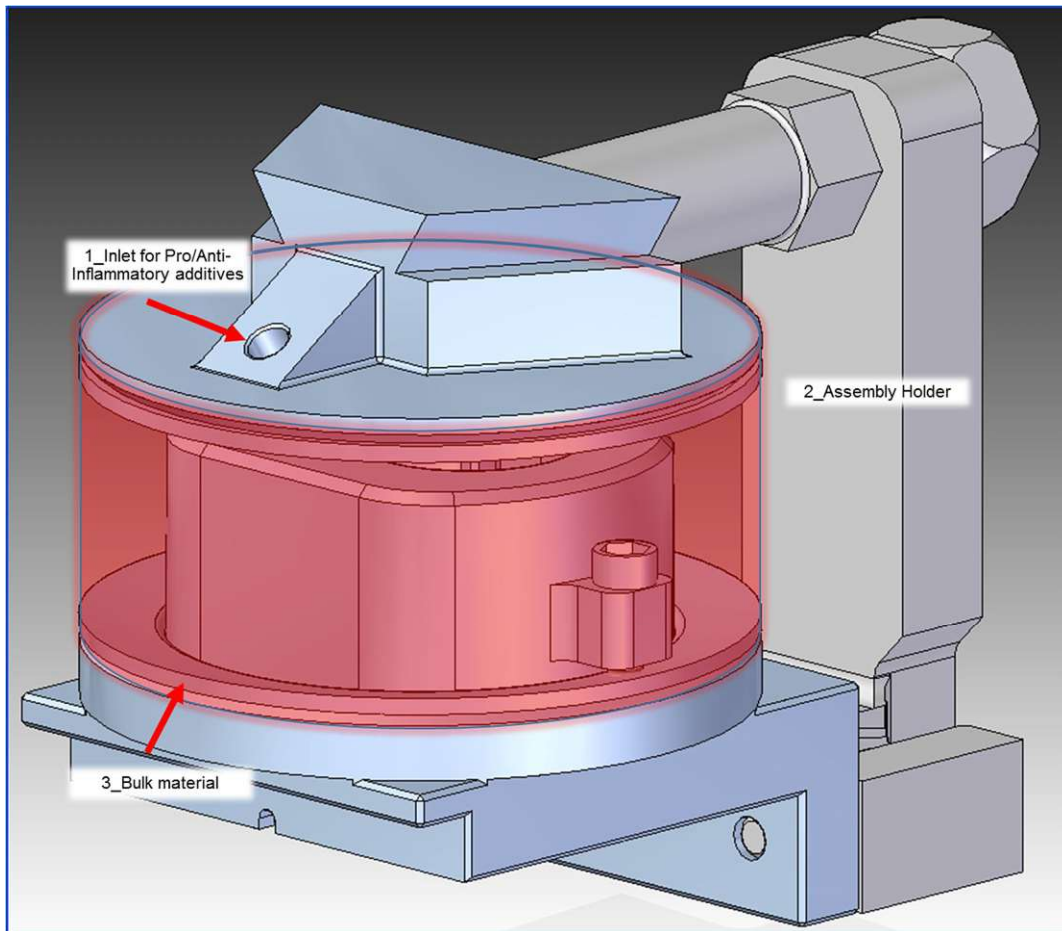**Fig. 3.22** Schematic view of the lower specimen holder.

Fig. 3.23 Schematic view of the complete assembly of the tribosystems.

To satisfy biosafety regulations and avoid contamination of the tribosystem, the entire system needed to be assembled in a Biosafety Level II cabinet [156]. This requirement underlined the necessity of an assembly holder (Figure 3.23 part 2) that the entire system could be built on and carried to the SRV® tribometer. An inlet for the introduction of pro-/anti-inflammatory additives during the test added to the design to observe in-situ effects (Figure 3.23 part 1). Eventually the space between the upper and lower specimen holders would be covered with the bulk material to avoid contamination (Figure 3.23 part 3).

3.3.2 Cartilage samples for the SRV® tests

For our initial tests, we preferred to focus on animal donors for the cartilage tests. There are multiple reasons for this preference, but above all, is the fact that it would be a rare occasion to have human donors with healthy joints [157]. Most of the knee joints derived for the tests would be patients within a certain age frame and with severe diseases, such as osteoarthritis, that led to a total or a partial knee replacement. These samples would be useful to identify mechanical changes in the joints due to the health conditions, and to observe the process of

certain treatments that would not require a live tissue to test [158–160]. On the other hand, in our study we would like to focus on the mechanical behavior of healthy cartilage tissue under daily life conditions. Pro-/anti- inflammatory additives would also give us an idea how to improve the life cycle of healthy cartilage and enable us to observe initiation phases of certain sicknesses and their tribological effects on the performance of a knee joint.

Athanasiou et al. compared different species (human, bovine, dog, monkey, and rabbit) and noticed that all donors achieved similar results for the aggregate modulus, but the permeability of bovine cartilage samples was considered closest to human femoral cartilage [161]. Frisbie et al., investigated the average cartilage thickness for various animal species [162]. Results showed that the bovine cartilage has similar thickness and a larger surface area compared to human femoral head chondral. Considering the availability of samples due to the greater surface area, similarities in mechanical properties and less complicated ethical verification procedures compared to a human tissue purchase, we decided to conduct our tribological tests with bovine cartilages. The selection of donors from the same gender and age division was preferred because these parameters also affect the mechanical properties and tribological response of the samples [163].

Samples are derived from the femoral part of the knee joint, as this part is the most influenced by the knee kinematics due to different shapes of the contact surface [164]. This is the reason why this compartment becomes the region where most severe cartilage tissue wear occurs [165]. The surface of the medial compartment is also more planar and the bone underlying the cartilage has lower hardness [166]. These qualities made the femoral part of the knee, and specifically the medial compartment, the target for specimen gathering.

Cartilage specimens of 8mm diameter were prepared using a single-use osteochondral autograft transplant system (OATS) punch (Arthrex Inc., Naples, USA) by placing them onto the surface of the cartilage at 90° to obtain a cylindrically shaped cartilage specimen. A maximum of six to eight cartilage specimens per joint were obtained by punching them out from the condyles as close as possible to the neighboring sample region. Obtained cartilage specimens were shortened to 8mm in length using a custom-made cartilage holder (Donau Universität Krems) by using a saw and a scalpel (Figure 3.24). This geometry of samples was selected as they have the same geometry with the autologous grafts used for mosaicplasty operation [167]. This surgical procedure is typically employed in cases involving small to medium-sized defects, where autologous grafts are harvested from a non-weight-bearing area of the femoral condyle and subsequently transplanted into a prepped and damaged region. [168].
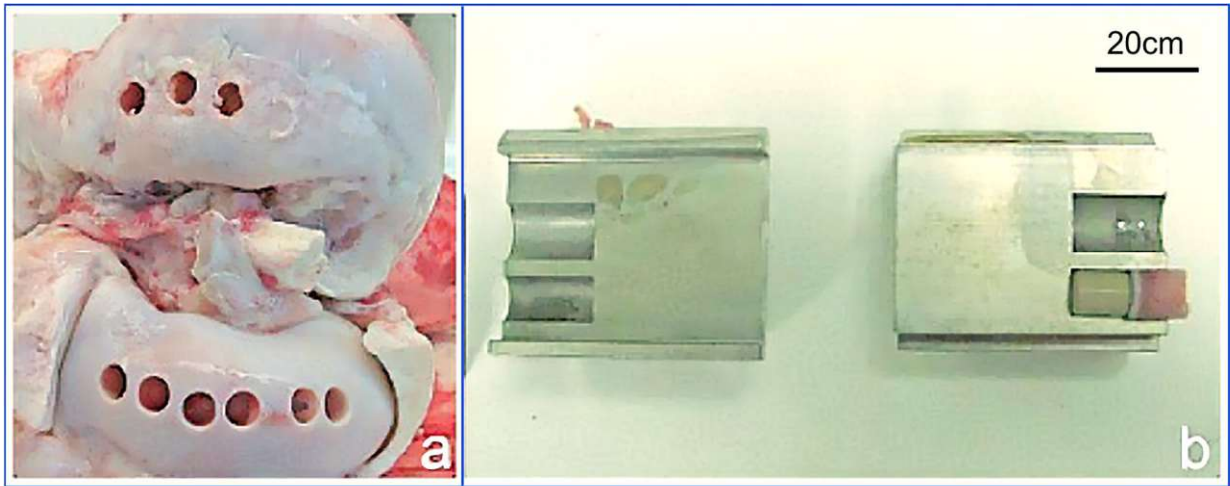
Fig. 3.24 (a) Locations of the cartilage samples punched out from the medial and lateral condyle of the femur; (b) Cartilage holder to adjust the height of the cartilage samples.

We can see the final geometry of the specimen and contact in cartilage-on-cartilage installment. Here it must be stressed that the alignment of the samples could play a vital role because the cartilage has a certain orientation for its matrix that develops naturally because of rolling and sliding during the movement of the patient [169]. Hence, all samples were marked to address the direction of movement.

As delineated earlier, the gender and age of the tissue donors constitute a critical parameter in this context. Accordingly, all selected specimens were sourced from female bovines aged between 18 and 20 months. A preparatory step involved subjecting all samples to a 2-hour washing procedure in phosphate-buffered saline (PBS, Sigma–Aldrich Chemie GmbH, Steinheim, Germany) at 37 °C to eliminate loose bone fragments and adipose tissue. Subsequently, all specimens were placed in a growth medium (GIBCO DMEM/F12 GlutaMAX-I, Invitrogen, LifeTech Austria, Vienna, Austria) supplemented with antibiotics (penicillin 200 U/ml; streptomycin 0.2 mg/ml) and Amphotericin B 2.5 mg/ml (Sigma–Aldrich Chemie GmbH) for a duration of 7 days. This step was undertaken with the aim of augmenting metabolic activity following the tissue harvesting process. The ensuing tribological assessments for each animal were conducted within the subsequent two days at a controlled temperature of 39 °C. Those specimens not subjected to immediate testing were also maintained at 39 °C to ensure uniform environmental conditions, with the sole distinction being the absence of tribological evaluations. Subsequently, all samples were stored at 4 °C until both tested and untested osteochondral grafts were scrutinized on the tenth day.
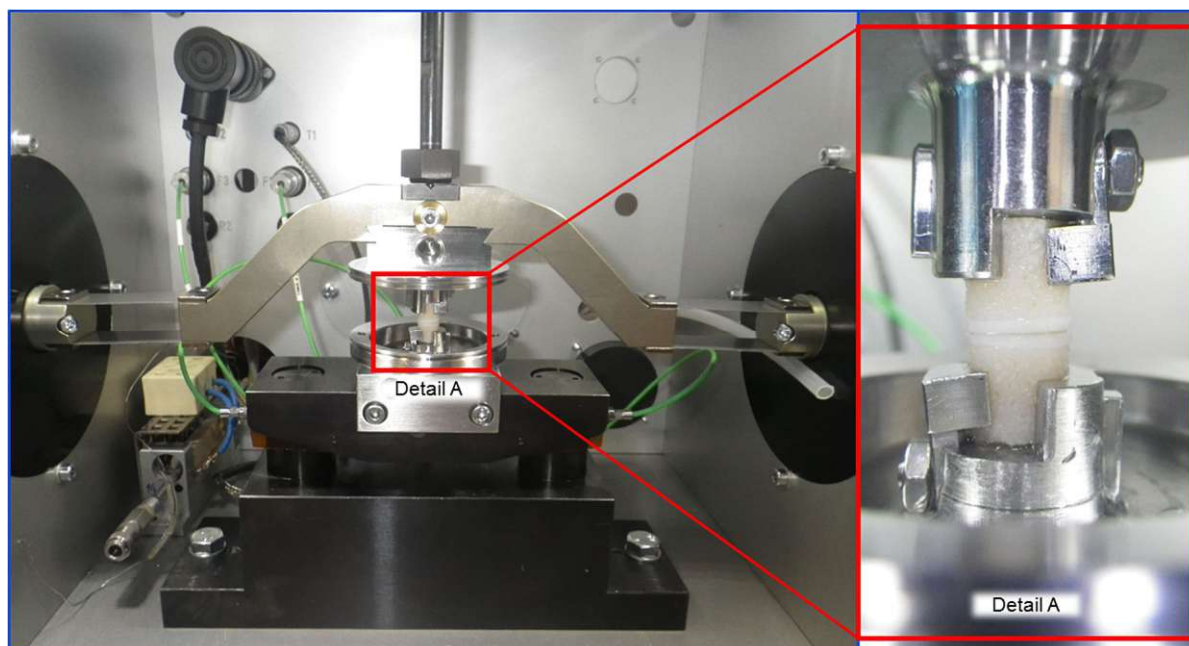
Fig. 3.25 Upper and lower specimen holders with cartilage samples in SRV® chamber and a close-up image of cartilage samples (Detail A).

In the latest stage of the tribological tests, we also worked on samples from human donors. Samples were collected also from the femoral heads. The diameter of the samples was 10 mm in this case, but the design of the specimen holders (Figure 3.25) allows us to adjust the diameter within a certain tolerance. On the other hand, the height of the samples is limited by the SRV® tribometer frame, so all samples were adjusted to 8 mm. The specimens were enveloped with a 10% gelatin methacryloyl (gelMA) coating, as depicted in Figure 3.26. This gelMA coating encapsulated three distinct components: (1) human articular chondrocytes expressing DiO fluorescence (hAC-DiO), (2) immortalized human adipose-derived mesenchymal stem cells (MSC) (ASC/TERT1, Evercyte) genetically modified to express green fluorescent protein (GFP), and (3) a co-culture of hAC-DiO (green fluorescence) and ASC/TERT1 cells transduced with mCherry (a red fluorescent protein), established at a 1:1 ratio [170].
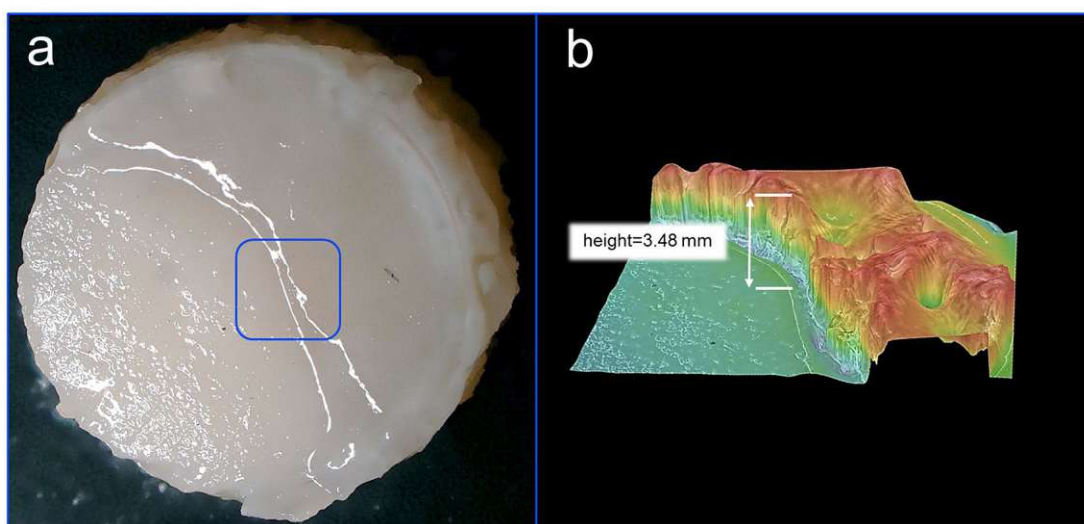
Fig. 3.26 Image of gel coating with the height detail from the 3D topography (captured with Keyence® microscope**).**

The cartilage sample was coated partially by the gelMA for imaging purposes. The main idea was to assess the coating height. The 3D image of the area enclosed with a blue line in Figure 3.26 (a) shows an average height value of 3.48 mm but with some variation. This variation is due to the cut profile for imaging and the surface would be smoother with continuous coating.

3.4 X-ray Photoelectron Spectroscopy (XPS)

When we consider biomaterials, engineered tissues, and biosensors, we require a fundamental understanding of how a physical environment influences biotribological behavior. In this case, the ability to characterize and/or manipulate interfacial events within the biotope becomes crucial. We mentioned different scanning probe microscopy techniques in Section 3.1, such as AFM, and different optical measurement techniques, such as surface plasmon reference (SPR) or optical waveguide lightmode spectroscopy (OWLS) [171], were discussed in the literature. These may give insight into the surface modification events but fail to provide specific information on the chemical details of the interface and interactions. X-ray Photoelectron Spectroscopy (XPS) is a analytical technique employed for the investigation of the elemental composition, chemical bonding state, and overall constitution of a sample's surface. This methodology entails the irradiation of the sample's surface with X-rays, followed by the precise measurement of the kinetic energy exhibited by the photoelectrons emitted from the sample's surface [172].
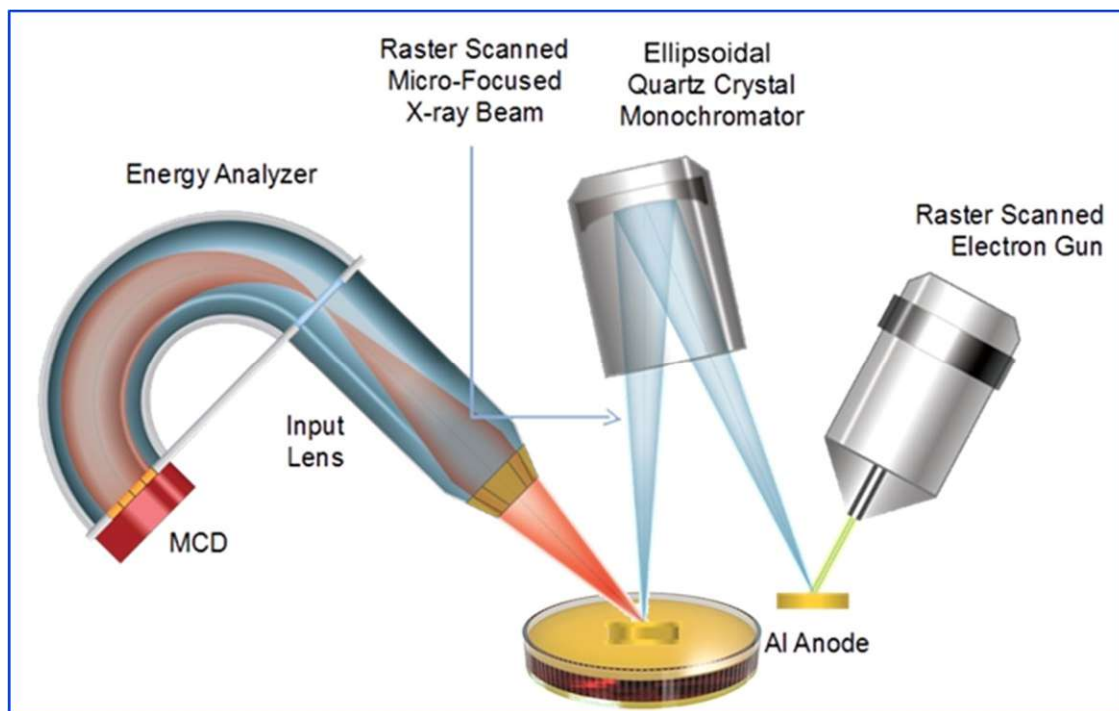
Fig. 3.27 Basic components of an XPS system.

In an X-ray Photoelectron Spectroscopy (XPS) experiment, a low-energy, often achromatic or monochromatic X-ray source (typically AlKα or MgKα) is employed to irradiate a sample within an ultrahigh vacuum (UHV) environment, inducing the ejection of core-level electrons from the constituent atoms (see Figure 3.27) [173]. The kinetic energy exhibited by a photo-emitted core electron is contingent upon its binding energy within the atom and is determined by the elemental composition of the material. Notably, a prominent relaxation mechanism at the typical X-ray energies utilized in XPS involves the filling of the resultant core-hole by an outer electron, which in turn triggers the emission of an Auger electron, effectively conserving the transition energy.

The analytical apparatus for XPS encompasses an electron energy analyzer and an electron detector, which record and quantify the emitted photoelectrons and Auger electrons as a function of their energy. The resultant spectrum serves as a representation of the composition of the material's surface. Specifically, the peak position on the energy scale is indicative of the constituent element, while the peak area provides information about its relative abundance. [173].

As the system already operates in the UHV, further contamination of the surface is avoided, but also XPS is very capable of surface contamination detection. The contaminant may influence the biological interactions of a biomaterial or tissue scaffold and can interfere with

the results. There is an abundance of literature related to the detection of surface contamination via XPS, and many reviews exist in the literature that specifically focus on biomedical applications and issues [174].

Our primary lubricant under investigation in eye drop tests, Lacrimera, was built on a natural polysaccharide, chitosan, and a well-known antioxidant, N acetylcysteine. The combination of these two yields a novel polymer, Chitosan-N-acetylcysteine, that has a prolonged and robust mucoadhesion on ocular surfaces [175]. X-ray Photoelectron Spectroscopy (XPS) investigations were executed employing a Theta Probe™ instrument, provided by Thermo Fisher Scientific. The primary objectives of these analyses were twofold: firstly, to validate the presence of disulfide bonds as indicators of mucin binding to the chitosan substrate, and secondly, to document variations in surface chemistry resulting from the tribological testing procedure. A schematic representation of the XPS chamber, depicting the specific measurement site within a wear track (highlighted by a red-lined area), is delineated in Figure 3.28, exemplified herein for the "Placebo" sample.

The X-ray source utilized in this analysis was a monochromatized Al Kα source, emitting X-rays at an energy level of 1386.6 eV. For precise measurements, the spectrometer underwent calibration, referencing the 368.21 eV binding energy (BE) associated with the Ag 3d5/2 line for metallic silver. Linearity corrections were applied, employing BE values for metallic silver (932.62 eV for the Cu 2p3/2 line) and gold (83.96 eV for the Au4f71/2 line). To compensate for charge effects, a flood gun was employed, employing low-energy electrons and argon ions at 1 eV.

Subsequently, the binding energies of the corrected spectra were further adjusted to align with the primary hydrocarbon peak of C1s, positioned at 284.6eV BE. The X-ray spot resolution was consistently set at 50 μm for all measurements. Survey spectra were acquired with a pass energy of 200 eV BE, while detailed spectra utilized a pass energy of 50 eV.

To maintain optimal analytical conditions, the analytical chamber was upheld at a base pressure below 5x10-8 Pa. Data analysis was undertaken employing the Avantage v5.9915 software by Thermo Fisher Scientific, and spectral peaks were fitted utilizing a convolution approach, employing Lorentzian and Gaussian peak shapes[176,177].
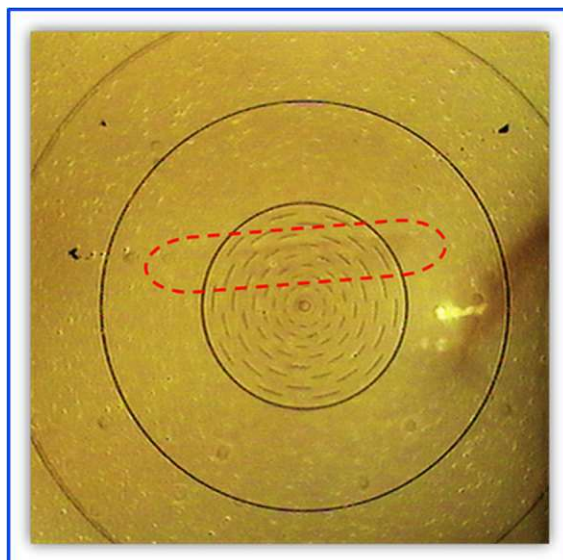
Fig. 3.28 Camera image inside the XPS chamber to spot area of contact (red line).

In preparation for X-ray Photoelectron Spectroscopy (XPS) analyses, specimens were excised to dimensions approximately 5x5 mm² using a scalpel. Subsequently, they underwent a gradual drying process in ethanol with incrementally rising concentration levels. To ensure the sustained integrity of vacuum conditions within the analytical XPS chamber, the evacuation within the fast entry lock was meticulously conducted over a period spanning several days.

3.5 Scanning electron microscopy (SEM)

The scanning electron microscope (SEM) stands as a highly versatile instrument, esteemed for its capacity to meticulously investigate and analyze the microstructural morphology and chemical composition characteristics, as exemplified in Figure 3.29 [178,179].

Light microscopy is of great importance to scientific research, and in our studies, we used it on many occasions for observing the general topography of a sample. But a limiting resolution of ~0.1 μm [180,181] due to the wavelength of visible light radiation, which ranges from 400 nm (blue) to 700 nm (red) led us to a different application to have a deeper observation on our samples. Electron microscopy has been developed by replacing the light source with high energy electron beam to image submicron-sized objects, even down to single atomic positions [182]. A resolution down to 0.1 nm [183] is possible in today's electron microscopy.
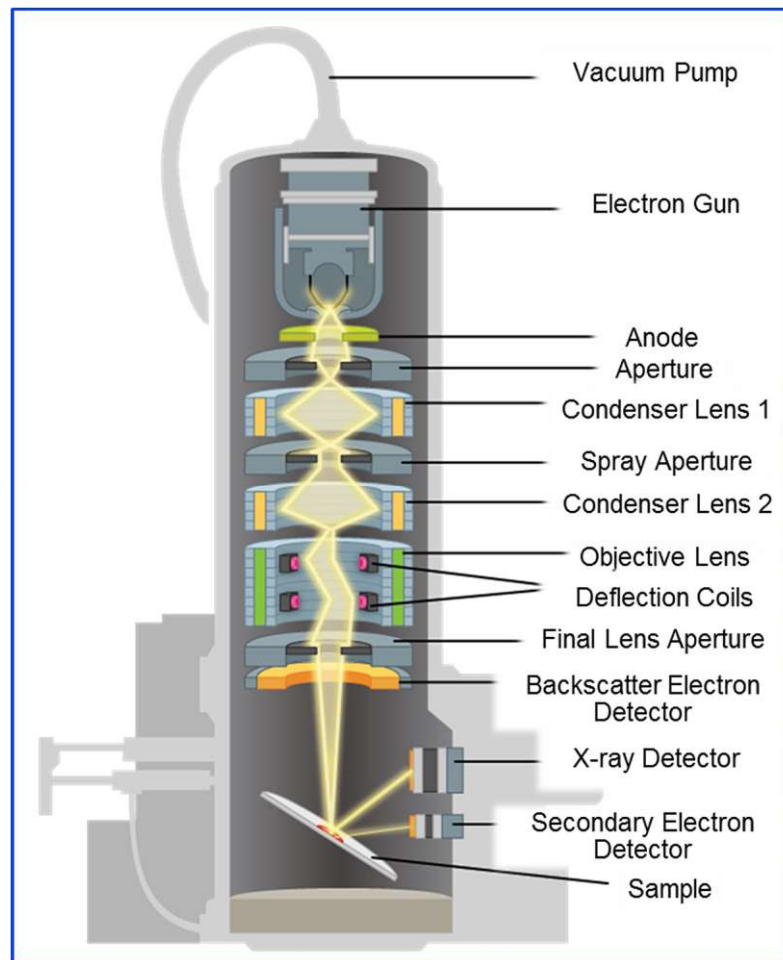
Fig. 3.29 Main components of an SEM [184].

Electron microscopy has been developed by replacing the light source with high energy electron beam to image submicron-sized objects, even down to single atomic positions [182]. A resolution down to 0.1 nm [183] is possible in today's electron microscopy. In an SEM, the electrons are emitted into the vacuumed environment from the cathode that is activated by heating [185]. This ray then goes through the anode that accelerates and focuses on the beam. Off-axis and off-energy electrons are blocked by the condenser lens. Then the spray aperture, with the help of magnetism, creates a helical path for the beam that will lead to a spot. The deflection coils within the objective lens deflect the electron beam to have a non-rasterized scan.

Random absorption and scatter of electrons will take place as the next stage and the X-Ray detector will be the primary detector of the high-energy electrons that can map the sample. Scattered electrons would be analyzed by the secondary electron detector, and this would generate the topography image. The backscatter electron is aiming to check chemical phase changes in the sample (Figure 3.29) [186].

3.6 3D Profilometry

We have chosen Keyence® VX-1100 for our analysis of cartilage surfaces (Figure 3.30). The profilometer uses two light sources: laser light and white light. Laser scanning of a surface in the X, Y, and Z directions allows image capture and height measurement with high horizontal resolution (0.5 nm vertical and 1 nm horizontal). The use of white light also makes it possible to capture the colour of the sample surface.
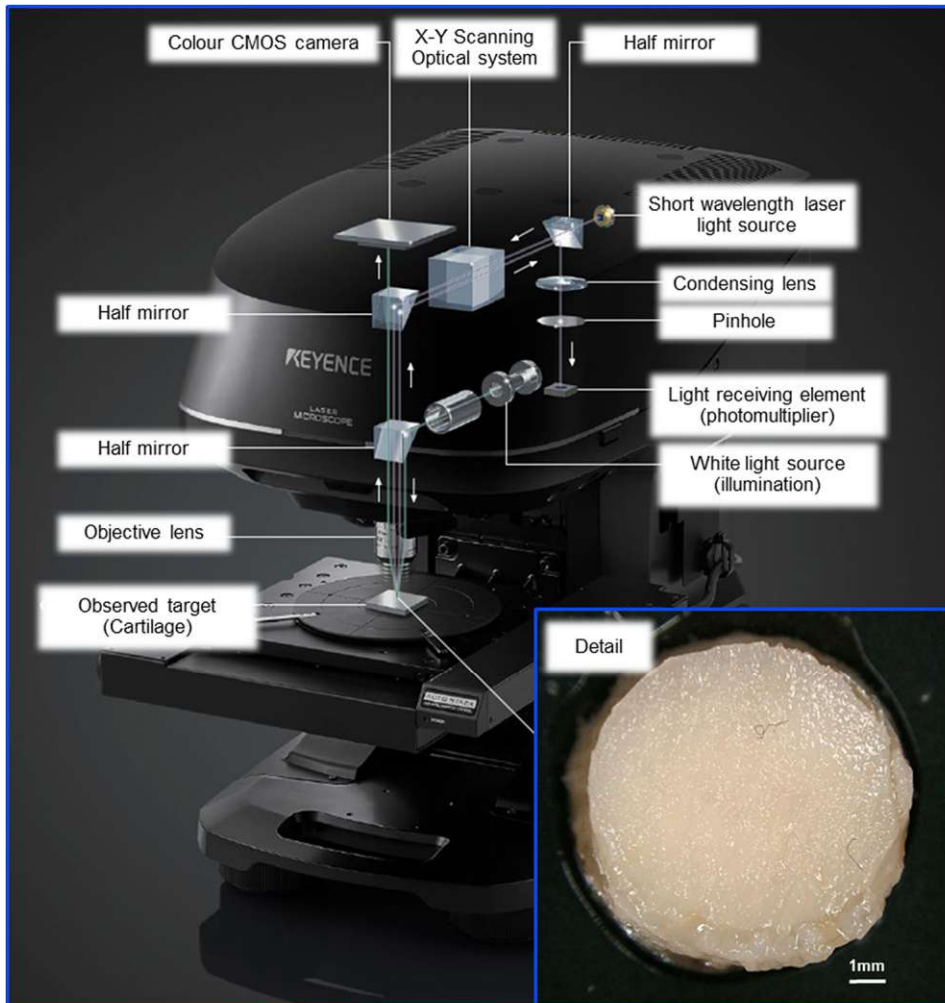
Fig. 3.30 Main components of Keyence WX-1100 with the detail of the captured cartilage surface.

Two types of laser sources are available for the system: a 404 nm violet semiconductor laser and a 661 nm red semiconductor laser [187]. As the resolution is limited to the wavelength of the laser source, we have chosen the violet laser for our research [188]. It was also possible to assure accuracy even with low-magnification lenses. A high accuracy photomultiplier, with 16-bit dynamic range capture, reduced the reflections from the wet surface of the cartilage samples, and cracks that might have edge angles up to 87.1° could be detected. Sudden rupture cracks

on the cartilage surface are generally deep and steep [189], and hence require this accuracy. There are multiple reasons for us to choose this profilometer but on top of the list is the ability to scan 10 mm diameter cartilage surface within a minute. Other systems tried on the samples managed the same area, with the same resolution in between 30 minutes to an hour. This would be unacceptable, as none of the systems were available to capture the image in solution, and the drying of the sample would give completely unrealistic surface parameters.

Chapter 4 Conclusion and Discussion

This project aimed to investigate tribology-related surface interactions in biological media at different scales, namely nano, micro, and macro level. The scaling can be related to the sample size, probe size, loading values, and surface characteristic values, not limited to geometrical constraints. The main idea arose during the initialization of the WEMESURF Marie Curie Research Training Network of the European Commission. With two partners, the University of Milano, and Philips Applied Technologies, we discussed the inadequacy of macro models investigating the tribological properties of the skin, and established a need for a test system that can identify the function and distribution of the sebum layer on the skin. The challenges related to the topic include:

➢ The choice of a tribometer capable of assessing interactions at a highly localized scale, with the capacity to discern specific regions of the stratum corneum overlaid with sebum or keratin, is a critical consideration.

➢ Design of a probe that can be assembled without a contaminant, that is robust enough to make a tribological test but also sensitive to surface adhesion forces

➢ Sample selection and also gathering of the sample

➢ Communication with the ethics commission if the sample is animal or human-origin

➢ Using imaging techniques to validate sample and probe selection

➢ Control of the environmental conditions to conduct the tribological tests

The first question was an obvious choice. The AFM stands as the sole tribometer that functions at exceptionally low applied loads and small spatial scales, offering both contact and non-contact modes, while concurrently preserving the integrity of the specimen under investigation throughout the testing process. The probe could be produced by just the melting of a glass probe, avoiding glue as a contaminant. The spherical probe would also have more significant adhesive force thanks to its larger surface area, compared to standard AFM tips, a defined geometry, and high mechanical strength of the tempered glass.

Sample selection was the challenging part. The necessity for biotribological research; a well-established communication between different university departments such as biology, chemistry, material science, mechanical engineering, physics, and a medical department is underlined. To conduct tests on animal or human tissue is only possible if tribotope of

research is certified accordingly. Since the main application was shaving, it would be logical to use the skin samples from the facial site. However, those samples are relatively rare, and if they are available, there is only a small number of samples derived from surgeries conducted on the human face. Our communication with the medical department of the University of Milano made it clear that the size and availability of the samples from the abdominal area would be suitable for our research. Identifying which side of the skin samples we were looking at was also crucial. Such a thin layer of skin has one side of the stratum corneum, but the other side is the stratum granulosum side. We cut each sample in half and derived a surface topography image via AFM to identify the side of the skin. Samples were placed on the glass cover slip with distilled water and surface tension. So, glue was used neither on the probe nor on the sample. During the tests, we observed a plateau on force curves that were not reported before in research related to the AFM studies. It was as if the colloidal probe was floating on a fluid. Our tests proved this only happens in the zones that were covered with sebum. It was also possible to conduct tribological tests on the zones that were not covered with the sebum.

It should be reported that the limited time available for the mobility programs at one project partner resulted in the research ending with a limited number of tests completed. The system should be further investigated to ascertain if it can also be used to identify lubricative properties of oil-based lubricants, with more friction results needed to have a statistical idea of skin friction. Changes in the atmosphere could also be implemented via a chamber with heating and nitrogen flux adaptations. Following the success of the first project, we decided to apply similar concepts on a micro level in Philips Applied Technologies. The challenge was to adapt a microtribometer to test different contact lenses on corneal cell cultures to observe friction and wear. So, the challenges that arose concerning the idea were;

➢ Culturing cells according to the application and keeping them alive in related physiological media

➢ Adapting the microtribometer that is not designed to conduct tests in that physiological media.

➢ Designing a probe that can work under sub-millinewton loads but also can be introduced in the environment of cell cultures

➢ Creating a specimen holder to mount the contact lenses without damaging the lenses and without using glue, but also having a defined geometry

The initial challenge was to culture corneal cells. Corneal cell lines do not have high adhesive properties due to their function. They are designed to be replaced periodically by the blink of the eyelids and a continuous supply of tear fluid. According to our communication with the biological experts within Philips Applied Technologies, we agreed to use mouse uterus cells due to their high adhesion properties and vitality.

The cantilever designed by Falex Inc. that can apply loads in the sub- millinewton regime was made of glass. The springs on the cantilevers were extremely fragile and hard to operate. Therefore, a new cantilever had to be designed. Our communications led to a cantilever made from biological steel that would not corrode in biological media or break easily. This cantilever also needed to be adapted to a probe that could host the contact lens and with a certain height to dip inside the cell culture, avoiding the cross talk of the cantilever. Even though all the tasks were fulfilled, the tests could only be performed with 0.5 mm/s maximum speed to avoid crosstalk.

Another challenge with the probe was the meniscus force between the probe and the biological media. This force was in the range of 1 mN and could not be mitigated via the software of Falex Inc. Our communications with the company led to an update of the software, and the system can now also recognize negative loads.

Extensive investigations into the mechanical characteristics of the ocular structures, particularly the cornea, commenced with the utilization of commercially available polymers, owing to the formidable challenges associated with the cultivation of cells individually for every experimentation aimed at prototyping purposes. A commercially available 3D cell construct was also suggested for the project. However, due to extended delivery times, the task could not be completed during the employment time within the mobility program. In another project, we wanted to observe the performance of different eye drops, the calculated budget for the production, and the analysis of the cell cultures, to be around € 100k. It should also be noted that transporting samples in biotribology-related projects is a big concern. Hence it is advised to have departments in the same complex. Transportation times also change the definition of ex-vivo samples, as a sample with different storage conditions must be labeled as another sample and cannot be used in the same statistical analysis.

For the eyedrop tests, a polymer coated with mucin layers was used. On the other hand, the counter body for the tests were ceramic balls. The tests were conducted in a liquid chamber without a constant supply of tear liquid, so the wash away properties of the eye could not be observed. For future studies, it is advised to supply the system with the periodic addition of tear fluid.

Finally, we came to our macro application that would include cartilage samples. Here the challenges were:

- Selection of cartilage donor animal that would be available before the tests on human-origin samples

- Finding a certified institution for supplies of the cartilage samples

- Selection of the sample geometry

- Design of sample holder for the selected sample geometry

- Creation of the housing for the solutions that should be used for the tests

- Heating the system to mimic the body temperature of the selected donor

- Enclosure of the system to avoid contamination and build the system in a biosafety chamber, then carry it to the tribometer

As it is difficult to obtain human samples, we made a broad literature survey on tests with ex-vivo and in-vitro samples we may use instead. Our research pointed to bovine samples due to availability, similar size to the human knee, and similar body temperatures. Synovial fluid can also be obtained from the bovine samples. These ex-vivo bovine samples would represent the human knee joint system better than implant materials on which tests could be conducted. Our literature research also focused on the lubrication regimes and mechanisms for the knee joint. One of the main discussions was the role of water in synovial fluid in lubricating properties for the knee. So, in our tests, we isolated water as a primary solution for the tests and compared it with the synovial fluid tests. Results show lower friction values for the water compared to synovial fluid in cartilage-on-cartilage tests that supported the role of water in the lubrication of knee joints.

Sample geometry was selected according to the standard procedure of mosaicplasty surgery. It requires a relatively small sample compared to the tests conducted on the entire joint, and submerging large samples while heating the solution would make it difficult for the total joint to be tested. The Donau University of Krems delivered the samples as project partners, and

work was conducted under the university's certification. The issue with the small samples was that we needed to punch them out and eventually discontinue the matrix integrity of the cartilage. In this case, the system delivers a relatable result for mosaicplasty surgery or similar applications, but not entirely healthy, continuous matrix knee joint.

As the knee joint is always loaded in the same direction, the matrix develops in the same direction to loading conditions unless an accident happens. In our study with DUK, we also checked if the directional placement of the samples would change the success rate of the operation. Even though we have not observed a radical difference between different directional placements of the cartilage samples in our test systems, we would be cautious to conclude on the actual system of the total knee joints. As we designed the system in a way to introduce additives, we also tested how the anti-inflammatory additives and their effect on cartilage samples. Results showed no significant changes in the friction behavior of the samples due to the orientation of the grafts, although the samples' wear properties and cell viability changed significantly.

We tested the developed tribotest system with bovine samples, on human samples with hydrogels used as wear protectors in the knee joint. Even though it was possible to create stable hydrogel layers on the cartilage, it was observed that the human samples were not very stable due to changing health conditions among the donors. An important parameter here is that the samples derived from humans are primarily from old donors with severe joint sickness due to fatigue or osteoporosis. Young people rarely have these problems unless they have an accident that would lead to the removal of the joint or some genetic issue appearing in the early stages of life. In this case, there would be minimal studies possible in-vivo for cartilaginous joints.

The final discussion would be on corrosion in implant technologies. The main idea was to develop knowledge on corrosion using non-biological systems and then move on with the studies in biological applications. Even though there was success in corrosion calculations of stainless steel in multiple aggressive environments, the first trials were less successful on biosystems. The major problem was that biological solutions like synovial fluid could be more conductive. Hence reading electrical signals was challenging. Also, even the artificial synovial fluid, designed for tribological tests, has five different salts in it. So, it was not possible to analyze the chemical mechanisms of the corrosion. Most of the tests were limited to saline solution only, and if the temperature was also introduced to the system. Evaporation

would change the system significantly in time. The evaporation requires a closed chamber, which is another challenge for the tribological tests.

In conclusion, this multi-scale investigation into tribology-related surface interactions in biological media has not only shed light on the intricacies of these interactions but also underscored the interdisciplinary nature of such research. The journey embarked upon during the initiation of the WEMESURF Marie Curie Research Training Network has unveiled a multitude of challenges and opportunities. From selecting the right tribometer and creating contamination-free probes to navigating the complex ethical considerations of working with animal and human tissues, this project has exemplified the need for collaboration across diverse fields.

The accomplishments achieved thus far, from the novel use of AFM in identifying sebum-covered skin zones to the adaptation of micro-tribometers for corneal cell culture tests, are significant milestones. The investigation into cartilage samples, although met with challenges regarding sample availability and size, has provided valuable insights into lubrication mechanisms within knee joints. The results regarding the role of water in knee joint lubrication are particularly promising, potentially impacting future treatments.

As we move forward, the path ahead is illuminated with new questions and challenges, from corrosion studies in implant technologies to the development of in-vivo studies for cartilaginous joints. The lessons learned from this project will continue to guide future endeavors in tribology and biotribology, where the boundaries of science are pushed further in pursuit of a deeper understanding of the complex world of surface interactions in biological systems.

Bibliography

1.   Mosteller, R. D. Simplified Calculation of Body-Surface Area. *New England Journal of Medicine* **317**, 1098–1098 (1987).

2.   Silver, F. H., Freeman, J. W. & DeVore, D. Viscoelastic properties of human skin and processed dermis. *Skin Res Technol* **7**, 18–23 (2001).

3.   van Smeden, J. & Bouwstra, J. A. Stratum Corneum Lipids: Their Role for the Skin Barrier Function in Healthy Subjects and Atopic Dermatitis Patients. in 8–26 (2016). doi:10.1159/000441540.

4.   Igarashi, T., Nishino, K. & Nayar, S. K. The Appearance of Human Skin: A Survey. *Foundations and Trends® in Computer Graphics and Vision* **3**, 1–95 (2007).

5.   De Luca, C. & Valacchi, G. Surface lipids as multifunctional mediators of skin responses to environmental stimuli. *Mediators Inflamm* **2010**, (2010).

6.   Ananthapadmanabhan, K. P., Mukherjee, S. & Chandar, P. Stratum corneum fatty acids: Their critical role in preserving barrier integrity during cleansing. *Int J Cosmet Sci* **35**, 337–345 (2013).

7.   Bertalmío, M. The biological basis of vision: the retina. in *Vision Models for High Dynamic Range and Wide Colour Gamut Imaging* 11–46 (Elsevier, 2020). doi:10.1016/B978-0-12-813894-6.00007-7.

8.   Gipson, I. K. The ocular surface: The challenge to enable and protect vision. The Friedenwald lecture. *Invest Ophthalmol Vis Sci* **48**, 4391–4398 (2007).

9.   McLaren, J. W. Control of Aqueous Humor Flow. in *Encyclopedia of the Eye* 389–397 (Elsevier, 2010). doi:10.1016/B978-0-12-374203-2.00089-0.

10.   Dunn, A. C., Tichy, J. A., Urueña, J. M. & Sawyer, W. G. Lubrication regimes in contact lens wear during a blink. *Tribol Int* **63**, 45–50 (2013).

11.   van Setten, G. B. Impact of attrition, intercellular shear in dry eye disease: When cells are challenged and neurons are triggered. *Int J Mol Sci* **21**, 1–17 (2020).

12.   Stachowiak, G. W., Batchelor, A. W. & Stachowiak, G. B. 3 - Tribometers. in *Experimental Methods in Tribology* (eds. Stachowiak, G. W., Batchelor, A. W. & Stachowiak, G. B. B. T.-T. S.) vol. 44 25–78 (Elsevier, 2004).

13.   Buckley, R. J. Assessment and management of dry eye disease. *Eye (Basingstoke)* **32**, 200–203 (2018).

14.   Wu, K. Y., Ashkar, S., Jain, S., Marchand, M. & Tran, S. D. Breaking Barriers in Eye Treatment: Polymeric Nano-Based Drug-Delivery System for Anterior Segment Diseases and Glaucoma. *Polymers (Basel)* **15**, 1373 (2023).

15.   Boyan, B. D., Doroudi, M., Scott, K. & Schwartz, Z. *Cartilage*. *Vitamin D: Fourth Edition* vol. 1 (Elsevier Inc., 2018).

16.   Loy, B. N. *et al.* A Biomechanical and Structural Comparison of Articular Cartilage and Subchondral Bone of the Glenoid and Humeral Head. *Orthop J Sports Med* **6**, 1–7 (2018).

17.   Safshekan, F., Tafazzoli-Shadpour, M., Abdouss, M. & Shadmehr, M. B. Viscoelastic Properties of Human Tracheal Tissues. *J Biomech Eng* **139**, 1–9 (2017).

18.   Chen, S., Fu, P., Wu, H. & Pei, M. Meniscus, articular cartilage and nucleus pulposus: a comparative review of cartilage-like tissues in anatomy, development and function. *Cell Tissue Res* **370**, 53–70 (2017).

19.   Sokolove, J. & Lepus, C. M. Role of inflammation in the pathogenesis of osteoarthritis: Latest findings and interpretations. *Ther Adv Musculoskelet Dis* **5**, 77–94 (2013).

20.   Loeser, R. F. Age-related changes in the musculoskeletal system and the development of osteoarthritis. *Clin Geriatr Med* **26**, 371–386 (2010).

21.   Ma, H. L., Hung, S. C., Wang, S. T., Chang, M. C. & Chen, T. H. Osteochondral autografts transfer for post-traumatic osteochondral defect of the knee - 2 to 5 years follow-up. *Injury* **35**, 1286–1292 (2004).

22. Patil, S. & Tapasvi, S. R. Osteochondral autografts. *Curr Rev Musculoskelet Med* **8**, 423–428 (2015).

23. Zoetebier, B. *et al.* Injectable Hydrogels for Articular Cartilage and Nucleus Pulposus Repair: Status Quo and Prospects. *Tissue Eng Part A* **28**, 478–499 (2022).

24. Mate, M. C. & Carpick, R. W. Tribology on the Small Scale - A Modern Textbook on Friction, Lubrication, and Wear. 59 (2019) doi:10.1093/oso/.

25. Jin, Z. & Fisher, J. Tribology in joint replacement. in *Joint Replacement Technology* 31–61 (Elsevier, 2014). doi:10.1533/9780857098474.1.31.

26. Science, D. of E. and. *Lubrication <tribology> : Education and research. A report on the present position and industry's needs*. *TA - TT -* (Her Maj.'s Stat. Off, 1966). doi:LK - https://worldcat.org/title/258437307.

27. Holmberg, K. & Erdemir, A. The impact of tribology on energy use and CO2 emission globally and in combustion engine and electric cars. *Tribol Int* **135**, 389–396 (2019).

28. Unsworth, A., Dowson, D. & Wright, V. The Frictional Behavior of Human Synovial Joints—Part I: Natural Joints. *Journal of Lubrication Technology* **97**, 369–376 (1975).

29. Na, J., Chen, Q. & Ren, X. Friction Dynamics and Modeling. *Adaptive Identification and Control of Uncertain Systems with Non-smooth Dynamics* 11–18 (2018) doi:10.1016/b978-0-12-813683-6.00003-9.

30. Friction, D. O. F., Laws, T. H. E. & Friction, O. F. *Friction 3.1*. (2017). doi:10.1016/B978-0-08-100910-9.00003-9.

31. Besson, U., Borghi, L., De Ambrosis, A. & Mascheretti, P. How to teach friction: Experiments and models. *Am J Phys* **75**, 1106–1113 (2007).

32. Schetz, J. A. *Skin Friction Measurements in Complex Turbulent Flows Using Direct Methods*. *Engineering Turbulence Modelling and Experiments 6* (Woodhead Publishing Limited, 2005). doi:10.1016/B978-008044544-1/50040-6.

33. Pitenis, A. A., Dowson, D. & Gregory Sawyer, W. Leonardo da Vinci's friction experiments: An old story acknowledged and repeated. *Tribol Lett* **56**, 509–515 (2014).

34. Hutchings, I. M. A note on Guillaume Amontons and the laws of friction. *Proceedings of the Institution of Mechanical Engineers, Part J: Journal of Engineering Tribology* **235**, 2530–2536 (2021).

35. Mills, A. The coefficient of friction, particularly of ice. *Phys Educ* **43**, 392–395 (2008).

36. Wiley, J., Gutenberg-universita, J., Urbakh, M. & Robbins, M. O. *Low-Velocity Kinetic Friction*. *Advances* vol. 126 (2003).

37. Varenberg, M. Towards a unified classification of wear. *Friction* **1**, 333–340 (2013).

38. Affatato, S. & Brando, D. Introduction to wear phenomena of orthopaedic implants. *Wear of Orthopaedic Implants and Artificial Joints* 3–26 (2013) doi:10.1533/9780857096128.1.3.

39. Azarhoushang, B. & Daneshi, A. *Mechanisms of tool wear*. *Tribology and Fundamentals of Abrasive Machining Processes: Third Edition* (Elsevier Inc., 2021). doi:10.1016/B978-0-12-823777-9.00020-3.

40. Blau, P. J. & Budinski, K. G. Development and use of ASTM standards for wear testing. *Wear* **225–229**, 1159–1170 (1999).

41. Gupta, B. R. Friction and wear mechanism of polymers, their composites and nanocomposites. in *Tribology of Polymers, Polymer Composites, and Polymer Nanocomposites* 51–117 (Elsevier, 2023). doi:10.1016/B978-0-323-90748-4.00012-1.

42. Fischer, A. & Mischler, S. Tribocorrosion: Fundamentals, materials and applications. *J Phys D Appl Phys* **39**, (2006).

43. Mischler, S., Spiegel, A. & Landolt, D. The role of passive oxide films on the degradation of steel in tribocorrosion systems. *Wear* **225–229**, 1078–1087 (1999).

44. McBagonluri, F. & Soboyejo, W. Mechanical Properties: Fatigue. in *Encyclopedia of Condensed Matter Physics* 291–298 (Elsevier, 2005). doi:10.1016/B0-12-369401-9/00573-8.

45. Shipway, P. H. Fretting Wear. in *Friction, Lubrication, and Wear Technology* 323–336 (ASM International, 2017). doi:10.31399/asm.hb.v18.a0006414.

46. Kedir, Y. A. & Lemu, H. G. Prediction of Fatigue Crack Initiation under Variable Amplitude Loading: Literature Review. *Metals (Basel)* **13**, 487 (2023).

47. Gassman, K. I. *et al.* The effect of surface roughness and chitosan deposition volume on microbial growth in biofilm involving titanium surfaces for orthopaedic applications. *Materialia (Oxf)* **24**, 101481 (2022).

48. Edachery, V., Swamybabu, V., Adarsh, D. & Kailas, S. V. Influence of surface roughness frequencies and roughness parameters on lubricant wettability transitions in micro-nano scale hierarchical surfaces. *Tribol Int* **165**, 107316 (2022).

49. Murakami, Y. Effect of Surface Roughness on Fatigue Strength. *Metal Fatigue* 305–320 (2002) doi:10.1016/b978-008044064-4/50016-5.

50. Liao, J. J., Liu, X., Miramini, S. & Zhang, L. Influences of variability and uncertainty in vertical and horizontal surface roughness on articular cartilage lubrication. *Comput Biol Med* **148**, 105904 (2022).

51. Jackson, R. L. Lubrication. *Handbook of Lubrication and Tribology, Volume II: Theory and Design, Second Edition* **123**, 14-1-14–14 (2012).

52. Gadelmawla, E. S., Koura, M. M., Maksoud, T. M. A., Elewa, I. M. & Soliman, H. H. Roughness parameters. *J Mater Process Technol* **123**, 133–145 (2002).

53. Zeng, Q., Qin, Y., Chang, W. & Luo, X. Correlating and evaluating the functionality-related properties with surface texture parameters and specific characteristics of machined components. *Int J Mech Sci* **149**, 62–72 (2018).

54. Senge, J. F., Astaraee, A. H., Dłotko, P., Bagherifard, S. & Bosbach, W. A. Extending conventional surface roughness ISO parameters using topological data analysis for shot peened surfaces. *Sci Rep* **12**, 1–12 (2022).

55. Goodhand, M. N. *et al.* The limitations of using 'RA' to describe surface roughness. *Proceedings of the ASME Turbo Expo* **5C**, (2015).

56. Standard, I. INTERNATIONAL iTeh STANDARD Determination PREVIEW iTeh STANDARD PREVIEW. **1994**, (1994).

57. Wang, Y., Wang, Q. J., Lin, C. & Shi, F. Development of a set of stribeck curves for conformal contacts of rough surfaces. *Tribology Transactions* **49**, 526–535 (2006).

58. Yan, Y. Tribology and tribo-corrosion testing and analysis of metallic biomaterials. *Metals for Biomedical Devices* 178–201 (2010) doi:10.1533/9781845699246.2.178.

59. Chong, W. W. F. & De La Cruz, M. Elastoplastic contact of rough surfaces: A line contact model for boundary regime of lubrication. *Meccanica* **49**, 1177–1191 (2014).

60. Korkmaz, M. E., Gupta, M. K. & Demirsöz, R. Understanding the lubrication regime phenomenon and its influence on tribological characteristics of additively manufactured 316 Steel under novel lubrication environment. *Tribol Int* **173**, (2022).

61. de Kraker, A., van Ostayen, R. A. J. & Rixen, D. J. Calculation of Stribeck curves for (water) lubricated journal bearings. *Tribol Int* **40**, 459–469 (2007).

62. Patel, R., Khan, Z. A., Saeed, A. & Bakolas, V. A Review of Mixed Lubrication Modelling and Simulation. *Tribology in Industry* **44**, 150–168 (2022).

63. Totten, G. E. & Liang, H. Surface Modification And Mechanisms: Friction, Stress And Reaction Engineering. in (2004).

64. Burstein, L. Lubrication and roughness. in *Tribology for Engineers* 65–120 (Elsevier, 2011). doi:10.1533/9780857091444.65.

65. Wang, Y., Wang, Q. J., Lin, C. & Shi, F. Development of a set of stribeck curves for conformal contacts of rough surfaces. *Tribology Transactions* **49**, 526–535 (2006).

66. McGrory, S. Lubrication. in *Plant Engineer's Handbook* 915–960 (Elsevier, 2001). doi:10.1016/B978-075067328-0/50054-9.

67. Chapter Three Types of Lubricants and their Compositions. in 125–254 (1992). doi:10.1016/S0167-8922(08)70350-X.

68. *Chemistry and Technology of Lubricants*. (Springer Netherlands, 2010). doi:10.1023/b105569.

69. Chong, W. W. F. & De La Cruz, M. Elastoplastic contact of rough surfaces: A line contact model

for boundary regime of lubrication. *Meccanica* **49**, 1177–1191 (2014).

70. Cameron, A. Basic lubrication theory. *(No Title)* (1976).

71. Dowson, D. Bio-tribology. *Faraday Discuss* **156**, 9–30 (2012).

72. Smith, R. D. & Levy, P. J. New techniques for assessment of vascular function. *Ther Adv Cardiovasc Dis* **2**, 373–385 (2008).

73. The, A. J. & States, U. *Biotribology*. (2005).

74. Zhou, Z. R. & Jin, Z. M. Biotribology: Recent progresses and future perspectives. *Biosurf Biotribol* **1**, 3–24 (2015).

75. Zhang, X., Zhang, Y. & Jin, Z. A review of the bio-tribology of medical devices. *Friction* **10**, 4–30 (2022).

76. Gotszalk, T. *et al.* Diagnostics of micro-and nanostructure using the scanning probe microscopy. *Journal of Telecommunications and Information Technology* **41**, 41–46 (2005).

77. Haus, J. W. Nanocharacterization. *Fundamentals and Applications of Nanophotonics* 185–210 (2016) doi:10.1016/B978-1-78242-464-2.00006-3.

78. Jandt, K. D. Developments and perspectives of scanning probe microscopy (SPM) on organic materials systems. *Materials Science and Engineering R: Reports* **21**, 221–295 (1998).

79. Kaul, A. D., Singh, N., Sonkusare, A., Kumar, P. & Wadhwa, S. S. Design of an atomic force microscope for topographic studies. *Curr Sci* **73**, 738–743 (1997).

80. Zhang, L. *et al.* A method to correct hysteresis of scanning probe microscope images based on a sinusoidal model. *Review of Scientific Instruments* **90**, (2019).

81. Haupt, B. J., Pelling, A. E. & Horton, M. A. Integrated confocal and scanning probe microscopy for biomedical research. *ScientificWorldJournal* **6**, 1609–1618 (2006).

82. Janko, M., Wiertlewski, M. & Visell, Y. Contact geometry and mechanics predict friction forces during tactile surface exploration. *Sci Rep* **8**, 1–11 (2018).

83. Xia, F. & Youcef-Toumi, K. Review: Advanced Atomic Force Microscopy Modes for Biomedical Research. *Biosensors (Basel)* **12**, 1–24 (2022).

84. Tomala, A., Göçerler, H. & Gebeshuber, I. C. Bridging Nano- and Microtribology in Mechanical and Biomolecular Layers. in 431–483 (2012). doi:10.1007/978-3-642-25414-7_16.

85. Gavara, N. A beginner's guide to atomic force microscopy probing for cell mechanics. *Microsc Res Tech* **80**, 75–84 (2017).

86. Kontomaris, S. V., Malamou, A. & Stylianou, A. The Hertzian theory in AFM nanoindentation experiments regarding biological samples: Overcoming limitations in data processing. *Micron* **155**, 103228 (2022).

87. Borodich, F. M. The Hertz-Type and Adhesive Contact Problems for Depth-Sensing Indentation. in 225–366 (2014). doi:10.1016/B978-0-12-800130-1.00003-5.

88. Prokopovich, P. & Perni, S. Comparison of JKR- and DMT-based multi-asperity adhesion model: Theory and experiment. *Colloids Surf A Physicochem Eng Asp* **383**, 95–101 (2011).

89. Mark, A., Helfricht, N., Rauh, A., Karg, M. & Papastavrou, G. The Next Generation of Colloidal Probes: A Universal Approach for Soft and Ultra-Small Particles. *Small* **15**, 1–11 (2019).

90. Indrieri, M., Podestà, A., Bongiorno, G., Marchesi, D. & Milani, P. Adhesive-free colloidal probes for nanoscale force measurements: Production and characterization. *Review of Scientific Instruments* **82**, (2011).

91. Gibson, C. T., Weeks, B. L., Abell, C., Rayment, T. & Myhra, S. Calibration of AFM cantilever spring constants. *Ultramicroscopy* **97**, 113–118 (2003).

92. Herskovitz, I., Macquhae, F., Fox, J. D. & Kirsner, R. S. Skin movement, wound repair and development of engineered skin. *Exp Dermatol* **25**, 99–100 (2016).

93. Menon, G. K., Cleary, G. W. & Lane, M. E. The structure and function of the stratum corneum. *Int J Pharm* **435**, 3–9 (2012).

94. Eckhart, L., Lippens, S., Tschachler, E. & Declercq, W. Cell death by cornification. *Biochim Biophys Acta Mol Cell Res* **1833**, 3471–3480 (2013).

95. Honari, G. & Maibach, H. *Skin Structure and Function*. *Applied Dermatotoxicology: Clinical Aspects* (Elsevier Inc., 2014). doi:10.1016/B978-0-12-420130-9.00001-3.

96. Lazarus, B. S. *et al.* Engineering with keratin: A functional material and a source of bioinspiration. *iScience* **24**, 102798 (2021).

97. Sheu, H. M., Chao, S. C., Wong, T. W., Lee, J. Y. Y. & Tsai, J. C. Human skin surface lipid film: An ultrastructural study and interaction with corneocytes and intercellular lipid lamellae of the stratum corneum. *British Journal of Dermatology* **140**, 385–391 (1999).

98. Staska, L. M. & Pike, J. T. *Skin and Mammary Gland*. *Atlas of Histology of the Juvenile Rat* (Elsevier Inc., 2016). doi:10.1016/b978-0-12-802682-3.00001-x.

99. Ro, B. I. & Dawson, T. L. The role of sebaceous gland activity and scalp microfloral metabolism in the etiology of seborrheic dermatitis and dandruff. *The journal of investigative dermatology. Symposium proceedings / the Society for Investigative Dermatology, Inc. [and] European Society for Dermatological Research* **10**, 194–197 (2005).

100. Guo, J. W. *et al.* Human sebum extract induces barrier disruption and cytokine expression in murine epidermis. *J Dermatol Sci* **78**, 34–43 (2015).

101. Jacques, S. L., McAuliffe, D. J., Blank, I. H. & Parrish, J. A. Controlled removal of human stratum corneum by pulsed laser. *Journal of Investigative Dermatology* **88**, 88–93 (1987).

102. Barbieri, J. S., Wanat, K. & Seykora, J. Skin: Basic Structure and Function. in *Pathobiology of Human Disease* 1134–1144 (Elsevier, 2014). doi:10.1016/B978-0-12-386456-7.03501-2.

103. Dunn, A. C., Zaveri, T. D., Keselowsky, B. G. & Sawyer, W. G. Macroscopic Friction Coefficient Measurements on Living Endothelial Cells. *Tribol Lett* **27**, 233–238 (2007).

104. Cobb, J. A. *et al.* A novel method for low load friction testing on living cells. *Biotechnol Lett* **30**, 801–806 (2008).

105. Delrio, F. W., Carraro, C. & Maboudian, R. Small-scale surface engineering problems. *Tribology and Dynamics of Engine and Powertrain: Fundamentals, Applications and Future Trends* 960–989 (2010) doi:10.1533/9781845699932.3.960.

106. Peter, F., Rüdiger, A. & Waser, R. Mechanical crosstalk between vertical and lateral piezoresponse force microscopy. *Review of Scientific Instruments* **77**, (2006).

107. Kwon, S. *et al.* Adhesive force measurement of steady-state water nano-meniscus: Effective surface tension at nanoscale. *Sci Rep* **8**, 1–7 (2018).

108. Hudu, S. A., Alshrari, A. S., Syahida, A. & Sekawi, Z. Cell culture, technology: Enhancing the culture of diagnosing human diseases. *Journal of Clinical and Diagnostic Research* **10**, DE01–DE05 (2016).

109. Roll, S. *et al.* Dacron® vs. PTFE as bypass materials in peripheral vascular surgery - Systematic review and meta-analysis. *BMC Surg* **8**, 1–8 (2008).

110. Puts, G. J., Crouse, P. & Ameduri, B. M. Polytetrafluoroethylene: Synthesis and Characterization of the Original Extreme Polymer. *Chem Rev* (2019) doi:10.1021/acs.chemrev.8b00458.

111. Anamelechi, C. C., Truskey, G. A. & Reichert, W. M. Mylar™ and Teflon-AF™ as cell culture substrates for studying endothelial cell adhesion. *Biomaterials* **26**, 6887–6896 (2005).

112. Ferruti, P., Bianchi, S., Ranucci, E., Chiellini, F. & Piras, A. M. Novel agmatine-containing poly(amidoamine) hydrogels as scaffolds for tissue engineering. *Biomacromolecules* **6**, 2229–2235 (2005).

113. Russeau, W., Mitchell, J., Tetteh, J., Lane, M. E. & Hadgraft, J. Investigation of the permeation of model formulations and a commercial ibuprofen formulation in Carbosil® and human skin using ATR-FTIR and multivariate spectral analysis. *Int J Pharm* **374**, 17–25 (2009).

114. Bernardo, B. *et al.* Characterization of cachexia in the human fibrosarcoma HT-1080 mouse tumour model. *J Cachexia Sarcopenia Muscle* **11**, 1813–1829 (2020).

115. Pitenis, A. A. *et al.* Corneal cell friction: Survival, lubricity, tear films, and mucin production over extended duration in vitro studies. *Biotribology* **11**, 77–83 (2017).

116. Efron, N. Lid Wiper Epitheliopathy. *Contact Lens Complications* 53–68 (2019) doi:10.1016/b978-0-7020-7611-4.00005-4.

117. Hofmann, G. *et al.* In-vitro method for determining corneal tissue friction and damage due to contact lens sliding. *Biotribology* **5**, 23–30 (2016).

118. Pult, H. *et al.* Spontaneous Blinking from a Tribological Viewpoint. *Ocular Surface* **13**, 236–249 (2015).

119. Hofmann, G. *et al.* In-vitro method for determining corneal tissue friction and damage due to contact lens sliding. *Biotribology* **5**, 23–30 (2016).

120. Carvalho, A. L., Vilhena, L. M. & Ramalho, A. Study of the frictional behavior of soft contact lenses by an innovative method. *Tribol Int* **153**, 106633 (2021).

121. Vidal-Rohr, M., Wolffsohn, J. S., Davies, L. N. & Cerviño, A. Effect of contact lens surface properties on comfort, tear stability and ocular physiology. *Contact Lens and Anterior Eye* **41**, 117–121 (2018).

122. Dogan, A. S., Gurdal, C. & Arslan, N. Corneal confocal microscopy and dry eye findings in contact lens discomfort patients. *Contact Lens and Anterior Eye* **41**, 101–104 (2018).

123. Mann, A. & Tighe, B. Contact lens interactions with the tear film. *Exp Eye Res* **117**, 88–98 (2013).

124. Ngai, V., Medley, J. B., Jones, L., Forrest, J. & Teichroeb, J. Friction of contact lenses: Silicone hydrogel versus conventional hydrogel. *Tribology and Interface Engineering Series* **48**, 371–379 (2005).

125. Corfield, A. P., Carrington, S. D., Hicks, S. J., Berry, M. & Ellingham, R. Ocular mucins: Purification, metabolism and functions. *Prog Retin Eye Res* **16**, 627–656 (1997).

126. Willcox, M. *et al.* CLEAR - Contact lens wettability, cleaning, disinfection and interactions with tears. *Contact Lens and Anterior Eye* **44**, 157–191 (2021).

127. Dunn, A. C., Tichy, J. A., Uruenã, J. M. & Sawyer, W. G. Lubrication regimes in contact lens wear during a blink. *Tribol Int* **63**, 45–50 (2013).

128. Song, Q., Liu, K., Sun, W. & Ye, J. Dead Weight Microtribometer Calibration for Improved Tolerance to Transducer Crosstalk and Cantilever Torsion. *Tribol Lett* **70**, 1–14 (2022).

129. Dünnhaupt, S. *et al.* S-protected thiolated chitosan: Synthesis and in vitro characterization. *Carbohydr Polym* **90**, 765–772 (2012).

130. Kafedjiiski, K., Krauland, A. H., Hoffer, M. H. & Bernkop-Schnürch, A. Synthesis and in vitro evaluation of a novel thiolated chitosan. *Biomaterials* **26**, 819–826 (2005).

131. Board, E., Abe, G. A., Long, L. T. E. & Vicent, T. M. *Chitosan for Biomaterials I | R. Jayakumar | Springer*. (2011).

132. Anitha, A. *et al.* Development of mucoadhesive thiolated chitosan nanoparticles for biomedical applications. *Carbohydr Polym* **83**, 66–73 (2011).

133. Bravo-Osuna, I., Vauthier, C., Farabollini, A., Palmieri, G. F. & Ponchel, G. Mucoadhesion mechanism of chitosan and thiolated chitosan-poly(isobutyl cyanoacrylate) core-shell nanoparticles. *Biomaterials* **28**, 2233–2243 (2007).

134. Nepp, J., Knoetzl, W., Prinz, A., Hoeller, S. & Prinz, M. Management of moderate-to-severe dry eye disease using chitosan-N-acetylcysteine (Lacrimera®) eye drops: a retrospective case series. *Int Ophthalmol* **40**, 1547–1552 (2020).

135. Lorenz, K. *et al.* Long-term management of dry eye by once-daily use of Chitosan-N-Acetylcysteine (Lacrimera®) eye drops. *Journal of Clinical Ophthalmology* **02**, (2018).

136. Allyn, M. M., Luo, R. H., Hellwarth, E. B. & Swindle-Reilly, K. E. Considerations for Polymers Used in Ocular Drug Delivery. *Front Med (Lausanne)* **8**, 1–25 (2022).

137. Mun, E. A., Morrison, P. W. J., Williams, A. C. & Khutoryanskiy, V. V. On the barrier properties of the cornea: A microscopy study of the penetration of fluorescently labeled nanoparticles, polymers, and sodium fluorescein. *Mol Pharm* **11**, 3556–3564 (2014).

138. Messina, M. & Dua, H. S. Early results on the use of chitosan-N-acetylcysteine (Lacrimera ®) in the management of dry eye disease of varied etiology. *Int Ophthalmol* **39**, 693–696 (2019).

139. Zamboulis, A. *et al.* Chitosan and its derivatives for ocular delivery formulations: Recent advances and developments. *Polymers (Basel)* **12**, 9–11 (2020).

140. Marti, A. Inert bioceramics (Al2O3, ZrO2) for medical application. *Injury* **31**, D33–D36 (2000).

141. Argüelles-Monal, W. M., Lizardi-Mendoza, J., Fernández-Quiroz, D., Recillas-Mota, M. T. & Montiel-Herrera, M. Chitosan derivatives: Introducing new functionalities with a controlled

molecular architecture for innovative materials. *Polymers (Basel)* **10**, (2018).

142.   Broitman, E. Indentation Hardness Measurements at Macro-, Micro-, and Nanoscale: A Critical Overview. *Tribol Lett* **65**, 1–18 (2017).

143.   Czerner, M., Fellay, L. S., Suárez, M. P., Frontini, P. M. & Fasce, L. A. Determination of Elastic Modulus of Gelatin Gels by Indentation Experiments. *Procedia Materials Science* **8**, 287–296 (2015).

144.   Tang, G., Galluzzi, M., Biswas, C. S. & Stadler, F. J. Investigation of micromechanical properties of hard sphere filled composite hydrogels by atomic force microscopy and finite element simulations. *J Mech Behav Biomed Mater* **78**, 496–504 (2018).

145.   Last, J. A., Liliensiek, S. J., Nealey, P. F. & Murphy, C. J. Determining the mechanical properties of human corneal basement membranes with atomic force microscopy. *J Struct Biol* **167**, 19–24 (2009).

146.   Wu, J. *et al.* The 3D Eyeball FEA Model with Needle Rotation. *APCBEE Procedia* **7**, 4–10 (2013).

147.   Shih, P. J. *et al.* Estimation of the Corneal Young's Modulus in Vivo Based on a Fluid-Filled Spherical-Shell Model with Scheimpflug Imaging. *J Ophthalmol* **2017**, (2017).

148.   Aloy, M. *et al.* Estimation of the mechanical properties of the eye through the study of its vibrational modes. *PLoS One* **12**, 1–19 (2017).

149.   Battaglioli, J. L. & Kamm, R. D. Measurements of the compressive properties of scleral tissue. *Invest Ophthalmol Vis Sci* **25**, 59–65 (1984).

150.   Prüftechnik, M.- & Untersu-, V. 8 Tribologische Mess- und Prüf technik.

151.   Rigo, J. & Feinle, P. SRV Tribometer. in *Encyclopedia of Lubricants and Lubrication* 1949–1956 (Springer Berlin Heidelberg, 2014). doi:10.1007/978-3-642-22647-2_497.

152.   Patil, S., Steklov, N., Song, L., Bae, W. C. & D'Lima, D. D. Comparative biomechanical analysis of human and caprine knee articular cartilage. *Knee* **21**, 119–125 (2014).

153.   Sugiyama, S., McGowan, M., Kafi, M., Phillips, N. & Young, M. Effects of increased ambient temperature on the development of in vitro derived bovine zygotes. *Theriogenology* **60**, 1039–1047 (2003).

154.   Rimington, C. Synovial Fluid Mucin. *Ann Rheum Dis* **8**, 34–41 (1949).

155.   Gebeshuber, I. C., Drack, M. & Scherge, M. Tribology in biology. *Tribology - Materials, Surfaces and Interfaces* **2**, 200–212 (2008).

156.   Permana, I., Wang, F., Rakhsit, D. & Huang, J. Ventilation Improvement in a Biosafety Laboratory Building. (2022).

157.   Timar, J. *et al.* Successful strategies to increase organ donation: the Gift of Life Donor Program Philadelphia model. *Indian J Thorac Cardiovasc Surg* **37**, 380–394 (2021).

158.   Heidari, B. Knee osteoarthritis diagnosis, treatment and associated factors of progression: Part II. *Caspian J Intern Med* **2**, 249–255 (2011).

159.   Gobbi, A., Nunag, P. & Malinowski, K. Treatment of full thickness chondral lesions of the knee with microfracture in a group of athletes. *Knee Surgery, Sports Traumatology, Arthroscopy* **13**, 213–221 (2005).

160.   Luyten, F. P., Denti, M., Filardo, G., Kon, E. & Engebretsen, L. Definition and classification of early osteoarthritis of the knee. *Knee Surgery, Sports Traumatology, Arthroscopy* **20**, 401–406 (2012).

161.   Athanasiou, K. A., Rosenwasser, M. P., Buckwalter, J. A., Malinin, T. I. & Mow, V. C. Interspecies comparisons of in situ intrinsic mechanical properties of distal femoral cartilage. *Journal of Orthopaedic Research* **9**, 330–340 (1991).

162.   Frisbie, D. D., Cross, M. W. & McIlwraith, C. W. A comparative study of articular cartilage thickness in the stifle of animal species used in human pre-clinical studies compared to articular cartilage thickness in the human knee. *Vet Comp Orthop Traumatol* **19**, 142–146 (2006).

163.   Sorushanova, A., Skoufos, I., Tzora, A., Mullen, A. M. & Zeugolis, D. I. The influence of animal species, gender and tissue on the structural, biophysical, biochemical and biological properties of collagen sponges. *J Mater Sci Mater Med* **32**, (2021).

164. Shiomi, T. *et al.* Influence of medial meniscectomy on stress distribution of the femoral cartilage in porcine knees: A 3D reconstructed T2 mapping study. *Osteoarthritis Cartilage* **20**, 1383–1390 (2012).

165. Arno, S. *et al.* Relation between cartilage volume and meniscal contact in medial osteoarthritis of the knee. *Knee* **19**, 896–901 (2012).

166. Marouane, H., Shirazi-Adl, A. & Adouni, M. 3D active-passive response of human knee joint in gait is markedly altered when simulated as a planar 2D joint. *Biomech Model Mechanobiol* **16**, 693–703 (2017).

167. Bartha, L., Vajda, A., Duska, Z., Rahmeh, H. & Hangody, L. Autologous osteochondral mosaicplasty grafting. *Journal of Orthopaedic and Sports Physical Therapy* **36**, 739–750 (2006).

168. Andrade, R. *et al.* Knee donor-site morbidity after mosaicplasty – a systematic review. *J Exp Orthop* **3**, (2016).

169. Accardi, M. A., Dini, D. & Cann, P. M. Experimental and numerical investigation of the behaviour of articular cartilage under shear loadingInterstitial fluid pressurisation and lubrication mechanisms. *Tribol Int* **44**, 565–578 (2011).

170. Hölzl, K. *et al.* Photosensitive gelatine-methacrylamide as engineered extracellular matrix for three-dimensional cell culture. in *Towards Future Regenerative Therapies* 215 (European Cells and Materials Journal, 2016).

171. Konradi, R., Textor, M. & Reimhult, E. Using complementary acoustic and optical techniques for quantitative monitoring of biomolecular adsorption at interfaces. *Biosensors (Basel)* **2**, 341–376 (2012).

172. Omidi, M. *et al. Characterization of biomaterials*. *Biomaterials for Oral and Dental Tissue Engineering* (Elsevier Ltd, 2017). doi:10.1016/B978-0-08-100961-1.00007-4.

173. Stevie, F. A. & Donley, C. L. Introduction to x-ray photoelectron spectroscopy. *Journal of Vacuum Science & Technology A* **38**, 063204 (2020).

174. Krishna, D. N. G. & Philip, J. Review on surface-characterization applications of X-ray photoelectron spectroscopy (XPS): Recent developments and challenges. *Applied Surface Science Advances* **12**, 100332 (2022).

175. Bonengel, S. & Bernkop-Schnürch, A. Thiomers - From bench to market. *Journal of Controlled Release* **195**, 120–129 (2014).

176. Ilakovac, K. Application of the integrated voigt function in analysis of experimental line spectra. *Acta Phys Pol A* **136**, 107–113 (2019).

177. Linford, B. M. R., Editor, C. & Functions, P. Used in Peak Fitting XPS Narrow Scans , and an Introduction to the Impulse Function. 2–9 (2014).

178. Raval, N. *et al. Importance of physicochemical characterization of nanoparticles in pharmaceutical product development*. *Basic Fundamentals of Drug Delivery* (Elsevier Inc., 2018). doi:10.1016/B978-0-12-817909-3.00010-8.

179. Potter, U. J. & Love, G. MICROSCOPY | Scanning Electron Microscopy. in *Encyclopedia of Food Microbiology* 1397–1406 (Elsevier, 1999). doi:10.1006/rwfm.1999.1070.

180. Sanderson, J. Introduction to Light Microscopy. *J Microsc* **193**, 90–91 (1999).

181. Mertz, J. *Introduction to Optical Microscopy*. (W. H. Freeman, 2009).

182. Gusain, M., Nagpal, R. & Zhan, Y. *Analysis and characterization of quantum dots*. *Graphene, Nanotubes and Quantum Dots-Based Nanotechnology: Fundamentals and Applications* (Elsevier Ltd., 2022). doi:10.1016/B978-0-323-85457-3.00027-X.

183. Spence, J. C. H. Future of atomic resolution electron microscopy for materials science. *Materials Science and Engineering R: Reports* **26**, 1–49 (1999).

184. Bruslind, L. Microscopes. https://open.oregonstate.education/generalmicrobiology/chapter/microscopes/.

185. Müllerová, I. Imaging of specimens at optimized low and very low energies in scanning electron microscopes. *Scanning* **23**, 379–394 (2001).

186. Schaber, J., Xiang, R. & Gaponik, N. Review of photocathodes for electron beam sources in particle accelerators. *J Mater Chem C Mater* **11**, 3162–3179 (2023).

187. Müller, A. *et al.* Diode laser based light sources for biomedical applications. *Laser Photon Rev* **7**, 605–627 (2013).

188. Franke, C. *Localization Microscopy*. *Microscope Image Processing, Second Edition* (Elsevier Inc., 2022). doi:10.1016/B978-0-12-821049-9.00016-2.

189. Moo, E. K. *et al.* Collagen fibres determine the crack morphology in articular cartilage. *Acta Biomater* **126**, 301–314 (2021).

APPENDICES

PAPER I

Skin as an interface: Understanding the synergy of dermatology, biomimetics and tribology

Hakan GÖÇERLER [1,*], **Carsten GACHOT** [1], **Philipp G. GRÜTZMACHER** [1], **Stefan J. EDER** [1,2]

[1] Institute of Engineering Design and Product Development, Vienna University of Technology, Vienna, Austria
[2] AC2T research GmbH, Wiener Neustadt, Austria
*Corresponding author: hakan.gocerler@tuwien.ac.at

Abstract

This review explores the intersection of tribology and dermatology, explicitly focusing on studying the human skin and drawing inspiration from natural systems. It investigates animal adaptations and their implications for biotribological applications, with examples such as the friction anisotropy and wear tolerance of snakeskin, the healing properties of fish skin and the lotus effect for reducing adhesion in biomedical devices. Understanding human skin presents challenges due to its complex structure and variability influenced by age, gender, race and environment. The paper discusses *in vivo* and *ex vivo* measurements, substitute models replicating human skin properties and contact mechanics considerations. It explores contact models, measurement methods and factors impacting skin friction, emphasising the interplay between adhesion and deformation components. Techniques such as atomic force microscopy and the colloidal probe technique provide insights into mechanical properties and molecular interactions. By comprehending the complexities of human skin and its tribological behaviour, researchers can develop innovative solutions in areas ranging from soft robotics to medical research and aerospace technology.

1. Introduction

Tribology is the science of friction, wear and lubrication. While many may think directly of things like machine elements and cars, all of us encounter tribological phenomena everyday even much more closely, namely in or on our bodies. The field that deals with these phenomena is a sub-category of tribology, called biotribology, which can have a significant impact on human well-being. Within biotribology, dermatology, ophthalmology, orthopaedics, dentistry, hematology/cardiology, gastroenterology and neurology are prominent fields of study. This review article aims to delve into the realm of dermatology, which involves comprehensive investigation, diagnosis and management of skin-related health conditions. By examining relevant studies, we shed light on the

fundamental theorems employed to comprehend contact conditions, which have also played a pivotal role in shaping the broader field of tribology. Exploring captivating animal kingdom instances before delving into human skin's intricate properties can provide valuable insights for many industrial applications.

At the crossroads of tribology and dermatology, an intriguing avenue of exploration lies in uncovering the design principles that govern the remarkable adaptability and performance of natural systems in response to their environments. Natural systems, while functionally complex, are usually optimised in terms of shape and performance. It is believed that the functional complexity of natural systems is what allows natural species to morph continuously to adapt to their respective operating environments [1]. Often, these adaptations concern surface design features. These may include superior functionality, the ability to harness functional complexity to achieve optimal performance and

1

harmony between shape, form and function. To deduce design rules, there exists a need for quantification of the relationship governing microstructure and mechanical properties of the bio-surface, exploring the influence of macro- and microstructures and finally devising working formulae that describe (and potentially predict) the load-carrying capacity of macro- and micro-scale features during relative motion.

The skin's appearance, health and well-being are inextricably bound to an individual's physiological and psychological well-being since its look, colour and features influence societal perception and personal interactions. The skin has many functions, but the most important is to be a blockade against the entrance of chemical, physical and microbiological agents, thus protecting all other body tissues. It is where hair, nails and certain glands, such as sweat glands and mammary tissue, form. The hair coat, cutaneous (skin) blood circulation and sweat glands are essential in temperature regulation. Electrolytes, water, vitamins, fat, carbohydrates, proteins and other materials are stored in the skin. The skin allows radiation from the sun to convert the inactive form of vitamin D to the active form. It then transfers active vitamin D to the rest of the body through the skin's capillary system, as the roughness dimension is smaller than the blood platelets [2]. Additionally, the skin changes colour to darker with the help of melanin and it helps prevent damage from ultraviolet light. We can also monitor a person's health as internal diseases, external diseases, and the effects of topical substances can change the visual look of the skin [3]. Skin is a primary sense organ for touch, heat, pain, itch, cold and pressure. It can also be identified as an extraction organ as it has a part in eliminating waste from the body.

2. Observations in nature

One of the most studied topics concerning the functionality of natural surfaces is their wetting behaviour, which has direct implications on tribological properties. Here the most famous effect is the lotus effect, which results in superhydrophobicity (i.e. contact angles > 150°). Plants have a skin called a cuticle that covers the above-ground surfaces. It is composed of waxes and a polymer network consisting of fatty acid building blocks called cutin. Barthlott and Neinhuis noticed that some plants seemed to have a self-cleaning effect, and this effect was most obvious for the lotus [4]. It is caused by combining two

features of the leaf surface: its waxiness and the microscopic bumps covering it. When the pre-requisite of water-repelling surface chemistry is met, the surface structure becomes dominant [5]. The resulting high water contact angles and the small roll-off angles lead to water droplets rolling easily off the leaves and dragging dirt particles with them. The most exciting application of the lotus effect related to this review is that it reduces the adhesion of blood cells to surfaces. Micro- or nanostructured surfaces mimicking the lotus effect therefore can be used for biomedical devices such as catheters, stents and artificial or prosthetic cardiovascular components [6]. Inspired by the natural blood vessel micro- or nanostructure, Fan et al. devised a strategy for mimicking the topography of the blood vessel tissue's inner cell layer. Using a self-assembly technique together with soft lithography, they fabricated an artificial blood vessel of polydimethylsiloxane (PDMS) with dimensions close to that of natural blood vessels, consisting of submicron ridges (500 nm wide and 100 nm high) and nanoscale protuberances (100 nm wide and 40 nm high) [7]. The results indicated that blood platelet adhesion was reduced only with multiscale-structured PDMS when the roughness matched the platelet size [8]. Liu et al. designed an *in vivo* experiment on the vascular graft of rats that connects to the abdominal aorta to evaluate its effect on the patency rate. They fabricated a longitudinally aligned graft topography on medically graded polyurethane with a surface mimicking the arterial vessel's inner coat. Thrombosis formation was significantly reduced for the aligned topography, and its patency rate was increased from 28.6 to 100 % for the smooth surface. They concluded that the blood compatibility of the aligned topography was observed because of the reduced contact area between the surface and the platelet, as the roughness dimension is smaller than that of the platelets [9].

Furthermore, specific microstructures on natural surfaces also induce anisotropic wetting behaviour. Thorny devils (*Moloch horridus*) and the Texas horned lizard (*Phrynosoma cornutum*) are two fascinating lizard species that can collect and transport water [10] with channel-like structures on their skin (Fig. 1). Specialised skin structures, comprising a microstructured surface with capillary channels between imbricate overlapping scales, enable the lizard to collect water by capillarity and transport it to the mouth for ingestion [11]. It has been suggested that these structures can also be

2

used in tribological settings to guide lubricants across surfaces to designated positions where lubrication is needed to reduce friction and wear [12].
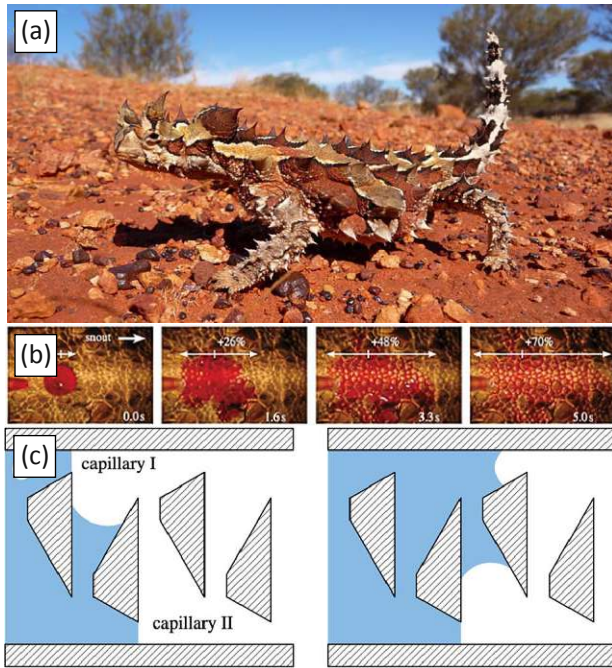

Figure 1. Capillary fluid transport mechanisms in *Moloch horridus*: (a) *Moloch horridus* can drink water from sand through its feet and back, reprinted from Wikimedia Commons, licensed under CC BY-SA 3.0, (b) the fluid transport properties through the channels on the surface of the Texas horned lizard (*Phrynosoma cornutum*) are demonstrated with the help of a coloured water droplet, adapted from Comanns et al. [13], licensed under CC BY 4.0 and (c) schematic illustrating the mechanism of fluid transport by capillary forces; the liquid stops at the sharp edge of capillary I and is picked up by the liquid going through the interconnection, forming a new liquid front, adapted from Comanns et al. [13], licensed under CC BY 4.0

An exciting example of animal skin, which has demonstrated fascinating tribological behaviour and has been investigated as a substitute for human skin, is the skin of a snake [14]. One advantage concerning its tribological evaluation is that snakeskin can be obtained without injury to the animal and does not have to be subjected to chemical or thermal stress prior to use. Shed snakeskin, a non-living tissue, can be stored for extended periods at room temperature and transported conveniently. Stored and fresh snakeskin does not appear to exhibit any differences in permeability. Moreover, snakeskin, lacking hair follicles, does not suffer from issues associated with transfollicular penetration encountered in mammalian skins. The shed skin of ball pythons is of particular interest in tribology

due to their locomotion within a non-breakable boundary lubrication regime [15]. The skin's ornamentation facilitates this performance feature, making it relevant for the design of sliding assemblies (e.g. cylinder piston) and prostheses.

Artificial snakeskin can be used in soft robotics [16]. Snakes can grasp objects with their body and move around using various gaits, including slithering and creeping. They need a surface structure that provides friction anisotropy, enabling them to navigate more quickly and efficiently through their environment. The critical part is not only in the actuation system but also in the design of the artificial skin. The skin should possess flexibility and stretchability, while the scales need to be positioned on a pliable base body at a specific angle of attack. In experimental investigations of artificial snakeskin, researchers observed friction anisotropy when using two different stiffness base materials and three angles of attack [17]. Interestingly, they discovered that employing a flexible base material reduces friction in the forward direction and increases it in the reverse direction, resulting in enhanced friction anisotropy. In a separate study by Sánchez-López et al., long-term low friction maintenance and wear reduction on snakes' ventral scales were explored [18]. The main issue is that even though the softness of the material in robotics is essential for friction anisotropy, how would such a material endure permanent friction and wear during sliding? The wear resistance is attributed to the fibrous layered composite material of the skin, comprising a gradient of material properties, surface microstructure and ordered layers of lipid molecules on the skin surface [19].

Shed snakeskin has also been considered as a substitute for human skin in tribological research. The frictional response of shed skin obtained from *Python regius* and human skin from different anatomical sites, gender and age, was compared. It was observed that the mechanisms governing the friction response of human skin are common to snakeskin despite differences in chemical composition and apparent surface structure. Both skin types display sensitivity to hysteresis and adhesive dissipation. This observation also means researchers can use shed snakeskin under certain circumstances as an *ex vivo* substitute for tribological evaluation [20]. However, the frictional performance of human skin is not solely determined by surface topography but is also influenced by water content within the skin cells. A study that focused on the skin's permeation parameters and

3

physiological characteristics, e.g. the water and lipid content and the thickness of shed snakeskin and human skin, demonstrated that the permeability coefficients of lipophilic drugs in shed snakeskin, were in the same range as those in human skin (0.9 to 1.8 times), whereas those of hydrophilic drugs were remarkably lower (3.3 to 6.1 times).

Frictional anisotropy like that of snakeskin can also be observed on many biological surfaces such as butterfly wings [21], animal attachment pads [22], insect unguitractor plates [23], spider tarsi [24], gecko toe [25], peristome of pitcher plants [26], wheat awns [27], plant fruits and leaves and fish skin [28]. On the other hand, some non-biological examples, such as single crystal surfaces [29], monolayer graphene [30] and engineered surfaces with texture patterns [31] also demonstrate this friction anisotropy, thus proving an association between these two worlds. If we understand the mechanical response depending on differently oriented micro- or nanostructures and the relationships between the topographic orientation and biological functions, such as locomotion [32], predation [33], cleaning [34] and transporting fluids and items [35], there is always a possibility to learn from nature and to apply this knowledge in other industrial applications. Therefore, frictional anisotropy increasingly attracts the interest of scientists and engineers [36].

There is another example of skin found in nature that has garnered significant attention across a wide range of industrial applications, i.e. shark skin [37]. The skin of fast-swimming sharks protects against the drag that sharks experience when swimming. The tiny scales covering the skin called dermal denticles (generally 0.2 − 0.5 mm small, with fine regularly spaced denticles of 30 − 100 µm), are shaped like small ribs and are oriented in the direction of fluid flow [38]. Riblets inspired by shark skin have been shown to reduce drag by up to 9.9 % [39]. In addition, the spacing between these skin ridges is enough to impede the attachment of microscopic aquatic organisms to the surface. Slower-swimming sharks also have skin protrusions, although they lack the riblet-shaped features that provide drag-reducing benefits [40].

Dean et al. highlighted the fact that different species of shark have different riblet formations, but also the same shark species have different formations on different parts of their bodies (Fig. 2). While certain riblet formations exhibit superior drag reduction properties, there is room for optimising material durability. The manufacturing

of riblets, both for research purposes and large-scale applications, has been a major challenge in the field. Due to the associated costs, typical microscale manufacturing techniques would fit better for large-scale applications. Various milling, grinding and rolling techniques, micro-moulding, micro-embossing and 3D printing were used to produce the riblets. These applications fail to mimic nanodetails on the riblets and focus on the form of the surface. To explore the potential of nanoroughness enhancing the overall hydrophobicity of shark skin, it is necessary to conduct atomic force microscope studies on the nanoscale surface characteristics of shark skin [40].
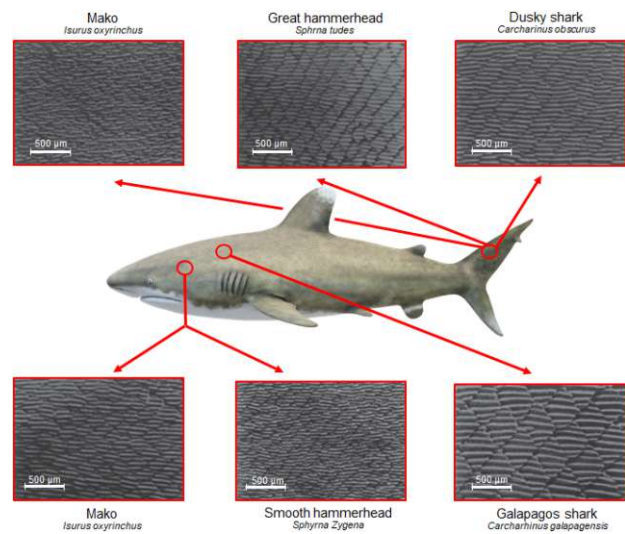

Figure 2. Different species of shark have different riblet formations, but also same shark species have different formations on different parts of their bodies; adapted from Dean and Bhushan [40], used with permission of The Royal Society (U.K.), from Shark-skin surfaces for fluid-drag reduction in turbulent flow: A review, B. Dean, B. Bhushan, 368, 1929, 2010; permission conveyed through Copyright Clearance Center, Inc.

One of the industrial applications of shark skin is swimsuits. The 83 % of the swimmers who won a medal at the Olympic Games in Sydney wore a shark skin suit. Due to the exceptional speed achievable with them, they were subsequently banned. This decision spurred scientific investigations to demonstrate the scientific advantages of the swimsuit. George Lauder, an ichthyologist, led a study that found shark skin does increase speed – in sharks [41]. However, the functionality of the swimsuit relies on many other factors such as non-textile parameters, how the suit ensures a particular posture during swimming, and how tight the swimsuit fits on the swimmer's body, but not on the biomimetic aspect, as the suit does not feature shark skin riblets [41].

Through parametric modelling to query a wide range of different designs, Domel et al. discovered a set of denticle-inspired surface structures that achieve simultaneous drag reduction and lift generation on an aerofoil, resulting in improvements of up to 323 % [42]. Lufthansa Group and BASF embraced this technology, and in 2022 Lufthansa Cargo equipped all Boeing 777 freighters with these structures to improve fuel efficiency and help airlines reach sustainability targets. The presence of the 50 µm riblets reduces aircraft drag by 10 % and fuel consumption by around 1 %. For the entire fleet of ten aircraft, this translates to annual savings of around 11,700 tons of CO_2 emissions, equivalent to worldwide commercial airliner savings of approx. $16.13 billion per year [43].

The skins of other types of fish are also noteworthy subjects due to their tribological properties and their relevance to medical applications for both humans and other species. Researchers in dermatology can gain valuable insights from the biology of fish skin, as it addresses several fundamental questions of great significance to mammalian skin. Fish, being constantly exposed to aqueous environments that harbour a higher concentration of pathogens compared to the aerial environment of mammals, have evolved a complex antimicrobial defence system [44]. The materials in fish skin have a natural anti-inflammatory effect that speeds healing, which can be used in human wound recovery [45].

Pape and Poll observed a correlation between the tribological properties and the occurrence and appearance of the fish flakes. While the mudskipper has soft skin adapted to the periods outside of the water, the fish scales protect the skin but provide higher friction in the case of rubbing contacts. Still, the coefficient of friction (COF) values were between $0.2 - 0.5$ [46]. Wu et al. investigated biomimicking lubrication using responsive hydrogels [47]. The slippery mucus produced by fish skin is the cause for its ultra-low COF with many counter-surfaces, which is vital to protect fish against predator attack and allow them to swim faster and remain elusive. The researchers developed responsive hydrogels that mimic this slick skin by responding to external stimuli such as pH and temperature. These hydrogels outperformed fish skin, achieving not only a low COF (in the range of 5×10^{-3}) but also demonstrating tuneable COFs from low to relatively high (higher than 0.1) through sequential regulation of pH and temperature.

While comparing the dermatological properties provides valuable insights into the skin properties of various animal species, it also forms the basis for our understanding of human skin. As part of the animal kingdom, we share fundamental biological processes and evolutionary history with other species. However, the unique characteristics of human skin, including its structure, composition and the diverse range of diseases it can develop, warrant a focused examination. By delving into the intricacies of human dermatology, we can uncover specific factors that contribute to skin health and diseases in our own species. This allows us to explore the interplay between genetics, environmental influences, and the intricate mechanisms underlying skin health and disease in the context of human dermatology.

3. Observations on human skin

Unlike other animals, humankind's evolution has influenced the body to have to withstand more extreme conditions. Social constructs made unnecessary applications to daily routines. Electric and non-electric razors, with shaving and after-shave creams, hair-removal creams and even lasers are frequently used. Humans go to places with temperatures between -50 to $70\,°C$, $80\,m$ deep under water, and even in space. No other animals touch electronic devices the entire day and use their fingertips as probes. So, very different test systems, using different materials, are needed to understand human skin's interaction with different environments.

3.1 Mechanical properties of human skin

One of the main challenges in the investigation of the skin is the complex structure of the skin (Fig. 3). The skin has a multi-layered structure, and its mechanical properties vary with the depth of the layers. The thickness of the various skin layers varies significantly, with the epidermis being the thinnest, ranging from 0.05 to 1.5 mm, the dermis ranging from 0.3 to 3 mm, and the subcutaneous tissue being the thickest, ranging from 1 to 2 cm. The *stratum corneum*, the top layer of the epidermis, thickness varies between 10 to 20 µm. Given its complex multi-layered structure, the skin exhibits a wide range of viscoelastic phenomena like most soft tissues, including creep, relaxation, hysteresis [48] and strain rate dependency [49]. In addition to multiple layers, the skin has a dermal matrix with embedded fibres, leading to viscoelastic and anisotropic mechanical behaviour [50]. The dermis,

5

due to its significant thickness compared to that of the *stratum corneum* and viable epidermis, is the main contributor to the tensile mechanical properties of the skin [51]. Other structures in the skin are sebaceous and eccrine glands and blood and lymph vessels. Sebaceous glands produce sebum, which keeps the skin and hair supple and protects the skin against bacteria and fungi. Eccrine glands produce sweat, which regulates body temperature but also significantly affects the skin's tribological behaviour, as we will discuss later in this chapter. The *stratum corneum* is often described as having a brick-and-mortar structure: the dense structure of corneocyte bricks and keratin mortar makes it very difficult for external hazards to attack the body through the skin and for body fluids to leave the body through the skin. A combination of substances like amino acids, salts and lactate, referred to as natural moisturising factors, play an essential role in the hydration of the *stratum corneum* [52]. A healthy *stratum corneum* is essential for the skin's defence mechanism and dehydration function as a whole [53].
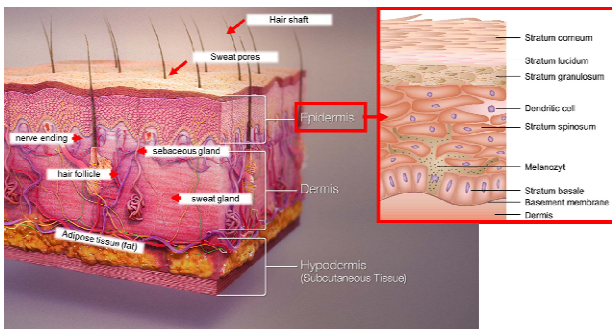
Figure 3. Schematic illustration of skin layers and main functioning parts (adapted from Wikimedia Commons, licensed under CC BY-SA 4.0) with a detailed image of layers of the epidermis (obtained from Alamy Limited, credited as MedicalStocks/Alamy Stock Vector)

The mechanical properties of the *stratum corneum* are fundamental in conditioning the transmission of loads and subsequent deformations of the other underlying skin layers across several length scales [54]. These mechanical aspects are vital for the stimulation of mechanoreceptors that convert mechanical energy into neural signalling (e.g. tactile perception [55]) or are involved in metabolic processes. Any variation in the mechanical properties of the *stratum corneum* is likely to affect the material's mechanical response; also, the subsequent altered external surface topography will eventually have evident and significant consequences for the tribological response of the skin [56].

The skin's characteristics (thickness, strength, elasticity and colour) also depend on various subject-related variables, such as age, gender, body composition, race, stress, season, nutrition and mechanical load, therefore rendering these properties very dynamic, particularly over the life course [57]. Moreover, there is substantial variability according to specific environmental conditions such as temperature and relative humidity, and the skin's properties are dependent on the locations on the body [58]. The skin on the palms and soles contains more eccrine glands per square centimetre than hairy skin. When people are nervous or anxious, the production of sweat is increased, which results in an increase in the coefficient of friction and finally increased grip of the palms and soles [59].

There remains an unresolved question concerning the consistency of skin stiffness measurements across various length scales, which have yielded values ranging from kPa [60], to several MPa [61]. The elastic modulus of human skin *in vivo* has been reported to vary over $4 – 5$ orders of magnitude (ranging from 4.4 kPa to 57 MPa) in the literature, depending on factors such as the measurement method, anatomical site, skin hydration level, age, person and theoretical model used [62-65]. Moreover, skin hydration also influences these values, leading to a reduction in the elasticity and stiffness of human skin, typically by one order of magnitude. For dry skin, elastic modulus ranges from 30 kPa to 1,000 MPa, while for wet skin, it range from 10 kPa to 100 MPa [66-69]. It should be noted that the elastic modulus of biological soft tissues, particularly skin, lacks significance unless the exact strain level and physiological conditions are specified. In summary, experimental evidence suggests that the *stratum corneum* exhibits stiffness values and elastic moduli (ranging from 10 kPa to 1 GPa) at least two orders of magnitude higher than those of the dermis (ranging from 0.5 kPa to 45 MPa) [57,70-72] and subcutaneous fat tissue ($0.12 – 30$ kPa) [70,73,74].

3.2 Measuring techniques for the mechanical properties of human skin

Skin testing involves various *in vivo* and *ex vivo* measurement methods, with suction, indentation and extension tests being the most common ones. Suction measurements play a vital role in determining both *in vivo* and *in situ* skin properties [75]. By applying negative pressure, tissue is drawn into the probe opening, and an optical system measures the resulting bulge height. The

relationship between pressure and bulge height is directly linked to the probe opening size and loading protocol. These suction measurements are essential for characterising the nonlinear, viscoelastic, and time- and location-dependent behaviour of the skin. Through suction tests, important skin properties such as compliance, elastic recovery, creep and permanent deformation can be quantified. These measurements help assess the influence of factors like fatigue, ageing, sex and body location on the skin's behaviour [76].

The *ex vivo* mechanical properties of the skin can be characterised with extension tests. They allow the investigation of the skin's anisotropic response related to the Langer lines (skin tension lines) distributed across the body [77]. Using a uniaxial or multiaxial loading rig, we can observe skin's time and history-dependent behaviour through monotonic and cyclic creep and relaxation experiments [78]. The mechanical properties of the samples vary based on their derivation and are significantly influenced by storage duration, conditions and temperature. Therefore, it becomes crucial to analyse the relevant application and control these parameters to ensure the validity of the research data. Sample preparation typically involves removing the epidermis and fat to isolate the dermal layer. However, this technique alters the skin tissue's physiological state and results in the loss of the *in vivo* multiaxial pre-tension, causing changes in the unique tensioned configuration of collagen and elastin networks. When studying skin extension, many research studies interpret experimental data using linear elasticity theory. They extract the slope of the linear regime from uniaxial or multiaxial measurements to determine the ultimate tensile strength and elastic modulus of the dermis [61].

The dynamic response of superficial skin can be measured by indentation. In a range of $10-60$ Hz and at a low indentation depth of 200 ± 3 µm skin stiffness and viscosity are frequency-independent [79]. For determining the skin's mechanical properties at higher resolution atomic force microscopy (AFM) can be used. In earlier studies, the influence of hydration on the mechanical response of the *stratum corneum* and epidermis was quantified using AFM [80]. The measurements involve indentation depths of up to 200 nm, which are three orders of magnitude smaller than the previously described indentation tests. As a result, they capture the mechanical response at a much finer length scale.

Previously, shear tests on individual skin layers were conducted, but due to experimental constraints, they were restricted to the linear regime. However, more recent developments have addressed this limitation. Gerhardt et al. [81] and Lamers et al. [82] introduced an innovative experimental approach to examine the shear response of full-thickness human skin. In their method, they combined large amplitude oscillatory shear tests, applying strains up to 0.1 on a rheometer, with digital image correlation techniques to analyse the cross-sectional area of the skin. This new method allows for a more comprehensive investigation of the skin's shear behaviour. The novel imaging-based method introduced in this study allows them to perform shear tests and to study layer-dependent skin properties using full-thickness skin; hence no need to separate skin layers which is a time-consuming procedure and possibly disrupts skin layers. Using this method, they investigated skin heterogeneity, namely the non-linear viscoelastic response, by determining local displacements. The visualisation of the shear experiment provides real-time optical feedback improving quality assurance and reliability of the results. Moreover, their method can be used to directly measure large strains, i.e. skin mechanics in the non-linear viscoelastic strain regime in which modulus is strain-dependent and the analysis and interpretation of conventional rheometer measurements is complicated [83]. With this modification, one short shear experiment provides raw datasets that can be used to fully characterise the viscoelastic, and local strain and layer-dependent shear properties of full-thickness skin.

Precise prediction of mechanical responses holds significant relevance in a wide range of applications. Examples include plastic surgery, where it aids in modelling artificial skin grafts; skin tissue engineering, enabling better design and development; cosmetics, for improved product formulations; shaving, to enhance razor performance; and research involving trans-epidermal drug delivery, which benefits from a better understanding of skin mechanics [84,85]. However, no constitutive model in literature can describe the complex mechanical response of full-thickness human skin, specifically to shear deformation. The decision to select a certain level of mechanical complexity with a constitutive model is application-dependent. A simplified constitutive skin model often simplifies the contact situation by neglecting parameters such as nonlinearity, viscosity and heterogeneity. On the other hand, for

accurate predictions more complex approaches are necessary. Experiments now employ the fusion of full-field deformation analysis, which tracks complex 3D tissue deformations, with local force measurement during *ex vivo* tests of global force-displacement curves under different loading conditions.

Besides the classical physical/mechanical parameters, skin bioengineering parameters have been introduced to characterise the viscoelastic properties of human skin. These parameters describe skin structural aspects rather than pure mechanics, making them somewhat limited in a strictly mechanical context. However, despite this limitation, dermatologists and cosmetic scientists frequently rely on skin bioengineering parameters, such as Cutometer values, in clinical, disease-related and biological interpretations of skin tissue integrity. In the existing literature, weak correlations between skin bioengineering parameters and skin friction coefficients have been reported. Specifically, the tangential stiffness of human skin and the interfacial shear strength in tribo-pair are believed to be crucial factors in determining the friction behaviour of the skin [86,87].

Concerning testing cosmetics on skin samples, animal skin substitutes became less eligible, as from 11 July 2013 trade-in cosmetics tested on animals is prohibited in EU member states under the EU cosmetics regulation. Every year almost 10 million mice, rats, rabbits and dogs are used in laboratories for research and testing. According to the global *in vitro* diagnostics (IVD) market, approximately $76 billion will be spent on product testing by 2023 in the skincare, cosmetics and pharmaceutical companies [88]. A series of standard tests require up to 12,000 animals and can take years to complete, so there is a need for replicated skin models, if possible, consisting of human skin cells, that feature the same properties and functions as normal human skin.

Various chemical and physical considerations must be considered when designing a skin model to produce a biomimetic design, which should mimic the skin's structural characteristics and mechanical strength. Various commercial products have made significant progress toward achieving a native skin alternative. One successful model, the ThinCert® cell culture insert, offers an ideal artificial environment for *in vitro* reconstruction and is thus perfect for cultivating skin cells [89]. The base of the cell culture inserts features a capillary pore membrane which consists of USP (United States Pharmacopeia) Class

VI certified polyethylene terephthalate (PET). The membrane enables oxygen to reach the cells from above while they are simultaneously supplied with nutrients from the multi-well plate below. This is important because skin cells need specific nutrients and contact with oxygen to develop the *stratum corneum*. The membrane surface is treated in a way that ensures optimum adhesion and growth for the cultivated cells. The hanging geometry of the ThinCert® cell culture inserts ensures the distance to the well base and the side walls, so it prevents capillary suction between the internal and external well walls. ThinCert® inserts are thus ideal for primary cell cultures, transport, secretion, diffusion studies, migration experiments, cytotoxicity tests, co-cultures and transepithelial electrical resistance (TEER) measurements. A biotech company, Genoskin, developed a method to keep human skin alive for up to a week, long enough to conduct a wide range of pharmaceutical and cosmetic tests [90]. Skin samples are collected from plastic surgery patients and classified as *in vivo*.

Further research perspectives involve the development of a functional bi-layered model that mimics the constituent properties such as viscoelasticity and organisation of the native epidermis and dermis, as well as incorporating dynamic elements to mimic skin's interactions with other organs. The models, therefore, react even more authentically than animal skin to cosmetics in testing.

3.3 Contact mechanics and friction behaviour of human skin

To gain a deeper understanding of the friction behaviour of human skin, researchers have turned their attention to the contact mechanics involved in the interaction between skin and various surfaces. From a contact mechanics point of view, most models trace back to the Hertz theory [91], assuming a pure elastic contact situation without adhesion between the surfaces. However, this can only be used for a first assumption and its accuracy is limited. A friction model for skin that also accounts for adhesion is summarised in Equation (1) [92,93].

$$F_{\text{friction}} \sim C\,(F_{\text{normal}})^{n}. \tag{1}$$

If we combine it with Equation (2)

$$\mu = F_{\text{friction}} / F_{\text{normal}}, \tag{2}$$

we can express the coefficient of friction as:

$$\mu \sim C\,(F_{\text{normal}})^{n-1}. \tag{3}$$

8

In Equation (3), the properties of the tribological system determine the constant n. The constant in the equations includes an estimation of the real area of contact, which can be calculated based on the roughness of the skin and the topography of the contact material. The estimation is based on parameters such as the elastic modulus and an indicator for the viscoelastic behaviour of the skin. Based on these models, in friction situations primarily influenced by adhesion n has a value of 2/3 [94], and in friction situations with skin deformations primarily right under the surface n is 4/3 [95]. According to Comaish and Bottoms [93], n should be smaller than 1, although El-Shimi [96] is more specific for the n value (between 0.66 and 1). Other values for n reported in the literature range from 0.73 to 1.07 [97-99].

Estimating the actual contact area can be calculated based on the skin's and the contact material's roughness, the elastic modulus and the indicator for the viscoelastic behaviour of the skin. Determining these parameters is complex and time-consuming. For example, the elastic modulus of the skin has been obtained through *in vitro* techniques or measuring techniques that are uncomfortable for the subjects. Furthermore, some studies conclude that "the" elastic modulus for the skin does not exist. This modulus depends on the position of the limb, the muscle tension and many more variables [100].

In terms of measuring skin friction, several methods are available. Initially, it was measured with a reciprocating linear movement [101]. Later, a handheld tribometer was designed [102] as a rotating indenter to measure skin friction. The axis of rotation of the annular contact material was perpendicular to the skin's surface. The vital part of this application was that the rotation allows for continuous movement with larger displacements without being affected by the anisotropic properties of the skin. Another application used a rotating contact material with the rotation axis parallel to the skin's surface [103], allowing for continuous movements. Dinc et al. employed a force transducer to measure the friction between the tip of a finger sliding over a flat sample of material. The force transducer measures both the applied load and the resulting shear load. The input conditions, such as the applied load and the sliding velocity in these setups, depend strongly on the subject and are therefore typically not very accurately controlled or constant during the test, but how close this system is to real-world application makes it very useful and used even in psychophysics investigations [104].

The results in the literature for skin friction measurements were obtained under vast variations of test parameters. The relative motion of the counterparts was changed, as well as the normal load $(0.01 - 70 \text{ N})$ and velocity $(0.13 \text{ mm/s} - 3.5 \text{ m/s})$ over a wide range. It is not surprising that the reported values for the kinematic coefficient of friction fluctuate between 0.071 [67] to 5.0 [96], and the values for the static coefficient of friction fluctuate between 0.11 [105] to 3.4 [97]. The results have significant differences according to loading conditions, lubrication and material couples. Bobjer et al. tested using fingers against polycarbonate (PC) (e.g. typical for bottles or mobile phone housings) under different loads and observed a strong load dependence when measuring skin friction. They observed a COF value of 2.22 for the test under 1 N load and 0.85 under 20 N loading [106]. Cua et al. used polytetrafluorethylene (PTFE) against the abdomen and forehead skin and observed 0.12 and 0.34, respectively showing how the location also strongly affects the tribological properties [107]. El-Shimi et al. used forearm skin against polished steel lubricated with silicone oil and without lubrication. COF value dropped from 0.31 to 0.07 due to the application of silicone oil [96]. They also applied the same test parameters on polished and rough stainless steel without lubrication. The rough sample represented a COF of 0.16, whereas the polished surface represented a COF of 0.63. This test hints at the role of surface roughness in skin contact. Gee et al. used different counter-bodies against the finger under the normal load of $2 - 20 \text{ N}$. PC against the finger had a COF value of 2.7, glass had 1.2 and paper 0.6 [108]. This shows how the COF is not only a material property but the property of the entire tribological system, and specifically how that material pairing influences friction. Koudine et al. showed that the loading condition is the dominant parameter for the forearm skin and glass tribo-pair, where the results varied between $0.6 - 3.6$ [97].

Additionally, several substances present on the skin can substantially affect skin friction. Such substances reported in the literature include oil, petrolatum, glycerine, isopropyl alcohol, ether, talcum powder and lard [67,95,96,98,99,109-113]. Another example of variation in test methods affecting the friction results is the preparation of the skin. Pre-testing treatments include removing hair [99,101,114], cleaning the skin with water,

detergents or alcohol [92,93,95,99,108,110,114-120] and finally, no pre-testing treatment [86,107, 109,113,121-123]. Cleaning the skin before measurements would enhance the repeatability, but it influences the skin's state of hydration; also, the skin may host some contaminants that influence the measured skin friction.

Depending on the intricate interplay of contact conditions, the presence of fluids or lubricants (such as sweat, water and sebum), and film thicknesses relative to the surface roughness of the contacting materials, diverse lubrication effects come into play, encompassing boundary lubrication, mixed lubrication and elastohydrodynamic lubrication (EHL). When a product interfaces with the skin through sliding motion, the lateral friction force governing the skin-product interaction is governed by the intricate interplay of adhesion and deformation phenomena, influenced by a multitude of intricate factors. The adhesion component emerges from the interfacial shear resistance arising due to the formation and subsequent breaking of interatomic junctions, primarily driven by short-range forces such as Van der Waals interactions within the contact zone. The existence of a naturally produced continuous thin lipid film on the outer skin surface assumes paramount importance in modulating adhesion forces while concurrently altering the area of contact and stress distribution [124]. Conversely, the deformation friction component arises from viscoelastic hysteresis. Depending on the sliding speed of the product, the strain energy might only exhibit partial recovery, leading to an additional loss in friction.

3.4 The main components of friction: Adhesion and deformation

Adhesion stands prominently as the principal contributor to the frictional characteristics of human skin, with deformation mechanisms deemed to play a secondary role [94,95]. Extensive scholarly literature has employed various theoretical models to elucidate the mechanical contact behaviour and friction mechanisms inherent to the skin [67,94,97]. Consideration of skin surface roughness's impact on friction reveals typical values of Ra and Rz falling within the range of $10-30$ μm and $30-140$ μm, respectively [125], with such values reportedly increasing with age [62,126-129]. Although a handful of studies have offered insights into the influence of skin topography on friction [87,130], the results remain

somewhat contradictory. For instance, a study on female patients' volar forearm friction coefficient did not exhibit a significant correlation with the surface roughness Ra of the skin. Nevertheless, the same study observed that surface roughness Ra significantly improved the predictability of the COF [87]. Additionally, Nakajima and Narasaka reported a correlation between the density of primary lines and skin friction, indicating that the lower the density of primary lines, the higher the friction. However, an additional parameter potentially assumes vital significance here, as the density of lines corresponds to the skin's elastic modulus, which itself changes with age [130].

Studies have provided additional evidence that the amplitude of the probe surface roughness assumes a commanding role in determining friction behaviour [131]. Particularly, in the context of highly rough surfaces, reaching up to Rq = 90 μm, a direct correlation has been observed, with the COF escalating alongside the increasing surface roughness [131,132]. Tomlinson et al. observed a constant plateau COF of ≈ 0.8 and ≈ 0.65 for roughness values Rq > 25 μm against steel and brass. On the other hand, in the case of hydrated skin, a Gaussian-like relationship between roughness (Rq = $0.004-2$ μm) and friction coefficients varying between $0.9-1.7$, with maximum values at intermediate roughness (Rq = $0.006-0.4$ μm) was reported [133]. The elevated friction observed within the intermediate roughness regime may be attributed to the intricate interplay of interacting adhesion and deformation components, especially in the context of the hydrated skin condition. It must be pointed out that in skin tribology the skewness and kurtosis parameters of the roughness, together with the surface texture, are essential factors [132,133]. This corroborates the findings of Derler et al. [131], whose investigations revealed a positive linear correlation between the slope of surface asperity peaks and friction coefficients during the sliding of plantar skin on various wet floor coverings. Furthermore, in a recent study focusing on friction between the finger and ridged surfaces, Tomlinson et al. [134] discovered that at low ridge height and width, adhesion played a dominant role in governing friction behaviour. However, as the ridge heights surpassed 42.5 μm, interlocking effects emerged, accounting for over 50 % of the total friction. Additionally, at a ridge height of 250 μm, hysteresis also became a contributing factor, albeit at a level below 10 %.

10

The observed phenomenon of skin friction rising in response to increasing material or probe roughness aligns with Moore's theory for elastomers [135]. This theory posits that the friction coefficient of compliant materials on rough surfaces escalates proportionally with the amplitude of surface roughness. Notably, the insightful work by Hendriks and Franklin [115] suggests that Moore's theory can indeed be extrapolated to the context of the skin interacting with rough surfaces ($Ra > 3 - 10$ μm) particularly in scenarios where interactions between surface asperities and skin ridges are prevalent, such as on the fingers, palm or feet.

The skin's surface is typically safeguarded by an acidic hydrolipid film, maintaining a pH range of 4 to 6. This protective film plays pivotal roles, such as governing the skin flora, forestalling colonisation by pathogenic organisms and serving as a potent defence mechanism against invading microorganisms [125]. Comprising a blend of water from sweat and sebum secreted by sebaceous glands, the hydrolipid film envelops the *stratum corneum*. In the domain of skin tribology, the role and significance of sebum lipids and their interactions with water have sparked debates and controversies [107,136-139]. A study conducted by Pailler-Mattei et al. [139] illuminated how the skin surface lipid film influences skin adhesion properties through capillary phenomena. Likewise, Gupta et al. [137] presented noteworthy findings, illustrating a moderate positive linear correlation between sebum levels and the forearm skin's friction when measured against steel.

Conversely, when exploring the forehead, a discovery of weak correlations between the skin surface lipid content and friction emerged [107]. This finding further emphasises the location-specific nature of the skin's tribological behaviour. Interestingly, in the same study, no significant correlation was evident between the parameters in nine other anatomical skin regions, indicating that surface lipids hold a restricted role in governing skin friction. Consequently, a deeper investigation and more fundamental studies are imperative to comprehensively elucidate the intricate influence of sebum lipids on the frictional properties of the skin.

Skin friction coefficients exhibit variations by factors ranging from 1.5 to 7 between wet and dry conditions, as documented in numerous studies [87,93-96,103,140-145]. In regions characterised by high humidity or under wet conditions, the skin becomes thoroughly hydrated, and friction values

surge to be 2 – 4 times higher than those observed during dry sliding conditions [115,116,143,146,147]. This substantial escalation in skin friction in moist environments may be ascribed to the plasticizing influence of water, which results in the smoothing of skin roughness asperities, consequently leading to a more substantial real contact area. Depending on the contact conditions and the relative fluid film thickness concerning the skin's surface roughness and the material it interacts with, a combination of mixed lubrication or boundary lubrication phenomena might also come into play [148]. Nonetheless, investigations revealed that the contribution solely due to elastohydrodynamic lubrication (EHL) is inadequate in fully explaining the friction behaviour of wet skin sliding against smooth glass. This discrepancy is attributed to the skin's surface roughness significantly surpassing the minimum film thickness required for EHL, leading to the supposition that water films between the skin and smooth glass are locally formed, while dry contact zones coexist in other regions [147].

As mentioned before, adhesion is the dominating friction mechanism on human skin. According to the adhesion model of friction [149], the friction force is given by $F = \tau A_r$, where τ is the interfacial shear strength and A_r is the real area of contact. For the interfacial shear strength of skin, Adams et al. [95] adopted the model $\tau = \tau_0 + \alpha p_r$ for shear properties of thin organic films [150], where τ_0 denotes the intrinsic shear strength, α a pressure coefficient and $p_r = N/A_r$ the real contact pressure with N the normal load. The friction coefficient can then be written as:

$$\mu(p_r) = \frac{\tau A_r}{N} = \frac{\tau_0}{p_r} + \alpha. \qquad (4)$$

Since the apparent and real contact areas and contact pressures are related by $Ap = A_r p_r$, the friction coefficient as a function of the apparent contact pressure $p = N/A$ is given by:

$$\mu(p) = \frac{A_r}{A}\frac{\tau_0}{p} + \alpha. \qquad (5)$$

When the real contact area aligns perfectly with the apparent contact area, the disparity between the apparent and actual contact pressure becomes negligible. Such a circumstance is postulated to occur when a soft material is in a state of complete conformational contact with the counter-surface. This particular scenario appears to be realistic in the context of hydrated skin, which softens and adheres closely to the counter-surface, facilitated

by the potential presence of minute quantities of interfacial water that function as adhesive liquid bridges [151].

The frictional response of dry skin stands in stark contrast to that of moist and wet skin, demonstrating relatively low friction coefficients. Multiple studies have shown that the friction coefficients of dry skin remain largely unaffected by variations in the applied normal load. This observation finds its rationale in the Greenwood and Williamson model [152], wherein the real contact area of rough solid surfaces is hypothesised to exhibit a linear increase with changes in the normal load. For a friction coefficient independent of the apparent contact pressure, $(A_r/A)\,(1/p) = A_r/N = \text{constant}$.

The frictional interactions involving the skin and underlying soft tissue during contact entail contributions to the friction coefficient through viscoelastic hysteresis or ploughing mechanisms [153]. It is anticipated that the contribution arising from hysteresis would increase proportionally with the applied normal load and contact pressure, whereas ploughing would lead to a load-independent effect on the friction coefficient [138,153]. Johnson et al. [154] and Adams et al. [95] investigated skin friction at the volar forearm, interacting with spherical probes, employing the approach proposed by Greenwood and Tabor [155]. They discerned that the contribution of hysteresis to the friction coefficient ranged at approximately 0.05. Notably, similar findings in the range of 0.04 to 0.06 were reported by Kwiatkowska et al. [124]. However, measurements on the forearm and cheek, using rotating probes, did not regard friction mechanisms associated with skin deformation as particularly relevant [115]. On the contrary, a recent study indicated that forces stemming from microscale deformations of the skin could significantly contribute to the overall friction experienced by the human finger pad [133]. Investigations concerning the friction of human skin against glass revealed contributions to the friction coefficient due to viscoelastic skin deformations, hovering below 0.2 [147]. Moreover, when studying foot skin sliding on wet floor coverings, contributions due to skin deformations were found to reach up to 0.4 [131], particularly on notably rough surfaces.

The confluence of hysteresis effects and the ploughing action of the skin by the asperities present on rough surfaces is likely responsible for the emergence of pronounced deformation components. Notably, in the context of friction between the finger and small, triangular ridged surfaces, Tomlinson et al. [134] documented substantial interlocking effects and prominent contributions of hysteresis to the overall friction, particularly when the ridge heights exceeded 42.5 and 250 μm, respectively. Moreover, it was posited that deformation also plays a pivotal role in the friction between human skin and textiles [156]. Sanders et al. [157] embarked on an investigation of the frictional interactions involving soft prosthetic interface materials and a sock fabric against the skin at the tibia (shin). The resulting measurements of friction coefficients for both material types exhibited an increasing trend with the applied normal load, hinting at the involvement of deformation in the observed friction. Likewise, in a study examining the skin of the volar forearm in both young and elderly subjects [86] it was observed that skin deformation mechanisms bear relevance to the frictional behaviour exhibited when the skin interacts with textiles.

Thoroughly determining the adhesion component of friction necessitates the measurement of the real contact area. However, the application of modern tools such as microtribometers and atomic force microscopy is presently constrained in connection with *in vivo* measurements of skin. Furthermore, optical methods used to assess the microscopic contact area between finger pads and smooth glass are unsuitable for rough surfaces and non-transparent materials.

Another aspect of inquiry revolves around whether friction's adhesion and deformation components remain as two non-interacting terms, as postulated in the two-term model [138]. The literature also underscores the substantial impact of skin hydration and interfacial water on the skin friction coefficient. Nevertheless, a more comprehensive and systematic investigation is warranted to discern the intricate transition from dry to moist skin. The influence of skin hydration and softening on the skin's surface and its micromechanical properties, as well as the accompanying alterations in the microscopic contact geometry, remain widely unknown. Additionally, the role of small quantities of water at the interface between the skin and the counter-surface, as well as the contribution of other substances like skin lipids, remains unclear.

Theoretical frameworks devised for solids, exemplified by the models of Greenwood and

Williamson [152] and Archard [158], have been harnessed to qualitatively elucidate specific facets of the contact and friction behaviour of dry skin [95,115,159]. However, the applicability of such models to the intricate surface topography of human skin remains a subject that requires further elucidation. Furthermore, an intriguing open question arises concerning the extent to which theoretical concepts governing the contact behaviour of soft materials [160-162] are applicable to hydrated skin.

The Hertz model relates the geometrical contact parameters (R = radius of the sphere, a = radius of the circular contact zone and d = vertical deformation), the normal force N and the reduced modulus E^* according to the following equations [163,164]:

$$a=\left(\frac{3RN}{4E^*}\right)^{1/3}, \quad d=\frac{a^2}{R}=\left(\frac{9N^2}{16RE^{*2}}\right)^{1/3},$$

$$E^*=\left(\frac{1-v_1^2}{E_1}+\frac{1-v_2^2}{E_2}\right)^{-1}. \tag{6}$$

The reduced modulus E^* is given by the elastic moduli $E_{1,2}$ and the Poisson's ratios $v_{1,2}$ of the two contacting materials. If one material is considerably softer (skin) than the other (spherical probe), E^* can be approximated by the elastic properties of the soft material.

$$E^* \approx \frac{E_{\text{skin}}}{1-v_{\text{skin}}^2}. \tag{7}$$

Adams et al. [95] employed an elastic modulus of 40 kPa, as deduced from loading data, combined with an assumed Poisson's ratio of 0.49. Similar outcomes regarding the elastic modulus were also reported in other investigations concerning forearm skin [124] and the skin of fingertips [165]. As posited by Hendriks and Franklin [115], the material constituting the probe brought into contact with the skin holds less significance compared to its surface roughness. Nonetheless, intriguingly, none of the studies employing spherical probes explicitly specified the surface roughness. While the most frequently used probe materials were steel and glass, other materials like ruby, PE, PP and PTFE probes were also utilised. Notably, measurements involving steel spheres yielded the highest friction coefficients. Moreover, in various friction experiments, wherein alternative probes were employed alongside linear sliding movements [114,130,137,140], the estimated

contact pressures were consistently maintained at relatively low levels.

The friction coefficient remains unaffected by the apparent contact area [165] and the sliding velocity [166]. However, it is essential to acknowledge that these laws are of a phenomenological nature, primarily applied at the macroscopic scale. When adhesion forces within the system fall within the range of the applied load, their influence effectively assumes that of an additional loading force. Because of this additional force, friction forces extend to negative applied loads according to Equation (8) proposed by Derjaguin [167,168]:

$$F_{\text{friction}}(F_{\text{load}})=\mu F_{\text{load}}+F_{\text{friction}}(0), \tag{8}$$

where $F_{\text{friction}}(0)$ corresponds to the friction force at zero applied load. This formulation is a useful simplification and allows the friction coefficient and adhesion to be obtained independently of each other, where the adhesion or "contact adhesion" [169] is obtained from the intercept of the friction-load relationship with the load axis (Fig. 4).
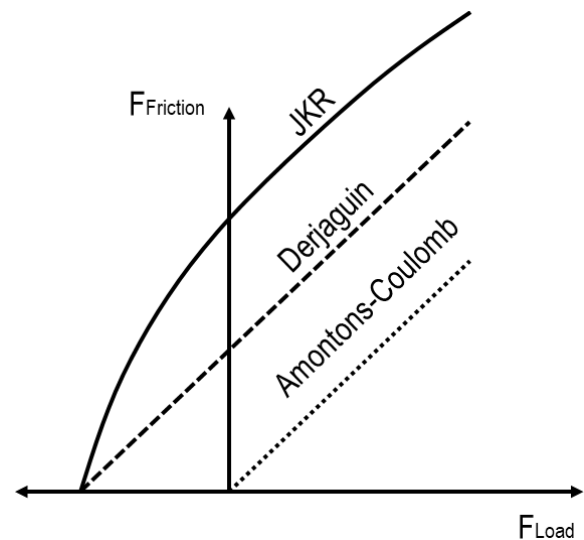
Figure 4. Effect of the applied load on the friction force according to three different approximations: the Amontons-Coulomb and Derjaguin friction laws, as well as the Johnson-Kendall-Roberts (JKR) theory

This simple model claims that the friction force is not proportional to the load but to the real area of contact A_r [170] according to:

$$F_{\text{friction}}(F_{\text{load}})=S_c A, \tag{9}$$

where S_c is the critical shear contact stress at the contacting. This friction-force relationship can be generally used and has been proven in many experimental systems [171-174]. Therefore, a good understanding is required of how surface

13

93

interactions, such as Van der Waals and capillary forces, affect friction and adhesion at the molecular and atomic scale [169,175,176].

3.5 The tribology is in the details: Atomic force microscopy on skin

The scientific community assumes that the secret to a deeper understanding of skin's macroscopic friction behaviour may reveal itself through studies examining the behaviour of human skin on a microscopic scale [177]. Around 1942, Bowden and Tabor [178], brought considerable insights to this subject, revealing that the actual contact area between two solids constitutes only a fraction of the apparent contact area, primarily owing to surface roughness. Consequently, as the normal load is applied, the real contact area augments due to the deformation of asperities. On the nanometre and micrometre scales, all surfaces are inherently rough, making contact only at discrete microscopic points referred to as asperities. Therefore, delving into the interactions between these asperities at the molecular and atomic levels holds the potential to offer a refined comprehension of contacts on the macroscopic scale. Considering the aforementioned observation, it would seem logical to focus on one of the most sophisticated techniques available for micron- and submicron-level force analysis. Atomic force microscopy (AFM) is a powerful tool to investigate molecular interactions at biointerfaces, as well as their mechanical properties, with nanometric spatial resolution and 1 to 10 pN force resolution [179,180]. AFM, originally designed to investigate topography by discerning height variations on the sample surface, has yielded pertinent insights from various studies. Notably, these investigations indicate that scar tissue tends to exhibit greater stiffness than healthy skin [110]. Moreover, it has been observed that the elastic modulus of the *stratum corneum* roughly doubles when compared to that of the epidermis [114]. Specifically, the latter study reported stiffness values ranging from 1 to 2 MPa, while values reported for "skin" range between 5 to 10 kPa [181-183]. These indentation experiments thus compellingly showcase the influence of length scale on the mechanical properties of skin.

The colloidal probe technique developed by Ducker et al. [184,185] and Butt [186] is based on the exchange of the AFM cantilever tip by a colloidal particle (1 – 20 µm in diameter), as shown in Figure 5.
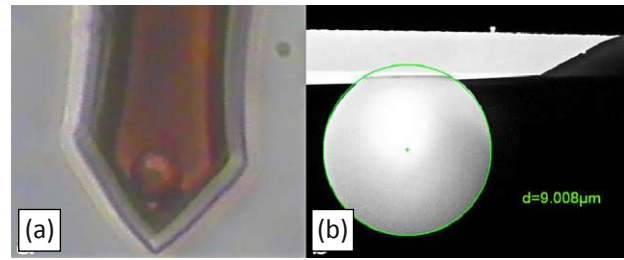
Figure 5. Figure 5 Colloidal probe produced without glue for stable adhesion forces: (a) image of the probe on cantilever with the microscope attached to the AFM and (b) scanning electron microscopy (SEM) image of the probe with geometrical detail; reprinted from Tomala et al. [187], copyrighted by Springer Nature and reproduced with permission from SNCSC

One of its advantageous aspects lies in its flexibility to enable force measurements with a probe crafted from virtually any material, provided the probe possesses a well-defined shape and is nearly incompressible. In these measurements, the magnitude of the acquired force is proportionate to the size of the probe. Nevertheless, when comparing forces obtained with distinct probes, straightforward comparisons prove elusive, necessitating the application of the Derjaguin approximation to normalise the results [167]. This approximation relates the normal force to the energy per unit area (W) between two flat surfaces, according to:

$$\frac{F(D)}{2\pi R_{\text{eff}}} = W(D), \tag{10}$$

where R_{eff} is the effective radius that depends on the interacting surfaces and D is the surface-surface distance. When a rigid sphere is sliding on a deformable surface, it should be noted that the energy dissipation is like that of a rolling sphere. The frictional force in such contact can be expressed by derivation from Greenwood and Tabor [155] as:

$$F_{\text{def}} = \beta \left(\frac{9}{128 R_{\text{eff}}}\right)^{2/3} \left(\frac{1-v^2}{E}\right)^{1/3} W^{4/3}. \tag{11}$$

In Equation (11), F_{def} is the frictional force due to the deformation component and β is the viscoelastic loss fraction. In the context of a colloidal probe interacting with a flat surface, the probe's spherical shape streamlines the computation of the effective radius, which can be reasonably approximated as the radius of the colloidal probe. In the realm of force and friction measurements, the precise determination of the normal and torsional spring constants is of utmost importance, as these

14

constants translate the cantilever's bending and twisting motions into corresponding forces. Over the past two decades, numerous solutions have been proposed, spanning theoretical, experimental or hybrid approaches. Among these, one technique has garnered widespread acceptance due to its combination of accuracy and simplicity. This method, pioneered by Sader et al. [188], derives from observing the effects of the surrounding fluid on the cantilever's vibration frequency response. Specifically, the cantilever is allowed to vibrate in response to thermal motion while submerged in a fluid, typically air. The normal resonance frequency (f_z) and the normal quality factor (Q_z) are obtained by fitting a simple harmonic oscillator function to the normal resonance peak obtained from the thermal power spectra of the cantilever, and afterwards, they are combined with the measured length (L) and width (w) of the cantilever, as well as, the density (ρ) of the fluid, to determine the normal spring constant k_z, where $\Gamma_i^z(Re_z)$ is the imaginary component of the hydrodynamic function for normal vibrations and Re is the Reynolds number [189,190].

$$k_z = 0.1906\rho w^4 L Q_z (2\pi f_z)^2 \Gamma_i^z(Re_z),$$

$$Re_z = \frac{\rho b^2 2\pi f_z}{4\eta}. \qquad (12)$$

The determination of the torsional spring constant k_ϕ is analogous to the calculation of k_z in Equation (12), but in this case, the torsional resonance frequency (f_ϕ) and the torsional quality factor (Q_ϕ) are obtained from the torsional resonance peak. Therefore, k_ϕ is calculated using:

$$k_\phi = 0.1592\rho w^4 L Q_\phi (2\pi f_\phi)^2 \Gamma_i^\phi(Re_\phi),$$

$$Re_\phi = \frac{\rho b^2 2\pi f_\phi}{4\eta}, \qquad (13)$$

where $\Gamma_i^\phi(Re_\phi)$ is the imaginary component of the hydrodynamic function for torsional vibrations [190]. There is a limitation in the determination of the torsional resonance frequency from the torsional thermal power spectra because of its lower resolution, and for stiffer cantilevers this resonance is difficult to measure.

The mechanical attributes of the *stratum corneum* assume paramount importance in facilitating its distinctive functions as the outer protective layer, encompassing roles such as skin barrier and photoprotection. An intriguing area of inquiry centres around biointeractions, examining factors like the extent of deflection occurring when human hair meets the skin. Nonetheless, data pertinent to this remain limited [191-193]. In an endeavour to deepen our comprehension of the *stratum corneum's* mechanical properties, surface indentation and PeakForce® QNM measurements were conducted [194].

The reduced modulus [195] was derived by fitting the contact mechanical theory of Derjaguin, Muller and Toporov (DMT) to the force curve obtained at each pixel. The resultant mean reduced modulus amounted to 0.51 GPa. Moreover, for purposes of comparison, the values of the reduced modulus were converted into elastic modulus (E_{SC}) by applying the equation below, duly omitting the contribution of silicon due to its substantially higher relative stiffness.

$$\frac{1}{E^*} = \frac{1-v_{SC}^2}{E_{SC}} + \frac{1-v_S^2}{E_S}, \quad \frac{1}{E^*} = \frac{1-v_{SC}^2}{E_{SC}}, \qquad (14)$$

where the subscript S corresponds to silicone, SC to the *stratum corneum*, and v to Poisson's ratio ($v_{SC} = 0.48$). Therefore, the reduced modulus of 0.51 GPa was transformed into a value of 0.39 GPa, which is consistent with the relatively high stiffness of the SC reported in the literature [193,196,197].

For example, in the design of shaving applications, it is crucial to describe in detail the behaviour of the top layers of the skin as well as the sebum distribution. Therefore, Indrieri et al. used AFM [198] and a spherical probe that was produced specifically for the AFM measurements. A novel approach for the production and characterisation of epoxy- and adhesive-free colloidal probes was introduced, which was important to avoid contamination of the skin samples. Borosilicate glass microspheres were attached to commercial AFM cantilevers, exploiting the capillary adhesion force due to the formation of a water meniscus. Then, thermal annealing of the sphere-cantilever system at a temperature slightly below the softening point of borosilicate glass was carried out. Moreover, Indrieri et al. presented a statistical characterisation protocol of the probe dimensions and roughness based on AFM inverse imaging of colloidal probes on spiked gratings [199]. In a "point-and-shoot" capture mode of the AFM, significant differences were observed between the lipid-covered and uncovered areas (see Fig. 6) [187]. In the area that was assumed to be covered with lipids, the force curve captured by the AFM reaches a plateau that looks as if the force exerted by the probe was damped by a viscous material.

This is assumed to be the first sign of phospholipids on the *stratum corneum* epidermis.
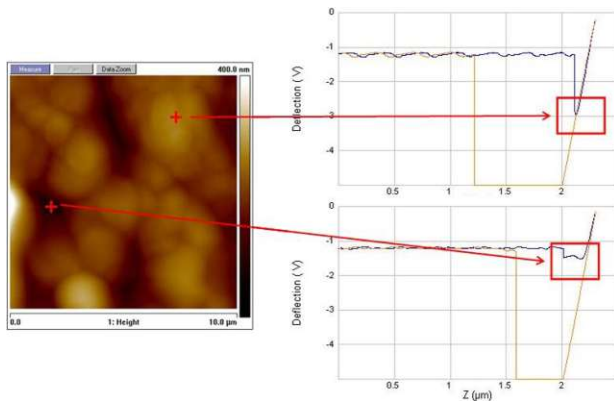
Figure 6. Observation of the plateau on the images acquired by the AFM using a colloidal probe in the darker zone of the image, assuming the presence of the sebum; reprinted from Tomala et al. [187], copyrighted by Springer Nature and reproduced with permission from SNCSC

Podestà et al. [200] delved into the intricacies of topographic correction and pondered the prospect of employing a model-independent approach, thereby obtaining friction versus load characteristics of the investigated system without resorting to postulating any contact-friction model. They adeptly addressed the topographic correction conundrum pertaining to adhesive multiasperity contact, a frequent occurrence in numerous experimental setups. Their calculations revealed a coefficient of friction values, hovering around 0.025 ± 0.002, wherein the relatively modest coefficient is attributed to the lubricative properties of the sebum. Subsequent investigations focusing on a specific area designated for friction measurements, aided by a comprehensive topography and adhesion map, illuminated that even on the micrometre scale, human skin showcases significantly diverse phases [187].

4. Conclusion

In conclusion, the study of dermatology and tribology in nature offers valuable insights and inspiration for various scientific and engineering fields. Observations from nature, including examples from snakes, fish, plants and sharks, have provided valuable knowledge about optimised shape, performance and friction characteristics. These insights have been applied in soft robotics, medical research, tribology and aerospace technology, leading to innovative solutions and improved functionality.

Human skin, as a complex and versatile organ, presents its own set of challenges in understanding its tribological properties. Factors such as skin structure, hydration, age and environmental conditions influence its behaviour. To overcome limitations in studying human skin directly, biomimetic skin models and *ex vivo* tests have been developed. These approaches have contributed to understanding skin compliance, stiffness and shear response.

Contact mechanics considerations are crucial for studying skin friction. The coefficient of friction is influenced by factors such as adhesion, deformation, lubrication and surface roughness. Skin roughness and material topography make the estimation of the real contact area complex. Adhesion is a significant contributor to skin friction, while deformation mechanisms play a minor role. The interplay between adhesion and deformation components and the transition from dry to moist skin require further investigation.

Various measurement techniques, including reciprocating linear movement, rotating contact materials, force transducers, atomic force microscopy and colloidal probe technique, have been employed to study skin friction at various scales. These techniques have provided valuable insights into the mechanical properties and molecular interactions involved in skin tribology.

Overall, the synergy between dermatology and tribology in nature has the potential to drive advancements in various scientific and engineering disciplines. By understanding and harnessing the unique properties of natural systems, researchers can develop innovative solutions for improved performance, efficiency and functionality in areas such as soft robotics, medical devices and biomaterials. Further research and exploration in this interdisciplinary field will continue to deepen our understanding and lead to exciting advancements in the future. The emergence of artificial intelligence (AI) is one of the examples of these advancements. The use of AI is becoming common in the diagnosis of skin cancer, psoriasis and dermatitis. Sensors and algorithms used in these applications could also be beneficial for tribological research. Enhancements in skin tissue equivalents for accuracy will play a vital role in the future, which will allow testing methods for consumer products and skin models, and also aid in several research efforts to provide treatments for different diseases. The confluence of shared applications observed between tribology and

dermatology in this scholarly work invites contemplation regarding the appropriateness of the neologism "dermatribology", suggesting that the prospect of its usage is not premature.

Acknowledgements

References

[1] H.A. Abdel-Aal, M. El Mansori, S. Mezghani, Multi-scale investigation of surface topography of ball python (*Python regius*) shed skin in comparison to human skin, Tribology Letters, Vol. 37, No. 3, 2010, pp. 517-527, DOI: 10.1007/s11249-009-9547-y

[2] D. Bikle, S. Christakos, New aspects of vitamin D metabolism and action – addressing the skin as source and target, Nature Reviews Endocrinology, Vol. 16, No. 4, 2020, pp. 234-252, DOI: 10.1038/s41574-019-0312-5

[3] L.M. Biga, S. Dawson, A. Harwell, R. Hopkins, J. Kaufmann, M. LeMaster, P. Matern, K. Morrison-Graham, D. Quick, J. Runyeon, The integumentary system, in Anatomy & Physiology, Oregon State University, Corvallis, 2019, pp. 213-264.

[4] W. Barthlott, C. Neinhuis, Purity of the sacred lotus, or escape from contamination in biological surfaces, Planta, Vol. 202, No. 1, 1997, pp. 1-8, DOI: 10.1007/s004250050096

[5] S.M. Lößlein, F. Mücklich, P.G. Grützmacher, Topography versus chemistry – How can we control surface wetting?, Journal of Colloid and Interface Science, Vol. 609, 2022, pp. 645-656, DOI: 10.1016/j.jcis.2021.11.071

[6] B. Bhushan, Y.C. Jung, M. Nosonovsky, Lotus effect: Surfaces with roughness-induced superhydrophobicity, self-cleaning, and low adhesion, in B. Bhushan (Ed.), Springer Handbook of Nanotechnology, Springer, Berlin, 2010, pp. 1437-1524, DOI: 10.1007/978-3-642-02525-9_42

[7] H. Fan, P. Chen, R. Qi, J. Zhai, J. Wang, L. Chen, L. Chen, Q. Sun, Y. Song, D. Han, L. Jiang, Greatly improved blood compatibility by microscopic multiscale design of surface architectures, Vol. 5, No. 19, 2009, pp. 2144-2148, DOI: 10.1002/smll.200900345

[8] L. Chen, D. Han, L. Jiang, On improving blood compatibility: From bioinspired to synthetic design and fabrication of biointerfacial topography at micro/nano scales, Colloids and Surfaces B: Biointerfaces, Vol. 85, No. 1, 2011, pp. 2-7, DOI: 10.1016/j.colsurfb.2010.10.034

[9] R. Liu, Y. Qin, H. Wang, Y. Zhao, Z. Hu, S. Wang, The *in vivo* blood compatibility of bio-inspired small diameter vascular graft: Effect of submicron longitudinally aligned topography, BMC Cardiovascular Disorders, Vol. 13, 2013, Paper 79, DOI: 10.1186/1471-2261-13-79

[10] A. Bouchard, This lizard can drink water from sand through its feet & back, available at: https://www.labroots.com/trending/plants-and-animals/4626/lizard-drink-water-sand-feet, accessed: 01.08.2023.

[11] P. Comanns, P.C. Withers, F.J. Esser, W. Baumgartner, Cutaneous water collection by a moisture-harvesting lizard, the thorny devil (*Moloch horridus*), Journal of Experimental Biology, Vol. 219, No. 21, 2016, pp. 3473-3479, DOI: 10.1242/jeb.148791

[12] P.G. Grützmacher, A. Rosenkranz, A. Szurdak, C. Gachot, G. Hirt, F. Mücklich, Lubricant migration on stainless steel induced by bio-inspired multi-scale surface patterns, Materials & Design, Vol. 150, 2018, pp. 55-63, DOI: 10.1016/j.matdes.2018.04.035

[13] P. Comanns, G. Buchberger, A. Buchsbaum, R. Baumgartner, A. Kogler, S. Bauer, W. Baumgartner, Directional, passive liquid transport: The Texas horned lizard as a model for a biomimetic 'liquid diode', Journal of The Royal Society Interface, Vol. 12, No. 109, 2015, Paper 20150415, DOI: 10.1098/rsif.2015.0415

[14] C.G. Scanes, Animal attributes exploited by humans (nonfood uses of animals), in C.G. Scanes, S.R. Toukhsati (Eds.), Animals and Human Society, Elsevier, Amsterdam, 2018, pp. 13-40, DOI: 10.1016/B978-0-12-805247-1.00002-2

[15] H.A. Abdel-Aal, M. El Mansori, Characterization of the frictional response of squamata shed skin in comparison to human skin, available at: https://arxiv.org/ftp/arxiv/papers/1008/1008.1367.pdf, accessed: 01.08.2023.

[16] F. Lamping, S.N. Gorb, K.M. de Payrebrune, Frictional properties of a novel artificial snakeskin for soft robotics, Biotribology, Vol. 30, 2022, Paper 100210, DOI: 10.1016/j.biotri.2022.100210

[17] H. Marvi, J.P. Cook, J.L. Streator, D.L. Hu, Snakes move their scales to increase friction, Biotribology, Vol. 5, 2016, pp. 52-60, DOI: 10.1016/j.biotri.2015.11.001

[18] J.C. Sánchez-López, C.F. Schaber, S.N. Gorb, Long-term low friction maintenance and wear

reduction on the ventral scales in snakes, Materials Letters, Vol. 285, 2021, Paper 129011, DOI: 10.1016/j.matlet.2020.129011

[19] J.E. Baio, M. Spinner, C. Jaye, D.A. Fischer, S.N. Gorb, T. Weidner, Evidence of a molecular boundary lubricant at snakeskin surfaces, Journal of The Royal Society Interface, Vol. 12, No. 113, 2015, Paper 20150817, 10.1098/rsif.2015.0817

[20] H.A. Abdel-Aal, M. El Mansori, H. Zahouani, A comparative study of frictional response of shed snakeskin and human skin, Wear, Vol. 376-377, No. A, 2017, pp. 281-294, DOI: 10.1016/j.wear.2016.12.055

[21] C. Liu, J. Ju, Y. Zheng, L. Jiang, Asymmetric ratchet effect for directional transport of fog drops on static and dynamic butterfly wings, ACS Nano, Vol. 8, No. 2, 2014, pp. 1321-1329, DOI: 10.1021/nn404761q

[22] D. Voigt, A. Schweikart, A. Fery, S. Gorb, Leaf beetle attachment on wrinkles: Isotropic friction on anisotropic surfaces, Journal of Experimental Biology, Vol. 215, No. 11, 2012, pp. 1975-1982, DOI: 10.1242/jeb.068320

[23] C.H. Nelson, Surface ultrastructure and evolution of tarsal attachment structures in Plecoptera (*Arthropoda*: *Hexapoda*), Aquatic Insects, Vol. 31, Supplement 1, 2009, pp. 523-545, DOI: 10.1080/01650420802598210

[24] S. Niederegger, S.N. Gorb, Friction and adhesion in the tarsal and metatarsal scopulae of spiders, Journal of Comparative Physiology A, Vol. 192, No. 11, 2006, pp. 1223-1232, DOI: 10.1007/s00359-006-0157-y

[25] M.P. Murphy, S. Kim, M. Sitti, Enhanced adhesion by gecko-inspired hierarchical fibrillar adhesives, ACS Applied Materials & Interfaces, Vol. 1, No. 4, 2009, pp. 849-855, DOI: 10.1021/am8002439

[26] E.V. Gorb, S.N. Gorb, The effect of surface anisotropy in the slippery zone of *Nepenthes alata* pitchers on beetle attachment, Beilstein Journal of Nanotechnology, Vol. 2, 2011, pp. 302-310, DOI: 10.3762/bjnano.2.35

[27] R. Elbaum, L. Zaltzman, I. Burgert P. Fratzl, The role of wheat awns in the seed dispersal unit, Science, Vol. 316, No. 5826, 2007, pp. 884-886, DOI: 10.1126/science.1140097

[28] M. Spinner, M. Kortmann, C. Traini, S.N. Gorb, Key role of scale morphology in flatfishes (*Pleuronectiformes*) in the ability to keep sand, Scientific Reports, Vol. 6, No. 1, 2016, Paper 26308, DOI: 10.1038/srep26308

[29] F.P. Bowden, C.A. Brookes, A.E. Hanwell, Anisotropy of friction in crystals, Nature, Vol. 203, No. 4940, 1964, pp. 27-30, DOI: 10.1038/203027b0

[30] J.S. Choi, J.-S. Kim, I.-S. Byun, D.H. Lee, M.J. Lee, B.H. Park, C. Lee, D. Yoon, H. Cheong, K.H. Lee, Y.-W. Son, J.Y. Park, M. Salmeron, Friction anisotropy-driven domain imaging on exfoliated monolayer graphene, Science, Vol. 333, No. 6042, 2011, pp. 607-610, DOI: 10.1126/science.1207110

[31] S. Aoki, D. Fukada, Y. Yamada, A. Suzuki, M. Masuko, Synergistic friction-reducing effects between the transverse direction of anisotropic surface roughness and the high-density adsorbed films under a boundary lubrication regime, Tribology International, Vol. 58, 2013, pp. 98-106, DOI: 10.1016/j.triboint.2012.10.003

[32] J. Hazel, M. Stone, M.S. Grace, V.V. Tsukruk, Nanoscale design of snake skin for reptation locomotions via friction anisotropy, Journal of Biomechanics, Vol. 32, No. 5, 1999, pp. 477-484, DOI: 10.1016/S0021-9290(99)00013-5

[33] H.F. Bohn, W. Federle, Insect aquaplaning: *Nepenthes* pitcher plants capture prey with the peristome, a fully wettable water-lubricated anisotropic surface, Proceedings of the National Academy of Sciences of the United States of America, Vol. 101, No. 39, 2004, pp. 14138-14143, DOI: 10.1073/pnas.0405885101

[34] G.J. Amador, D.L. Hu, Cleanliness is next to godliness: Mechanisms for staying clean, Journal of Experimental Biology, Vol. 218, No. 20, 2015, pp. 3164-3174, DOI: 10.1242/jeb.103937

[35] J. Li, Q.H. Qin, A. Shah, R.H.A. Ras, X. Tian, V. Jokinen, Oil droplet self-transportation on oleophobic surfaces, Science Advances, Vol. 2, No. 6, 2016, Paper e160014, DOI: 10.1126/sciadv.1600148

[36] Z. Ji, C. Yan, S. Ma, S. Gorb, X. Jia, B. Yu, X. Wang, F. Zhou, 3D printing of bioinspired topographically oriented surfaces with frictional anisotropy for directional driving, Tribology International, Vol. 132, 2019, pp. 99-107, DOI: 10.1016/j.triboint.2018.12.010

[37] J.A. Musick, G. Burgess, G. Cailliet, M. Camhi, S. Fordham, Management of sharks and their relatives (*Elasmobranchii*), Fisheries, Vol. 25, No. 3, 2000, pp. 9-13, DOI: 10.1577/1548-8446(2000)025<0009:MOSATR>2.0.CO;2

[38] B. Bhushan, Shark skin effect, in B. Bhushan (Ed.), Encyclopedia of Nanotechnology, Springer, Dordrecht, 2012, pp. 2401-2412, DOI: 10.1007/978-90-481-9751-4_159

[39] Y.F. Fu, C.Q. Yuan, X.Q. Bai, Marine drag reduction of shark skin inspired riblet surfaces, Biosurface and Biotribology, Vol. 3, No. 1, 2017, pp. 11-24, DOI: 10.1016/j.bsbt.2017.02.001

[40] B. Dean, B. Bhushan, Shark-skin surfaces for fluid-drag reduction in turbulent flow: A review, Philosophical Transactions of the Royal Society

A: Mathematical, Physical and Engineering Sciences, Vol. 368, No. 1929, 2010, pp. 4775-4806, DOI: 10.1098/rsta.2010.0201

[41] L. Wen, J.C. Weaver, G.V. Lauder, Biomimetic shark skin: Design, fabrication and hydrodynamic function, Journal of Experimental Biology, Vol. 217, No. 10, 2014, pp. 1656-1666, DOI: 10.1242/jeb.097097

[42] A.G. Domel, M. Saadat, J.C. Weaver, H. Haj-Hariri, K. Bertoldi, G.V. Lauder, Shark skin-inspired designs that improve aerodynamic performance, Journal of The Royal Society Interface, Vol. 15, No. 139, 2018, Paper 20170828, DOI: 10.1098/rsif.2017.0828

[43] Nature as a role model: Lufthansa group and BASF roll out sharkskin technology, available at: https://www.basf.com/global/en/media/news-releases/2021/05/p-21-204.html, accessed: 01.08.2023.

[44] S. Dash, S.K. Das, J. Samal, H.N. Thatoi, Epidermal mucus, a major determinant in fish health: A review, Iranian Journal of Veterinary Research, Vol. 19, No. 2, 2018, pp. 72-81, DOI: 10.22099/ijvr.2018.4849

[45] E. Biazar, S.H. Keshel, M.R. Tavirani, M. Kamalvand, Healing effect of acellular fish skin with plasma rich in growth factor on full-thickness skin defects, International Wound Journal, Vol. 19, No. 8, 2022, pp. 2154-2162, DOI: 10.1111/iwj.13821

[46] F. Pape, G. Poll, Frictional properties of freshwater fish skin, in Proceedings of the 3rd African Congress in Tribology, 26-29.04.2020, Dakar, Senegal, p. 1.

[47] Y. Wu, X. Pei, X. Wang, Y. Liang, W. Liu, F. Zhou, Biomimicking lubrication superior to fish skin using responsive hydrogels, NPG Asia Materials, Vol. 6, No. 10, 2014, Paper e136, DOI: 10.1038/am.2014.82

[48] W.L.E. Wong, T.J. Joyce, K.L. Goh, Resolving the viscoelasticity and anisotropy dependence of the mechanical properties of skin from a porcine model, Biomechanics and Modeling in Mechanobiology, Vol. 15, No. 2, 2016, pp. 433-446, DOI: 10.1007/s10237-015-0700-2

[49] M. Ottenio, D. Tran, A. Ní Annaidh, M.D. Gilchrist, K. Bruyère, Strain rate and anisotropy effects on the tensile failure characteristics of human skin, Journal of the Mechanical Behavior of Biomedical Materials, Vol. 41, 2015, pp. 241-250, DOI: 10.1016/j.jmbbm.2014.10.006

[50] J. van Smeden, J.A. Bouwstra, Stratum corneum lipids: Their role for the skin barrier function in healthy subjects and atopic dermatitis patients, in T. Agner (Ed.), Skin Barrier Function, Karger, Basel, 2016, pp. 8-26, DOI: 10.1159/000441540

[51] J.C.J. Wei, G.A. Edwards, D.J. Martin, H. Huang, M.L. Crichton, M.A.F. Kendall, Allometric scaling of skin thickness, elasticity, viscoelasticity to mass for micro-medical device translation: From mice, rats, rabbits, pigs to humans, Scientific Reports, Vol. 7, 2017, Paper 15885, DOI: 10.1038/s41598-017-15830-7

[52] J. Fowler, Understanding the role of natural moisturizing factor in skin hydration, Practical Dermatology, No. 7, 2012, pp. 36-40.

[53] M.B. Murphrey, J.H. Miao, P.M. Zito, Histology, Stratum Corneum, StatPearls Publishing, St. Petersburg, 2023.

[54] M.F. Leyva-Mendivil, A. Page, N.W. Bressloff, G. Limbert, A mechanistic insight into the mechanical role of the stratum corneum during stretching and compression of the skin, Journal of the Mechanical Behavior of Biomedical Materials, Vol. 49, 2015, pp. 197-219, DOI: 10.1016/j.jmbbm.2015.05.010

[55] C.R. Dunkley, C.D. Henshaw, S.K. Henshaw, L.A. Brotto, Physical pain as pleasure: A theoretical perspective, The Journal of Sex Research, Vol. 57, No. 4, 2020, pp. 421-437, DOI: 10.1080/00224499.2019.160532

[56] M.F. Leyva-Mendivil, J. Lengiewicz, A. Page, N.W. Bressloff, G. Limbert, Skin microstructure is a key contributor to its friction behaviour, Tribology Letters, Vol. 65, No. 1, 2016, Paper 12, DOI: 10.1007/s11249-016-0794-4

[57] F.H. Silver, J.W. Freeman, D. DeVore, Viscoelastic properties of human skin and processed dermis, Skin Research and Technology, Vol. 7, No. 1, 2001, pp. 18-23, DOI: 10.1034/j.1600-0846.2001.007001018.x

[58] R.E. Burgeson, A.M. Christiano, The dermal-epidermal junction, Current Opinion in Cell Biology, Vol. 9, No. 5, 1997, pp. 651-658, DOI: 10.1016/S0955-0674(97)80118-4

[59] M. Asahina, A. Poudel, S. Hirano, Sweating on the palm and sole: Physiological and clinical relevance, Clinical Autonomic Research, Vol. 25, No. 3, 2015, pp. 153-159, DOI: 10.1007/s10286-015-0282-1

[60] V.F. Achterberg, L. Buscemi, H. Diekmann, J. Smith-Clerc, H. Schwengler, J.-J. Meister, H. Wenck, S. Gallinat, B. Hinz, The nano-scale mechanical properties of the extracellular matrix regulate dermal fibroblast function, Journal of Investigative Dermatology, Vol. 134, No. 7, 2014, pp. 1862-1872, DOI: 10.1038/jid.2014.90

[61] A. Ní Annaidh, K. Bruyère, M. Destrade, M.D. Gilchrist, M. Otténio, Characterization of the anisotropic mechanical properties of excised human skin, Journal of the Mechanical Behavior of Biomedical Materials, Vol. 5, No. 1, 2012, pp. 139-148, DOI: 10.1016/j.jmbbm.2011.08.016

[62] S. Diridollou, V. Vabre, M. Berson, L. Vaillant, D. Black, J.M. Lagarde, J.M. Grégoire, Y. Gall, F. Patat, Skin ageing: Changes of physical properties of human skin *in vivo*, International Journal of Cosmetic Science, Vol. 23, No. 6, 2001, pp. 353-362, DOI: 10.1046/j.0412-5463.2001.00105.x

[63] C. Pailler-Mattei, S. Bec, H. Zahouani, *In vivo* measurements of the elastic mechanical properties of human skin by indentation tests, Medical Engineering & Physics, Vol. 30, No. 5, 2008, pp. 599-606, DOI: 10.1016/j.medengphy.2007.06.011

[64] L. Pan, L. Zan, F.S. Foster, *In vivo* high frequency ultrasound assessment of skin elasticity, in Proceedings of the 1997 IEEE Ultrasonics Symposium, 05-08.10.1997, Toronto, Canada, pp. 1087-1091, DOI: 10.1109/ULTSYM.1997.661769

[65] Q. Wang, V. Hayward, *In vivo* biomechanics of the fingerpad skin under local tangential traction, Journal of Biomechanics, Vol. 40, No. 4, 2007, pp. 851-860, DOI: 10.1016/j.jbiomech.2006.03.004

[66] X. Liang, S.A. Boppart, Biomechanical properties of *in vivo* human skin from dynamic optical coherence elastography, IEEE Transactions on Biomedical Engineering, Vol. 57, No. 4, 2010, pp. 953-959, DOI: 10.1109/TBME.2009.2033464

[67] C. Pailler-Mattei, S. Pavan, R. Vargiolu, F. Pirot, F. Falson, H. Zahouani, Contribution of *stratum corneum* in determining bio-tribological properties of the human skin, Wear, Vol. 263, No. 7-12, 2007, pp. 1038-1043, DOI: 10.1016/j.wear.2007.01.128

[68] B.F. Van Duzee, The influence of water content, chemical treatment and temperature on the rheological properties of *stratum corneum*, Journal of Investigative Dermatology, Vol. 71, No. 2, 1978, pp. 140-144, DOI: 10.1111/1523-1747.ep12546836

[69] G.L. Wilkes, A.-L. Nguyen, R. Wildnauer, Structure-property relations of human and neonatal rat *stratum corneum* I. Thermal stability of the crystalline lipid structure as studied by X-ray diffraction and differential thermal analysis, Biochimica et Biophysica Acta: General Subjects, Vol. 304, No. 2, 1973, pp. 267-275, DOI: 10.1016/0304-4165(73)90244-4

[70] M. Geerligs, L. van Breemen, G. Peters, P. Ackermans, F. Baaijens, C. Oomens, *In vitro* indentation to determine the mechanical properties of epidermis, Journal of Biomechanics, Vol. 44, No. 6, 2011, pp. 1176-1181, DOI: 10.1016/j.jbiomech.2011.01.015

[71] F.H. Silver, G.P. Seehra, J.W. Freeman, D. DeVore, Viscoelastic properties of young and old human dermis: A proposed molecular mechanism for elastic energy storage in collagen and elastin, Journal of Applied Polymer Science, Vol. 86, No. 8, 2002, pp. 1978-1985, DOI: 10.1002/app.11119

[72] B. Holt, A. Tripathi, J. Morgan, Viscoelastic response of human skin to low magnitude physiologically relevant shear, Journal of Biomechanics, Vol. 41, No. 12, 2008, pp. 2689-2695, DOI: 10.1016/j.jbiomech.2008.06.008

[73] F.M. Hendriks, D. Brokken, J.T.W.M. Van Eemeren, C.W.J. Oomens, F.P.T. Baaijens, J.B.A.M. Horsten, A numerical-experimental method to characterize the non-linear mechanical behaviour of human skin, Skin Research and Technology, Vol. 9, No. 3, 2003, pp. 274-283, DOI: 10.1034/j.1600-0846.2003.00019.x

[74] J. Su, H. Zou, T. Guo, The study of mechanical properties on soft tissue of human forearm *in vivo*, in Proceedings of the 3rd International Conference on Bioinformatics and Biomedical Engineering, 11-16.06.2009, Beijing, China, Paper: 10778606, DOI: 10.1109/ICBBE.2009.5163671

[75] J.W.Y. Jor, M.D. Parker, A.J. Taberner, M.P. Nash, P.M.F. Nielsen, Computational and experimental characterization of skin mechanics: identifying current challenges and future directions, Wiley Interdisciplinary Reviews: Systems Biology and Medicine, Vol. 5, No. 5, 2013, pp. 539-556, DOI: 10.1002/wsbm.1228

[76] J. Weickenmeier, E. Mazza, Inverse methods, in G. Limbert (Ed.), Skin Biophysics, Springer, Cham, 2019, pp. 193-213, DOI: 10.1007/978-3-030-13279-8_6

[77] K. Langer, On the anatomy and physiology of the skin I. The cleavability of the cutis, British Journal of Plastic Surgery, Vol. 31, No. 1, 1978, pp. 3-8, DOI: 10.1016/0007-1226(78)90003-6

[78] M.B. Rubin, S.R. Bodner, A three-dimensional nonlinear model for dissipative response of soft tissue, International Journal of Solids and Structures, Vol. 39, No. 19, 2002, pp. 5081-5099, DOI: 10.1016/S0020-7683(02)00237-8

[79] S. Park, J. Tao, L. Sun, C.-M. Fan, Y. Chen, An economic, modular, and portable skin viscoelasticity measurement device for *in situ* longitudinal studies, Molecules, Vol. 24, No. 5, 2019, Paper 907, DOI: 10.3390/molecules24050907

[80] H. Zahouani, R. Vargiolu, G. Boyer, C. Pailler-Mattei, L. Laquièze, A. Mavon, Friction noise of human skin *in vivo*, Wear, Vol. 267, No. 5-8, 2009, pp. 1274-1280, DOI: 10.1016/j.wear.2009.03.007

[81] L.-C. Gerhardt, J. Schmidt, J.A. Sanz-Herrera, F.P.T. Baaijens, T. Ansari, G.W.M. Peters, C.W.J Oomens, A novel method for visualising and quantifying through-plane skin layer deformations, Journal of the Mechanical Behavior of Biomedical Materials, Vol. 14, 2012, pp. 199-207, DOI: 10.1016/j.jmbbm.2012.05.014

100

[82] E. Lamers, T.H.S. van Kempen, F.P.T. Baaijens, G.W.M. Peters, C.W.J. Oomens, Large amplitude oscillatory shear properties of human skin, Journal of the Mechanical Behavior of Biomedical Materials, Vol. 28, 2013, pp. 462-470, DOI: 10.1016/j.jmbbm.2013.01.024

[83] K. Hyun, M. Wilhelm, C.O. Klein, K.S. Cho, J.G. Nam, K.H. Ahn, S.J. Lee, R.H. Ewoldt, G.H. McKinley, A review of nonlinear oscillatory shear tests: Analysis and application of large amplitude oscillatory shear (LAOS), Progress in Polymer Science, Vol. 36, No. 12, 2011, pp. 1697-1753, DOI: 10.1016/j.progpolymsci.2011.02.002

[84] R.E. Horch, J. Kopp, U. Kneser, J. Beier, A.D. Bach, Tissue engineering of cultured skin substitutes, Journal of Cellular and Molecular Medicine, Vol. 9, No. 3, 2005, pp. 592-608, DOI: 10.1111/j.1582-4934.2005.tb00491.x

[85] L.-P. Kamolz, P. Kotzbeck, M. Schintler, S. Spendel, Skin regeneration, repair, and reconstruction: present and future, European Surgery, Vol. 54, No. 3, 2022, pp. 163-169, DOI: 10.1007/s10353-022-00757-9

[86] L.-C. Gerhardt, A. Lenz, N.D. Spencer, T. Münzer, S. Derler, Skin-textile friction and skin elasticity in young and aged persons, Skin Research and Technology, Vol. 15, No. 3, 2009, pp. 288-298, DOI: 10.1111/j.1600-0846.2009.00363.x

[87] M. Egawa, M. Oguri, T. Hirao, M. Takahashi, M. Miyakawa, The evaluation of skin friction using a frictional feel analyzer, Skin Research and Technology, Vol. 8, No. 1, 2002, pp. 41-51, DOI: 10.1034/j.1600-0846.2002.080107.x

[88] *In vitro* diagnostics market size, share & trends analysis report by product (reagents, services), by test location (PoC, homecare), by end-use (hospitals, laboratory), by application, by technology, and segment forecasts, 2023-2030, available at: https://www.grandviewresearch.com/industry-analysis/in-vitro-diagnostics-ivd-market, accessed: 01.08.2023.

[89] S. Mühlfriedel, G. Knebel, The establishment of *in vivo*-like tissue culture conditions in ThinCert™ tissue culture products, BioTechniques, Vol. 43, No. 6, 2007, pp. 812-813, DOI: 10.2144/000112701

[90] S. Abadie, P. Bedos, J. Rouquette, A human skin model to evaluate the protective effect of compounds against UVA damage, International Journal of Cosmetic Science, Vol. 41, No. 6, 2019, pp. 594-603, DOI: 10.1111/ics.12579

[91] K.L. Johnson, Contact Mechanics, Cambridge University Press, Cambridge, 1985.

[92] J. van Kuilenburg, M.A. Masen, M.N.W. Groenendijk, V. Bana, E. van der Heide, An experimental study on the relation between surface texture and tactile friction, Tribology International, Vol. 48, 2012, pp. 15-21, DOI: 10.1016/j.triboint.2011.06.003

[93] S. Comaish, E. Bottoms, The skin and friction: Deviations from Amonton's laws, and the effects of hydration and lubrication, British Journal of Dermatology, Vol. 84, No. 1, 1971, pp. 37-43, DOI: 10.1111/j.1365-2133.1971.tb14194.x

[94] L.J. Wolfram, Friction of skin, Journal of the Society of Cosmetic Chemists, Vol. 34, No. 8, 1983, pp. 465-476.

[95] M.J. Adams, B.J. Briscoe, S.A. Johnson, Friction and lubrication of human skin, Tribology Letters, Vol. 26, No. 3, 2007, pp. 239-253, DOI: 10.1007/ s11249-007-9206-0

[96] A.F. El-Shimi, *In vivo* skin friction measurements, Journal of the Society of Cosmetic Chemists, Vol. 28, No. 2, 1977, pp. 37-51.

[97] A.A. Koudine, M. Barquins, P.H. Anthoine, L. Aubert, J.-L. Lévêque, Frictional properties of skin: Proposal of a new approach, International Journal of Cosmetic Science, Vol. 22, No. 1, 2000, pp. 11-20, DOI: 10.1046/j.1467-2494.2000.00006.x

[98] R.K. Sivamani, J. Goodman, N.V. Gitis, H.I. Maibach, Friction coefficient of skin in real-time, Skin Research and Technology, Vol. 9, No. 3, 2003, pp. 235-239, DOI: 10.1034/j.1600-0846.2003.20361.x

[99] N. Gitis, R. Sivamani, Tribometrology of skin, Tribology Transactions, Vol. 47, No. 4, 2004, pp. 461-469, DOI: 10.1080/05698190490493355

[100] K. Subramanyan, M. Misra, S. Mukherjee, K.P. Ananthapadmanabhan, Advances in the materials science of skin: A composite structure with multiple functions, MRS Bulletin, Vol. 32, No. 10, 2007, pp. 770-778, DOI: 10.1557/mrs2007.163

[101] P.F.D. Naylor, The skin surface and friction, British Journal of Dermatology, Vol. 67, No. 7, 1955, pp. 239-248, DOI: 10.1111/j.1365-2133.1955.tb12729.x

[102] J.S. Comaish, P.R.H. Harborow, D.A. Hofman, A hand-held friction meter, British Journal of Dermatology, Vol. 89, No. 1, 1973, pp. 33-35, DOI: 10.1111/j.1365-2133.1973.tb01914.x

[103] D.R. Highley, M. Coomey, M. DenBeste, L.J. Wolfram, Frictional properties of skin, The Journal of Investigative Dermatology, Vol. 69, No. 3, 1977, pp. 303-305, DOI: 10.1111/1523-1747.ep12507530

[104] O.S. Dinc, C.M. Ettles, S.J. Calabrese, H.A. Scarton, Some parameters affecting tactile friction, Journal of Tribology, Vol. 113, No. 3, 1991, pp. 512-517, DOI: 10.1115/1.2920653

[105] R. Lewis, C. Menardi, A. Yoxall, J. Langley, Finger friction: Grip and opening packaging, Wear, Vol.

263, No. 7-12, 2007, pp. 1124-1132, DOI: 10.1016/j.wear.2006.12.024

[106] O. Bobjer, S.-E. Johansson, S. Piguet, Friction between hand and handle. Effects of oil and lard on textured and non-textured surfaces; perception of discomfort, Applied Ergonomics, Vol. 24, No. 3, 1993, pp. 190-202, DOI: 10.1016/0003-6870(93)90007-V

[107] A.B. Cua, K.-P. Wilhelm, H.I. Maibach, Frictional properties of human skin: Relation to age, sex and anatomical region, *stratum corneum* hydration and transepidermal water loss, British Journal of Dermatology, Vol. 123, No. 4, 1990, pp. 473-479, DOI: 10.1111/j.1365-2133.1990.tb01452.x

[108] M.G. Gee, P. Tomlins, A. Calver, R.H. Darling, M. Rides, A new friction measurement system for the frictional component of touch, Wear, Vol. 259, No. 7-12, 2005, pp. 1437-1442, DOI: 10.1016/j.wear.2005.02.053

[109] J. Asserin, H. Zahouani, P. Humbert, V. Couturaud, D. Mougin, Measurement of the friction coefficient of the human skin *in vivo*: Quantification of the cutaneous smoothness, Colloids and Surfaces B: Biointerfaces, Vol. 19, No. 1, 2000, pp. 1-12, DOI: 10.1016/S0927-7765(99)00169-1

[110] W. Li, M. Kong, X.D. Liu, Z.R. Zhou, Tribological behavior of scar skin and prosthetic skin *in vivo*, Tribology International, Vol. 41, No. 7, 2008, pp. 640-647, DOI: 10.1016/j.triboint.2007.11.009

[111] H.-J. Bullinger, P. Kern, J.J. Solf, Reibung zwischen Hand und Griff: der Einfluss von Material und Oberfläche auf das Reibungsverhalten zwischen Hand und Arbeitsmittelhandseite [Friction between hand and handle: The influence of material and surface on the friction behaviour between the hand and the handle of the tool], Wirtschaftsverlag NW, Bremerhaven, 1979 [in German].

[112] A. Ramalho, C.L. Silva, A.A.C.C. Pais, J.J.S. Sousa, *In vivo* friction study of human palmoplantar skin against glass, Tribologia, Vol. 25, No. 3, 2006, pp. 14-23.

[113] A. Ramalho, C.L. Silva, A.A.C.C. Pais, J.J.S. Sousa, *In vivo* friction study of human skin: Influence of moisturizers on different anatomical sites, Wear, Vol. 263, No. 7-12, 2007, pp. 1044-1049, DOI: 10.1016/j.wear.2006.11.051

[114] W. Li, S.X. Qu, Z.R. Zhou, Reciprocating sliding behaviour of human skin *in vivo* at lower number of cycles, Tribology Letters, Vol. 23, No. 2, 2006, pp. 165-170, DOI: 10.1007/s11249-006-9111-y

[115] C.P. Hendriks, S.E. Franklin, Influence of surface roughness, material and climate conditions on the friction of human skin, Tribology Letters, Vol. 37, No. 2, 2010, pp. 361-373, DOI: 10.1007/s11249-009-9530-7

[116] S.E. Tomlinson, R. Lewis, X. Liu, C. Texier, M.J. Carré, Understanding the friction mechanisms between the human finger and flat contacting surfaces in moist conditions, Tribology Letters, Vol. 41, No. 1, 2011, pp. 283-294, DOI: 10.1007/s11249-010-9709-y

[117] F.-X. Li, S. Margetts, I. Fowler, Use of 'chalk' in rock climbing: Sine qua non or myth?, Journal of Sports Sciences, Vol. 19, No.6, 2001, pp. 427-432, DOI: 10.1080/026404101300149375

[118] N. Nakazawa, R. Ikeura, H. Inooka, Characteristics of human fingertips in the shearing direction, Biological Cybernetics, Vol. 82, No. 2, 2000, pp. 207-214, DOI: 10.1007/s004220050020

[119] Y. Nonomura, T. Fujii, Y. Arashi, T. Miura, T. Maeno, K. Tashiro, Y. Kamikawa, R. Monchi, Tactile impression and friction of water on human skin, Colloids and Surfaces B: Biointerfaces, Vol. 69, No. 2, 2009, pp. 264-267, DOI: 10.1016/j.colsurfb.2008.11.024

[120] M. Uygur, P.B. de Freitas, S. Jaric, Frictional properties of different hand skin areas and grasping techniques, Ergonomics, Vol. 53, No. 6, 2010, pp. 812-817, DOI: 10.1080/00140131003734237

[121] M. Besser, M. Marpet, H. Medoff, Barefoot-pedestrian tribometry: *In vivo* method of measurement of available friction between the human heel and the walkway, Industrial Health, Vol. 46, No. 1, 2008, pp. 51-58, DOI: 10.2486/indhealth.46.51

[122] B.L. Davis, Foot ulceration: Hypotheses concerning shear and vertical forces acting on adjacent regions of skin, Medical Hypotheses, Vol. 40, No. 1, 1993, pp. 44-47, DOI: 10.1016/0306-9877(93)90195-V

[123] M. Zhang, A.F.T. Mak, *In vivo* friction properties of human skin, Prosthetics and Orthotics International, Vol. 23, No. 2, 1999, pp. 135-141, DOI: 10.3109/03093649909071625

[124] M. Kwiatkowska, S.E. Franklin, C.P. Hendriks, K. Kwiatkowski, Friction and deformation behaviour of human skin, Wear, Vol. 267, No. 5-8, 2009, pp. 1264-1273, DOI: 10.1016/j.wear.2008.12.030

[125] P. Humbert, F. Fanian, H.I. Maibach, P. Agache (Eds.), Agache's Measuring the Skin, Springer, Cham, 2017, DOI: 10.1007/978-3-319-32383-1

[126] G. Boyer, L. Laquièze, A. Le Bot, S. Laquièze, H. Zahouani, Dynamic indentation on human skin *in vivo*: Ageing effects, Skin Research and Technology, Vol. 15, No. 1, 2009, pp. 55-67, DOI: 10.1111/j.1600-0846.2008.00324.x

[127] U. Jacobi, M. Chen, G. Frankowski, R. Sinkgraven, M. Hund, B. Rzany, W. Sterry, J. Lademann, *In*

vivo determination of skin surface topography using an optical 3D device, Skin Research and Technology, Vol. 10, No. 4, 2004, pp. 207-214, DOI: 10.1111/j.1600-0846.2004.00075.x

[128] L. Li, S. Mac-Mary, D. Marsaut, J.M. Sainthillier, S. Nouveau, T. Gharbi, O. de Lacharriere, P. Humbert, Age-related changes in skin topography and microcirculation, Archives of Dermatological Research, Vol. 297, No. 9, 2006; pp. 412-416, DOI: 10.1007/s00403-005-0628-y

[129] T. Fujimura, K. Haketa, M. Hotta, T. Kitahara, Loss of skin elasticity precedes to rapid increase of wrinkle levels, Journal of Dermatological Science, Vol. 47, No. 3, 2007, pp. 233-239, DOI: 10.1016/j.jdermsci.2007.05.002

[130] K. Nakajima, H. Narasaka, Evaluation of skin surface associated with morphology and coefficient of friction, International Journal of Cosmetic Science, Vol. 15, No. 4, 1993, pp. 135-151, DOI: 10.1111/j.1468-2494.1993.tb00594.x

[131] S. Derler, R. Huber, H.-P. Feuz, M. Hadad, Influence of surface microstructure on the sliding friction of plantar skin against hard substrates, Wear, Vol. 267, No. 5-8, 2009, pp. 1281-1288, DOI: 10.1016/j.wear.2008.12.053

[132] S.E. Tomlinson, R. Lewis, M.J. Carré, The effect of normal force and roughness on friction in human finger contact, Wear, Vol. 267, No. 5-8, 2009, pp. 1311-1318, DOI: 10.1016/j.wear.2008.12.084

[133] M.A. Masen, A systems based experimental approach to tactile friction, Journal of the Mechanical Behavior of Biomedical Materials, Vol. 4, No. 8, 2011, pp. 1620-1626, DOI: 10.1016/j.jmbbm.2011.04.007

[134] S.E. Tomlinson, M.J. Carré, R. Lewis, S.E Franklin, Human finger contact with small, triangular ridged surfaces, Wear, Vol. 271, No. 9-10, 2011, pp. 2346-2353, DOI: 10.1016/j.wear.2010.12.055

[135] D.F. Moore, The Friction and Lubrication of Elastomers, Pergamon Press, Oxford, 1972.

[136] A. El Khyat, A. Mavon, M. Leduc, P. Agache, P. Humbert, Skin critical surface tension, Skin Research and Technology, Vol. 2, No. 2, 1996, pp. 91-96, DOI: 10.1111/j.1600-0846.1996.tb00066.x

[137] A.B Gupta, B Haldar, M. Bhattacharya, A simple device for measuring skin friction, Indian Journal of Dermatology, Vol. 40, No. 3, 1995, pp. 116-121.

[138] A. Mavon, H. Zahouani, D. Redoules, P. Agache, Y. Gall, P. Humbert, Sebum and *stratum corneum* lipids increase human skin surface free energy as determined from contact angle measurements: A study on two anatomical sites, Colloids and Surfaces B: Biointerfaces, Vol. 8, No. 3, 1997, pp. 147-155, DOI: 10.1016/S0927-7765(96)01317-3

[139] C. Pailler-Mattei, S. Nicoli, F. Pirot, R. Vargiolu, H. Zahouani, A new approach to describe the skin surface physical properties *in vivo*, Colloids and Surfaces B: Biointerfaces, Vol. 68, No. 2, 2009, pp. 200-206, DOI: 10.1016/j.colsurfb.2008.10.005

[140] R.K. Sivamani, G.C. Wu, N.V. Gitis, H.I. Maibach, Tribological testing of skin products: gender, age, and ethnicity on the volar forearm, Skin Research and Technology, Vol. 9, No. 4, 2003, pp. 299-305, DOI: 10.1034/j.1600-0846.2003.00034.x

[141] M. Lodén, H. Olsson, T. Axéll, Y. Werner Linde, Friction, capacitance and transepidermal water loss (TEWL) in dry atopic and normal skin, British Journal of Dermatology, Vol. 126, No. 2, 1992, pp. 137-141, DOI: 10.1111/j.1365-2133.1992.tb07810.x

[142] Y.H. Zhu, S.P. Song, W. Luo, P.M. Elias, M.Q. Man, Characterization of skin friction coefficient, and relationship to *stratum corneum* hydration in a normal Chinese population, Skin Pharmacol Physiol, Vol. 24, No. 2, 2011, pp. 81-86, DOI: 10.1159/000321993

[143] P. Kenins, Influence of fiber type and moisture on measured fabric-to-skin friction, Textile Research Journal, Vol. 64, No. 12, 1994, pp. 722-728, DOI: 10.1177/004051759406401204

[144] P. Eisner, D. Wilhelm, H.I. Maibach, Frictional properties of human forearm and vulvar skin: Influence of age and correlation with transepidermal water loss and capacitance, Dermatologica, Vol. 181, No. 2, 1990, pp. 88-91, DOI: 10.1159/000247892

[145] S.M. Pasumarty, S.A. Johnson, S.A. Watson, M.J. Adams, Friction of the human finger pad: Influence of moisture, occlusion and velocity, Tribology Letters, Vol. 44, No. 2, 2011, pp. 117-137, DOI: 10.1007/s11249-011-9828-0

[146] L.-C. Gerhardt, V. Strässle, A. Lenz, N.D. Spencer, S. Derler, Influence of epidermal hydration on the friction of human skin against textiles, Journal of The Royal Society Interface, Vol. 5, No. 28, 2008, pp. 1317-1328, DOI: 10.1098/rsif.2008.0034

[147] S. Derler, L.-C. Gerhardt, A. Lenz, E. Bertaux, M. Hadad, Friction of human skin against smooth and rough glass as a function of the contact pressure, Tribology International, Vol. 42, No. 11-12, 2009, pp. 1565-1574, DOI: 10.1016/j.triboint.2008.11.009

[148] K.A. Flack, M.P. Schultz, J.M. Barros, Skin friction measurements of systematically-varied roughness: Probing the role of roughness amplitude and skewness, Flow, Turbulence and Combustion, Vol. 104, No. 2-3, 2020, pp. 317-329, DOI: 10.1007/s10494-019-00077-1

[149] F.P. Bowden, D. Tabor, F. Palmer, The friction and lubrication of solids, American Journal of

Physics, Vol. 19, No. 7, 1951, pp. 428-429, DOI: 10.1119/1.1933017

[150] B.J. Briscoe, D. Tabor, Shear properties of thin polymeric films, The Journal of Adhesion, Vol. 9, No. 2, 1978, pp. 145-155, DOI: 10.1080/00218467808075110

[151] S. Derler, L.-C. Gerhardt, Tribology of skin: Review and analysis of experimental results for the friction coefficient of human skin, Tribology Letters, Vol. 45, No. 1, 2012, pp. 1-27, DOI: 10.1007/s11249-011-9854-y

[152] J.A. Greenwood, J.B.P. Williamson, Contact of nominally flat surfaces, Proceedings of the Royal Society of London. Series A, Mathematical and Physical Sciences, Vol. 295, No. 1442, 1966, pp. 300-319, DOI: 10.1098/rspa.1966.0242

[153] D. Dowson, Tribology and the skin surface, in K.-P. Wilhelm, P. Elsner, E. Berardesca, H.I. Maibach (Eds.), Bioengineering of the Skin, CRC Press, Boca Raton, 1997, pp. 159-179.

[154] S.A. Johnson, D.M. Gorman, M.J. Adams, B.J. Briscoe, The friction and lubrication of human *stratum corneum*, in D. Dowson, C.M. Taylor, T.H.C. Childs, M. Godet, G. Dalmaz (Eds.), Thin Films in Tribology, Elsevier, Amsterdam, 1993, pp. 663-672, DOI: 10.1016/S0167-8922(08)70419-X

[155] J.A. Greenwood, D. Tabor, The friction of hard sliders on lubricated rubber: The importance of deformation losses, Proceedings of the Physical Society, Vol. 71, No. 6, 1958, 989-1001, DOI: 10.1088/0370-1328/71/6/312

[156] S. Derler, U. Schrade, L.-C. Gerhardt, Tribology of human skin and mechanical skin equivalents in contact with textiles, Wear, Vol. 263, No. 7-12, 2007, pp. 1112-1116, DOI: 10.1016/j.wear.2006.11.031

[157] J.E. Sanders, J.M. Greve, S.B. Mitchell, S.G. Zachariah, Material properties of commonly-used interface materials and their static coefficients of friction with skin and socks, Journal of Rehabilitation Research and Development, Vol. 35, No. 2, 1998, pp. 161-176.

[158] J.F. Archard, Elastic deformation and the laws of friction, Proceedings of the Royal Society of London. Series A, Mathematical and Physical Sciences, Vol. 243, No. 1233, 1957, pp. 190-205, DOI: 10.1098/rspa.1957.0214

[159] T. Soneda, K. Nakano, Investigation of vibrotactile sensation of human fingerpads by observation of contact zones, Tribology International, Vol. 43, No. 1-2, 2010, pp. 210-217, DOI: 10.1016/j.triboint.2009.05.016

[160] B.N.J. Persson, Theory of rubber friction and contact mechanics, The Journal of Chemical Physics, Vol. 115, No. 8, 2001, pp. 3840-3861, DOI: 10.1063/1.1388626

[161] B.N.J. Persson, Capillary adhesion between elastic solids with randomly rough surfaces, Journal of Physics: Condensed Matter, Vol. 20, No. 31, 2008, Paper 315007, DOI: 10.1088/0953-8984/20/31/315007

[162] B.N.J. Persson, O. Albohr, C. Creton, V. Peveri, Contact area between a viscoelastic solid and a hard, randomly rough, substrate, The Journal of Chemical Physics, Vol. 120, No. 18, 2004, pp. 8779-8793, DOI: 10.1063/1.1697376

[163] K.R. Shull, Contact mechanics and the adhesion of soft solids, Materials Science & Engineering R: Reports, Vol. 36, No. 1, 2002, pp. 1-45, DOI: 10.1016/S0927-796X(01)00039-0

[164] L.D. Landau, E.M. Lifschitz, Elastizitätstheorie [Theory of Elasticity], Verlag Harri Deutsch, Frankfurt, 1991 [in German].

[165] M. Amontons, De la resistance causée dans les machines [About Resistance and Force in Machines], Mémoires de l'Académie Royale des Sciences, 1969, pp. 206-222 [in French].

[166] D. Dowson, History of Tribology, Professional Engineering Publishing, London, 1998.

[167] B. Derjaguin, Molekulartheorie der äußeren Reibung [Molecular Theory of External Friction], Zeitschrift für Physik, Vol. 88, No. 9-10, 1934, pp. 661-675, DOI: 10.1007/BF01333114 [in German].

[168] S.J. Eder, A. Vernes, G. Betz, On the Derjaguin offset in boundary-lubricated nanotribological systems, Langmuir, Vol. 29, No. 45, 2013, pp. 13760-13772, DOI: 10.1021/la4026443

[169] J. Gao, W.D. Luedtke, D. Gourdon, M. Ruths, J. N. Israelachvili, U. Landman, Frictional forces and Amontons' law: From the molecular to the macroscopic scale, The Journal of Physical Chemistry B, Vol. 108, No. 11, 2004, pp. 3410-3425, DOI: 10.1021/jp036362l

[170] A.M. Homola, J.N. Israelachvili, M.L. Gee, P.M. McGuiggan, Measurements of and relation between the adhesion and friction of two surfaces separated by molecularly thin liquid films, Journal of Tribology, Vol. 111, No. 4, 1989, pp. 675-682, DOI: 10.1115/1.3261994

[171] G. Bogdanovic, F. Tiberg, M.W. Rutland, Sliding friction between cellulose and silica surfaces, Langmuir, Vol. 17, No. 19, 2001, pp. 5911-5916, DOI: 10.1021/la010330c

[172] A.A. Feiler, P. Jenkins, M.W. Rutland, Effect of relative humidity on adhesion and frictional properties of micro- and nano-scopic contacts, Journal of Adhesion Science and Technology, Vol. 19, No. 3-5, 2005, pp. 165-179, DOI: 10.1163/1568561054352595

[173] A. Feiler, M.A. Plunkett, M.W. Rutland, Atomic force microscopy measurements of adsorbed

24

polyelectrolyte layers. 1. Dynamics of forces and friction, Langmuir, Vol. 19, No. 10, 2003, pp. 4173-4179, DOI: 10.1021/la026570p

[174] A.A. Feiler, J. Stiernstedt, K. Theander, P. Jenkins, M.W. Rutland, Effect of capillary condensation on friction force and adhesion, Langmuir, Vol. 23, No. 2, 2007, pp. 517-522, DOI: 10.1021/la060456f

[175] S. Yamada, J. Israelachvili, Friction and adhesion hysteresis of fluorocarbon surfactant monolayer-coated surfaces measured with the surface forces apparatus, The Journal of Physical Chemistry B, Vol. 102, No. 1, 1998, pp. 234-244, DOI: 10.1021/jp972875e

[176] A. Berman, C. Drummond, J. Israelachvili, Amontons' law at the molecular level, Tribology Letters, Vol. 4, No. 2, 1998, pp. 95-101, DOI: 10.1023/A:1019103205079

[177] R. D'Amato, A. Ruggiero, Skin tribology: Overview and insights on frictional properties of human skin, in S. Marcos-Pablos, J.A. Juanes-Méndez (Eds.), Technological Adoption and Trends in Health Sciences Teaching, Learning, and Practice, IGI Global, Hershey, 2022, pp. 1-25, DOI: 10.4018/978-1-7998-8871-0.ch001

[178] F.P. Bowden, D. Tabor, Mechanism of metallic friction, Nature, Vol. 150, No. 3798, 1942, pp. 197-199, DOI: 10.1038/150197a0

[179] Y. Martin, C.C. Williams, H.K. Wickramasinghe, Atomic force microscope-force mapping and profiling on a sub 100-Å scale, Journal of Applied Physics, Vol. 61, No. 10, 1987, pp. 4723-4729, DOI: 10.1063/1.338807

[180] G. Binnig, C.F. Quate, C. Gerber, Atomic force microscope, Physical Review Letters, Vol. 56, No. 9, 1986, pp. 930-934, DOI: 10.1103/PhysRevLett.56.930

[181] R.S. Johansson, Tactile sensibility in the human hand: Receptive field characteristics of mechanoreceptive units in the glabrous skin area, The Journal of Physiology, Vol. 281, No. 1, 1978, pp. 101-125, DOI: 10.1113/jphysiol.1978.sp012411

[182] I. Brody, The ultrastructure of the epidermis in *psoriasis vulgaris* as revealed by electron microscopy: 1. The dermo-epidermal junction and the stratum basale in parakeratosis without keratohyalin, Journal of Ultrastructure Research, Vol. 6, No. 3-4, 1962, pp. 304-323, DOI: 10.1016/S0022-5320(62)80037-9

[183] M. Klaassen, E.G. de Vries, M.A. Masen, The static friction response of non-glabrous skin as a function of surface energy and environmental conditions, Biotribology, Vol. 11, 2017, pp. 124-131, DOI: 10.1016/j.biotri.2017.05.004

[184] W.A. Ducker, T.J. Senden, R.M. Pashley, Measurement of forces in liquids using a force

microscope, Langmuir, Vol. 8, No. 7, 1992, pp. 1831-1836, DOI: 10.1021/la00043a024

[185] W.A. Ducker, T.J. Senden, R.M. Pashley, Direct measurement of colloidal forces using an atomic force microscope, Nature, Vol. 353, No. 6341, 1991, pp. 239-241, DOI: 10.1038/353239a0

[186] H.-J. Butt, Measuring electrostatic, van der Waals, and hydration forces in electrolyte solutions with an atomic force microscope, Biophysical Journal, Vol. 60, No. 6, 1991, pp. 1438-1444, DOI: 10.1016/S0006-3495(91)82180-4

[187] A. Tomala, H. Göçerler, I.C. Gebeshuber, Bridging nano- and microtribology in mechanical and biomolecular layers, in B. Bhushan (Ed.), Scanning Probe Microscopy in Nanoscience and Nanotechnology 3, Springer, Berlin, 2012, pp. 431-483, DOI: 10.1007/978-3-642-25414-7_16

[188] J.E. Sader, I. Larson, P. Mulvaney, L.R. White, Method for the calibration of atomic force microscope cantilevers, Review of Scientific Instruments, Vol. 66, No. 7, 1995, pp. 3789-3798, DOI: 10.1063/1.1145439

[189] C.P. Green, H. Lioe, J.P. Cleveland, R. Proksch, P. Mulvaney, J.E. Sader, Normal and torsional spring constants of atomic force microscope cantilevers, Review of Scientific Instruments, Vol. 75, No. 6, 2004, pp. 1988-1996, DOI: 10.1063/1.1753100

[190] C.P. Green, J.E. Sader, Torsional frequency response of cantilever beams immersed in viscous fluids with applications to the atomic force microscope, Journal of Applied Physics, Vol. 92, No. 10, 2002, pp. 6262-6274, DOI: 10.1063/1.1512318

[191] W. Tang, B. Bhushan, Adhesion, friction and wear characterization of skin and skin cream using atomic force microscope, Colloids and Surfaces B: Biointerfaces, Vol. 76, No. 1, 2010, pp. 1-15, DOI: 10.1016/j.colsurfb.2009.09.039

[192] A. Potter, G. Luengo, R. Santoprete, B. Querleux, *Stratum corneum* biomechanics, in A.V. Rawlings, J.J. Leyden (Eds.), Skin Moisturization, Informa Healthcare, New York, 2009, pp. 259-278.

[193] Y. Yuan, R. Verma, Measuring microelastic properties of *stratum corneum*, Colloids and Surfaces B: Biointerfaces, Vol. 48, No. 1, 2006, pp. 6-12, DOI: 10.1016/j.colsurfb.2005.12.013

[194] R. Álvarez-Asencio, V. Wallqvist, M. Kjellin, M.W. Rutland, A. Camacho, N. Nordgren, G.S. Luengo, Nanomechanical properties of human skin and introduction of a novel hair indenter, Journal of the Mechanical Behavior of Biomedical Materials, Vol. 54, 2016, pp. 185-193, DOI: 10.1016/j.jmbbm.2015.09.014

[195] B.V. Derjaguin, V.M. Muller, Y.P. Toporov, Effect of contact deformations on the adhesion of particles, Journal of Colloid and Interface

Science, Vol. 53, No. 2, 1975, pp. 314-326, DOI: 10.1016/0021-9797(75)90018-1

[196] F. Xu, T. Lu, Introduction to Skin Biothermomechanics and Thermal Pain, Springer, Berlin, 2011, DOI: 10.1007/978-3-642-13202-5

[197] P.G. Agache, C. Monneur, J.L. Leveque, J. De Rigal, Mechanical properties and Young's modulus of human skin *in vivo*, Archives of Dermatological Research, Vol. 269, No. 3, 1980, pp. 221-232, DOI: 10.1007/BF00406415

[198] M. Indrieri, M. Suardi, A. Podestà, E. Ranucci, P. Ferruti, P. Milani, Quantitative investigation by atomic force microscopy of supported phospholipid layers and nanostructures on cholesterol-functionalized glass surfaces, Langmuir, Vol. 24, No. 15, 2008, pp. 7830-7841, DOI: 10.1021/la703725b

[199] M. Indrieri, A. Podestà, G. Bongiorno, D. Marchesi, P. Milani, Adhesive-free colloidal probes for nanoscale force measurements: Production and characterization, Review of Scientific Instruments, Vol. 82, No. 2, 2011, Paper 023708, DOI: 10.1063/1.3553499

[200] A. Podestà, G. Fantoni, P. Milani, Quantitative nanofriction characterization of corrugated surfaces by atomic force microscopy, Review of Scientific Instruments, Vol. 75, No. 5, 2004, pp. 1228-1242, DOI: 10.1063/1.1710692

106

BOOK CHAPTER I

Chapter 16
Bridging Nano- and Microtribology in Mechanical and Biomolecular Layers

Agnieszka Tomala, Hakan Göçerler, and Ille C. Gebeshuber

Abstract The physical and chemical composition of surfaces determine various important properties of solids such as corrosion rates, adhesive properties, frictional properties, catalytic activity, wettability, contact potential and – finally and most importantly – failure mechanisms. Very thin, weak layers (of man-made and biological origin) on much harder substrates that reduce friction are the focus of the micro- and nanotribological investigations presented in this chapter.

Biomolecular layers fulfil various functions in organs of the human body. Examples comprise the skin that provides a protective physical barrier between the body and the environment, preventing unwanted inward and outward passage of water and electrolytes, reducing penetration by destructive chemicals, arresting the penetration of microorganisms and external antigens and absorbing radiation from the sun, or the epithelium of the cornea that blocks the passage of foreign material, such as dust, water and bacteria, into the eye and that contributes to the lubrication layer that ensures smooth movement of the eyelids over the eyeballs.

Monomolecular thin films, additive-derived reaction layers and hard coatings are widely used to tailor tribological properties of surfaces. Nanotribological investigations on these substrates can reveal novel properties regarding the orientation of chemisorbed additive layers, development of rubbing films with time and the relation of frictional properties to surface characteristics in diamond coatings.

Depending on the questions to be answered with the tribological research, various micro- and nanotribological measurement methods are applied, including scanning probe microscopy (AFM, FFM), scanning electron microscopy, microtribometer investigations, angle-resolved photoelectron spectroscopy and optical microscopy. Thoughts on the feasibility of a unified approach to energy-dissipating systems and how it might be reached (touching upon new ways of scientific publishing, dealing with over-information regarding the literature and the importance of specialists as well as generalists in tribology) conclude this chapter.

16.1 Introduction to Nanotribology and Microtribology

Micro- and nanotribology involve studies of friction and wear processes ranging from microscopic to atomic levels. In this section, experimental studies in the field of nano-/microtribology requiring applications with scanning probe microscopy, electron scanning techniques and microtribometres are investigated. Micro- and nanotribological tests presented in this section would be useful to better understand how mechanical and biological layers behave under shearing stress.

Even though atomic force microscopy (AFM) can be operated in the wearless regime, it is also possible to operate the instrument at higher loads for friction studies (e.g. friction vs. load plots) as well as for scratch/wear and indentation studies. These types of operation modules allow the probing of the elastic/plastic response of mechanical and biological films and are the focus of this chapter. Angle-resolved X-ray photoelectron spectroscopy (AR-XPS) helps to understand adsorption mechanisms of molecules on surfaces. At most solid–solid interfaces, the contact occurs in numerous asperities.

Bowden and Tabor's solid/solid adhesion model explains Amonton's friction law on the basis of the small real contact area A_c which is proportional to the applied load and independent of the geometrical area. Since the friction is proportional to the contact area A_c, friction is proportional to the load L. However, the described model is relevant for plastic deformation of asperities. In practice, the applied load is also supported by elastic deformation of asperities. Archard (1957) and subsequently Greenwood and Wiliamson (1966) confirmed that even for elastic asperity deformation, a statistically distributed, rough surface will result in $A_c \sim L$ [1]:

$$\mu = \tau_f / H \tag{16.1}$$

When asperities adhere and a shearing force is applied, the junctions can grow plastically since both the normal force and the shear force will couple to produce deformation. This will result in an increase in real contact area and thus in friction coefficient [2]. Tabor used this thought to extend his simple model to

$$\mu = \frac{1}{\delta^{1/2}(f^{-2} - 1)^{1/2}} \tag{16.2}$$

where $f = \tau_f / p_y$ is the ratio of the shear strength of the film to the yield stress of the bulk deformation material, and δ is a constant with value of ≈ 9 (assuming that hardness equals three times the yield stress).

This means that Amonton's law of friction results from adhesion of plastically deformed asperities (Tabor's theory), even if also elastic deformation occurs. The ratio of the interfacial shear strength τ_f to solid yield strength or hardness is a crucial parameter in determining adhesive friction. To obtain a low adhesive friction coefficient between rubbing rough surfaces in contact, one needs low surface shear strength τ_f and/or high hardness H. These requirements are incompatible for clean

metals but can be met if a thin low shear strength layer is formed on a hard metal substrate. Such a layer has to be thin enough not to bend significantly and thereby increase A_c.

This concept, namely, using a very thin, weak layer on a much harder substrate to reduce friction is the basis of boundary lubrication and will be used throughout this chapter. Clearly, the state of the surface, for example, adsorbates, the differences of materials in contact and lubricants can greatly affect the interaction and in consequence the friction process.

The tribological mechanical layers and the biotribological biomolecular layers investigated in this chapter serve as protective material of substrates from different environmental conditions.

Chemisorbed layers of ethanolamines (corrosion inhibitors) are the typical examples of adsorbed monomolecular thin films treated in this chapter. The tribochemically additive-derived reaction layer example is tribofilm from zinc dialkyldithiophosphates (ZnDDP). Other examples are hard coatings deposited by chemical or physical vapour deposition.

16.1.1   Monomolecular Thin Films

Boundary films can be formed by several processes: physisorption, chemisorption and chemical reactions [3]. In the case of physisorption, no exchange of electrons takes place between the lubricant molecule and the surface – this process involves weak van der Waals forces. Chemisorption means the sharing of electrons and electron interchange between chemisorbed species and the solid surface, resulting in the formation of chemical bonds. Finally, chemical reactions comprise the formation of surface layers with considerable chemical alteration of both additive and surface. The stability and durability of surface films (Fig. 16.1) decrease in the following order: chemical reaction layers (thick films), chemisorbed films (with monomolecular thickness) and physisorbed films (monolayers or multilayers) [4].

In this section, the example of a monomolecular thin film will be the chemisorbed film of a corrosion inhibitor: ethanolamine oligomers. Ethanolamines or aminoethanols are known as multidentate ligands with the possibility to form chelates with metals via their amino, hydroxyl and deprotonated hydroxyl groups. The total formula of these water-soluble compounds is $NH_{3-n}R_n \setminus (R = CH_2CH_2OH, n = 1 - 3)$. Ethanolamines are widely used as cleaning agents. In the field of lubrication, they are utilized as anti-corrosion additives, for example, in metalworking fluids.

Chemisorbed layers of the ethanolamine oligomers were studied with AFM and AR-XPS methods to investigate their lubrication properties in the nanoscale. Therefore, the ethanolamines were dissolved in double distilled water. Copper-sputtered silicon wafers served as substrates.
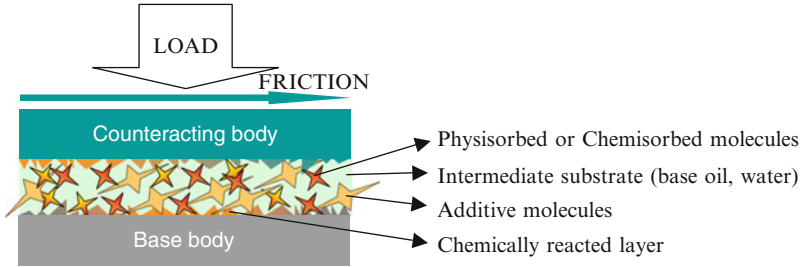
Fig. 16.1 Scheme of interacting additive molecules between surfaces in tribological contact

16.1.2 Additive-Derived Reaction Layers

Commercially available lubricants are formulated products composed of a base oil (mineral or synthetic) and a functional additive package designed to achieve a required performance for a specific application. Zinc dialkyldithiophosphates (ZnDDPs) have been widely used in the past decades as additives in engine lubrication oil. ZDDP was initially used as an antioxidant, but its excellent anti-wear properties were quickly recognized. The anti-wear properties of ZDDP additives arise from their ability to chemically interact with rubbing metal surfaces to form a protective layer. It protects the surface under conditions where elastohydrodynamic lubrication breaks down. In order to perform effectively, films of this kind must possess a shear strength that is sufficiently low to ensure that the shear plane resists within the protective layer itself, while being high enough to maintain layer integrity [5].

The thickness and distribution of reaction layers formed by ZDDP additives on lubricated contacts is controlled by several operating parameters, including load, temperature, sliding speed, slide-roll ratio and additive concentration. Measurements of additive-derived layer thickness have been performed using a wide range of techniques, showing that ZDDP forms several hundred monolayers thick layers on rubbing surfaces. X-ray photoelectron spectroscopy (XPS), Auger electron microscopy (AES) and secondary ion mass spectroscopy (SIMS) measured an estimated layer thickness of 50–100 nm [5].

A variety of mechanisms have been proposed for the formation of the ZDDP-derived reaction layers, involving oxidative (by reaction with hydroperoxides or peroxy radicals) [6], catalytic (chemisorption on metal), hydrolytic [7] and thermal [8] decomposition of the ZDDP.

The layers are composed of a mixture of short and long polyphosphates with the presence of sulphides and oxides in the layer bulk. A two-layer structure for the ZDDP-derived reaction layers has also been proposed, where a thin long-chain zinc poly(thio)phosphate layer is superimposed on a thicker short-chain mixed Fe/Zn polyphosphate layer, containing embedded nanocrystallites of ZnO and ZnS [9].

The anti-wear films produced particularly by ZDDP are highly uneven. Sheasby and Nisenholz [10] detected the existence of 20-μm-diameter 'pads' of ZDDP-derived anti-wear films by means of SEM. Graham et al. [11] found that ZDDP indeed yielded 10–20-μm pads with flattened tops, elongated in the sliding direction and surrounded by lower smaller pads. They also measure mechanical properties of these pads and found that at the centre of the large pads, indentation modulus values were as high as 209 GPa (compared to 220 GPa for the 52100 steel substrate!). An agglomeration of large long pads of polyphosphate chains perform as sacrificing load-carrying 'platforms' [5].

16.1.3   Hard Coatings

In the past 50 years, during the industrial revolution, solid tribological materials and coatings have continued to play important roles in many engineering areas mainly because mechanical systems rely on them for high performance, durability and efficiency. Recent developments in deposition technologies have provided the flexibility needed for design and development of multifunctional coatings. The use of thin surface coatings (such as diamond, diamond-like carbon, Molybdenum disulfide, nitrides, carbides and their composites and dopants) affords low friction and long wear life of rolling, rotating or sliding mechanical parts and components in recent years [12]. Application of the thin coatings on solid surfaces ensures that premature failures due to thermal, mechanical or chemical incompatibility are virtually nonexistent. In this field, there are almost unlimited numbers of material combinations, surface parameters and application conditions that one can manipulate to achieve better performance and longer durability.

16.1.4   Biomolecular Layers

The special types of biomolecular layers that will be in the interest of this study are epithelial tissues. As the term implies in Greek, with 'epi' meaning 'on, upon' and 'theli' meaning 'tissue', this type of tissue is covering connective tissues and therefore is the first layer to experience tribology-related mechanochemical contacts in many applications (Fig. 16.2).

Epithelial tissues are generally classified by the morphology of their cells and the number of layers they are composed of. Epithelial tissue that is only one cell thick is known as simple epithelium. If it is two or more cells thick, it is known as stratified epithelium. However, when larger simple epithelial cells are viewed in cross section with several nuclei appearing at different heights, they can be confused with stratified epithelia. This kind of epithelium is therefore described as 'pseudostratified' epithelium [13, 14].
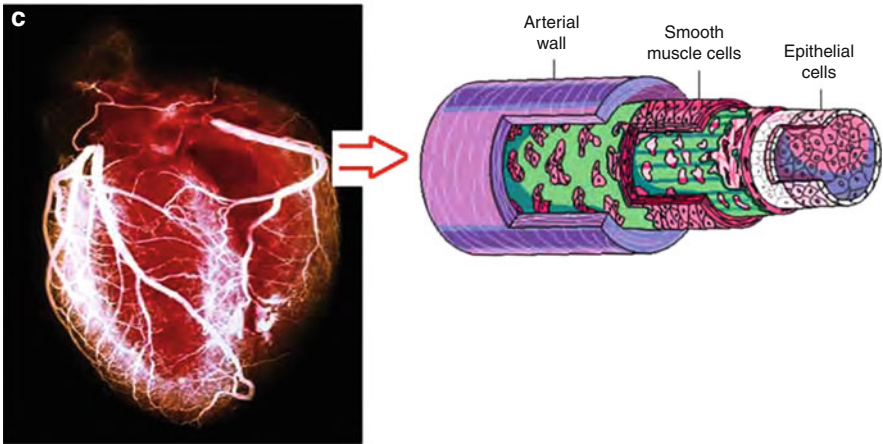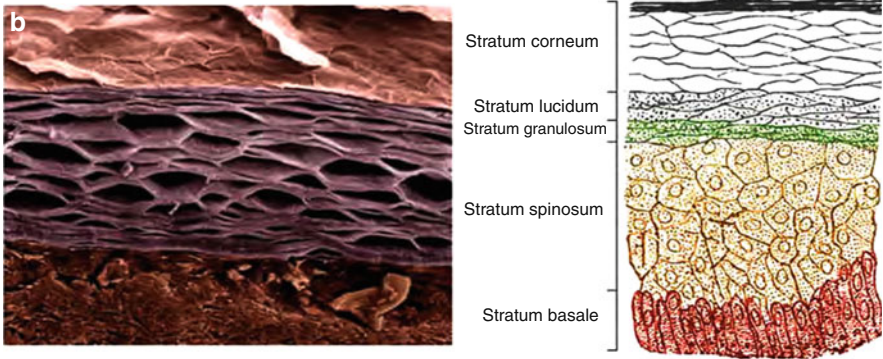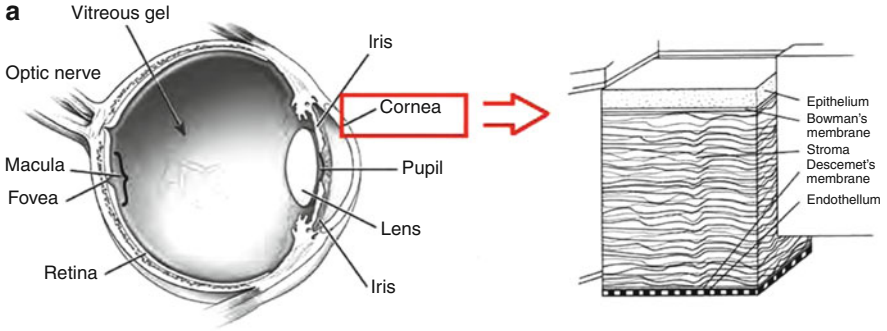
Fig. 16.2 Different examples of epithelial layers from (**a**) human eye and the cornea, (**b**) human skin and stratum corneum and (**c**) human artery [15, 16]

16.1.4.1   Simple Epithelium

Simple epithelium is one cell thick, that is, every cell is in direct contact with the underlying basement membrane. It is generally found in locations of the organisms where absorption and filtration occur. The thinness of the epithelial barrier facilitates these processes.

Simple epithelial tissues are generally classified by the shape of their cells. The four major classes of simple epithelium are squamous, cuboidal, columnar and pseudostratified.

Squamous Epithelial Cells

Squamous cells have the appearance of thin, flat plates. They fit closely together in tissues, providing a smooth, low-friction surface over which fluids can move easily. The shape of the nucleus usually corresponds to the cell form and helps one to identify the type of epithelium. Squamous cells tend to have horizontally flattened, elliptical (oval or egg-shaped) nuclei because of the thin flattened form of the cell. Classically, squamous epithelia are found lining surfaces utilizing simple passive diffusion such as the alveolar epithelium in the lungs. Specialized squamous epithelia also form the lining of cavities such as the blood vessels (endothelium) and pericardium (mesothelium) and the major cavities found within the body.

Cuboidal Epithelial Cells

As their name implies, cuboidal cells are roughly cuboidal in shape, appearing square in cross section. Each cell has a spherical nucleus in the centre. Cuboidal epithelium is commonly found in secretive or absorptive tissue, for example, the (secretive) exocrine gland the pancreas and the (absorptive) lining of the kidney tubules as well as in the ducts of the glands. They also constitute the germinal epithelium that covers the female ovary.

Columnar Epithelial Cells

Columnar epithelial cells are elongated and column-shaped. Their nuclei are elongated and are usually located near the base of the cells. Columnar epithelium forms the lining of the stomach and intestines. Some columnar cells are specialized for sensory reception such as in the nose, ears and the taste buds of the tongue. Goblet cells (unicellular glands) are found between the columnar epithelial cells of the duodenum, the first section of the small intestine in most higher vertebrates. They secrete mucus, which acts as a lubricant.

Pseudostratified Epithelial Cells

These are simple columnar epithelial cells whose nuclei appear at different heights, giving the misleading (hence 'pseudo') impression that the epithelium is stratified when the cells are viewed in cross section. Pseudostratified epithelium can also possess fine hair-like extensions of their apical (luminal) membrane called cilia. In this case, the epithelium is described as 'ciliated' pseudostratified epithelium. Cilia are capable of energy-dependent pulsatile beating in a certain direction through interaction of cytoskeletal microtubules and connecting structural proteins and enzymes. The wafting effect produced causes mucus secreted locally by the goblet cells (to lubricate and to trap pathogens and particles) to flow in that direction (typically out of the body). Ciliated epithelium is found in the airways (nose, bronchi) but is also found in the uterus and fallopian tubes of females, where the cilia propel the ovum to the uterus.

16.1.4.2 Stratified Epithelium

Stratified epithelium differs from simple epithelium in that it is multilayered. It is therefore found where body linings have to withstand mechanical or chemical insult such that layers can be abraded and lost without exposing subepithelial layers. Cells flatten as the layers become more apical, though in their most basal layers the cells can be squamous, cuboidal or columnar.

Stratified epithelial tissue also differs from simple epithelial tissue in that stratified epithelial tissues do not contain junctional complexes and have their cells bound together only by desmosomes.

Stratified epithelia (of columnar, cuboidal or squamous type) can have the following specializations:

Keratinized: In this particular case, the most apical layers (exterior) of cells are dead and lose their nucleus and cytoplasm and instead contain a tough, resistant protein called keratin. This specialization makes the epithelium waterproof, and so is found in the mammalian skin. The lining of the oesophagus is an example of a non-keratinized or 'moist' stratified epithelium.

Transitional: Transitional epithelium is found in tissues that stretch, and it can appear to be stratified cuboidal when the tissue is not stretched or stratified squamous when the organ is distended and the tissue stretches. It is sometimes called the urothelium since it is almost exclusively found in the bladder, ureters and urethra.

In this chapter, we will focus on the stratified epithelium. Apart from the natural functions of these tissues as reacting and sensing mechanochemical effects in the body and environment, developments in personal care and health-monitoring systems increased the severity and the frequency of the interactions. Human skin is treated not only with mechanical intruders such as razors, shaving machines, epilating systems, heat treatments, laser treatments and clothing produced from

unnatural materials but also chemical intruders such as shaving creams, shampoos, shower gels, perfumes and detergents used to clean clothes that are in contact with the skin. For the people who use contact lenses for medical or aesthetic reasons, the eye is also under the effect of extra force of eyelid and foreign body combined with the hygienic solutions necessary to assure the health of the eye. People who have problems with the arterial or digestive systems may experience arthroscopy or colonoscopy and may have disturbances on the interior walls of the related organs. All these applications show that unlike their natural life cycles and accidental disturbances, epithelial tissues have to respond periodic and more severe insults, sometimes even on daily basis. In this chapter, investigations on human skin stratum corneum (the outermost layer of the epidermis) using atomic force microscopy and the corneal cell lines using microtribotesters will be represented. The suggested techniques are universal and applicable on different cell lines.

16.2   Experimental Approach

16.2.1   AFM

Micro-/nanotribological studies are needed to develop a fundamental understanding of interfacial phenomena on a small scale. These investigations of interfacial phenomena also involve ultra thin films and micro-/nanostructures – both currently being used in magnetic storage systems, micro-/nanomechanical systems (MEMS/NEMS) and other industrial applications. Probe-based microscopes, for example, the atomic force microscope (AFM), and the surface force apparatus are widely used for such micro-/nanotribological studies [4, 5].

AFM is suitable to study engineering surfaces under dry or wet conditions down to atomic resolution. One of the most notable extensions of AFM imaging capabilities is the possibility to measure lateral forces between the tip and the sample. Thus, the atomic-scale origins of friction can be observed with this technique, usually denoted as lateral or friction force microscopy (LFM or FFM). These possibilities established the AFM as an important tool in the emerging field of nanotribology: the study of the atomic-scale interactions between surfaces in relative motion, such as friction, adhesion, lubrication and wear.

Moreover, the gap between this atomic-scale understanding, microscopic and subsequently macroscopic applications will need to be bridged. Transition from single (nanoscale) asperities to multiple asperity contacts holds the promise to predict tribological behaviour. Much effort has been invested to resolve and quantify tribological phenomena also on nanometre scales.

AFM techniques for quantitative, fundamental nanotribology are in a nascent stage, still some key issues such as force calibration, tip characterization or effects of the environment are neither fully resolved nor standardized.

16.2.1.1 Closed Fluid Cell

Part of this work was performed in fluid environment in a closed fluid cell. The fluid cell is a chamber consisting of two halves (Fig. 16.3a) screwed together mechanically: The samples are glued onto glass on the lower part of the closed fluid cell while the upper half basically consists of the electronic interface, the cantilever and a flexible membrane. After screwing together both halves, the fluid cell can be flooded with double distilled water (Fig. 16.3b). Two channels of the cell can be used to inject fluid into the cell and to drain it, respectively. In the next step, the fluid cell is attached to the head of the AFM. After placing the head with the cell onto the moving table, the head is lowered until the cell attaches to the table (Fig. 16.3c). The reference scans in double distilled water environment are carried out when the mounting and calibration procedure of the system is completed. The lateral trace and retrace data are recorded. Then, the additive solutions are injected into the cell with a syringe, and the AFM experiments are performed analogously to the reference measurements.

For reproducibility of the results, it is very important that all parts of the fluid cell have to be properly cleaned (e.g. with isopropanol), and the cantilever and tubes are replaced after every contact with additive solution.

Measurements were performed with an AFM MFP-3D atomic force microscopy (by Asylum Research, Santa Barbara, CA) in a closed fluid cell using non conductive silicon nitride cantilevers with a spring constant $k = 0.01$ N/m and a resonant frequency $f_0 = 4$–10 kHz (Veeco). The main measurement parameters were a scan size of $5 \times 5 \, \mu m^2$ (512 scan points and 512 scan lines), a scan rate of 2 Hz, a scan angle of 90° and a set point of 3.3 nN in contact mode. The recorded data was each trace/retrace of height, deflection and lateral force.

16.2.1.2 Friction Measurements

A reliable quantification of the surface morphology based on any AFM lateral image requires determination of the friction coefficient (lateral force dependent on normal forces). However, quantitative determination of friction forces is a challenge, due to difficulties with the calibration of the instrument and cantilever.

Typically, this calibration involves the conversion of the lateral force signal (also named output voltage signal) of the sector area-sensitive photodiode to values of absolute lateral force using (a) the torsional spring constant of the cantilever and (b) the lateral sensitivity of the photodiode. Many existing methods provide calibration approaches with large errors (30–50%) and suffer from poor reproducibility [17,18].

Bhushan introduced two methods to measure the friction in AFM experiments [19]. For the presented measurements, the lateral force technique has been chosen since it is described as more reliable and objective: The sample is scanned perpendicularly to the long axis of the cantilever beam, to record the lateral force signals in trace and retrace (LT, LRT).

Fig. 16.3 Assembling the closed fluid cell. (**a**) Sealing the cell and mounting the appropriate tubes to the four inlet/outlet ports. (**b**) Filling the cell with fluid and performing a leak test (**c**) Putting the closed cell assembly onto the head and setting up the tube clamp
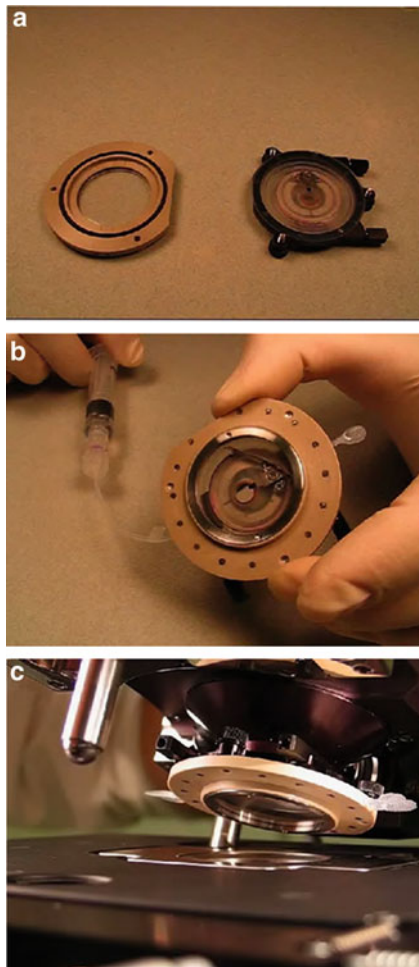
Using this arrangement, the friction force between tip and surface will cause the cantilever to twist as soon as the sample moves under the tip. Therefore, the signal intensity between the left and the right detectors will vary as

$$FFM = \frac{L - R}{L + R} \tag{16.3}$$

where FFM denotes the friction force signal. This signal can be related to the degree of twisting, hence to the magnitude of friction force. By changing the set point parameter in the feedback loop, the normal force applied between probing tip and sample surface can be changed.

The scan area was $5 \times 5 \ \mu m^2$, consisting of 512 scan lines with each 512 scan points. First, the average values of all 512 lines with 512 points for lateral trace

(LTV_{avg}) and lateral retrace $(LRTV_{avg})$ from every scan were calculated. To obtain the friction force value (FFV), these two mean values have to be subtracted from each other and divided by two:

$$FFV = \frac{\left|LTV_{avg} - LRTV_{avg}\right|}{2} \qquad (16.4)$$

The measurements of the friction force values were repeated ten times in every environment (water, water + oligomer) to obtain representative and repeatable results.

Assuming that the friction in the nanoscale follows Amonton's law, the friction force is given by

$$FFV = \mu(SP + F_0) \qquad (16.5)$$

where μ is the friction coefficient, the set point (SP) is the applied load and F_0 is a force constant. Following the procedure suggested by Beake et al. [20], the force constant is nearly equal to the pull-off force determined from the force–distance curves.

Usually, the FFV and SP values are given in [V] volts as acquired from lateral force measurements.

However, the results can be easily compared with each other because findings in volts are connected with the forces between tip and surface. In order to obtain commonly used units ([N] Newton), the lateral force needs to be calibrated by the determination of the slope of deflection vs. LVDT. The calibration delivers an accurate value of the inverse optical lever sensitivity (*InvOLS*) describing the sensitivity of the detector-cantilever combination. With the knowledge of the accurate value of *InvOLS*, it is possible to calculate FFV and SP in Newton:

$$FFV\ [V] \times InvOLS\ [nm/V] \times \text{spring constant } k\ [nN/nm] = FFV[nN] \quad (16.6)$$

$$SP\ [V] \times InvOLS\ [nm/V] \times \text{spring constant } [nN/nm] = SP\ [nN] \qquad (16.7)$$

Another solution for calibrating the lateral force signal is the wedge calibration method, introduced by Ogletree et al. [21] and improved after Tocha et al. [22] which gives an error in the calibration factors of about 5%. The 'wedge' method of force calibration is an *in situ* method and is applicable for a wide range of cantilevers and materials. This method is based on comparing lateral force signals on surfaces with different well-defined slopes. The known geometrical contribution to the total lateral force gives a different calibration of lateral force response in terms of normal force response. If the normal force constant is known, a quantitative friction measurement can be performed. If it is not known, the ratio of normal to lateral forces (the friction coefficient) can be determined.

An experimental force calibration is performed by sliding the tip across a surface of known slope (grating) and measuring the lateral force signal as a function of applied load. In this work, silicon calibration gratings (MikroMash test structure TGG01, Tallin, Estonia) were used. Such a calibration grating is a 1-D array

of triangular steps having precise linear and angular dimensions defined by the crystallography of silicon (111) planes. The edges of the triangular steps have radii of curvature of less than 10 nm.

Using the wedge calibration method, we experimentally measured the voltage output from the lateral force transducer LT_0, where $\alpha \, LT_0 = LT$ (here the subscript '$_0$' indicates that the value is measured in volts, LT is lateral signal). If we can find α (Newtons per Volt), we have a direct calibration of the lateral force response to the FFV signal. The calibration constant α is the product of all the factors of the experiment: the lever lateral force constant, the deflection of the reflected laser as a function of cantilever displacement and the photodiode angular sensitivity.

16.2.1.3   Nano-Wear Tests

Silicon tips on an Aluminium-coated cantilever (OLYMPUS OMCL-HA) were used to perform nanowear tests. The cantilevers were calibrated for topography mode and pull-off force mode using a silicon chip. The value of the spring constant for the silicon tips was 42 N/m. The scan area was $5 \times 5 \, \mu m^2$. Images were recorded in the contact mode, that is, the feedback electronics and the corresponding software were used to keep the cantilever at constant deflection measuring the sample topography. In order to obtain the maximum LFM signal (torsion motion), the sample was scanned along the direction perpendicular to the cantilever long axis. For each applied force, 512 lateral force loops on an area of $5 \times 5 \, \mu m^2$ were obtained from different regions. For the nanowear measurement, all samples were scratched 40 times using a silicon tip on an aluminium-coated cantilever with a very high spring constant (42 N/m). The load applied to cantilever was $22 \, \mu N$ (equal to a set point of 8 V), the scratching speed was $25 \, \mu m/s$ and the scanning direction was perpendicular to the cantilever long axis and perpendicular to the wear track direction. After the scratching, topography of the scratched area was measured with lower load. The extent of wear was estimated by determining the average depth and width of the scratched area.

16.2.1.4   Colloidal Probes Designed Specifically for *ex vivo* Human Skin Tests

The role of tribology in biomedical and personal care devices is becoming more crucial since it is recognized that the sliding interaction between biomaterials and human tissue is critical for the health and comfort of the patent and the handling performance of these devices. Currently, the tribology of such devices is not well understood, and it is difficult to investigate and optimize frictional properties of the surfaces and materials. The devices operate in a challenging environment that is difficult to simulate: The human tissue surfaces are often very compliant, they respond to mechanical stimulation and the lubrication conditions are variable. Furthermore, existing macroscopic test methods are mostly application-oriented,
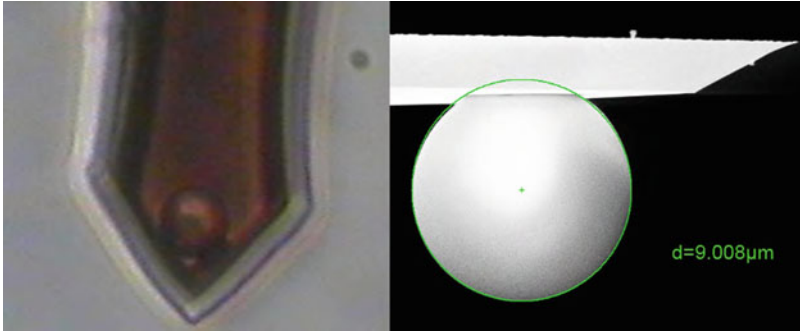
Fig. 16.4 The colloidal probe

and the results depend on many factors such as handling, environment, operator, test subject, bulk material properties, sample macrogeometry and lubrication conditions. Due to the inconsistency in test results there is a strong need for *in vitro*, microscale lubricity tests to investigate and pre-select surfaces, coatings and materials for medical and personal care devices. The other focus point is the determination of essential mechanical properties of tissues at different scales (cellular level, nano-/micro-/macro-scales) including the response to medical and cosmetic additives.

The aim was to determine the coefficient of friction and adhesive properties of the stratum corneum layer of the human skin, and to identify the microscale distribution of phospholipids, for the correlation to the observed variability of local friction.

The initial step for the research was the production of the colloidal probe for the AFM in order to obtain:

- defined geometry in order to apply models of contact mechanics more accurately,
- increased lateral force sensitivity,
- increase the adhesive interaction between the probe and the skin tissue.

Borosilicate glass microspheres with a diameter of $10 \, \mu m$ were selected for the application. The main reasons to choose borosilicate were:

- Their roundness is >90%.
- Their density is the lowest of most glasses ($2.2 \, g/cm^3$).
- They have a very low thermal expansion coefficient ($32 \times 10^{-7}/°C$, for 30–300°C).

Another challenge was the epoxy- and adhesive-free production of the colloidal probe in order to avoid contamination on the human stratum corneum. The possibility of material transfer between the tip and the sample would change the sample-tip interaction by changing the surface energies and also jeopardize the storage conditions standardized for the *ex vivo* biological samples. A novel technique for the production of epoxy- and adhesive-free colloidal probes for atomic force microscopy is reported by Indrieri [23], inspired by the work of Bonaccurso (Fig. 16.4).
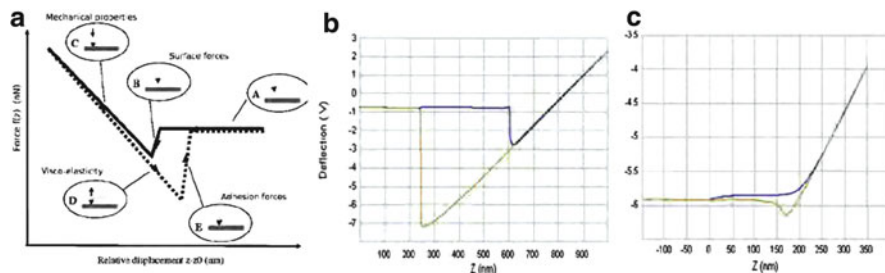
Fig. 16.5 (**a**) Typical force curve expected from the interaction of probe and the sample. (**b**) Adhesion forces observed before contamination. (**c**) Adhesion forces observed after contamination

Using a cantilever-moving approach, the capillary adhesion between a borosilicate glass microsphere and the AFM cantilever was utilized to attach the sphere to the cantilever free end. A suitable modification of the adhesive properties of the glass substrate makes adhesion of spheres to the substrate weaker than that between sphere and cantilever; this in turn facilitates the detachment of the sphere from the substrate once it has been hooked by the cantilever.

Subsequently, the cantilever-sphere system was cured at 780°C for a few hours to covalently bind the sphere to the cantilever. The procedure is relatively quick and very reliable and produces clean, epoxy-free colloidal probes. The produced probes were characterized with scanning electron microscopy (SEM) and the statistical method of AFM reverse imaging [23].

After three consecutive friction tests conducted in different locations of the stratum corneum, it has been observed that the adhesion forces between the probe and the sample decreased drastically possibly related to the contamination of the probe due to transfer of phospholipids from the skin (Fig. 16.5).

The robustness of the colloidal probe was put to test, and in order to remove contamination, it was subjected to ultraviolet treatment, 15 min of sonication in acetone followed by twice 15 min of sonication in distilled water. The probe was intact after these procedures, no abnormality was observed in functions and expected adhesion forces, observed in force curves from the AFM.

16.2.2   AR-XPS

In order to obtain detailed information about the elemental composition, chemical bonds, structure and morphology of a surface, analytical methods such as X-ray photoelectron spectroscopy (XPS) and Auger electron spectroscopy (AES) are favourable candidates. To get in-depth information, depth profiling using ion sputtering is typically used. However, for very thin films (such as monomolecular
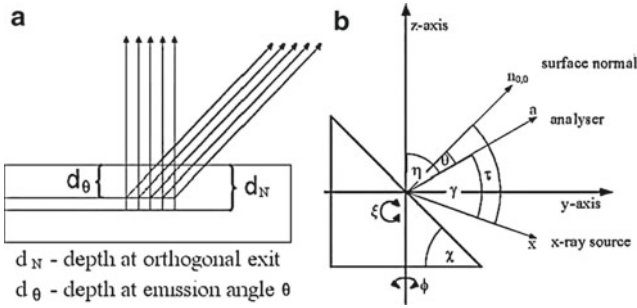
Fig. 16.6 Geometry of angle-resolved XPS used in calculations. (**a**) Information depth at normal to the sample surface (orthogonal) and at emission angle θ and (**b**) instrumental and sample geometry used in the AR-XPS measurements

thin films of additives on surfaces), the XPS/AES methodology using sputter depth profiling has got its limitations. Because the ion sputtering process is always accompanied by energy impact, various processes in the analysing region occur, for example, atomic mixing, phase changes or roughening [24, 25].

One way to achieve quantitative results on the near-surface structure of the material is to vary the detection angle in electron spectroscopy for depth-dependent analysis. Due to the finite mean free path of electrons within the solid, the information depth in XPS analysis is of the order of a few nanometres if the electrons are detected at a direction normal to the sample surface. If the electrons are detected at a different angle to the normal, then the information depth is reduced by an amount equal to the cosine of the angle between the surface normal and the analysis direction (emission angle), as shown in Fig. 16.6a. This is the basis for the powerful analysis technique angle-resolved XPS (AR-XPS). The instrument geometry of angle-resolved XPS for the microlab instrument MKII is shown in Fig. 16.6b. In the figure, the emission angle θ refers to the angle between surface normal and analyser. In the geometry of our spectrometer, the angle η between the z-axis and the analyser is 60°, and the angle γ between the X-ray source and the analyser is also 60°. The sample holder has a slant angle χ equal to 45°.

The stage in the analysis chamber can be moved in x-, y- and z-directions. Additionally, the sample can be tilted and rotated. Before the AR-XPS experiments the stage was positioned in such a way that the analyser axis was pointing directly at the centre of the samples (as shown in Fig. 16.6b).

For AR-XPS measurements in our spectrometer, the emission angle θ was varied by rotating the sample around the z-axis by two revolutions of a step motor controller that corresponds to rotations over an angle of 20°. For the measurements taken at rotation angles 0°, 20°, 40°, 60° and 80°, the corresponding emission angles calculated for geometry of our spectrometer in these experiments were 15°, 22°, 35°, 49° and 63°.
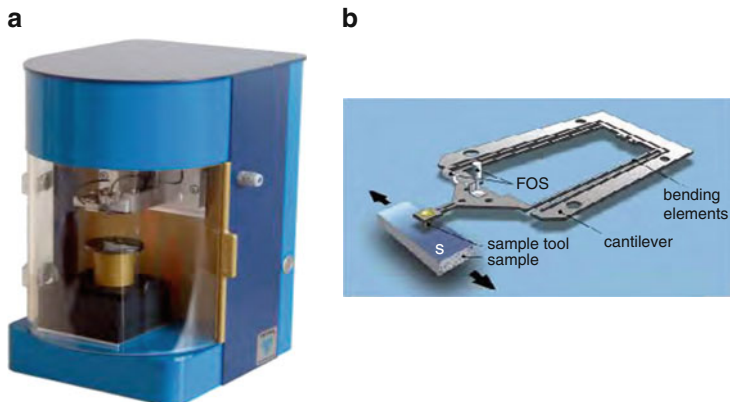
a   **b**

FOS

bending
elements

cantilever

sample tool
sample

S

Fig. 16.7 (**a**) General appearance of the Falex MUST MTT. (**b**) Details of the force transducer

16.2.3 Microtribometer

A Falex MUST microtribotester (MTT) was used for the measurements on the corneal cell cultures in order to evaluate/rank lens designs and materials, develop a basic understanding of damage mechanisms, reduce epithelial damage via lens design and determine influencing parameters of the interaction between the eyeball-contact lens-eyelid system such as material composition, material stiffness, friction coefficient, lubrication conditions (buffer solution), normal pressure, shear stress, contact area and sliding speed.

The device operates in a challenging environment that is difficult to simulate: The human tissue surfaces are often very compliant, they respond to mechanical stimulation and the lubrication conditions are variable. Furthermore, existing macroscopic test methods are mostly application-oriented and the results depend on many factors such as the handling, environment, operator, test subject, bulk material properties, sample macrogeometry and the lubrication conditions. Due to the inconsistency in test results, there is a strong need for *in vitro*, microscale lubricity tests to investigate and preselect surfaces, coatings and materials for medical and personal care devices. But the major objective would be to develop a platform that is not only for corneal epithelium for contact lens application but also using cell cultures of different human tissues, for example, vascular endothelium for cardiovascular applications or columnar endothelium for intestinal applications.

The basic functional components of the Falex MUST are a 2-D micro force transducer and various precision motion modules (Fig. 16.7). Relative movements can therefore be carried between a microtool and a probe under control of the power changing effects. The two basic tests, reciprocating or pin-on-disc, are practicable for the applications in microtribology. For our applications, we use the reciprocating mode of the device.

Fig. 16.8 Characteristic line of fibre optic sensor
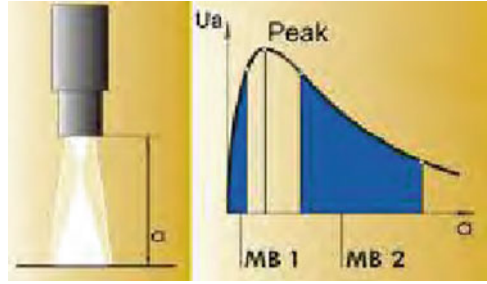
16.2.3.1 Operational Principle of the Force Transducer

The force transducer consists of a cantilever (based on a parallel spring system), two mirrors fixed on the moving part of the cantilever and a mechanical support. The geometric dimension of the cantilevers is so that the normal force F_N and the tangential force F_T according to the measuring task are optimally coordinated. The cantilever is fixed in a mechanical carrier. With the help of the carrier the force transducer can be changed in the measurement module. Two micromirrors (orthogonal to each other) are used for the fibre optic sensors as reflective surfaces.

16.2.3.2 Operational Principle of the Fibre Optic Sensor

For the measurement of the deflection of the force transducer and the positioning of the piezo drives, fibre optic sensors (FOS) are used. In the tip of the FOS glass fibre bundles are joined and finished to an optical flat. The light radiated from a light conductor bundle (transmission light conductor) is taken up to reflection at a mirror by a further light conductor bundle (reception light conductor) and converted by optoelectronic transducers to electrical signals. The variable projection of the light bundle on the fibres influences the light-induced current.

The process of the sensing rate characteristic $U_a = f(a)$ is determined by the optical behaviour and the photometric distance law. A characteristic of the sensor consists that it can be operated in two measuring ranges. In the first measuring range (*MB*1, near range), a very distinct rise occurs with a relatively small change in distance. In the second measuring section (*MB*2, far range), the measuring range is larger and the related rise smaller. The maximum of the characteristic is called optical peak. The FOS is calibrated by the manufacturer (Fig. 16.8).

16.2.3.3 Working in Liquid Environment and Tare Values

The difficulty of working in liquid environment has been mentioned before, especially when using devices that are not specifically designed for that purpose. One of the challenges during the work with the Falex MUST MTT was the relatively

small issue that the lifting force of the liquid media during the approach to the surface was not taken into account since the machine was designed to work in dry conditions. The usual operating medium is air (that can be conditioned, thanks to the closed chamber, to different levels of humidity and temperature) for most of the applications with the MTT, so the aforementioned effect on the tare values could be neglected, but since the applications with contact lenses require buffer solutions such as lens solutions or MEM+Glutamax^{TM}-1 with high viscosity levels, this effect for our tests could not be neglected.

During the calibration of the MTT, it was observed that even though the voltage values given by the internal software change from 1198.596 to 1520.256 mV, the value of the tare forces remained relatively constant (Fig. 16.9). The device eventually gave an error message that the spring reached its maximum displacement even though there was an obvious distance to the bottom surface of the petri dish (Fig. 16.10). The explanation for the error can be found in the concept of tare forces. For each step that the probe automatically approaches the surface, a resisting force is applied by the buffer solution against the probe. This lifting effect of the liquid medium is not stored as the actual tare value and nullified after each step so when the cumulative of these forces equals the target value of the system, the device starts the tests. If the system is handled manually, these forces may equal the maximum force that the spring can support, and then, the system stops the test and retracts the probe.

$$
\left.
\begin{array}{l}
d_1 \to F_1 \\
d_2 \to F_2 \\
\quad . \\
\quad . \\
\ldots \ldots \\
d_n \to F_n
\end{array}
\right\}
\quad
F_1 + F_2 \ldots + F_n = F_t \to \text{Start Test}
\qquad
\begin{array}{l}
d_T \to F_T = k_{\text{spring}} \times (\Delta X_{\text{limit}})_{\text{spring}} \\
\to \text{Stop Test} \ldots d_T : \text{single} \\
\text{continuous displacement}
\end{array}
$$

$$\text{Automatic Mode} \qquad\qquad\qquad \text{Manual Mode}$$

This issue was solved by a software update from Falex Tribology that nullifies the tare values after each step of approach. Note that research on biological samples that requires the application of normal forces in the ranges less than a millinewton is sensitive to the natural reactive or surface forces such as lifting forces or meniscus forces. In this case, the weight and the surface area of the probe, approaching velocities and inter-material affinities would play a significant role in the experiment and the parameters need to be revised thoroughly.

16.2.3.4   Probe Designs for Tests on Epithelial Tissues and Cell Lines

The test apparatus coupled with the Falex MUST MTT requires not only specific design in order to apply sub-millinewton forces but also works completely submerged in the solutions related to the application in focus such as lens solutions
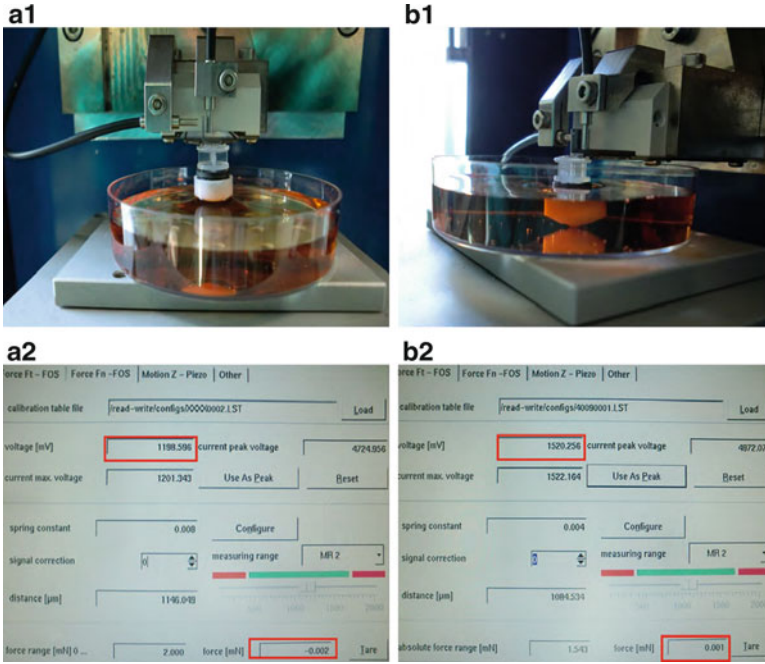
Fig. 16.9 (**a1**) Initial contact of the designed probe with the buffer solution surface and the formation of the meniscus. (**a2**) The related voltage and tare values of a1, screen-captured from the internal software. (**b1**) The probe at the maximum depth before the actual contact with the petri dish surface. (**b2**) The related voltage and tare values of b1, screen-captured from the internal software
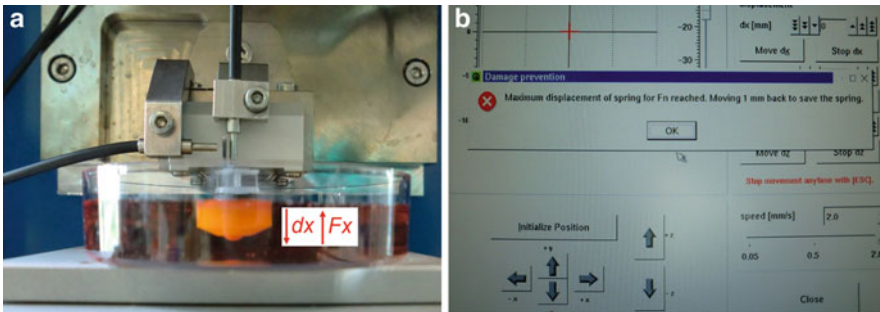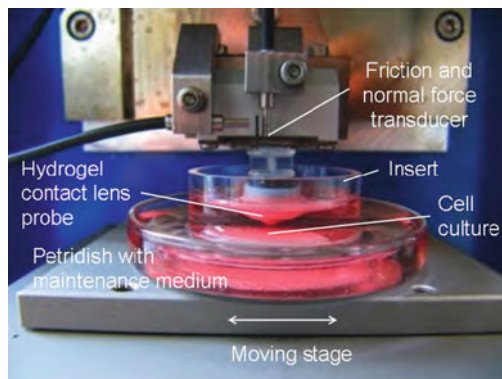

Fig. 16.10 (**a**) The position at which the error message of maximum displacement is given. (**b**) The error massage provided by the MTT

Fig. 16.11 Experimental setup

for corneal tissue applications or buffer solutions to keep the cell lines in healthy conditions during the tribological tests.

The selection of the appropriate cantilever for the system was the initial step of the probe design. The applications would not only focus on 3-D matrices of stratified epithelial tissues but also on pseudostratified versions of the epithelial cell lines cultured to mimic other organ types of the human body, so the cantilever should be able to apply stabile normal forces as low as $200\,\mu N$ [50, 51]. For this study, cantilevers with the following specifications were selected: $k_n = 16\,N/m$, $k_t = 7\,N/m$, $(F_n)_{max} = 4\,mN$, $(F_t)_{max} = 3.5\,mN$, $(F_n)_{min} = 0.04\,mN$ and $(F_t)_{min} = 0.0035\,mN$ (resolution). The maximum normal load that was applied to the samples during the study was $700\,\mu N$, and the minimum normal load of $200\,\mu N$ with the expected minimum value of COF would result in a minimum friction force value of $5\,\mu N$. In both cases, the selected cantilever would function agreeably for all range of forces in the envisaged application.

The probe needs to be large enough to be completely drawn in the buffer solution in order to eliminate strong effects of meniscus force that could play a critical role in the interaction of the body and the samples. On the other hand, the system should not be so large and lightweight that its self-bending would interfere with the transition of the force from the transducer to the sample, and it should not initiate any crosstalk effect during the test. These two considerations were the driving points that grounded the base of probe design. The final appearance of the probe together with the 3-D tissue construct model can be seen in Fig. 16.11.

Another critical point for the design was the practical mount and dismount of the system without applying any destructive force on the contact lens samples and to avoid any interference that may affect the biological investigation of wear such as dead cells on the contact lens surface. The whole contact lens body was put in the plastic cover and secured by a compliant silicon rubber moulded with a tip of variable diameters (Fig. 16.12a, b). The reason that the tip of the silicon rubber has a defined geometry and shows similarities with the design of the colloidal probe designed for the AFM is to apply models of contact mechanics more accurately
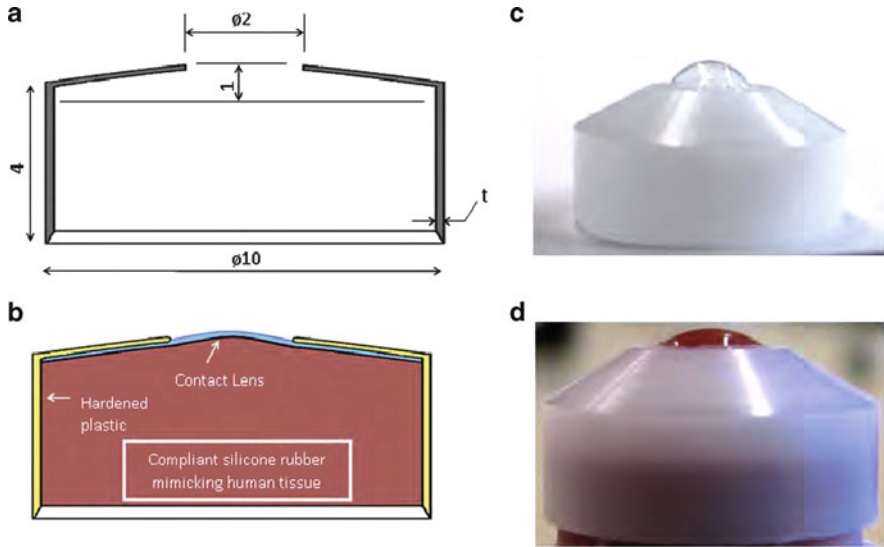
Fig. 16.12 Details of the hydrogel contact lens probe. (**a**) Technical drawing of hardened plastic cover. (**b**) Sketch of final assembly. (**c**) Photograph of hardened plastic cover and passing form of hydrogel contact lens. (**d**) Photograph of final assembly

but also to observe the influence of the contact area by means of different mould diameters for future applications. In Fig. 16.12c, it can be seen how the contact lens complies with the supporting silicon rubber. The silicon rubber also has advantages over metal supports, such as mimicking the damping effect of connective tissues supporting the epithelial tissues and making it easier to work in hygienic biological media.

16.3 Results and Discussion

16.3.1 Monomolecular Thin Films

This section reports on nanoscale tribological investigations on ethanolamine oligomers in aqueous solutions investigated with an AFM closed fluid cell and AR-XPS methods. This work shows oligomer specific lubrication: The most efficient additive reduced friction by 76% with respect to reference friction measurements performed in double distilled water. Further studies with AR-XPS explain the influence of hydroxyl groups and nitrogen-containing ethanolamines on their nanotribological behaviour.
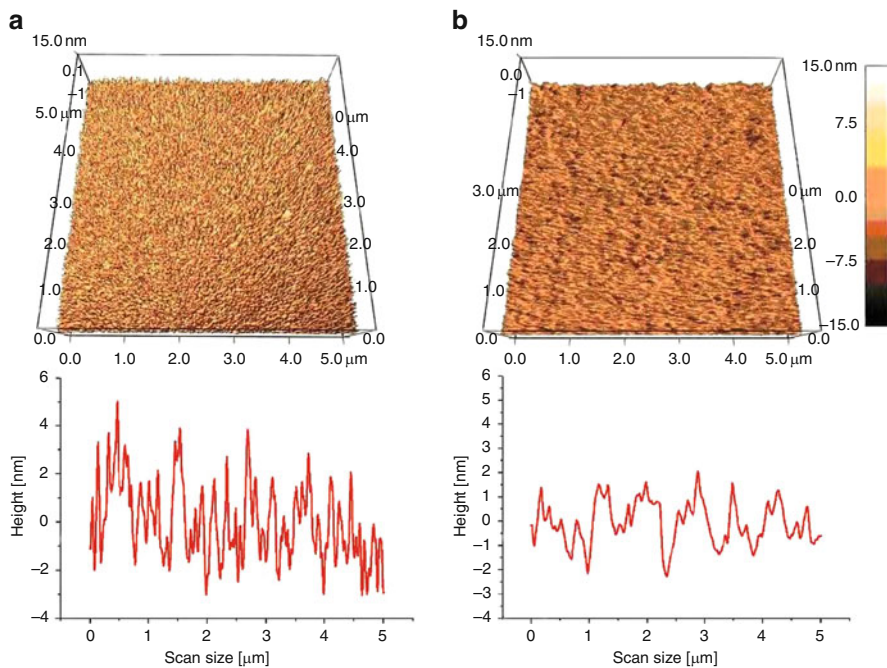
Fig. 16.13 Topography images. (**a**) Copper sample in double distilled water, RMS $= 3.59 \pm 1.97$ nm. (**b**) Copper sample with double distilled water $+$ MEA, RMS $= 0.89 \pm 0.58$ nm

16.3.1.1 Topography

The friction force values and friction coefficient of the virgin surfaces were determined. Then, the additives were introduced into the fluid cell, and the measurements were repeated with the lubricant present [21]. Representative 3-D topography of the ethanolamine monomolecular films is displayed in Fig. 16.13 with section graphs and the root mean square (RMS) parameter.

In the case of ethanolamine film, the surface roughness and RMS parameter were significantly lower compared to pure double distilled water (Fig. 16.13).

16.3.1.2 Force–Distance Plots

Force plots are often used to measure the interaction forces between the tip and the surface. This is done by pushing the tip against the surface and then separating the tip and surface. From this data, a number of viscoelastic properties can be studied, such as adhesion, indentation or tribolayer elasticity. There are different force regimes in which forces can be measured with the AFM. Figure 16.14 describes in
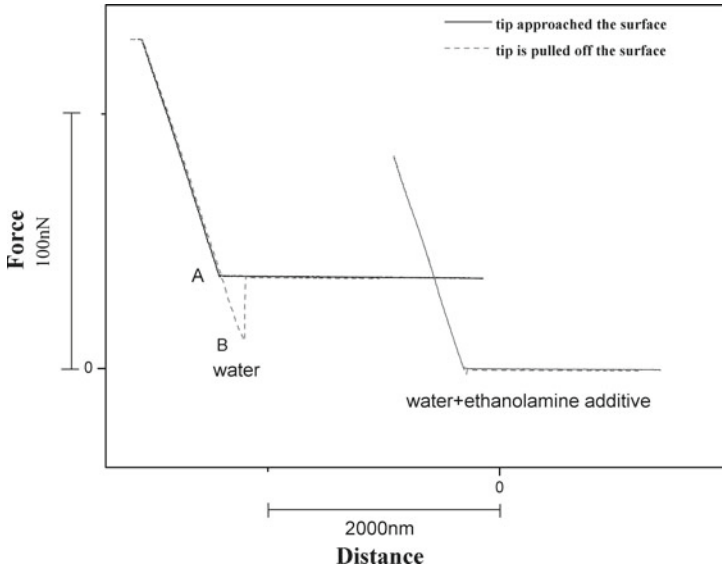
Fig. 16.14 Force-distance curves of the investigated monolayers

detail the normal force typically experienced by the tip when it is brought towards a sample surface [26].

It can clearly be seen that pull-off forces for double distilled water without any additives are larger than pull of forces for water with ethanolamines. This fact may be related to an increase of surface energy due to the additives. The hydroxyl groups, being components of ethanolamine oligomers, increase the surface energy, and the increased surface energy in turn increases the pull-off forces.

16.3.1.3 Friction Results

The friction force values and friction coefficient of the virgin surfaces were determined. Then, the additives were introduced into the fluid cell, and the measurements were repeated with the lubricant present.

The results show a significant drop in the friction force value after 10 min after introducing ethanolamine oligomer to the solvent (Fig. 16.15).

16.3.1.4 Molecular Structure

Orientation of ethanolamine molecules on the steel surface was evaluated using AR-XPS method using ARCtick (angle-resolved XPS spreadsheet) and the SESSA simulation tool (simulation of electron spectra for surface analysis).
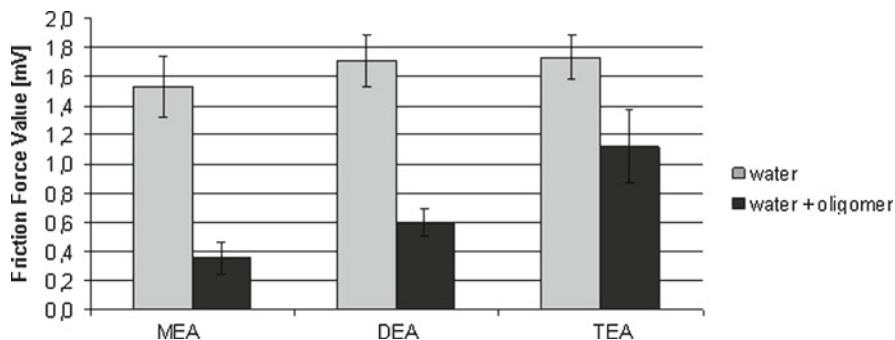
Fig. 16.15 FFV of double distilled water and decrease of FFV after the addition of solutions with 0.025% ethanolamine oligomer

The survey spectra of all steel samples showed only peaks of iron, oxygen, nitrogen and carbon, as expected. The position of photoelectron peaks was determined using Casa XPS, and a combination of Gaussian and Lorentzian peaks was used for fit. The adsorption of ethanolamine oligomers onto a flat steel surface (Ra < 5 nm) layer takes less than 1 min. The survey spectra show that, after this time, the surface had adsorbed a measurable amount of the oligomers. The quantification of the O1s and C1s peaks showed that there was an equal amount of both oxygen and carbon in the adsorbed films. The C1s peak was in the region typical for alcohols and organic compounds containing nitrogen. The Fe photoelectron region of ethanolamines showed a completely different intensity ratio of the iron and the iron oxide peak (Fig. 16.6a). The loss in intensity of the iron peak was due to the coverage of the surface with the chemisorbed diethanolamine oligomer film. At an emission angle of 63°, the Fe metal peak almost vanished in the spectra recorded from samples with ethanolamine film [27].

Results obtained for ethanolamine clearly reveal the orientation of the molecules on the surface. The intensities of the oxygen peak O1s and the carbon peak C1s increase with increasing analyser angle, and the iron peaks Fe 2p 1/2 and Fe 2p 3/2 and the nitrogen N1s peak decrease with emission angle (Fig. 16.16b). This result indicates that oxygen and carbon were located on top, and iron and nitrogen were beneath. Therefore, it was deduced that the molecules stand upright on the surface, bound to it by the nitrogen atom [27].

Detail analysis of angular-resolved measurements using ARCtick (Fig. 16.17a) and the SESSA simulation tool (Fig. 16.17b) [28] of peaks from Fe, O, C and N confirms our theory that the molecules of ethanolamine oligomer stand upright on the surface, bound to it by the nitrogen atom.

16.3.2   Tribochemical Additive-Derived Reaction Layer

The formation of a ZDDP-derived reaction layer with rubbing time was studied using a ball-on-disc test rig under mixed rolling-sliding conditions in the boundary lubrication regime. The evolution of the topography and mechanical properties of
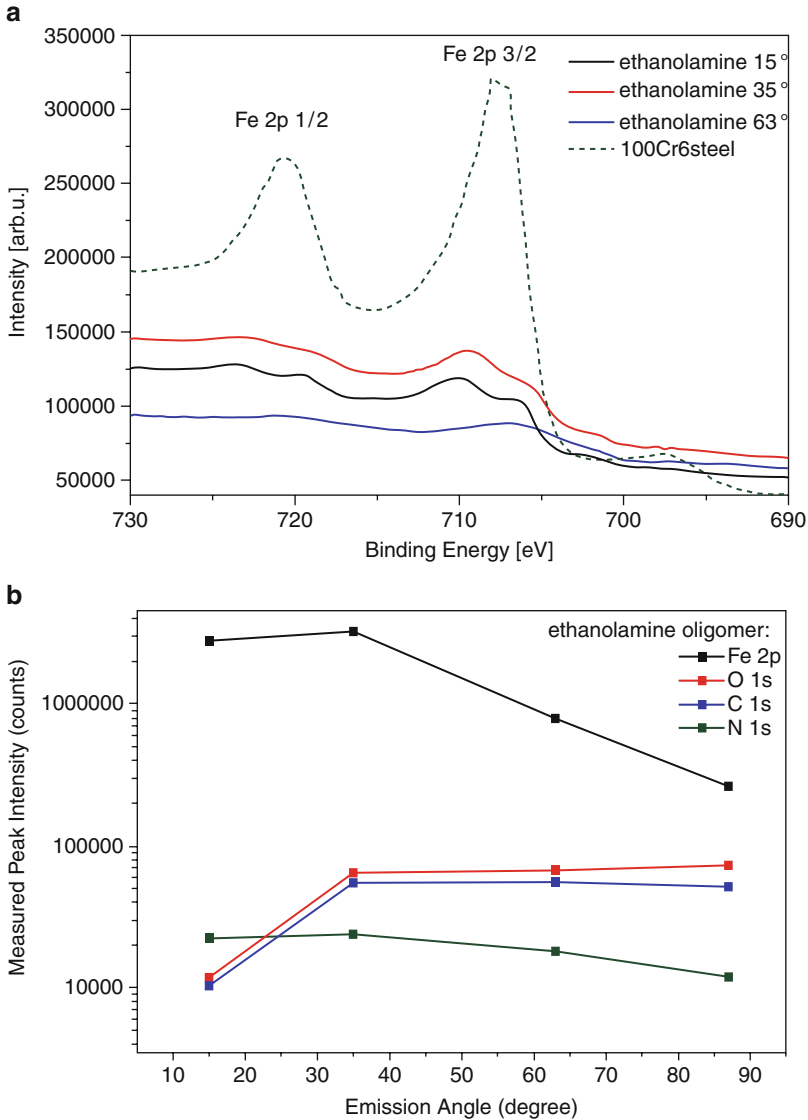
a

b

Fig. 16.16 (**a**) Fe 2p region of monolayers of ethanolamine film on 100Cr6 steel. The spectra are shown for three different electron take-off angles. For comparison, the spectra of clean 100Cr6 steel are marked in a dashed line. (**b**) Intensity ratio of XPS peaks depending on the emission angle

the layers with rubbing time were studied using AFM. The tribotests were carried out at an applied load of 300 N which resulted in a maximum Hertzian contact pressure of 1.9 GPa (contact diameter 540 μm) at a slide to roll ratio SRR $= -10\%$. The temperature was set constant at 90°C for all the tests [29].

a

b
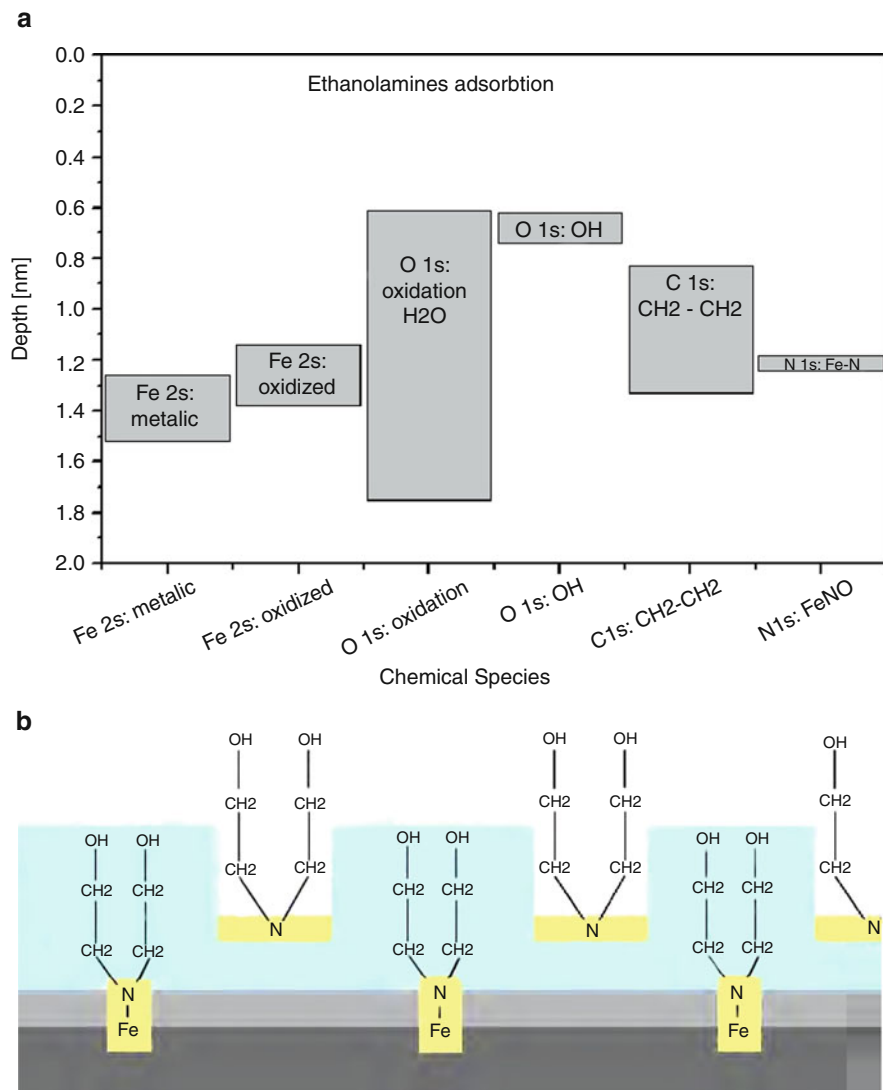
Fig. 16.17 Proposed mechanism of a chemisorbed monomolecular thin layer of ethanolamine oligomer on a steel surface based on (**a**) the stratification method with the ARCtick tool and (**b**) based on the SESSA simulation tool

In order to understand the nature of the interaction between the cantilever tip and the formed reaction layer, deflection displacement curves were recorded. Figure 16.18 shows the deflection of the cantilever tip as a function of the distance from the reaction layer formed in the rubbing steel surfaces. The solid line indicates the tip approach to the surface, while the dashed line represents the tip being pulled away from the surface. The vertical separation between the point where the tip was touching the layer and the point where the tip was pulled away from it together with
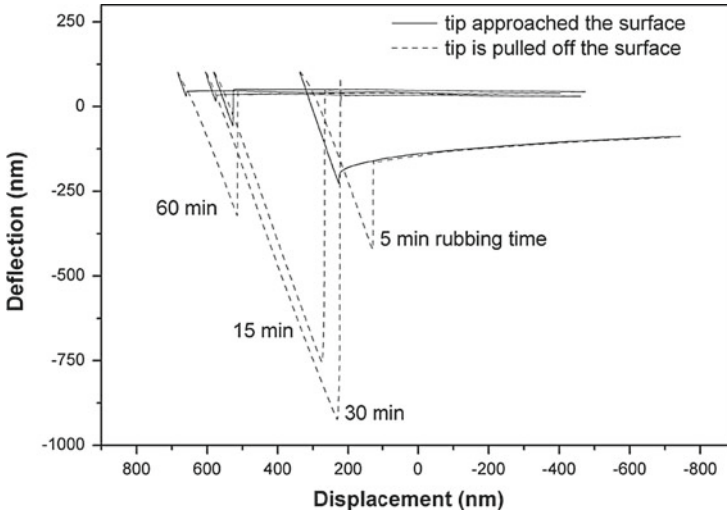
Fig. 16.18 The deflection of the cantilever tip as a function of the distance from the wear track surface for the investigated samples

the spring constant of the cantilever (0.1 nN/nm) was used to calculate the pull-off (adhesive) force [4].

Figure 16.18 shows that with increasing ZDDP-derived reaction layer thickness, the force needed to pull off the cantilever from the surface increases. This fact is related to high adhesion and plastic deformation, due to the presence of a soft surface layer formed by ZDDP.

Samples after a 5 min test exhibit a thin reaction layer, the cantilever has alternate contact with asperities from the steel surface and the layer. This results in small pull-off values when the tip engages the elevated asperities and in high lateral force response.

Samples after a 15 min test and after a 30 min test present a thick and soft reaction layer that entirely covers the steel surface. The cantilever interacts only with the soft layer covering the surfaces, resulting in long-distance curves, low friction but high wear volume on the nanoscale. The larger adhesive properties of the soft layer are caused by the molecular interactions between the molecules attached to the tip and the molecules in the layer.

When rubbing progresses further, the additive-derived layer experiences a constant roughening and hardening with rubbing time, as indicated by the nano-wear tests (Fig. 16.19d), which show no indentation for the layer after 1 h rubbing time. These processes may be responsible for the observed increase in friction and wear protection with rubbing time of the additive-derived reaction layers, in both the macro- and the nanoscale.

The 3-D AFM images showing the topographies of the ZDDP-derived layers are illustrated in Fig. 16.19. Section graphs attached to the AFM images show the height
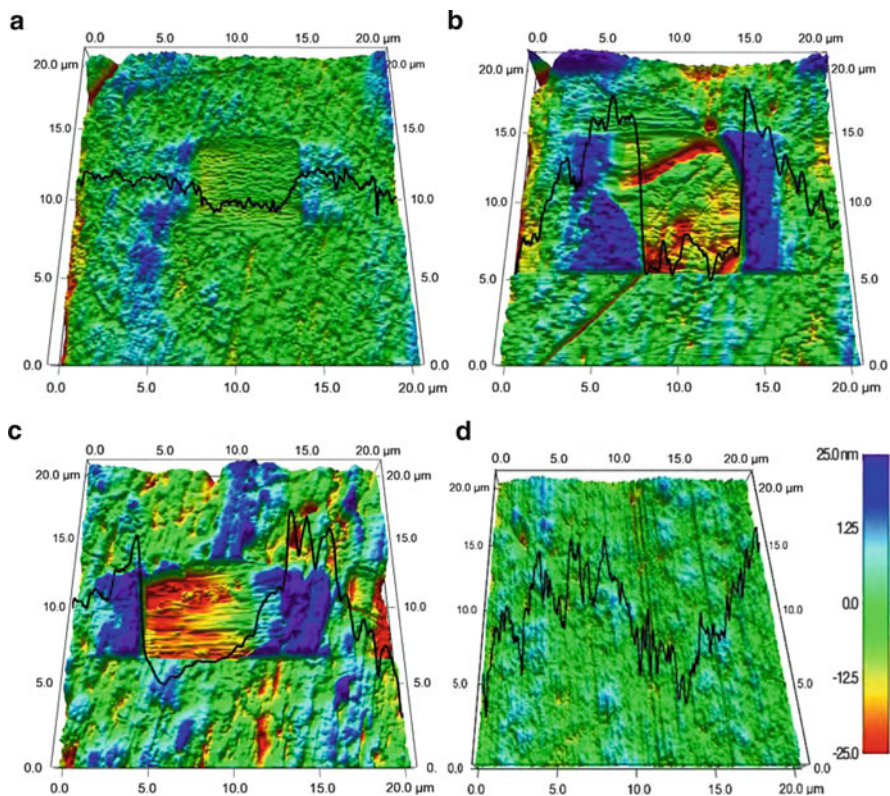
Fig. 16.19 AFM images showing the $20 \times 20\text{-}\mu\text{m}^2$ topographies of the investigated samples after nano-wear indentation with horizontal section graph of height distribution. (**a**) After 5 min ball-on-disc test time, (**b**) after 15 min, (**c**) after 30 min and (**d**) after 60 min

distribution across the scan. Section graphs have the same scale as the colour scale on the right side of the AFM images.

ZDDP reaction layers form only in the rubbing tracks, where actual tribological contact occurs [30]. The reaction layer forms initially as separate patches on the steel surfaces and gradually develops to form a continuous-like structure, as illustrated in Fig. 16.19. A three-stage process can be used to describe the evolution of the layer morphology. In the first stage (Fig. 16.19a, b), the layer growth mechanism begins on micro-asperity contacts at the steel surface, leading to the formation of thin pads. In the second stage as rubbing progresses, the pads continue to grow and coalesce to form a complete layer formed over the surface (Fig. 16.19c). AFM investigations showed that such an additive-derived reaction layer consists of large wear pads, smaller anti-wear pads and lower valleys between the anti-wear pads [11]. In the final stage, the continuous rubbing of the surface causes the disintegration and spreading of the tribolayer to form progressively smaller pads (Fig. 16.19d) [26]. A rough and hard layer develops, reaching a 'limited thickness' of approximately 70 nm.
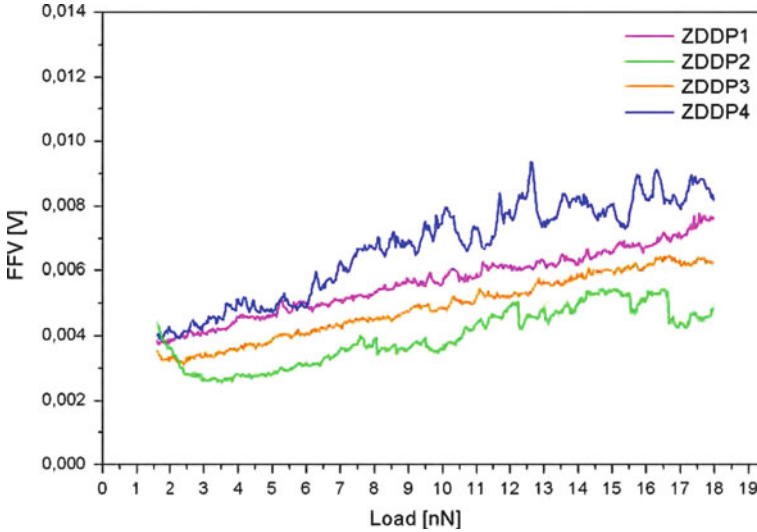
Fig. 16.20 The variation of friction force as a function of applied load for the investigated samples

Nanowear tests using a cantilever with high spring constant showed that ZDDP-derived layer is initially softer, undergoing a hardening process with rubbing time. The indentation reaches the steel substrate for a sample after 5 min test. The wear depths for samples after 15 and 30 min tests are very similar (between 20 and 30 nm), and despite the uncertainty on the layer base line, none of the indentations reached the substrate. The results obtained for a sample after 1 h test, where no indentation was observed after the nanowear test, indicate a possible hardening process parallel to the roughening process of the layer that has also been observed, with the development of pad-like features [31]. Previous studies [19,32] have shown how those features are higher than the surroundings and present a higher hardness and elastic modulus, which is attributed to the load-carrying capacity of the layer (Fig. 16.20).

16.3.3 Hard Coatings

Diamond film is one of the hardest materials and is well known for several extraordinary features such as high mechanical strength [33], excellent thermal conductivity, outstanding wear and friction properties [34], high chemical inertness [35], etc. These films exhibit high surface roughness because of their columnar growth [36], making them unsuitable for many applications such as in microelectronics and as optical components [37]. However, end use tends to favour
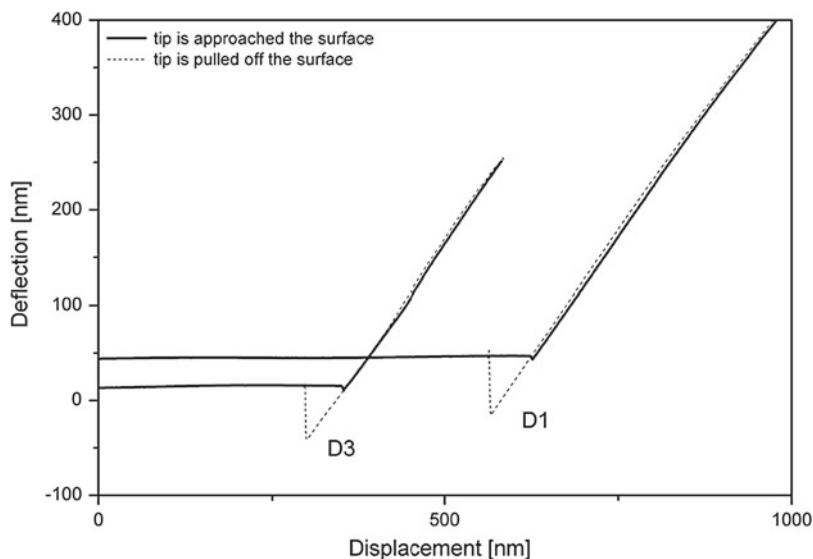
Fig. 16.21 Force spectroscopy of the investigated diamond films

a particular crystallographic surface texture, purity and thickness matched to the surface that offers the most compatible properties. Thus, properties such as broad optical transparency, high refractive index, wide band gap, low or negative electron affinity, transparency to light from deep ultra violet to far infrared and low thermal expansion make these films suitable for numerous industrial applications [38].

The morphologies of chemical vapour deposited (CVD) diamond films can be changed over a wide range by controlling the process parameters of the deposition. The surface morphologies of the film govern the micro- and nanomechanical properties of the film. In view of these points, diamond film having faceted morphology is presented in this section. It has been deposited using the microwave chemical vapour deposition (MWCVD) technique.

Figure 16.21 shows the deflection of the cantilever tip as a function of the distance from the film surfaces for all two films. In all cases, the darker line indicates the tip approach and the lighter line represents the tip being pulled away. The vertical separation between the point where the tip is touching the film and point where the tip is pulled off the film is a measure of the pull-off (adhesive) force. The product of this horizontal distance of separation and the spring constant of the cantilever (0.1 nN/nm) gives the pull-off forces [4]. The pull-off forces for two diamond films D1 and D3 are 21.3 and 13.1 nN, respectively. Film D1 represents faceted morphology with mainly sp^3 bonding, whereas film D3 represents fine ballas morphology with mainly sp^2 bonding.
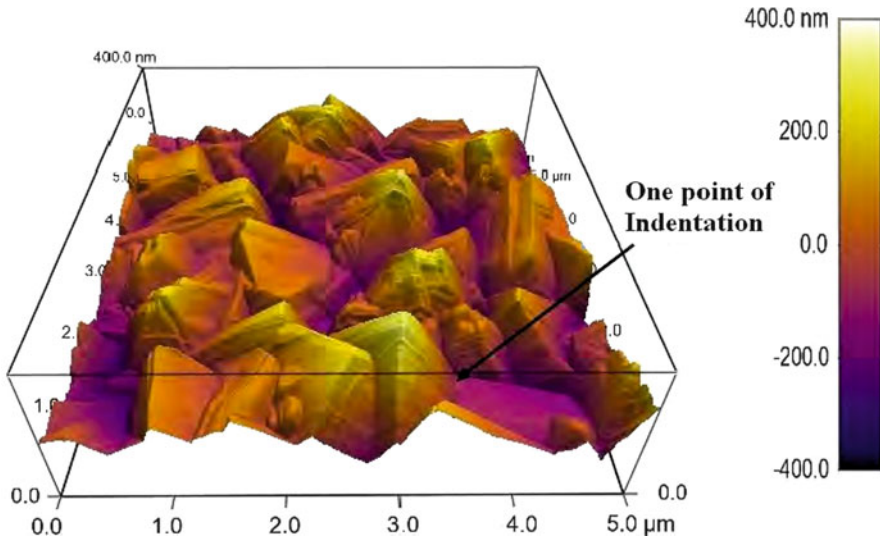
138

Fig. 16.22 Topography of the investigated diamond film

The 3-D AFM image showing the topography of the investigated diamond film is given in Fig. 16.22. For the investigated sample, the diamond growth conditions were 'optimal,' this results in well-faceted pure diamond crystals with mainly sp^3 bondings.

The influence of the applied load on the friction force is depicted in Fig. 16.23. The friction force decreases with increase of the applied load. This suggests that friction force is not governed by ploughing mechanism since in this case, the friction force would increase with an increase of applied load when ploughing plays important role. Rather, it is controlled by surface force.

16.3.4 Biomolecular Layers: Tribological Investigation on Human Stratum Corneum Epidermis Using Atomic Force Microscopy

16.3.4.1 Topography

Forming the interface with a desiccating external environment, the primary function of the stratum corneum is to retard evaporative water loss from the aqueous interior. The stratum corneum also protects against mechanical insults and the ingress of foreign chemicals and microorganisms. It provides the first defence against ultraviolet light, screening out more than 80% of incident ultraviolet *B* irradiation. Taking these considerations into account, stratum corneum epidermis
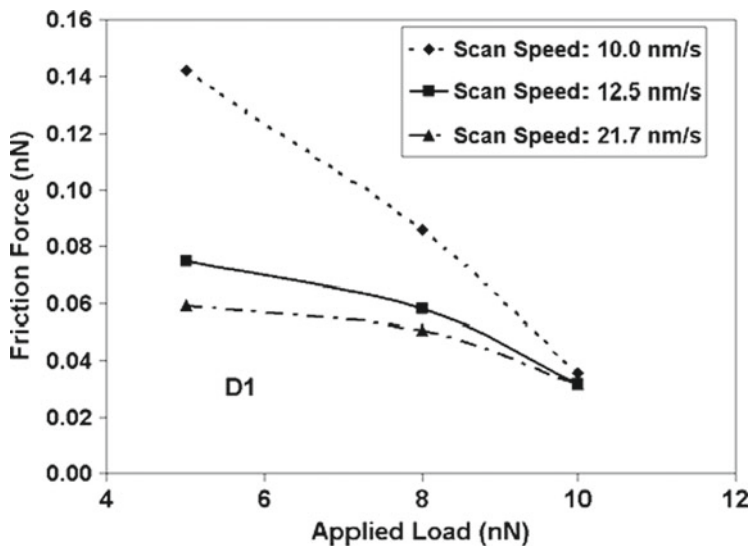
139

Fig. 16.23 The influence of applied load on the friction force of the investigated film

can be viewed as a hard coating material, comparable to the ones used in mechanical applications.

Understanding the structure and function of the stratum corneum is vital because it is the key to healthy skin and its associated attractive appearance. During cornification, the process whereby living keratinocytes are transformed into nonliving corneocytes, the cell membrane is replaced by a layer of ceramides that become covalently linked to an envelope of structural proteins (the cornified envelope) [39, 40]. This complex surrounds cells in the stratum corneum and contributes to the skin's barrier function. Corneodesmosomes (modified desmosomes) facilitate cellular adhesion by linking adjacent cells within this epidermal layer. These complexes are degraded by proteases, eventually permitting cells to be shed at the surface. Desquamation (skin peeling) and formation of the cornified envelope are both required for the maintenance of skin homeostasis. A failure to correctly regulate these processes leads to the development of skin disorders [39].

Cells of the stratum corneum contain a dense network of keratin, a protein that helps keep the skin hydrated by preventing water evaporation. These cells can also absorb water, further aiding in hydration and explaining why humans and other animals experience wrinkling of the skin on the fingers and toes ('pruning') when immersed in water for prolonged periods. In addition, this layer is responsible for the 'spring back' or stretchy properties of skin. A weak glutenous protein bond pulls the skin back to its natural shape.
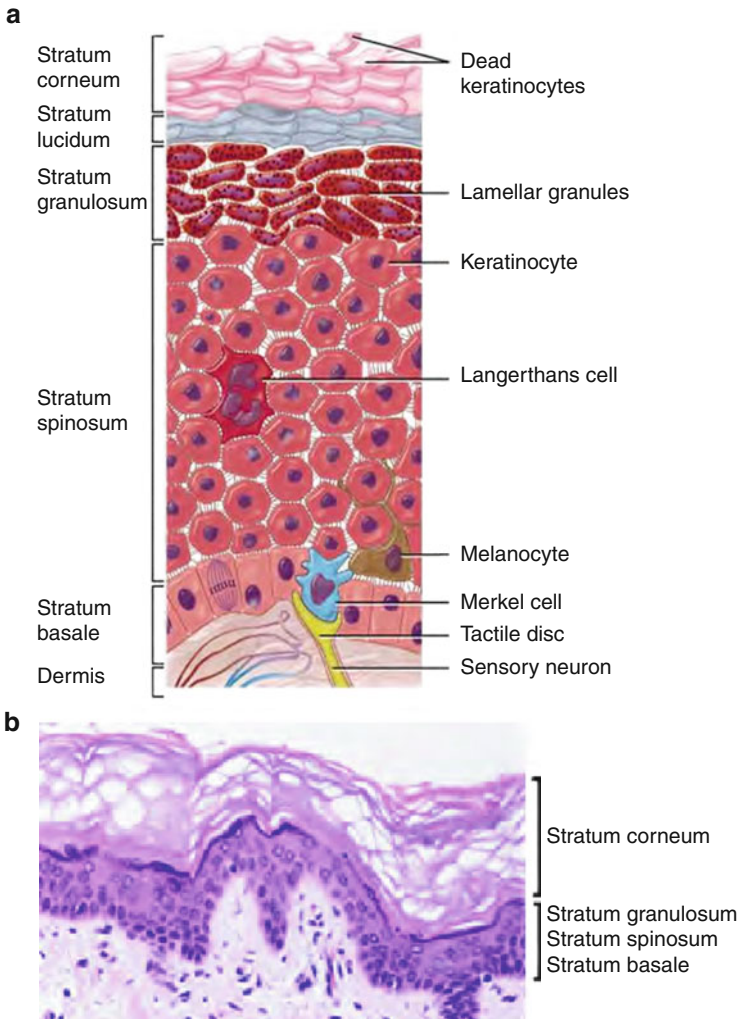
Fig. 16.24 (**a**) Layers of the epidermis. (**b**) Details of the upper three levels of the epidermis [41]

The thickness of the stratum corneum varies throughout the body. In the palms of the hands and the soles of the feet, this layer is typically thicker since these regions require additional protection in order to grasp objects and avoid injury. In general, the stratum corneum contains 15–20 layers of dead cells. The stratum corneum has a thickness between 10 and 40 μm (Fig. 16.24).

Skin samples were obtained from the Department of Pharmacy, University of Milano, after aesthetic surgery following the standards introduced by Blank and McAuliffe [42]. Full-thickness skin was sealed in evacuated plastic bags and frozen at −20°C within 24 h of the removal. Prior to the preparation, skin was thawed to

141

a) Scanning Electron Microscope Image. Bottom Surface of Stratum Corneum (Scale: 825μm)

b) Optical Microscope Image. Bottom Surface of Stratum Corneum (Scale: 325μm)

c) Atomic Force Microscope Image. Bottom Surface of Stratum Corneum (Scale: 50μm)

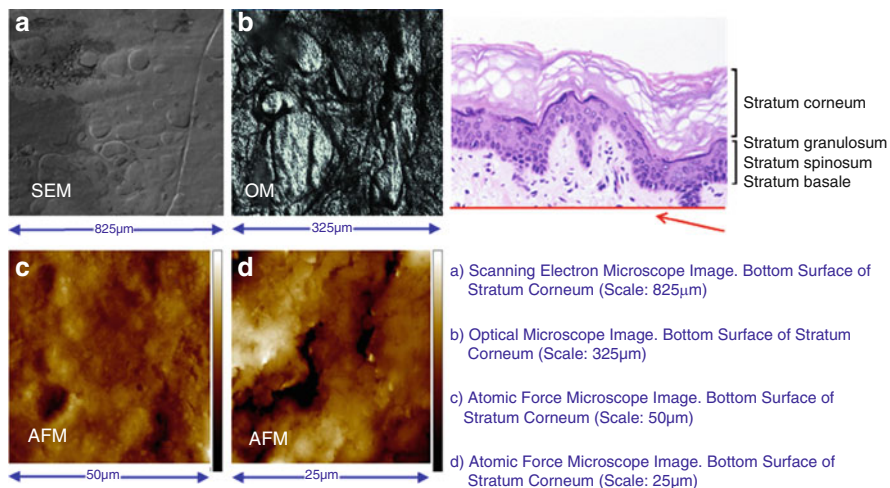d) Atomic Force Microscope Image. Bottom Surface of Stratum Corneum (Scale: 25μm)

Fig. 16.25 Bottom view of stratum corneum acquired with different kinds of microscopy

room temperature, and the excess fat was carefully removed. The skin sections were cut into square pieces, and after immersing the skin in water at 60°C for 1 min, the epidermis was gently separated from the remaining tissue with forceps and left to dry. The dried samples were wrapped in Aluminium foil and sealed in plastic bags. When the skin samples were received, they were cut into pieces that are suitable for AFM investigations, and the pieces were put into the freezer at −40°C. Before the measurements, each piece was first thawed in the fridge at −4°C for 2–3 h and then at room temperature for 4 h. No extra procedures such as nitrogen fluxing and cleaning with distilled water were conducted before the measurements.

The initial challenge for the investigation on stratum corneum epidermis was to identify the proper side to conduct the tests. Both sides of stratum corneum, open to the environment and laying over stratum granulosum, show significantly different morphologies. These differences would play a vital role in the tribology-related applications. For this purpose, images of both sides of the skin samples were taken, without any assumptions on the 'proper side' beforehand.

In order to understand the morphology of the two sides of the stratum corneum samples, the following imaging techniques were used: SEM, optical microscopy and AFM. The side laying over stratum granulosum shows significant round patterns as the mark patterns of granules that gives the name to the layer (Fig. 16.25). On the other side, the top layer of stratum corneum, laminar patterns can be seen, as expected (Fig. 16.26).

The detailed images gathered by AFM show formations that resemble layers of corneocytes, that is, protein complexes that are made of tiny threads of keratin in an organized matrix (Fig. 16.27).
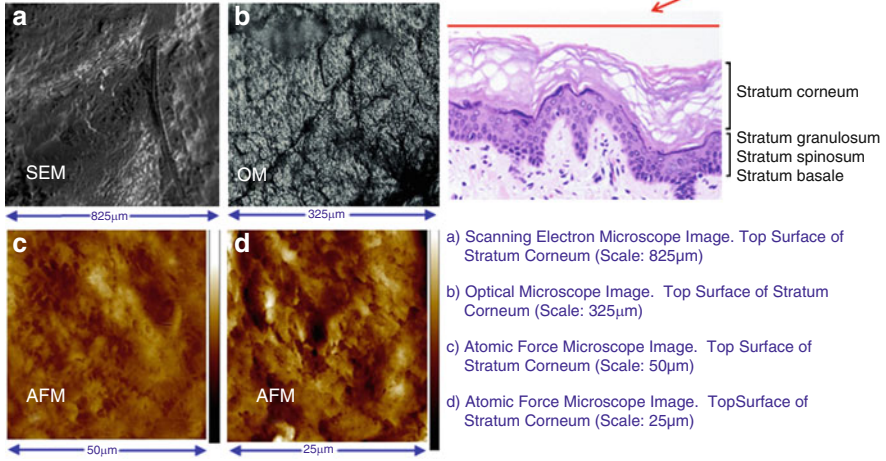
a) Scanning Electron Microscope Image. Top Surface of Stratum Corneum (Scale: 825μm)

b) Optical Microscope Image. Top Surface of Stratum Corneum (Scale: 325μm)

c) Atomic Force Microscope Image. Top Surface of Stratum Corneum (Scale: 50μm)

d) Atomic Force Microscope Image. TopSurface of Stratum Corneum (Scale: 25μm)

Fig. 16.26 Top view of stratum corneum acquired with different kinds of microscopy
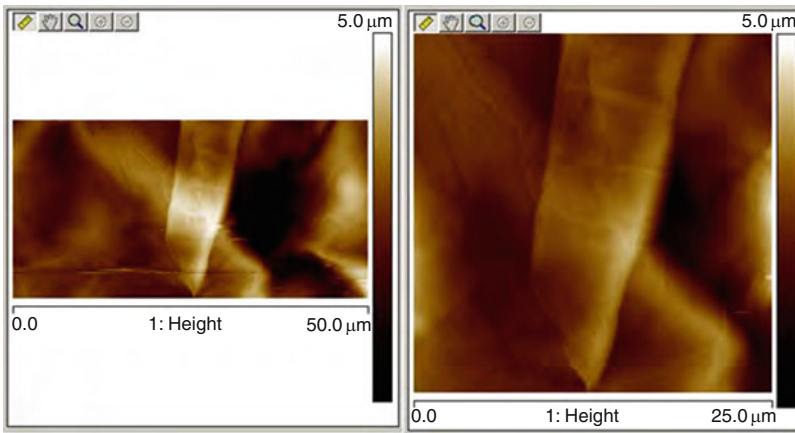
Fig. 16.27 AFM images with formations that resemble layers of corneocytes

16.3.4.2 Force–Distance Plots

Investigations on the topography of the stratum corneum were conducted using a rectangular tip with the Nanoscope V Bioscope 2 AFM (Veeco Instruments). Following the capture of the topography image, the 'point and shoot mode' of the AFM was used in order to investigate the mechanical properties of the stratum corneum epidermis.

'Point and shoot' is a new function of the Nanoscope V controller. By this function, force or tunnelling spectroscopy can be precisely located at any *XY* coordinate in an image, with a single click of the mouse. To operate this function,
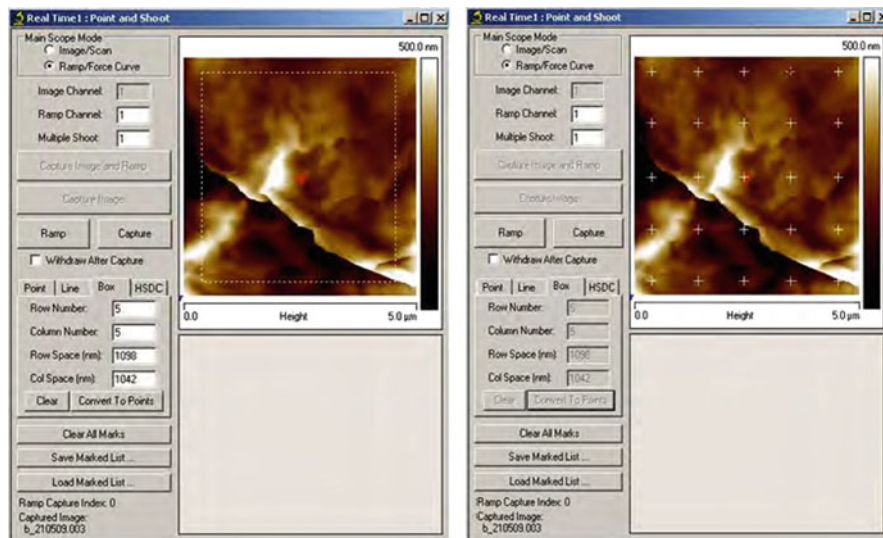
143

Fig. 16.28 'Point and shoot' selection on selected area of stratum corneum epidermis

some parameters should be set similar as is done in the normal force mode at the beginning. Then, clicking the mouse at the respective location marks points of interest. The tip ramps simultaneously. In Fig. 16.28, the area of interest for mechanical observation can be seen. Selecting different numbers for columns and rows for the selected area can change the amount of the points, and the AFM stores the force curve information for the selected points on the area. Each point can be selected afterwards to be represented on a scaled diagram to be observed or compared with each other. Two extreme points on the topography map have been carefully chosen to reveal the differences in the force plots (Fig. 16.29).

Significant differences were observed between the dark area and the bright areas. In the dark area, the force curve reaches a plateau that looks as if the force exerted by the probe was damped by a viscous material – this is assumed to be the first sign of phospholipids on the stratum corneum epidermis.

The test was repeated using the force-volume mode of the AFM. Force volume produces a 2-D array of force-distance measurements over a specified area to display images of force variations and topography along with individual force curves at any point.

Any point on the image acquired by AFM (Fig. 16.30) can be chosen for investigation, thanks to the abilities of force-volume mode. By reproducing the preceding point-wise analysis and by scanning the sample surface, a force-volume image $f(x, y, z)^1$ is obtained. This image is formed from the collection of force spectra $f(z)$ on a grid (x, y) representing the sample surface (Fig. 16.30) [43].

It can be seen that the aforementioned plateau on the force curves related to the selected point on dark area was observed. This shows the postulate is repeatable and
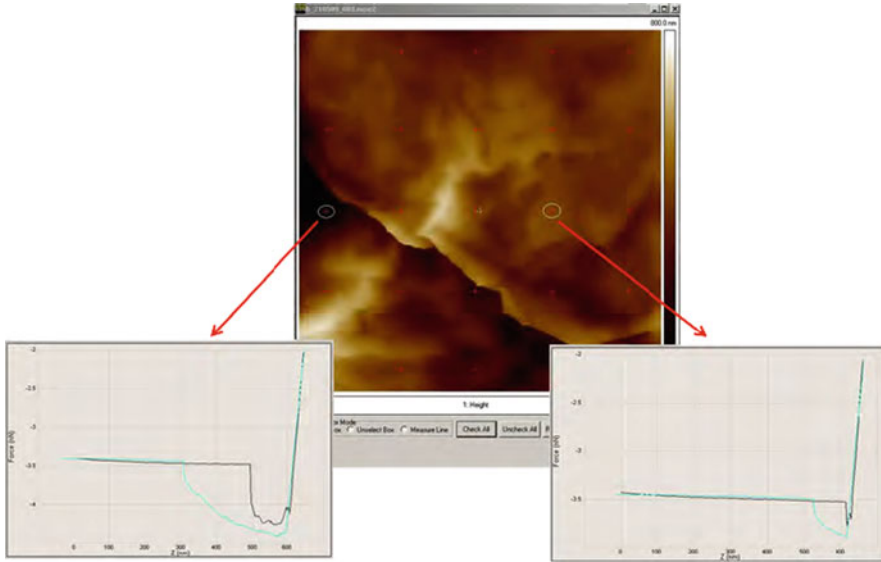
Fig. 16.29 Force curves stored for two different zones of stratum corneum

is a rational approach to have better understanding of the phospholipid distribution on the stratum corneum epidermis (Fig. 16.31).

The force curves provided by the force-volume test can be interpreted both in the approaching and retracting parts. The analysis of these two parts separately will give us a better understanding of topography and possible distribution of the phospholipid layers (Fig. 16.32).

Finally, the approach was tested one more time, this time not in order to test repeatability but to ensure that the system is navigable when the colloidal probe designed specifically for the friction measurements on the stratum corneum is used (Fig. 16.33).

No reportable issues have been experienced during the acquisition of the topography and lateral force images with the colloidal probe. The force-volume results gave a clear capture of the plateau on the force curve when the point is selected on the dark area (Fig. 16.34).

16.3.4.3 Friction Measurements

AFM is one of the most powerful techniques for the investigation of tribology and, in particular, of nanofriction [44]. An AFM can simultaneously acquire topographic and friction maps of surfaces, operating in the so-called friction force mode, with nanometre resolution. Friction force microscopy (FFM) is possible since the vertical and lateral deflections of the cantilever supporting the AFM tip can be acquired
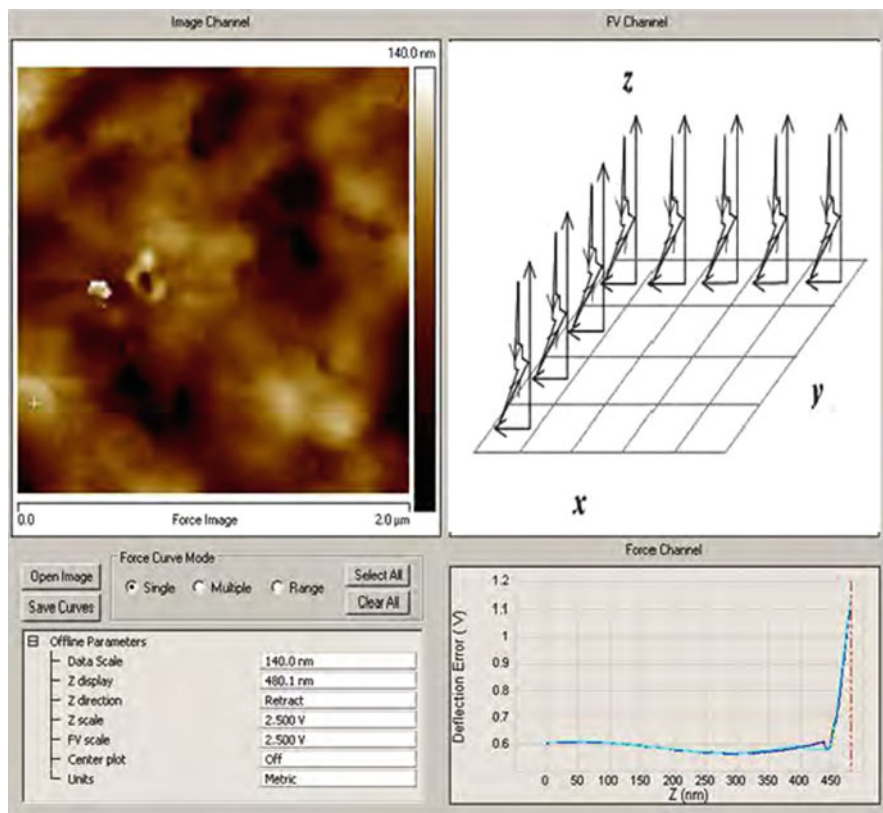
Fig. 16.30 Data acquired by AFM during force-volume measurements

simultaneously. The former are related to changes in the topography, while the latter are proportional to the friction force between the tip and the sample surface [45].

In order to perform quantitative nanofriction measurements, it is necessary to control and accurately measure both the magnitude and the direction of the forces acting on the AFM tip. However, because of the local tilt of the surface, forces acting on the tip can be different from those inferred using the standard reference frame of the laboratory. The effects of surface topography on nanofriction measurements have been studied, although a general theory is still lacking [46, 47].

Podestà et al. considered the topographic correction and inquired whether it was possible to follow a model-independent approach, providing the friction vs. load characteristics of the system under investigation without the need for postulating any particular contact-friction model [48]. They solved the problem of the topographic correction in the particular case of the adhesive multiasperity contact, which is common in many experimental setups. To this purpose, they introduced a modified version of Amonton's law for friction [49] (linear dependence of friction on load) that should better apply to the case of low loads and few asperities in contact.
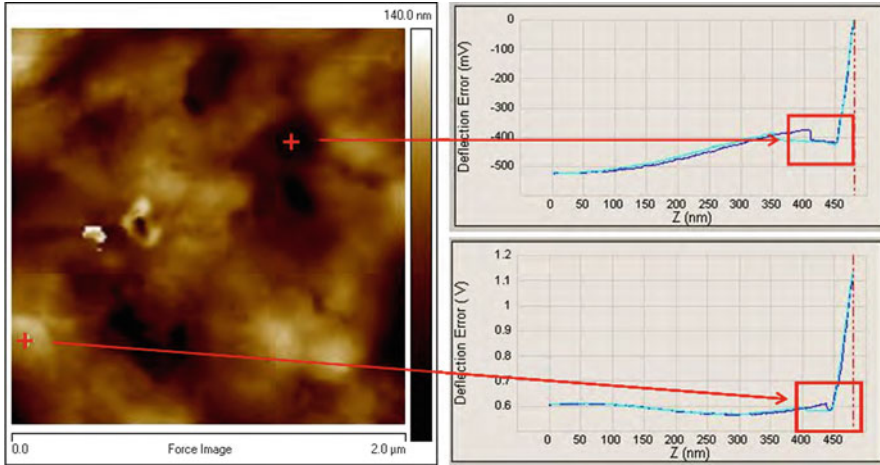
Fig. 16.31 Selected points on the image acquired during force-volume mode
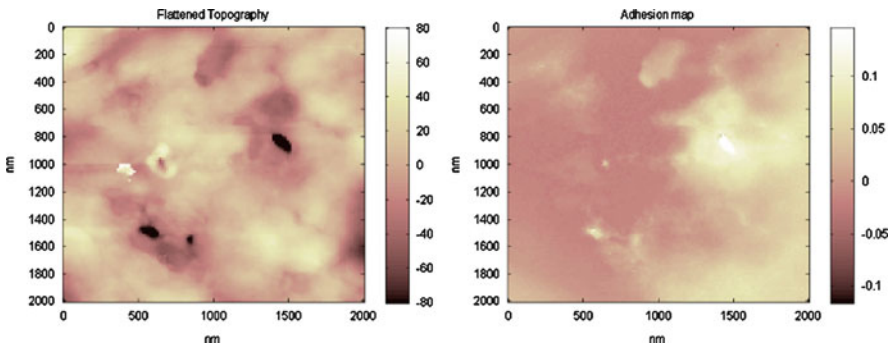

Fig. 16.32 Images of the topography and adhesion maps of the force-volume application (Fig. 16.30)

On the basis of this model, they discuss the mechanisms, which determine the appearance of the experimentally acquired lateral force maps. Note the importance of topographic correction for corrugated samples. They present their topographic correction procedure in the framework of a complete quantitative statistical protocol based on AFM for the characterization of frictional properties of materials at the submicrometer scale and show the results of the application of the protocol used in this chapter to different materials. Stratum corneum fits the sample definition for the method introduced above.

Three different zones were selected for the frictions measurements. No phospholipid interaction is expected in the selected areas, and decent force curves can be achieved (Fig. 16.35).
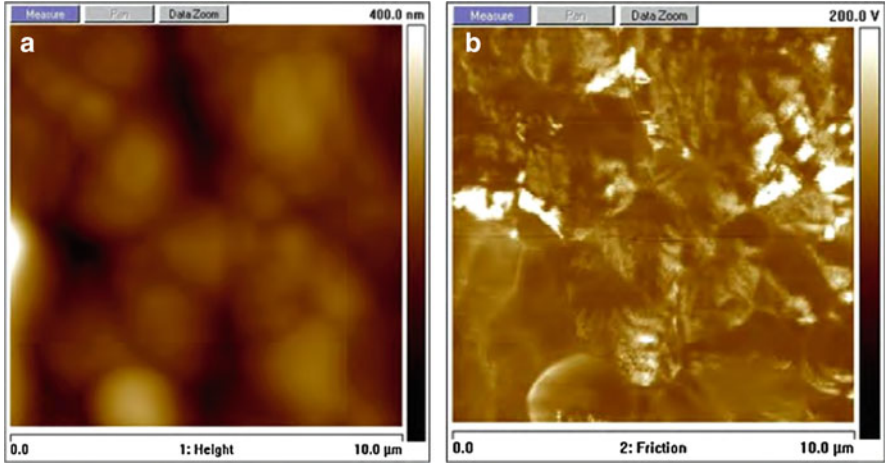
Fig. 16.33 (**a**) Topography. (**b**) Subtracted lateral force images of stratum corneum, acquired with the colloidal probe
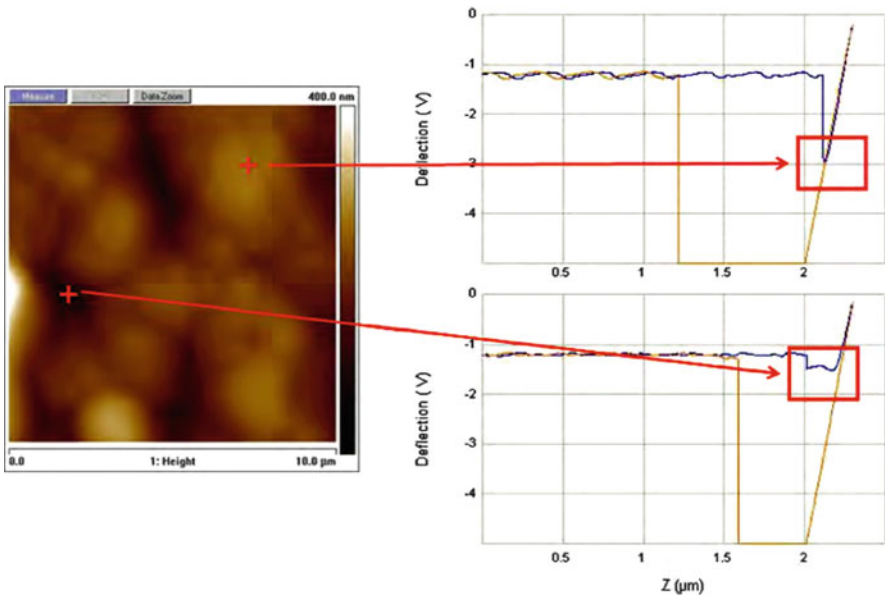

Fig. 16.34 Observation of the plateau on the images acquired by the AFM using the colloidal probe

Friction varies considerably in 1.1-μm $\times$ 1.1-μm areas selected from a 10-μm $\times$ 10-μm area: In some areas, 0.025 ± 0.002 is measured, in others, the maximum value is 0.006 (Fig. 16.36). The small coefficient of friction might be due to lipids
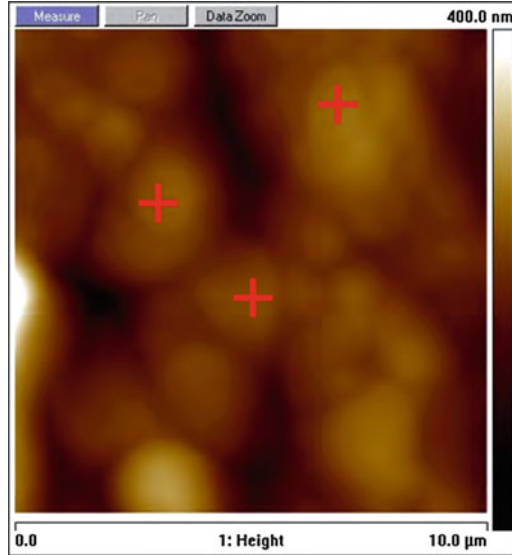
148

Fig. 16.35 Selected areas for friction measurements

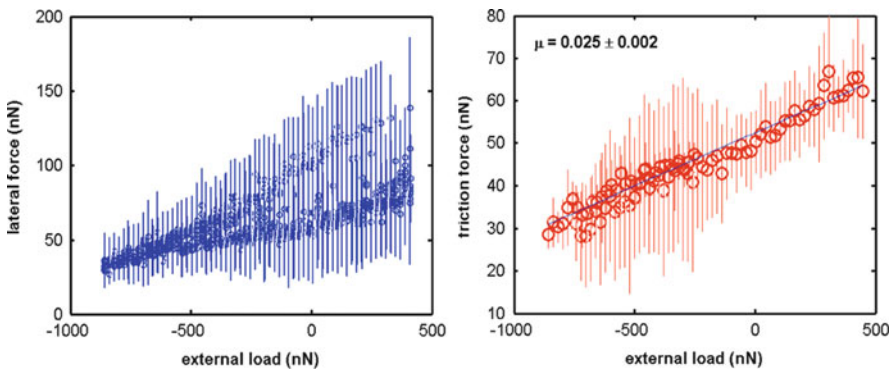**Fig. 16.36** (**a**) Double trend in friction measurements. (**b**) Overlapping trend in two different areas

acting as lubricants. Topography and adhesion maps of such areas reveal that human skin exhibits significantly different phases on the micrometer scale (Fig. 16.37).

16.3.4.4 Further Applications

The tests in this section were conducted in environmental conditions with 25°C temperature and 42.5% of relative humidity. Stratum corneum epidermis was also tested in a chamber with nitrogen flux providing dry conditions (RH: 0–5%) and with nitrogen and water flux providing wet conditions (RH: 90–95%) to better
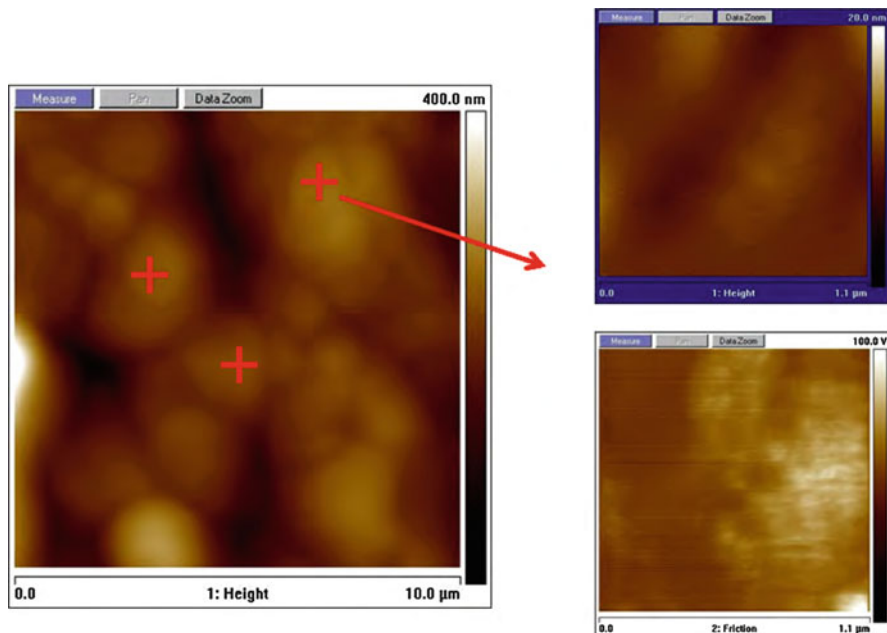
Fig. 16.37 Topography and subtracted lateral force images of an area selected for friction measurements

understand the effects of environmental conditions and to observe contact area dependence related to colloidal probes of different sizes.

16.3.5   Staining Experiments Related to the Interactions Between Contact Lenses and Ocular Tissues

16.3.5.1   Topography

Calibration tests of the system were performed on the endothelium biomimic, DSM-PTG CarboSil® 40 90A (biocompatible silicone polycarbonate urethane). CarboSil® combines the biocompatibility and biostability of conventional silicone elastomers with the processability and toughness of thermoplastic polycarbonate urethane (TPU).

The system allowed for repeatable and stable imaging, thereby encouraging continuing experiments on the cellular level (Fig. 16.38).

When the test was repeated with 1.2 and 2.0 mN, wear tracks with a width of 277 and 352 μm were observed (Fig. 16.39).
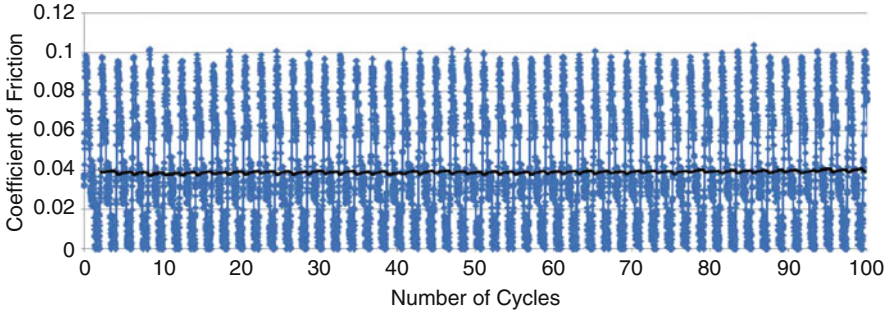
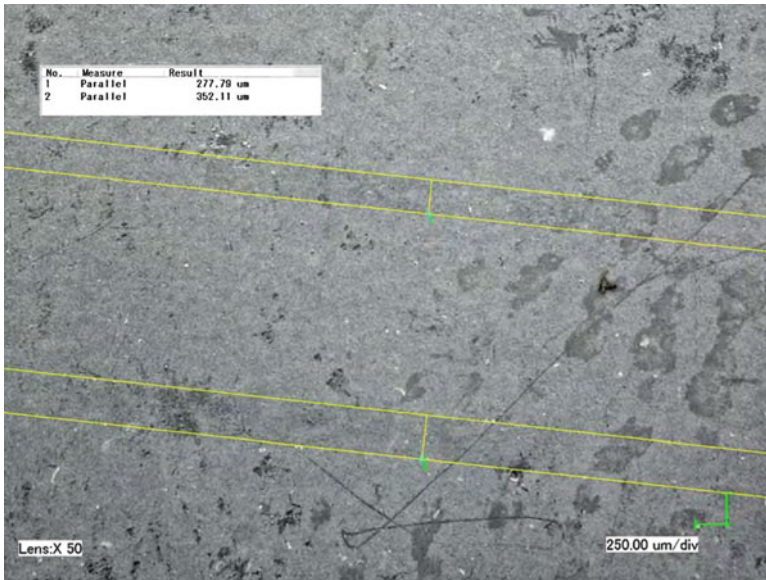**Fig. 16.38** Stable signal during 100 strokes

Fig. 16.39 Wear tracks recorded by optical microscopy related to the MTT tests with normal force values of 1.2 and 2.0 mN

If we consider constant contact pressure for both tests, we would expect

$$F_1/F_2 = (w_1)^2/(w_2)^2 \rightarrow (1.2)/(2.0) = 0.6 \approx 0.62 = (277.79)^2/(352.11)^2$$

The values are in good agreement with each other, yielding 20.55 kPa as first assumption of the contact pressure.

Further tests were conducted on HT-1080 muscle cells, derived from mouse uterus. These cells are selected for the tests due to their classification as Biosafety Level 1, significant resemblance with human samples, strong adherence to selected petri dishes and immortality ratios.
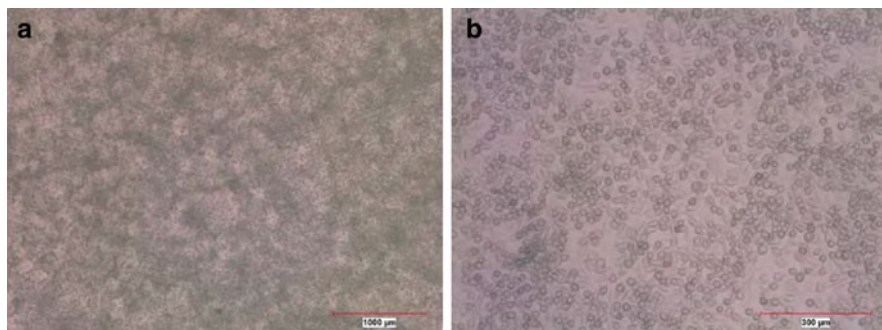
Fig. 16.40 Cultured HT-1080 muscle cells under the optical microscope. (**a**) Scale bar 1,000 μm and (**b**) scale bar 300 μm
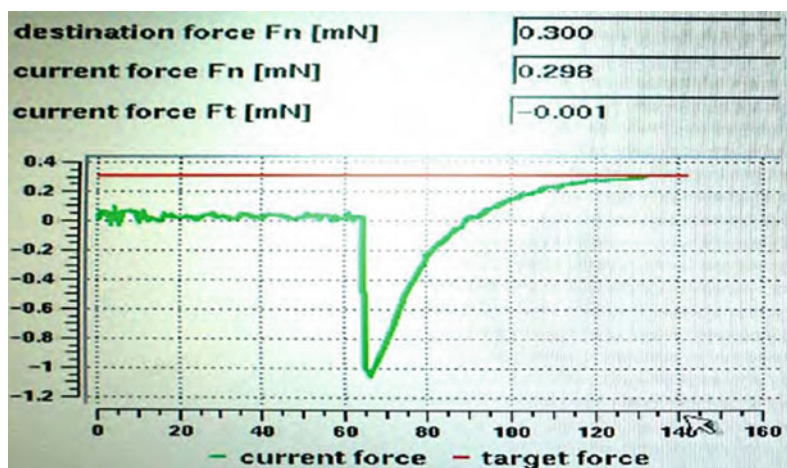
Fig. 16.41 Force curve recorded during the approach of the tip to the cell line surface with a target force (F_t) of 300 mN

The morphology of the muscle cells, cultured on Corning® culture dishes, represents pseudostratified simple epithelium properties that are similar to examples of liquid lubricant interfaces and sufficient to conduct the tribological tests (Fig. 16.40).

16.3.5.2   Force–Distance Plots

The force–distance plots acquired during the tests with the Falex MUST MTT revealed the issue concerning the meniscus and the tare force described in Sect. 16.2.3.3. In Fig. 16.41, a strong meniscus force of 1 mN can be observed during the approach of the tip to the cell lines.

Fig. 16.42 Complete wipe of cells under the exerted normal load of 1.3 mN. Scale bar 1,000 μm

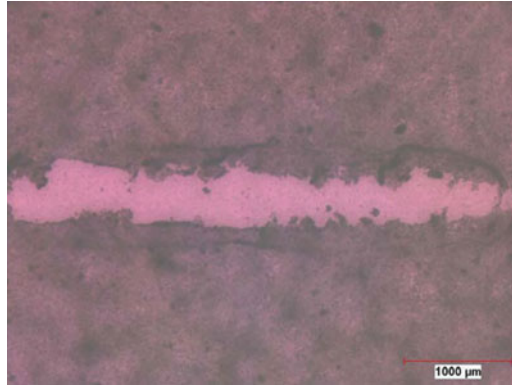The reason that the TARE function does not work after the tip totally dipped in to the buffer solution is that the meniscus force F_m is exerted in opposite direction to the forces that are recorded by the sensor as a result of the deflection of the cantilever. So the minus values of the deflection of the cantilever due to the pulling effect by the meniscus would not be nullified. In this case, the total force F_T exerted on the cell lines is

$$F_T = F_t + F_m = 0.3 + 1 = 1.3 \text{ mN}$$

This value of exerted normal load on cells is exceeding the adherence forces between the cells and the petri dishes, leading to complete wipe of the cells through the wear track (Fig. 16.42).

Subsequent to a software update on Falex MUST MTT, the total forces on both directions could have been tared to zero, and the actual value of the target force became the total force exerted on the cell lines. Proper friction measurements could be conducted and will be reported in the following section.

16.3.5.3 Friction Measurements

The initial tests conducted on HT-1080 muscle cells with a normal load of 0.3 mN show a partially stripped wear track (50–70% cell coverage) (Fig. 16.43a).

The probe velocity was 0.1 mm/s with a 3-mm single stroke. Results represent a stable friction force and similar coefficient of friction values for the first and the second pass of the stroke. This leads to the conclusion that insignificant or negligible ploughing occurs during the tests (Fig. 16.43b).

In Fig. 16.44, a slight deviation in the normal load values of the test can be observed. This effect is expected due to the small inclination on the surface of the petri dishes. Even though very stable values of friction force and coefficient of friction are acquired, for further application, a petri dish specially certified for

153
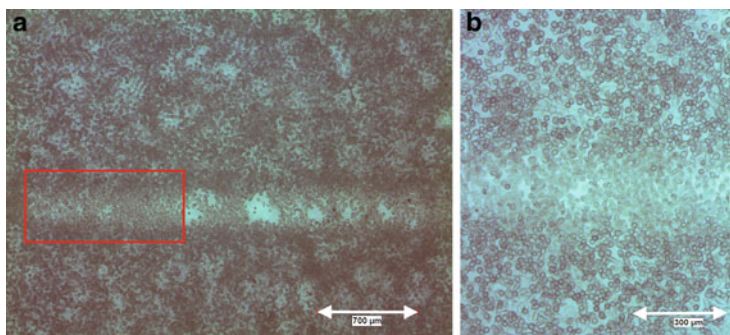
Fig. 16.43 (**a**) Partially stripped wear track on cell lines with normal load of 0.3 mN, scale bar 700 μm. (**b**) Zoom into the area marked with the red rectangle, scale bar 300 μm
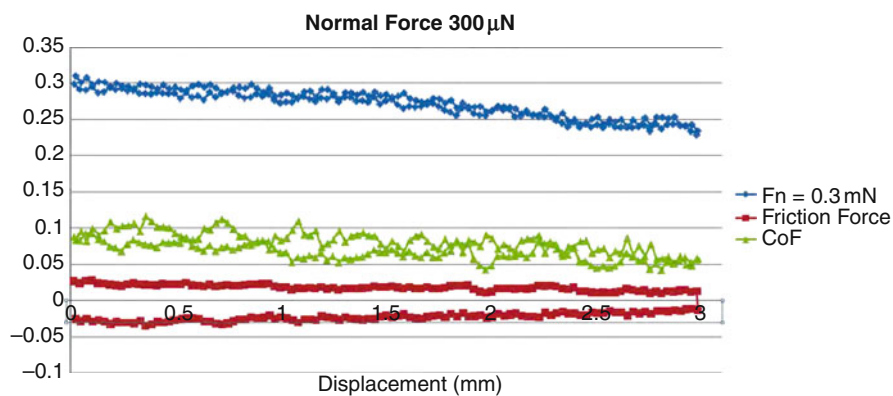
Fig. 16.44 Normal force, friction force and coefficient of friction values for the test with assigned total force of 0.3 mN

flatness values is advised. The test was repeated with varying normal force values of 0.2, 0.5 and 0.7 mN.

From the friction results of five consecutive tests (marked as red squares in Fig. 16.45) it can be seen that friction behaviour and cell response are very similar to the studies of Sawyer with the coefficient of friction values varying stably between 0.008 and 0.11 considering 70–100% cell coverage [50].

16.3.5.4 Further Applications

Following the success of the prototype universal experimental setup, the system was used for experiments on human corneal epithelium (HCE) after minor changes of the probe design. The general approach to the samples varies also due to the
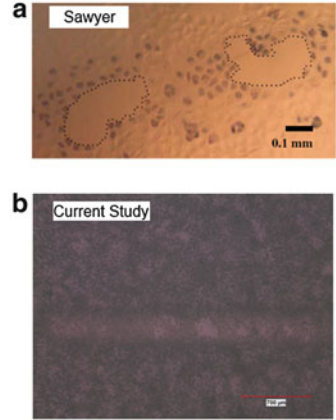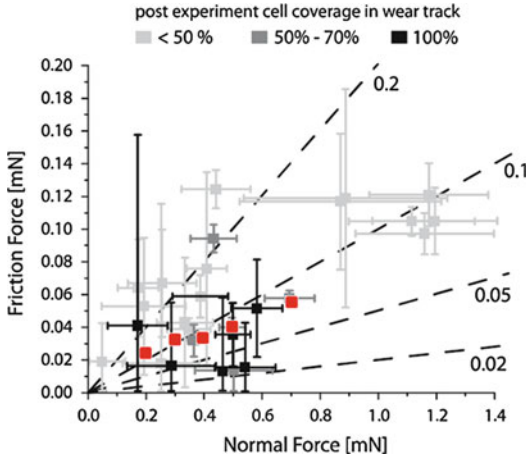
Fig. 16.45 Comparison of results (red squares: 70–100% cell coverage) with Sawyer [50, 51]
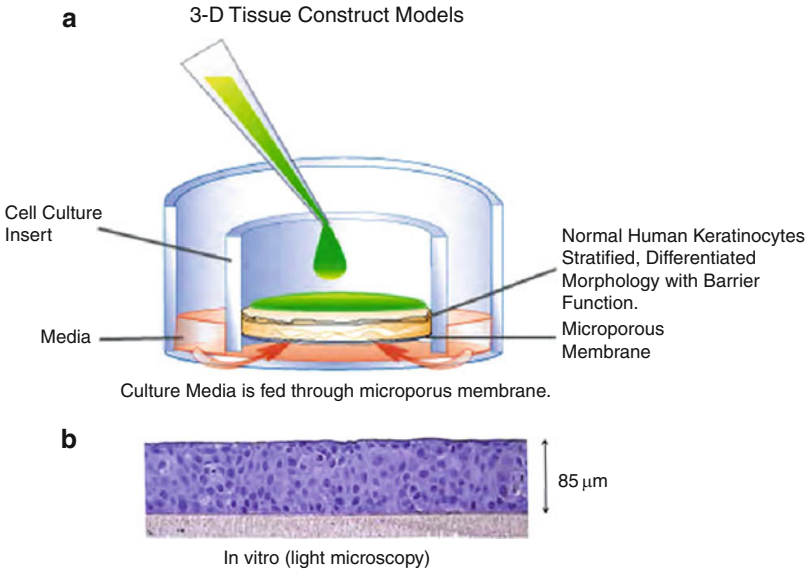
Fig. 16.46 (**a**) Sketch of the tissue construction model. (**b**) *In vitro* light microscopy image of the constructed tissue

classification of HCE as Biosafety Level 2. Final applications envisaged would be 3-D tissue construct models from pseudostratified cell lines (Fig. 16.46).

When cultivated at the air-liquid interface in a chemically defined medium, the immortalized human corneal epithelial cells from the cell line HCE reconstruct a corneal epithelial tissue (mucosa), devoid of stratum corneum, ultrastructurally

155

(tissue morphology and thickness) similar to the corneal mucosa of the human eye [52]. This construction would provide a more stabile base for the tests without sacrificing from the *in vitro* behaviour of actual human cornea. The tests would also be repeated for different kinds of contact lenses to evaluate efficiency and comfort of the products while reducing staining effect on the actual tissues. It is suggested to vary the tip diameter of the designed probe in order to investigate the contact area dependence of the system since the contact lenses are in touch with the corneal epithelia in more than one point, representing different models of contact.

16.4   Conclusion and Outlook: Bridging the Gap

In the sections above, measurements on two different kinds of surfaces were introduced. Chemisorbed monomolecular thin films of ethanolamines, ZnDDP tribofilms and hard coatings deposited by CVD or PVD were mainly investigated with scanning probe microscopy (atomic force microscopy, friction force microscopy) and angle-resolved photoelectron spectroscopy, whereas for the biomolecular layers, the methods of choice comprised scanning probe microscopy with a colloidal probe of several micrometres in diameter, a microtribometer, scanning electron microscopy and optical microscopy. The different questions asked in the respective studies require scientific investigations at different resolutions.

Scale effects need to be addressed when establishing tribological models across scales [53]. The type of instrument used depends on the questions that are addressed with the research. It is not always necessary (or even useful) to perform micro- or nanotribological investigations. Macrotribological investigations can give very useful general impressions of surfaces, without going too much into detail regarding distinct subparts. Certain indicators in macroscopic investigations allow for extrapolation to smaller scales – not in an exact way, of course, but in a timesaving way. Microtribological investigations yield important information concerning wear, surface fractures, the formation of structures between microscopic parts of the tribosystem and their boundaries (tensions, shears, rupture, deformation, etc.). On the nanoscale, molecular properties can be probed. Depending on the questions to answer, investigations on all three length scales (surfaces, clusters, molecules) might be necessary.

An interesting and challenging fact about tribology is that it is a systems science. Detailed understanding of a whole tribosystem is dependent on understanding of the connections, interdependences and single functionalities on all length scales of functionalities.

Due to increased specialization in science and engineering, many people work just in one small aspect of their respective field. Such specialists increasingly get to know their area better and better but in many cases have no time or think they have no reason to talk to specialists of related but slightly different fields. In the extreme, the specialist languages become too detailed, no joint language can be

reached across fields, and writings and oral presentations of authors only reach an audience coming from the same field.

If we are to understand tribosystems and to build models across scales that can perform the requirements we pose to models in science and technology, namely, to provide a way to predict the behaviour and performance of other, unrelated systems, knowledge transfer from one field of specialisation to the other needs to be ensured. Functionalities on the nanoscale influence functionalities on the microscale and subsequently on the macroscale. *What one hopes for is a unified approach to energy-dissipating systems that encompasses most tribological but also other phenomena, for example in biology and geology.* [54].

Three needs can be identified regarding successful development of such a unified approach to energy-dissipating systems: We need a joint language, a joint way of publishing results and joint seminars, workshops and conferences. Developing these three needs further results in a general concept concerning the future of scientific publications and ordering as well as accessing the knowledge of our time [55]. Currently, over-information in almost any field is a problem. Jack Sandweiss, editor of *Physical Review Letters*, stated in 2009 in an editorial address *For example, it is currently impossible for anyone to read all of Physical Review Letters or even to casually browse each issue*. [56]. Sandweiss refers to just one single journal!

Dynamic publications of variable length that use various types of multimedia with adaptive information content have been suggested [55]. One and the same paper would be accessible to readers from various backgrounds and areas of specialisation. In case more detailed information is needed, simple clicks on the links would expand the 'paper' in the direction(s) wanted. 'Recommendation agents' of the future could constrain information and thereby protect users from over-information by making the number of recommendations a function of the user's ability and readiness information intake [55].

In this way, tribology generalists would emerge; people who ensure knowledge transfer from one area of specialisation to the other – contributing to a sound foundation to establish a unified approach to energy-dissipating systems across scales.

References

1. J.A. Greenwood, J.B.P. Williamson, Contact of nominally flat surfaces, Proc. Roy. Soc. Lond. **A295**, 300–319 (1966)
2. D. Tabor, Junction growth in metallic friction, Proc. Roy. Soc. Lond. **A259**, 378–393 (1959)

3. G.W. Stachowiak, A.W. Batchelor, in *Engineering Tribology*, 2nd edn. (Butterworth-Heinemann, Boston, 2001)

4. B. Bhushan, in *Handbook of Nanotechnology*, 2nd edn. (Springer, Berlin, 2003)

5. S. Bec, A. Tonck, J.M. Georges, R.C. Coy, J.C. Bell, G.W. Roper, A relationship between mechanical properties and structures of zinc dithiophosphate anti-wear films, Proc. Roy. Soc. Lon. **455**, 4181–4203 (1999)

6. P.A. Willermet, D.P. Dailey, R.O. Carter, P.J. Schmitz, W. Zhu, Mechanism of formation of antiwear films from zinc dialkyldithiophosphates, Tribol. Int. **28**(3), 177–187 (1995)

7. H. Spedding, R.C. Watkins, Antiwear mechanism of ZDDP's—1, Tribol. Int. **15**(1), 9–12 (1982)

8. G.M. Bancroft, M. Kasrai, M. Fuller, Z. Yin, Mechanism of tribochemical film formation: Stability of tribo- and thermally-generated ZDDP films, Tribol. Lett. **3**, 47–51 (1997)

9. P.A. Willermet, D.P. Dailey, R.O. Carter III, P.J. Schmitz, W. Zhu, J.C. Bell, D. Park, The composition of lubricant-derived surface layers formed in a lubricated cam/tappet contact II. Effects of adding overbased detergent and dispersant to a simple ZDTP solution, Tribol. Int. **28**, 163–175 (1995)

10. J.S. Sheasby, Z. Nisenholz Rafael, Antiwear characteristics of a commercial secondary ZDDP additives, Tribol. Transact. **36**, 399–401 (1933)

11. J.F. Graham, C. McCague, P.R. Norton, Topography and nanomechanical properties of tribochemical films derived from zinc dialkyl and diaryl dithiophosphates, Tribol. Lett. **6**, 149–157 (1999)

12. B. Bhushan, in *Modern Tribology Handbook*. Material Coatings, and Industrial Applications, Vol. 2, 1st edn. (CRC Press LLC, Boca Raton, 2001)

13. M. Marieb, *Human Anatomy and Physiology*, 3rd edn. (Benjamin/Cummings, Redwood City, 1995)

14. J.A. Eurell, B.L. Frappier, *Dellmann's Textbook of Veterinary Histology*, 6th edn. (Wiley/Blackwell, Ames, 2006)

15. W. Ming, *Lasik Vision Correction* (Med World Publishing, Provo, 2000)

16. H. Kawano, H. Yasue, A. Kitagawa, N. Hirai, T. Yoshida, H. Soejima, S. Miyamoto, M. Nakano, H. Ogawa, Dehydroepiandrosterone supplementation improves endothelial function and insulin sensitivity in men, J. Clin. Endocrinol. Metab. **88**, 3190–3195 (2003)

17. O. Marti, J. Colchero, J. Mlynek, Nanosources and manipulation of atoms under high fields and temperatures, Nanotechnology **1**, 253–260 (1991)

18. G. Mayer, N.M. Amer, Simultaneous measurement of lateral and normal forces with an optical-beam-deflection atomic force microscope, Appl. Phys. Lett. **57**(20), 2089–2095 (1990)

19. B. Bhushan, *Nanotribology and Nanomechanics—An Introduction*, 2nd edn. (Springer, Berlin, 2005)

20. B.D. Beake, I.U. Hassan, C.A. Rego, W. Ahmed, Friction force microscopy study of diamond films modified by a glow discharge treatment, Diamond Rel. Mat. **9**, 1421–1429 (2000)

21. D.F. Ogletree, R.W. Carpick, M. Salmeron, Calibration of frictional forces in atomic force microscopy, Rev. Sci. Instrum. **67**(9), 3298–3306 (1996)

22. E. Tocha, H. Schonherr, G. Vancso, Calibration of frictional forces in atomic force microscopy, Langmuir **22**(5), 2340–2350 (2006)

23. M. Indrieri, A. Podestà, G. Bongiorno, D. Marchesi, P. Milani, Adhesive-free colloidal probes for nanoscale force measurements: Production and characterization, Rev. Sci. Instrum. **82**, 023708 (2011)

24. H. Oechsner (ed.), *Thin Film and Depth Profile Analysis*. Topics in Current Physics, Vol. 37 (Springer, Berlin, Heidelberg, New York, Tokyo, 1984)

25. R. Behrisch (ed.), *Sputtering by Particle Bombardment*. Topics in Applied Physics, Vol. 47 (Springer, Berlin, 1981)

26. A. Tomala, C.A. Vasko, N. Dörr, H. Störi, I.C. Gebeshuber, Oligomer specific lubrication, *Proceedings of the 34th Leeds-Lyon Symposium on Tribology*, Vol. 30, Lyon, 2007, pp. 2–3

27. A. Tomala, W.S.M. Werner, I.C. Gebeshuber, N. Dörr, H. Störi, Tribochemistry of monomolecular lubricant films of ethanolamine oligomers, Tribol. Int. **42**, 1513–1518 (2009)

28. A. Tomala, A. Naveira-Suarez, R. Pasaribu, N. Doerr, W.S.M. Werner, H. Stoeri, Behavior of corrosion inhibitors under different tribological contact, Tribol. Lett. **45**, 397–409 (2012)

29. A. Naveira-Suarez, A. Tomala, R. Pasaribu, R. Larsson, I.C. Gebeshuber, Evolution of ZDDP-derived reaction layer morphology with rubbing time, Scanning **31**, 1–10 (2010)

30. H. Fujita, H.A. Spikes, The formation of zinc dithiophosphate antiwear films, Proc. Inst. Mech. Eng. Part J J. Eng. Tribol. **218**(4), 265–277 (2004).

31. A. Naveira-Suarez, A. Tomala, M. Grahn, M. Zaccheddu, R. Pasaribu, R. Larsson, The influence of base oil polarity and slide-roll ratio on additive-derived reaction layer formation, Proc. Inst. Mech. Eng. Part J J. Eng. Tribol. **225**(7), 565–576 (2011)

32. M. Aktary, M.T. McDermott, G.A. McAlpine, Morphology and nanomechanical properties of ZDDP antiwear films as a function of tribological contact time, Tribol. Lett. **12**(3), 155–162 (2002)

33. K.A. Dean, B.R. Chalamala, Current saturation mechanisms in carbon nanotube field emitters, Appl. Phys. Lett. **76**, 375 (2000)

34. T. Zehnder, J. Patscheider, Nanocomposite TiC/a-C:H hard coatings. Deposited by reactive PVD, Surf. Coat. Technol. **138**, 133–134 (2000)

35. L.C. Wu, K. Miyoshi, R. Vuppuladhadium, H.E. Jackson, Physical and tribological properties of rapid thermal annealed diamond-like carbon films, Surf. Coat. Technol. **54–55**, 576–580 (1992)

36. R. Haubner, B. Lux, Diamond growth by hot-filament CVD: State of the art, Diamond Rel. Mat. **2**, 1277–1294 (1993)

37. K. Miyoshi, R.L.C. Wu, A. Garscadden, Friction and wear of diamond and diamondlike carbon coatings, Surf. Coat. Technol. **54/55**, 428–434 (1992)

38. J. Robertson, Diamond-like amorphous carbon, Mat. Sci. Eng. **R37**, 129–281 (2002)

39. P. Ovaere, S. Lippens, P. Vandenabeele, W. Declercq, The emerging roles of serine protease cascades in the epidermis, Trends Biochem. Sci. **34**(9), 453–463 (2009)

40. M. Haftek, S. Callejon, Y. Sandjeu, K. Padois, F. Falson, F. Pirot, P. Portes, F. Demarne, V. Jannin, Compartmentalization of the human stratum corneum by persistent tight junction-like structures, Exp. Dermatol. **20**(8), 617–621 (2011)

41. T. Igarashi, K. Nishino, S.K. Nayar, The appearance of the human skin: A survey, Found. Trends Comp. Graph. Vis. **3**(1), 1–95 (2007)

42. I.H. Blank, D.J. McAuliffe, Penetration of benzene through human skin, J. Invest. Dermatol. **85**, 522–526 (1985)

43. C. Soussen, D. Brie, C. Goboriaud, C. Kessler, Modelling of force volume images in atomic force microscopy, in *5th IEEE International Symposium on Biomedical Imaging: From Nano to Macro*, IEEE, Paris, 2008, pp. 1605–1608

44. B. Bhushan, in *Handbook of Micro and Nano Tribology* (CRC Press, Boca Raton, 1999)

45. G. Meyer, N.M. Amer, Simultaneous measurement of lateral and normal forces with an optical—beam—deflection atomic force microscope, Appl. Phys. Lett. **57**(20), 2089–2091 (1990)

46. M. Labardi, M. Allegrini, M. Salerno, C. Frediani, C. Ascoli, Dynamical friction coefficient maps using a scanning force and friction microscope, Appl. Phys. A Solids Surf. **59**, 3–10 (1994)

47. S. Sundararajan, B. Bushan, Topography-induced contributions to friction forces measured using an atomic force/friction force microscope, J. Appl. Phys. **88**, 4825 (2000)

48. A. Podestà, G. Fantoni, P. Milani, Quantitative nanofriction characterization of corrugated surfaces by atomic force microscopy, Rev. Sci. Instrum. **75**(5), 1228–1241 (2004)

49. F. Bowden, D. Tabor, in *The Friction and Lubrication of Solids* (Clarendon, Oxford, 1950)

50. A.C. Dunn, T.D. Zaveri, B.G. Keselowsky, W.G. Sawyer, Macroscopic friction coefficient measurements on living endothelial cells, Tribol. Lett. **27**, 233–238 (2007)

51. J.A. Cobb, A.C. Dunn, J. Kwon, M. Sarntinoranont, W.G. Sawyer, R. Tran-Son-Tay, A novel method for low load friction testing on living cells, Biotechnol. Lett. **30**, 801–806 (2008)

52. F.H. Kruszewski, T.L. Walker, L.C. Dipasquale, Evaluation of a human corneal epithelial cell line as an in vitro model for assessing ocular irritation, Toxicol. Sci. **36**(2), 130–140 (1997)

53. B. Bhushan, M. Nosonovsky, Scale effects in mechanical properties and tribology, in *Nanotribology and Nanomechanics—An Introduction*, 2nd edn., ed. by B. Bhushan (Springer, Berlin, 2008), pp. 791–840
54. M. Urbakh, J. Klafter, D. Gourdon, J. Israelachvili, The nonlinear nature of friction, Nature **430**, 525–528 (2004)
55. I.C. Gebeshuber, B.Y. Majlis, New ways of scientific publishing and accessing human knowledge inspired by transdisciplinary approaches, Tribol. Surf. Mat. Interf. **4**(3), 143–151 (2010)
56. J. Sandweiss, Essay: The future of scientific publishing, Phys. Rev. Lett. **102**(19), 190001(2p) (2009)

PAPER II

A simple cornea model for the tribological performance assessment of the lubricating eye drops

Hakan Göcerler and Simon Medina
Department of Tribology, TU Wien Institute of Engineering Design and Product Development, Wien, Austria

Michael Adler and Josef Brenner
AC2T Research GmbH, Wiener Neustadt, Austria, and

Andreas Tadler, Michael Nagl and Christine Hohenadl
Croma-Pharma GmbH, Leobendorf, Austria

Abstract

Purpose – Dry eye syndrome is one of the most common reasons for eye-related discomfort which, without treatment, in some cases may even lead to corneal damage. Blinking, baseline and reflex lachrymation and drainage compromise the topical application of therapeutics demanding repeated, often hourly applications of common lubricants. In contrast, topically administered chitosan-N-acetylcysteine-based eye drops were reported to sustain on the ocular surface for more than 24 h. The thiolated biopolymer can interact with the corneal mucin layer thereby forming covalent disulphide bridges, which may contribute to extended residence times.

Design/methodology/approach – In this study, the tribological characteristics of four different lubricants including hyaluronic acid and chitosan-N-acetylcysteine containing commercially available eye drops were investigated. For this purpose, a representative test setup was developed, which mimics the contact between the cornea and the eyelid wiper. Gels with different elastic properties coated with a mucin layer were used as a substrate to mimic the corneal surface. Tests were conducted with a micro-tribometer, and friction values were recorded. Contact zones were characterized by X-ray photoelectron spectroscopy to investigate wear and thiol bonding on the surface.

Findings – Results revealed the lowest average coefficient of friction values for chitosan-N-acetylcysteine-based eye drops and substrate dependence of the test setup.

Originality/value – In this study, the authors introduced an in vitro system to test different types of eye drops so that chemical interaction with the mucin layer can be observed. These interactions change the tribological performance significantly and must be considered to have results relevant to the actual application.

Keywords Biotribology, Biomimetic, Cornea, Eye drops, Tribometry

Paper type Research paper

1. Introduction

Dry eye syndrome (DES) is a multifactorial disease of the ocular surface characterized by a loss of homeostasis of the tear film. Eventually the disease makes the eye vulnerable to external stimuli and inflammation (Thulasi and Djalilian, 2017; Ludwig, 2005). A new treatment approach involves the use of chitosan–N-acetylcysteine-based eye drops (C-NAC-BED). These eye drops lead to the formation of a long-lasting, mucoadhesive protective layer on the surface of the cornea (Fischak *et al.*, 2017). C-NAC-BEDs were accordingly approved in Europe as a class III medical device for alleviation of DES symptoms.

Blinking, baseline and reflex lachrymation and drainage compromise the topical application of therapeutics, demanding repeated, often hourly applications of common lubricants. Topically administered C-NAC-BED, however, were reported to sustain on the ocular surface for more than 24 h. This indicates distinct tribological properties of the thiolated chitosan functioning as a lubricant between the eyelid and the cornea, which have not yet been investigated.

To evaluate the mechano-chemical behavior of chitosan-N-acetylcysteine, it was crucial to define the mechanical properties of the model substrate to be used in tribological tests.

The first step was to create a substrate mimicking the ocular mucins, which structure themselves in a gradient from a solute in the aqueous tear film to a gel on the corneal surface, with accurate Young's modulus. Young's modulus (elastic modulus) is a material property and is a measure of the ability of a material to withstand changes in length when under lengthwise tension or compression. Reported values for Young's modulus of the cornea exhibit a considerable variation due to different measurement techniques. A simulation model of an eyeball based on finite element analysis suggested 20 kPa for retina (Wu *et al.*, 2013), and biomechanical studies of a fluid-filled spherical shell model with Scheimpflug imaging calculated values between 54–359 kPa for the cornea (Shih *et al.*, 2017). Studying compliance profiles of the human cornea using atomic force microscopy (AFM) focused on different layers of the cornea and obtained values of 7.5 ± 4.2 kPa (anterior basement membrane), 109.8 ± 13.2 kPa (Bowman's layer), 33.1 ± 6.1 kPa (anterior stroma) and 50 ± 17.8 kPa (Descemet's membrane) (Last *et al.*, 2012). In vivo determinations of Young's modulus for the human corneal basement membranes using AFM also reveal values of 25 ± 7 kPa (Last *et al.*, 2009). The corneal epithelial cell response to the substrate stiffness was underlined by using polyacrylamide substrates with different elastic moduli (Molladavoodi *et al.*, 2014). Also, it is observed that Young's modulus of the anterior corneal stroma is altered with the initiation of oedema and inflammation (Raghunatan *et al.*, 2017). In this study, we designed two types of gels with the same composition but different Young's modulus values (18 kPa and 36 kPa) to simulate the mucin layer and to establish the interaction of the mucin layer and chitosan-N-acetylcysteine. By this means we should be able to observe differences in the coefficient of friction (COF) values, not only due to different solutions but also due to different grades of stiffness of the substrate.

Another critical parameter for tribological systems is the load to be applied. As seen with Young's modulus values, also the load applied onto the system within the literature varies within a broad range. Three possible models of eyelid contact with the pressure cell were introduced for eyelid pressure calculations: the eyelid contacts with the whole cell [Figure 1(A)], contact is over the imprint width determined by micro paper imprint [Figure 1(B)] and finally contact over Marx's line width determined by lissamine-green staining and digital imaging [Figure 1(C)] (Shaw *et al.*, 2010). In a whole cell contact the calculated eyelid pressure was as small as 0.3 kPa, whereas in Marx's line contact, this value was measured to be 18.6 kPa. We presume in an eye with DES, a whole cell contact could be observed rarely due to lack of tear fluid; thus, the maximum eyelid pressure should be considered for modelling a test system so that a contact system described in (Raghunatan *et al.*, 2017) is preferred [Figure 1(C)]. 12 kPa was calculated for the test system designed to measure COF values for murine cornea *in vivo* (Dunn *et al.*, 2013a). Normal load values between 10–50 mN were applied to observe COF values for soft contact lenses (Rennie *et al.*, 2005). Normal loading forces of 22.7 mN and 81.4 mN were applied, to observe differences between silicone hydrogel versus conventional hydrogel contact lenses (Ngai *et al.*, 2005). Finally, Aston Biomaterials Research Unit (ABRU) used assay standards with a load of 30 mN for tests on Hypotears^{TM} (Mann and Tighe, 2006). In our study, 20 mN normal load was applied to achieve 12 kPa pressure on the substrate, which is matching with eyelid pressure calculations and tests conducted in the literature. Of course, it should be expected that this value varies *in situ* due to personal health condition, age and gender of people (Rico-del-Viejo *et al.*, 2017). In this work, we consider most common and relatively high pressure values of Marx's line to evaluate the limits of C-NAC-BED.

Figure 1 Three possible models of eyelid contact with the pressure cell were introduced for eyelid pressure calculations (Shaw *et al.*, 2010)

A) "whole cell" eyelid pressure

B) "imprint width" eyelid pressure

C) "Marx's line" eyelid pressure

163
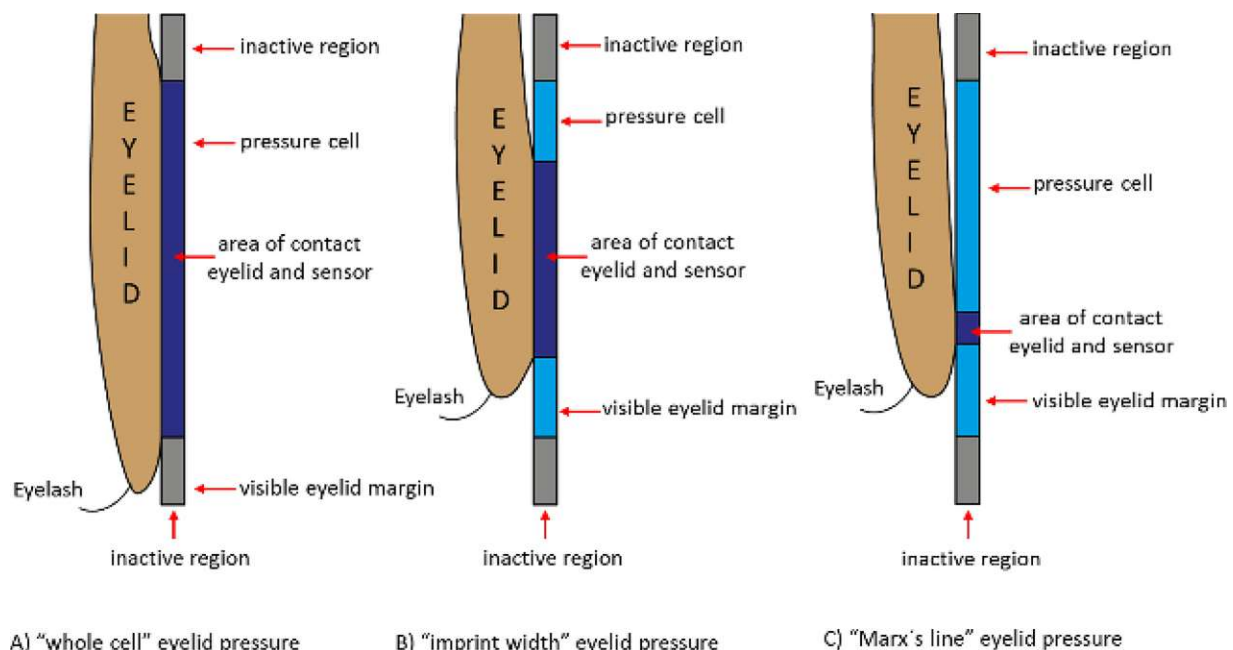
Even though the maximum velocity during a blink was reported as 300 mm/s (closing) and 100 mm/s (opening) (Jones *et al.*, 2008), the standard condition used at ABRU was 0.5 mm/s. In our study, a velocity of 2 mm/s was chosen to avoid additional vibrations and provide a stable translational movement for the micro-tribometer. We selected a stroke of 2 mm to observe the contact zone and to evaluate the tribological performance of the lubricative solutions.

Finally, to observe the described mucoadhesive properties of C-NAC-BED, chemical analysis was conducted using X-ray photoelectron spectroscopy (XPS). Bonded chitosan-N-acetylcysteine layers were investigated in the wear track following the tests.

2. Experimental details

2.1 Specimen preparation
The base body for the following tribological measurements consisted of petri dishes filled with stabilized (glutaraldehyde crosslinked) gelatine (platinum grade) in layers of different thickness ranging from 0.5 mm (generally higher hardness due to collapsing) to 3 mm (lower hardness). The gelatine surfaces were coated with a mucin layer (porcine stomach Type III, bound sialic acid 0.5–1.5%). After coating, the gelatine plate was washed five times with water for injection, and the integrity of the mucin layer was tested by alcian-blue staining.

Four different solutions were used as lubricants for the tribological tests, namely saline (0.9% NaCl w/w, denoted below as "NaCl"), chitosan-hydrochloride (1 mg/mL) in a physiological buffer system (denoted as "Placebo"), and the commercially available eye drops Lacrimera®, Croma-Pharma GmbH. ("C-NAC-BED", based on chitosan-N-acetylcysteine) and Hylo Comod®, Ursapharm GmbH. ("H-BED", based on hyaluronate). Basically "Placebo" is a solution of non-derivatized chitosan, identically buffered as C-NAC-BED. Prior to testing, each plate was pre-conditioned by soaking in a physiological sodium chloride solution. Two drops of each solution were applied onto the test zones, given 5 min of soaking time, and tests were conducted at room temperature with a 45% humidity level.

2.1.1 Determination of Young's modulus
Identification of Young's modulus (E) is crucial to evaluate contact conditions in tribological tests. Macro-indentation tests were conducted to calculate the E value of the gelatine hydrogel substrates (Figure 2) produced for the designed tribological system. In such a test, the surface is dented by a probe of defined shape while the required force is measured with a spring. The tribometer was also used as an indenter, using vertical instead of lateral movement. A 5 mm alumina oxide ceramic ball, identical to those used for tribological experiments, was used as an indentation probe (Figure 3). The indentation mode, based on the identified penetration depth and indentation speed, was used. A maximum penetration depth of 0.5 mm was selected to remain in the elastic range of the gels and to ensure that no rupture occurs in the mucin layer. The indentation speed was 0.01 mm/s, to avoid sudden changes due to the visco-elastic behavior of the gels.

The micro-tribometer (TETRA BASALT®-N2) recorded the deflection of the spring during the approach. The calibrated system then translated this data into the normal load values [Figures 4 and 5(a)]. Black dots on Figure 5(b) show the locations of the indentation tests (each plate once on each location); the Young's modulus was obtained by fitting the indentation force vs. indentation depth of the plate with an overlay of the theoretical force based on the Hertz model, as shown in equation (1) (Thomasy *et al.*, 2014) (Figure 4, dashed lines):

Equation (1): Force at indentation test

$$F = \frac{4}{3} * \frac{E}{(1 - v^2)} * \delta^{3/2} * R^{1/2}$$

where F is the force applied by the indenter, E is Young's modulus, v is Poisson's ratio, d is the indentation depth and R is the radius of the tip. Poisson's ratio of 0.49 is selected for evaluating material parameters of both the cornea and sclera in a numerical model (Śródka, 2011).

Elasticity modulus for the soft (not collapsed) and hard (collapsed) gel samples was calculated by iteration using the initial value given by Equation (1) as 18 kPa and 36 kPa, respectively.

2.2 Setup of tribological test
The tribometer used for indentation tests [Figure 5(a)] was used in translational mode for tribological tests. Similar tribometer installations have been used in ocular bio-tribology

Figure 2 Sample configuration, supporting gel layer poured into petri dish and coated with mucin layer
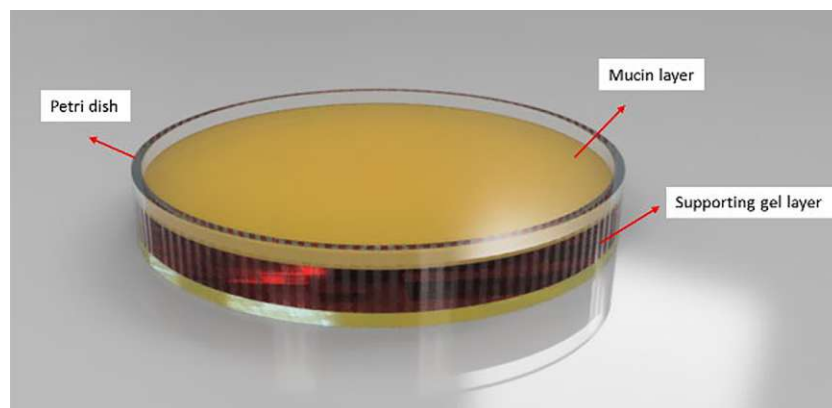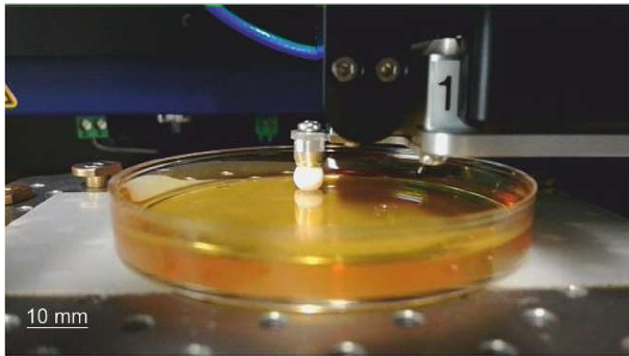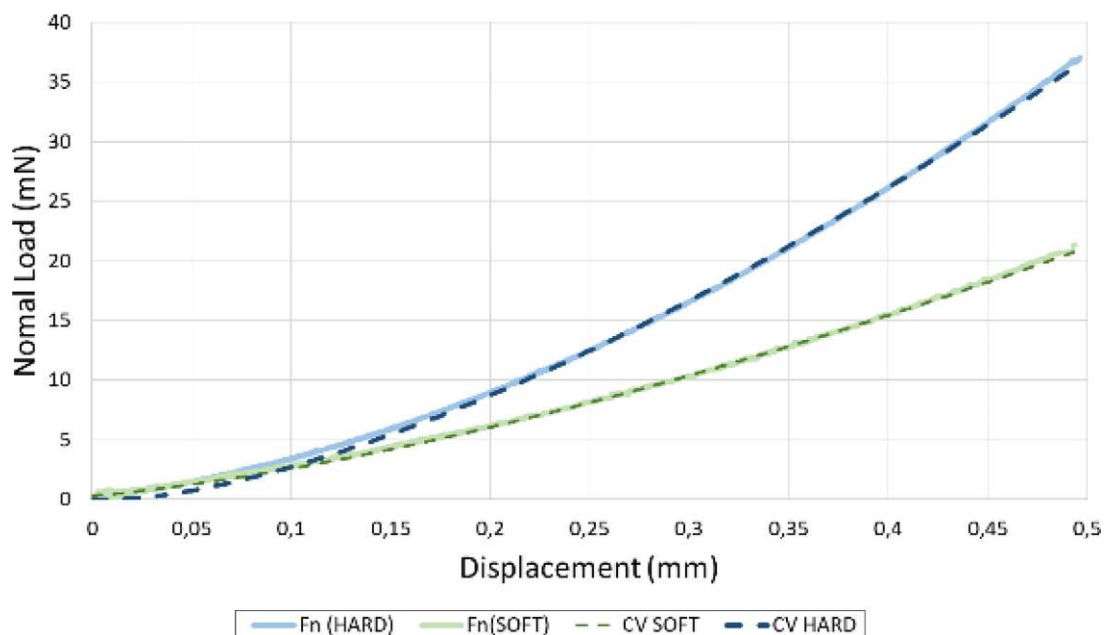
164

Figure 3 Image captured during the indentation test

(Urueña *et al.*, 2018; Samsom *et al.*, 2015; Colter *et al.*, 2017; Mollenhauer *et al.*, 2006) for measurements of the friction force between biological base bodies and several counter bodies. Due to relatively low applied load values (Fn ≤ 1 N), tribometers mentioned in these installations are called micro-tribometers.

Modules and sensors were selected according to the loading conditions and movement of the eye-eyelid system, as described in literature (Dunn *et al.*, 2013b; Sterner *et al.*, 2017; Cobb *et al.*, 2008; Tomala *et al.*, 2013).

Tribological tests were conducted on two types of coated hydrogel plates (soft and hard) with a normal load of 20 mN, a reciprocal motion at a frequency of 2 Hz and a stroke of 2 mm. All experiments were performed with 1000 cycles, on a total of eight different plates. Friction data is recorded via data acquisition software in TETRA BASALT®-N2 that captures 100 data points for each cycle and takes the average value discarding the acceleration and deceleration parts of the probe

movement. Eventually the average of 8 tests for each specimen on each substrate was taken for establishing the data for the friction values represented in Figures 7 and 8.

2.3 Surface chemistry determination X-ray photoelectron spectroscopy

XPS measurements were performed on a Theta Probe™ (Thermo Fisher Scientific) to investigate the presence of disulphide bonds confirming the binding of mucin with C-NAC or with itself and to document changes in surface chemistry due to tribological testing. A typical camera image inside the XPS chamber with the selected measurement position in a wear track (red lined area) is given in Figure 6 exemplarily for the sample "Placebo."

The X-ray source is a monochromatic Al K(alpha) source at 1386.6 eV. The spectrometer is calibrated to 368.21 eV binding energy (BE) of the Ag 3d5/2 line for metallic silver and the linearity is corrected to BE of metallic 932.62 eV for the Cu 2p3/2 line and 83.96 eV and Au 4f71/2. Charge compensation is done using a flood gun for low-energy electrons and argon ions at 1 eV. The binding energy of the corrected spectra are corrected to the main hydrocarbon peak of C1s at 284.6 eV BE.

The resolution of the X-ray spot was set to 50 μm for all measurements. The survey spectra were recorded with a pass energy of 200 eV BE and the detail spectra with a pass energy of 50 eV. The base pressure in the analytical chamber was $< 5^{*}10^{-8}$ Pa. Avantage v5.9915 (Thermo Fischer Scientific) was used to evaluate the XPS spectra. Peaks were fitted using a convolution of Lorentzian and Gaussian peak shapes. Binding states of elements detected were analyzed in reference to the NIST XPS database (NIST, 2012).

Figure 4 Force as function of displacement for soft (continuous light green) and hard (continuous light blue line) gelatine gels vs calculated value (CV) by iteration for each material (in dashed lines)

165

Figure 5 (a) Details of the capacitive sensor and ceramic probe attached on the spring of the tribometer and (b) Schematic presentation of a gelatine hydrogel plate with locations of applied solutions and performed tests (strokes)
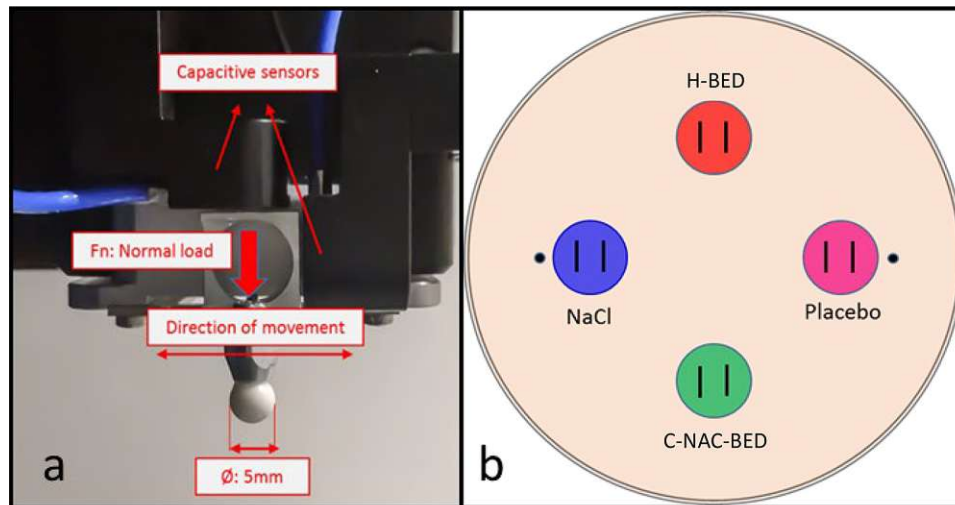
Notes: Dark dots represent positions of indentation tests

Figure 6 Camera image inside the XPS chamber to spot area of contact (red line)
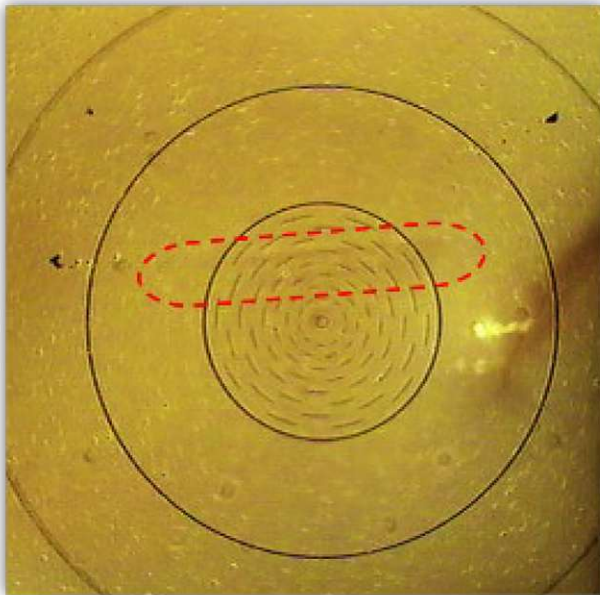
For the XPS analyses, samples were cut out with a scalpel to a size of approximately 5x5 mm^2. They were dried in four steps using ethanol of increasing concentration. The evacuation in the fast entry lock was performed for several days to maintain the vacuum performance in the analytical XPS chamber.

3. Results and discussion

3.1 Micro-tribometer tests

Tests were conducted in a rotational manner; each plate started with another solution and continued with the next solution counter clockwise [Figure 5(b)], to reduce the effect of drying for each solution. Results represent the average value of four repetitions for each sample. Average COF values calculated by averaging every data point for four tests per cycle show the same ranking for both soft and hard substrates. COF values for C-NAC-BED, H-BED, NaCl and Placebo are 0.32, 0.35, 0.37 and 0.40, respectively, for hard hydrogels (Figure 7).

A slight increase in average COF was observed for soft hydrogel substrates. COF for C-NAC-BED increased to 0.37, for H-BED to 0.40, NaCl to 0.45 and for the Placebo to 0.47 (Figure 8). The ranking among the test solutions did not change. Differences are possibly due to a larger area of interaction that is expected with the greater surface conformity of softer gels. Similar observation reported for the effect of dwell time in creeping elastic-plastic polymers (Malamut *et al.*, 2009) and articular cartilages that was reinforced with tissue-interpenetrating polymers (Cooper *et al.*, 2017). COF values of hard gels, more like a solid base body, stayed at a constant friction level, in contrast to soft gels, for which a slight steady increase was observed during the duration of the tribological tests. C-NAC-BED produced the lowest COF values in both configurations.

3.2 X-ray photoelectron spectroscopy results

On the reference surfaces outside the wear track, sulphur can be detected essentially on all samples at about 1%, so that coating with mucin can be assumed. The sample "Placebo" has the highest content of sulphur, and the detailed analysis shows that it is present in oxidized form, mainly in the state +4$^-$ (Figure 9). BE of 167 eV to 168 eV are attributed to oxidized states, whereas S-S binding types are reported app. at BE of 163 to 165 eV (NIST, 2012).

Sample C-NAC-BED shows a similar total S content outside the wear track, compared to reference surface as sample "Placebo." To a small extent, disulphide binding energy is

Figure 7 COF results for hard hydrogel substrate samples
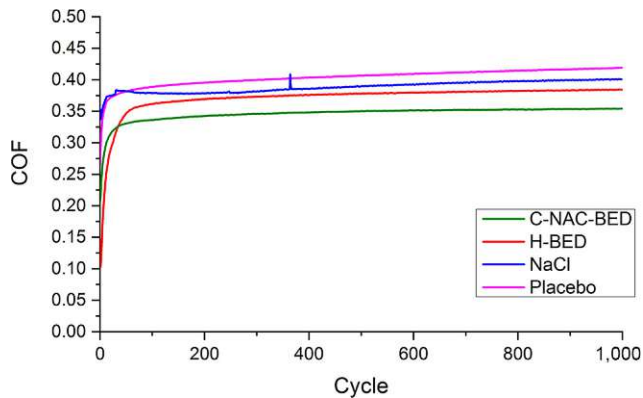
Figure 8 COF results for soft hydrogel substrate samples
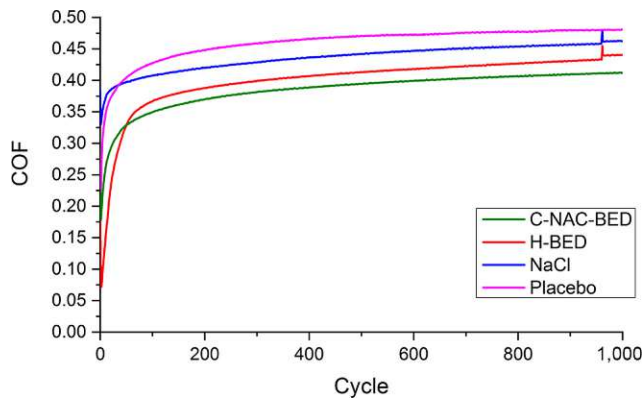
Figure 9 XPS S 2p outside the wear track (reference) of sample Placebo
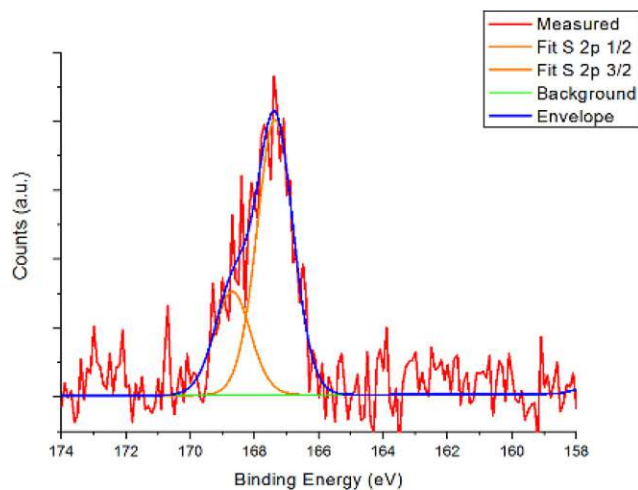
detectable (Figure 10), whereas most of the S is present in oxidized states, mainly +4. On sample H-BED, the lowest S concentration is detected, with the disulphide value below the detection limit (Figure 11).

Figure 10 XPS S 2p spectrum of sample C-NAC-BED outside the wear track (reference) Presence of S-S chemical state is evident through necessary peak fittings at BE ∼162 to 164 eV (NIST, 2012)[a]
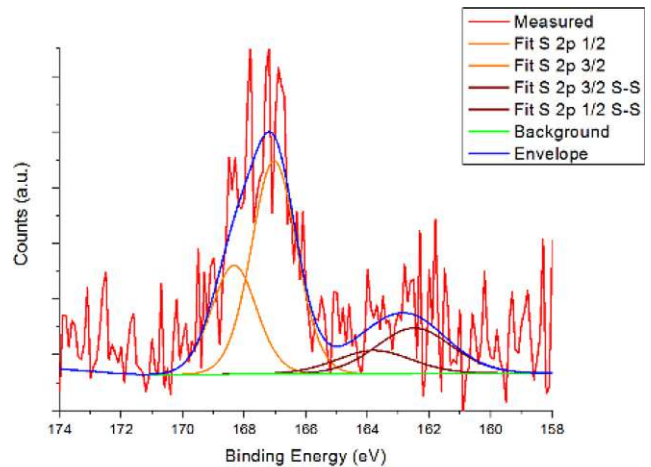
Note: [a]Original spectra without applied correction for charge compensation is shown. A correction to C1s at reference BE at 184.6 eV shifts the binding energies app. 1.5 eV to higher BE

Figure 11 XPS S 2p spectrum of sample HBED
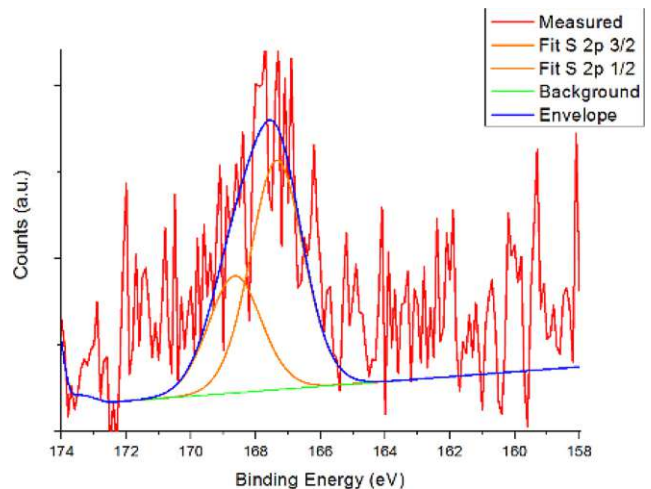
Table 1 summarizes the relative concentrations of the detected elements for each sample, for both worn and reference surfaces. A reduction of contaminations (Si, Ca) in the wear track is detectable due to the frictional load on all samples. The sample "Placebo" shows a slightly different behavior than "H-BED" and "C-NAC-BED" regarding the element composition for N and O in the wear track compared to the reference surface. While in the sample "Placebo" the N (∼10%) and O (∼32%) content do not vary noticeably, an increase in concentration in the wear tracks "H-BED" (N from 7% to 14%, O from 19% to 22%) and "C-NAC-BED" (N from 5% to 12%, O from 16% to 22%) samples is significantly detectable. The measurable increase of N and O can be attributed to the wear of the protective layer of the H-BED and C-NAC-BED, compared to the sample "Placebo" in which there is no activated protective

Table 1 XPS Relative element concentration on the reference and the worn surface of samples "placebo," "H-BED" and "C-NAC-BED," respectively

Sample	Position	Relative elemental concentration (at%)						
		S	S-chem states	C	N	O	Si	Ca
Placebo	Reference	1	$(SO3/SO4)^{2-}$	55	9	34	<1	n.d.
Placebo	Wear track	1	$(SO3/SO4)^{2-}$	56	10	33	n.d.	n.d.
H-BED	Reference	<1	$(SO3/SO4)^{2-}$	66	7	19	7	<1
H-BED	Wear track	<1	$(SO3/SO4)^{2-}$	63	14	22	<1	n.d.
C-NAC-BED	Reference	<1	$S-S/(SO3/SO4)^{2-}$	74	5	16	4	1
C-NAC-BED	Wear track	<1	$(SO3/SO4)^{2-}$	61	12	26	<1	<1

Notes: Values are rounded to whole numbers; it is indicated where less than 1% (<1) was detected and the value was below the detection limit (n.d.)

layer present. The distribution of carbon, oxygen and nitrogen atoms in the samples was characterized to confirm the chitosan immobilization observed in a similar study (Ashtiana *et al.*, 2019)

The total S amount remains unchanged within the experimental and measuring uncertainties on all samples. In detailed analyses, no disulfide (thio compounds) are detectable in the wear marks, only oxidation states of +4 are detectable. It is concluded that essentially one existing mucin layer was consumed in the tribo-test.

4. Conclusions

In this study, we have developed a cornea model for tribological testing of different types of eye drops. The presence of a mucin layer covering the top of the sample was verified using XPS, and changes in elemental composition following the tribological tests were detectable. Especially, disulphide bridges (S-S) could be uniquely proven on the surface of unworn C-NAC-BED samples. This indicates effectively bonding support of active substances in this solution. On all other tested systems, no disulphide bridges could be measured; however, S is present only in oxidized states, i.e. $(SO_3/SO_{4'})^{2-}$. The system is capable of identifying not only differences between the friction behavior (by means of COF) of three different lubricant formulations compared to a control consisting of 0.9% NaCl solution, but also showed the difference between C-NAC-BED and a placebo formulation containing non-thiolated chitosan. In addition to COF comparisons of the samples, the developed model is also sensitive to relatively small changes in Young's modulus. This observation is very important for the discussion focusing on DES (Efraim *et al.*, 2020) or intraocular pressure changes that lead to changes in corneal stiffness (Liu and He, 2009). In this study, C-NAC-BED revealed the lowest COF in both configurations with different Young's modi. For future studies, authors advise to perform long-term tribological tests that will take the drop application period into consideration and also the wear of the mucin layer covering the supporting gel.

References

Ashtiana, M.K., Zandi, M., Shokrollahi, P., Ehsani, M. and Baharvand, H. (2019), "Chitosan surface modified hydrogel as a therapeutic contact lens", *Polymers for Advanced Technologies*, Vol. 31 No. 4, pp. 741-748.

Cobb, J.A., Dunn, A.C., Kwon, J., Sarntinoranont, M., Sawyer, W.G. and Tran-Son-Tay, R. (2008), "A novel method for low load friction testing on living cells", *Biotechnology Letters*, Vol. 30 No. 5, pp. 801-806.

Colter, J., Wirostko, B. and Coats, B. (2017), "Coefficient of friction between carboxymethylated hyaluronic acid-based polymer films and the ocular surface", *Investigative Ophthalmology & Visual Science*, Vol. 58 No. 14, pp. 6165-6174.

Cooper, B.G., Lawson, T.B., Snyder, B.D. and Grinstaff, M. W. (2017), "Reinforcement of articular cartilage with a tissue-interpenetrating polymer network reduces friction and modulates interstitial fluid load support", *Osteoarthritis and Cartilage*, Vol. 25 No. 7, pp. 1143-1149.

Dunn, A.C., Tichy, J.A., Urueña, J.M. and Sawyer, W.G. (2013b), "Lubrication regimes in contact lens wear during a blink", *Tribology International*, Vol. 63, pp. 45-50.

Dunn, A.C., Urueña, J.M., Puig, E., Perez, V.L. and Sawyer, W.G. (2013a), "Friction coefficient measurement of an in vivo murine cornea", *Tribology Letters*, Vol. 49 No. 1, pp. 145-149.

Efraim, Y., Chen, F.-Y.T., Stashko, C., Cheong, K.N., Gaylord, E., McNamara, N. and Knox, S.M. (2020), "Alterations in corneal biomechanics underlie early stages of autoimmune-mediated dry eye disease", *Journal of Autoimmunity*, Vol. 114, p. 102500.

Fischak, C., Klaus, R., Werkmeister, R.M., Hohenadl, C., Prinz, M., Schmetterer, L. and Garhöfer, G. (2017), "Effect of topically administered Chitosan-N-acetylcysteine on corneal wound healing in a rabbit model", *Journal of Ophthalmology*, p. 6.

Jones, M.B., Fulford, G.R., Please, C.P., McElwain, D.L.S. and Collins, M.J. (2008), "Elastohydrodynamics of eyelid wiper", *Bulletin of Mathematical Biology*, Vol. 70 No. 2, pp. 323-343.

Last, J.A., Liliensiek, S.J., Nealey, P.F. and Murphya, C.J. (2009), "Determining the mechanical properties of human corneal basement membranes with atomic force microscopy", *Journal of Structural Biology*, Vol. 167 No. 1, pp. 19-24.

Last, J.A., Thomasy, S.M., Croasdale, C.R. and Russell, P. (2012), "Compliance profile of the human cornea as measured by an atomic force microscopy", *Micron*, Vol. 43 No. 12, pp. 1293-1298.

Liu, J. and He, X. (2009), "Corneal stiffness affects IOP elevation during rapid volume change in the eye", *Investigative Opthalmology & Visual Science*, Vol. 50 No. 5, pp. 2224-2229.

Ludwig, A. (2005), "The use of mucoadhesive polymers in ocular drug delivery", *Advanced Drug Delivery Reviews*, Vol. 57 No. 11, pp. 1594-1639.

168

Malamut, S., Kligerman, Y. and Etsion, I. (2009), "The effect of dwell time on the static friction in creeping elastic–plastic polymer spherical contact", *Tribology Letters*, Vol. 35 No. 3, pp. 159-170.

Mann, A. and Tighe, B.J. (2006), "Ocular biotribology and the contact lens: surface interactions and ocular response", *Biomaterials and Regenerative Medicine on Ophthalmology*, 2nd ed., pp. 45-74.

Molladavoodi, S., Kwon, H., Medley, J. and Gorbet, M. (2014), "Human corneal epithelial cell response to substrate stiffness", *Acta Biomaterialia*, Vol. 11, pp. 324-332.

Mollenhauer, O., Ahmed, S.I.-U., Spiller, F. and Haefke, H. (2006), "High-precision positioning and measurement systems for microtribotesting", *Tribotest*, Vol. 12 No. 3, pp. 189-199.

Ngai, V., Medley, J.B., Jones, L., Forrest, J. and Teichroeb, J. (2005), "Friction of contact lenses: silicone hydrogel versus conventional hydrogel", *Life Cycle Tribology*, pp. 371-379.

NIST (2012), "X-ray photoelectron spectroscopy database", Version 4.1, National Institute of Standards and Technology, Gaithersburg, available at: http://srdata.nist.gov/xps/

Raghunatan, V.K., Thomasy, S.M., Strøm, P., Yañez-Soto, B., Garland, S.P., Sermeno, J., Reilly, C.M. and Murphy, C.J. (2017), "Tissue and cellular biomechanics during corneal wound injury and repair", *Acta Biomaterialia*, Vol. 58, pp. 291-301.

Rennie, A.C., Dickrell, P.L. and Sawyer, W.G. (2005), "Friction coefficient of soft contact lenses: measurements and modelling", *Tribology Letters*, Vol. 18 No. 4, pp. 499-504.

Rico-del-Viejo, L., Lorente-Velázquez, A., Hernández-Verdejo, J.L., García-Mata, R., Benítez-del-Castillo, J.M. and Madrid-Costa, D. (2017), "The effect of ageing on the ocular surface parameters", *Contact Lens and Anterior Eye*, Vol. 41 No. 1, pp. 5-12.

Samsom, M., Chan, A., Iwabuchi, Y., Subbaraman, L., Jones, L. and Schmidt, T.A. (2015), "In vitro friction testing of contact lenses and human ocular tissue: effect of proteoglycan (PRG4)", *Tribology International*, Vol. 89, pp. 27-33.

Shaw, A.J., Collins, M.J., Davis, B.A. and Carney, L.G. (2010), "Eyelid pressure and contact with the ocular surface", *Investigative Opthalmology & Visual Science*, Vol. 51 No. 4, pp. 1911-1917.

Shih, P., Huang, C., Huang, T., Lin, H., Yen, J., Wang, I., Cao, H., Shih, W. and Dai, C. (2017), "Estimation of the corneal Youngs's modulus in vivo based on a fluid-filled spherical-shell model with", *Journal of Ophthalmology*, Vol. 2017, p. 11.

Śródka, W. (2011), "Evaluating the material parameters of the human cornea in a numerical model", *Acta of Bioengineering and Biomechanics*, Vol. 13 No. 3, pp. 77-85.

Sterner, O., Karageorgaki, C., Zürcher, M., Zürcher, S., Scales, C.W., Fadli, Z., Spencer, N.D. and Tosatti, S.G.P. (2017), "Reducing friction in the eye: a comparative study of lubrication by surface-anchored synthetic and natural ocular mucin analogues", *ACS Applied Materials & Interfaces*, Vol. 9 No. 23, pp. 20150-20160.

Thomasy, S.M., Raghunathan, V.K., Winkler, M., Reilly, C.M., Sadeli, A.R., Russell, P., Jester, J.V. and Murphy, C.J. (2014), "Elastic modulus and collagen organization of the rabbit cornea: epithelium to endothelium", *Acta Biomaterialia*, Vol. 10 No. 2, pp. 785-791.

Thulasi, P. and Djalilian, A. (2017), "Update in current diagnostics and therapeutics of dry eye disease", *Ophthalmology*, Vol. 124 No. 11, pp. 27-33.

Tomala, A., Göçerler, H. and Gebeshuber, I.C. (2013), "Bridging nano- and microtribology in mechanical and biomolecular layers", *Scanning Probe Microscopy in Nanoscience and Nanotechnology*, Vol. 3, pp. 431-485.

Urueña, J.M., McGhee, E.O., Angelini, T.E., Dowson, D., Sawyer, G.S. and Pitenis, A.A. (2018), "Normal load scaling of friction in gemini hydrogels", *Biotribology*, Vol. 13, pp. 30-35.

Wu, J., Nasseri, M.A., Eder, M., Gavaldon, M.A., Lohmann, C.P. and Knoll, A. (2013), "The 3D eyeball FEA model with needle rotation", *APCBEE Procedia*, Vol. 7, pp. 4-10.

Corresponding author

Hakan Göcerler can be contacted at: hakan.gocerler@tuwien.ac.at

PAPER III

The dominance of water on lubrication properties of articular joints

Hakan Göçerler, Bernhard Pfeil and Friedrich Franek
AC2T research GmbH, Wiener Neustadt, Austria, and

Christoph Bauer, Eugenia Niculescu-Morzsa and Stefan Nehrer
Danube University Krems, Krems, Austria

Abstract

Purpose – The paper aims to focus on the individual contribution of water to the lubrication regimes in articular joints because understanding of these regimes is crucial not only for the treatment of diseases like osteoarthritis but also for the development of new implants to have a longer service cycle.

Design/methodology/approach – Cartilage specimen and the synovial fluid were both isolated from bovine knee joints that are enclosed by a synovial membrane under sterile conditions of a biosafety Level 2 (BSL2) cabinet. Subchondral bone was removed from the cartilage because it not only creates a stable base to place the specimen on the holder, but it also acts as a primary shock absorber protecting the overlaying cartilage under high-impact loads. A specimen holder specially designed for tests and was attached to the linear oscillation (SRV) test machine. The SRV test machine provides a reciprocating sliding motion between the cartilage samples that are submerged into the selected biological media. The entire system can be mounted on the BSL2 cabinet, sealed with the convoluted gaiter and transported to the SRV machine with a specifically designed handle for the entire system. The process ensures sterile conditions for tests on biological samples that are highly sensitive to the environmental conditions.

Findings – A remarkably low coefficient of friction value for distilled water constitutes more evidence to support the assumption of the impact of water in the friction behaviour of the cartilage-against-cartilage contact. As the fluid in articular cartilage (AC) effectively serves as a synovial fluid reserve and 70-80 per cent of its composition is distilled water, it can be stated that the tribotest system mimics the natural working conditions of an actual knee joint adequately.

Research limitations/implications – Time and limited availability of the animal-driven samples led to a focus on certain parameters mentioned in the approach. A planned scan of parameter matrix, such as variation of load and speed, would allow deeper knowledge on the lubrication regimes.

Practical implications – Study of relevant tribological contact in human joints might give ideas on new designs for artificial joints.

Social implications – Understanding of lubrication regimes is crucial not only for the treatment of diseases like osteoarthritis but also for the development of new implants to adapt motion of related joint.

Originality/value – Exclusion of water and application as the primary lubricant in the test system brings a new perspective to joint lubrication.

Keywords Biotribology, Articular cartilage, Lubrication regimes, *Ex vivo* tissue, Synovial fluid, Tribometry

Paper type Research paper

1. Introduction

Enhancements in material and surface finishing technologies ensured arthroplasty applications to be an alternative solution for people who have various complications related to articular joints. However, recent reports reveal complications long before the expected lifetime. Major issues are material wear, aseptic loosening, various infections, arthrofibrosis, malalignment or malposition (Lum *et al.*, 2018). One of the main reasons for these issues is the mismatch between the mechanical properties of artificial materials and the host tissue under *in situ* tribological conditions. Even though a wide portfolio of biomaterials incorporated with cell-based technologies was introduced in clinical applications, inconsistency in success rates is apparent (Escobar Ivirico, 2017). To increase success rates, a deeper knowledge about highly loaded biomechanical systems in the human body, natural functions of the tissues and advanced biomedical investigations in the field of tribology are required.

Tribological analysis in natural joints focuses on the lubricating mechanisms and the actual working conditions where a failure of cartilage is generally observed. Researchers have proposed various tribological theories such as boundary lubrication, hydrodynamic lubrication, weeping, squeeze film lubrication, boosted lubrication, biphasic lubrication, elastohydrodynamic lubrication and complex-mode

lubrication (Linn, 1968; Martin *et al.*, 1998; Mabuchi *et al.*, 1998; Krishnan *et al.*, 2004; Unsworth, 1995; Dowson and Jin, 1992; Jin and Dowson, 2005). But, for the articular cartilage, the main lubricating mechanisms coming forward are boosted and weeping lubrication. The critical point that distinguishes these two mechanisms is the direction of the fluid in the joint. In weeping lubrication, load on the AC results in a flow from the tissue into the contact zone and creates a lubricating film between the counter bodies. Correspondingly, boosted lubrication predicts, fluid flow in the opposite direction and due to the permeability of AC to water, synovial fluid losses water and forms a gel on the contact area (Accardi *et al.*, 2011). In this study, we predict that weeping lubrication is the dominating lubrication mechanism for the AC, as water constitutes 80 per cent of AC composition. This would restrain complete penetration of the water out of the contact zone and water would have a crucial role in the formation of the lubricating film.

Another important consideration for the tribological behaviour of natural joints is the biphasic behaviour of the articular cartilage (Milner *et al.*, 2018). One of the reasons that many artificial biomaterials fail is that they are not able to replicate this behaviour during the dynamic loading of the system. In this case, using *ex vivo* material for the design of tribosystem has an advantage compared to the *in vitro* materials such as metals, ceramics or polymers. Initial studies should be conducted on animal-derived tissues before extending the study to be applied to human tissue cultures, though experiments on human tissues have also been taken into consideration for comparison (Qian and Ge, 2012; Merkher *et al.*, 2006).

Lubricants are significantly sensitive to the temperature of the contact zone. Hence, the tribosystem is designed to perform under the body temperature of the selected donor animal. The results were compared with the tests conducted under room temperature to underline the differences by means of the coefficient of friction (COF). Finally, tribosystem is designed to allow various additives to observe pro-/anti-inflammatory markers and the effect of lubrication enhancers. The enclosed chamber also assures sterile conditions necessary for highly sensitive chemical follow-up tests such as high performance liquid chromatography (Hutson *et al.*, 2003), to analyse wear materials that could be vital for health conditions of the patients.

2. Experimental details

2.1 Specimen preparation

Interspecies comparisons have been concluded between human, bovine, dog, monkey and rabbit achieving similar results for the aggregate modulus of all donors, but the permeability of bovine cartilage samples was considered closest to human femoral cartilage (Athanasiou *et al.*, 1991). Studies also focused on the average cartilage thickness for various animal species, which showed that bovine cartilage has similar thickness and a larger surface area compared to human femoral head chondral (Patil *et al.*, 2014). Better availability of samples because of the greater surface area, similarities in mechanical properties and less complicated ethical verification procedures compared to a human tissue purchase make bovine tissue a more suitable candidate for tribological studies

Following the selection of the donor animal species and the joint of interest, the further focus was put on the selection of a suitable location on the sample joint tissue. To identify the area of interest on the joint that the study should be focusing on, various imaging techniques were used in different studies. Traditional techniques using pressure-sensitive films (Harris *et al.*, 1999) have difficulty in quantifying the contact of curved surfaces, and measurements may be impeded by the interposition of media or joint exposure (Willing *et al.*, 2014). Various imaging and mapping techniques such as Raman spectroscopy, magnetic resonance imaging (MRI), dual-fluoroscopic imaging, a stereo-photogrammetric method and atomic force microscopy (AFM) for micromechanical mapping have been used to investigate critical zones that are in contact during the movement of the joints (Takahashi *et al.*, 2014; Song *et al.*, 2006; Suzuki *et al.*, 2012; Cohen *et al.*, 1999; Wilusz *et al.*, 2013). Aberrant knee joint loading was observed in the knee of patients who have progressed osteoarthritis. Elevated knee adduction moment and the external knee joint moment in the frontal plane led to elevated medial tibiofemoral loading (Meireles *et al.*, 2017). It is also suggested that only the medial compartment of a human knee joint is influenced by the knee kinematics due to different shapes of the contact surface (convex–concave) (Shiomi *et al.*, 2012). Hence, this compartment becomes the region where most severe cartilage tissue wear occurs (Arno *et al.*, 2012). In addition to these observations, less rough and more planar surface of medial zone made it a suitable location to investigate tribological behaviour.

Cartilage specimen and the synovial fluid (SF) were both isolated from bovine knee joints that are enclosed by a synovial membrane. Under sterile conditions of a biosafety Level 2 (BSL2) (MDPI, 2016) laminar flow box, a small incision was made in each joint between the femoral and tibial condyle. Using a serological pipette, SF was removed through the incision and filtered (filter mesh size: 40 μm) before storing at 4°C. After this step, the knee joint was severed into two pieces by slicing the synovial membrane, ligaments and tendons. Cartilage specimens for of 8 mm diameter were prepared using a single-use osteochondral autograft transplant system (OATS) punch (Arthrex Inc., Naples, USA) by placing them onto the surface of the cartilage at 90° to obtain a cylindrically shaped cartilage specimen. A maximum of six to eight cartilage specimens per joint were obtained by punching them out from the condyles as close as possible to the neighbouring sample region. Obtained cartilage specimens were shortened to 8 mm in length using a custom-made cartilage holder by using a saw and a scalpel (Figure 1(b)). Subchondral bone does not only create a stable base to place the specimen on the holder, but it also acts as a primary shock absorber protecting the overlaying cartilage under high-impact loads (Malekipour *et al.*, 2013). Hence, for the tribological tests, it is essential to keep the subchondral bone as a part of the tribological system. Specimens were stored in phosphate-buffered saline (Sigma-Aldrich Chemie GmbH, Steinheim, Germany) containing 10 per cent antibiotics solution (penicillin 200 U/ml; streptomycin 0.2 mg/ml and amphotericin B 2.5 μg/ml) at 4°C. Similar conservation methods were proven to be viable to keep specimens in a condition that they can be classified as *ex vivo* (Cetinkaya *et al.*, 2014).

172

Figure 1 (a) Location of the cartilage samples punched out from the medial and lateral condyle of the femur; (b) Custom-made cartilage-holder to adjust the height of the cartilage samples
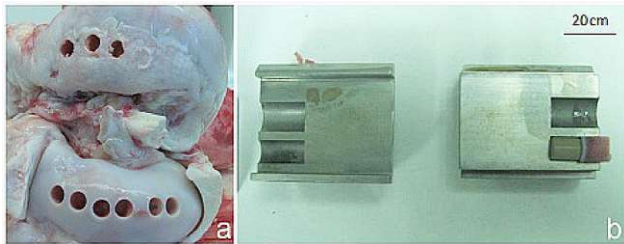

2.2 Setup of the tribotest

In Figure 2(a), a schematic of the designed specimen holder that is attached to the linear oscillation (SRV) test machine (DIN 51834-1, 2010) is presented. The SRV test machine provides a reciprocating sliding motion between the cartilage samples (Figure 2(b)) that are submerged into the selected biological media. The entire system can be mounted on the BSL2 cabinet, sealed with the convoluted gaiter and transported to the SRV machine with a specifically designed handle for the entire system. The process ensures sterile conditions for tests on biological samples that are highly sensitive to the environmental conditions. As the setup is designed for consecutive projects (Bauer *et al.*, 2019) that require possible analysis techniques, such as mass spectroscopy, cell counting with a hemocytometer or microarray methods, it is crucial to inhibit interaction with common ambient conditions that may generate artefacts.

To suppress the possible effects of the elastic behaviour of the rubber gaiter on the movement of the lubricant during the reciprocating motion, a voluminizer was added to the system. The voluminizer also helps to reduce the amount of SF required for a single test (ca. 6 ml). This quantity is enough to conduct six consecutive tests because the total amount of SF that can be derived from a single donor is approximately 40 ml.
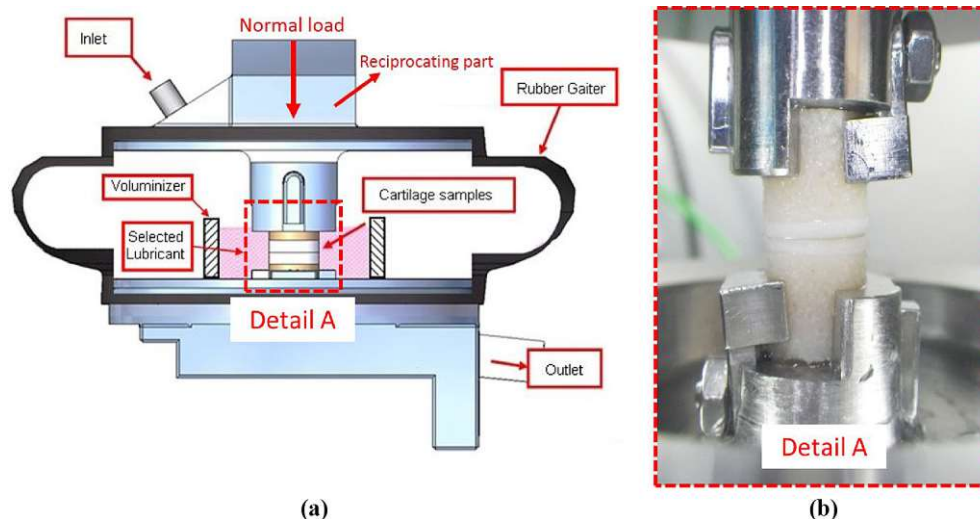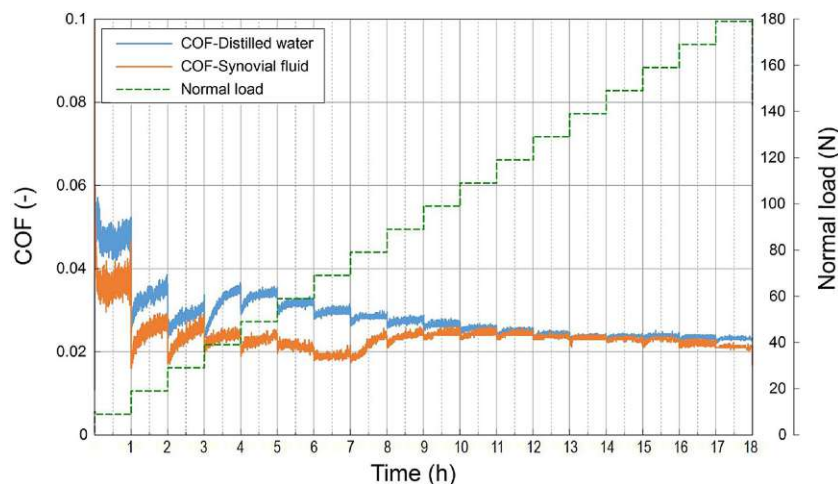
For the consistency of the test results, it must be stressed that the alignment of the samples plays a vital role because the cartilage-against-cartilage system has a certain orientation for its matrix that develops naturally because of rolling and sliding during the movement of the patient (Accardi *et al.*, 2013). These phenomena have not been considered for the initial tests represented here, but for the consecutive projects, the location where the tissue is derived with the orientation information will be marked so that the tissue can be placed in the holder correctly aligned. Apart from the location of the sample, a selection of donors from the same gender and age division will be preferred because these parameters also affect the mechanical properties and tribological response of the samples significantly too.

2.3 Test parameters and procedure

To observe the elastic behaviour of cartilage samples, a stepwise increasing load (10-180 N) with a step value of 10 N for each hour) was utilized on the cartilage samples using the specimen holder represented in Figure 2. Distilled water and SF were used for this set of tests. The system was oscillating with a frequency of 1 Hz and a stroke of 1 mm (ISO 14243-1, 2009). Mean value of COF during a single cycle was saved as a single data point.

As can be seen in Figure 3, the COF values were not influenced significantly by the increasing load after the load had surpassed 130 N. Lubrication was being pushed into the direction of weeping lubrication, and the role of lubricant entrapment (Chan *et al.*, 2011) could become visible by means of reduction of friction. The normal load was increased to 180 N and, considering the contact area of 50.26 mm^2 for 8 mm cartilage samples, a pressure value of 3.57 MPa was achieved. In this case, tribo-model matches with contact pressure measurements for the tibio-femoral compartment of a human knee under the normal load of body weight with 0° flexion (Patil *et al.*, 2014) and contact pressure distributions on the articular cartilage surfaces of the medial tibial plateau for anterior–posterior movement (Meireles *et al.*, 2017). It should be noted that the load range that SF represents a lower COF corresponds

Figure 2 (a) Schematic of the designed specimen holder; (b) image of cartilage-against-cartilage contact in the tribotest

(a)

(b)

Figure 3 COF values for SF and H$_2$O in response to stepwise increasing load

to the unloaded knee and loaded conditions more relevant to the scope of this study. Another point is that the decrease is similar in both cases, so observation in this study supports the weeping lubrication mechanism as the decrease in the COF was also observed in the tests using only water as a lubricant.

Similar pressure and loading conditions were also used for testing biomolecular additives for artificial joint systems (3 MPa, 159 N (Su *et al.*, 2017)) and porous architected biomaterial for tibial-knee implants (170 N, (Rahimizadeh *et al.*, 2018)). The normal load was applied as the static load, with a stroke of 1 mm, frequency of 1 Hz and duration of 1 h, for the tests conducted using biological media of SF and distilled water (H$_2$O). It is also demonstrated that cartilage can retain and recover interstitial fluid without migration or unloading, so static loading would not conflict with *in situ* conditions by means of dehydration (Moore and Burris, 2017).

With the aim of gaining a better understanding of the rheological behaviour of the aforementioned biological media, temperature values were also varied. In this study, we did not focus on the variation of speed (hence, shear rate) changes as patients with knee problems (but also healthy people during the daily life) do not excite their knees more frequent than 1 Hz in a regular walk. All the tests were conducted using this fixed parameter, so viscosity changes due to variation of speed were discarded. On the other hand, the temperature effect on viscosity for water and SF was investigated and reported in the literature. As the absolute values vary for different methods and the health, age, sex, nationality of the donors, it was important for the study how it is expected to decrease and if this would be observed in the COF values as the temperature increased to the actual working condition of the related media. The results gathered at room temperature (RT, 24°C) were compared to results obtained at a temperature of 39°C (internal bovine body temperature) (Sugiyama *et al.*, 2007). Samples were thawed at room temperature for 30 min, followed by another 30 min in the specimen holder, submerged in the related biological medium and temperature, under the pretension load of 180 N. Finally, a 3D profilometer (Leica DCM 3D Leica Microsystems) was used to investigate the wear patterns on the surface of the cartilage samples.

3. Results and discussion

3.1 Friction response of the cartilage samples

Healthy cartilage is expected to maintain extremely low friction values under the loads exerted on the joint during daily routines. The results of the tests (five tests for both SF and H$_2$O) conducted in this study at RT gave average coefficient of friction (ACOF) values 0.0077 and 0.0114 for H$_2$O and SF, respectively (Figure 4). Values are well within the range reported in the literature for bovine articular cartilage (Su *et al.*, 2017; Kawano *et al.*, 2013; Krishnan *et al.*, 2005; Merkher *et al.*, 2006; Linn, 1968; Basalo *et al.*, 2007). Note that SF has higher ACOF value compared to H$_2$O at RT. The temperature plays a vital role in this phenomenon and is especially critical for the natural lubricants in a biological environment [e.g. an increase of only 1°C body temperature can have a significant effect on a patient's health condition (Mace *et al.*, 2011)]. Considering this important parameter, tests were repeated at 39°C, which is the internal body temperature of a bovine.

The results of the tests conducted at 39°C (five tests for H$_2$O and three tests for SF) yield ACOF values between 0.0064 and 0.0085 (Figure 4). Individual values for each biological medium changed significantly. Value for the distilled water shows a decrease of 16.8 per cent (0.0077 → 0.0064) for 39°C compared to RT experiments. This may look like a small
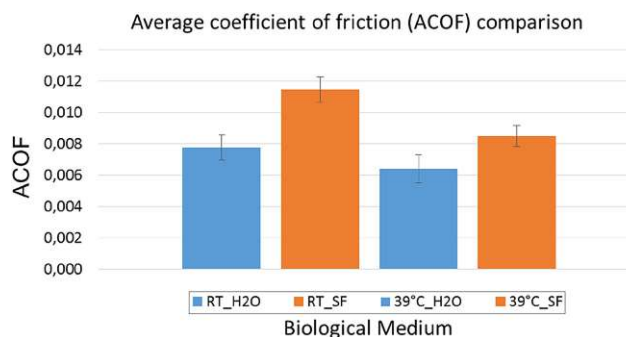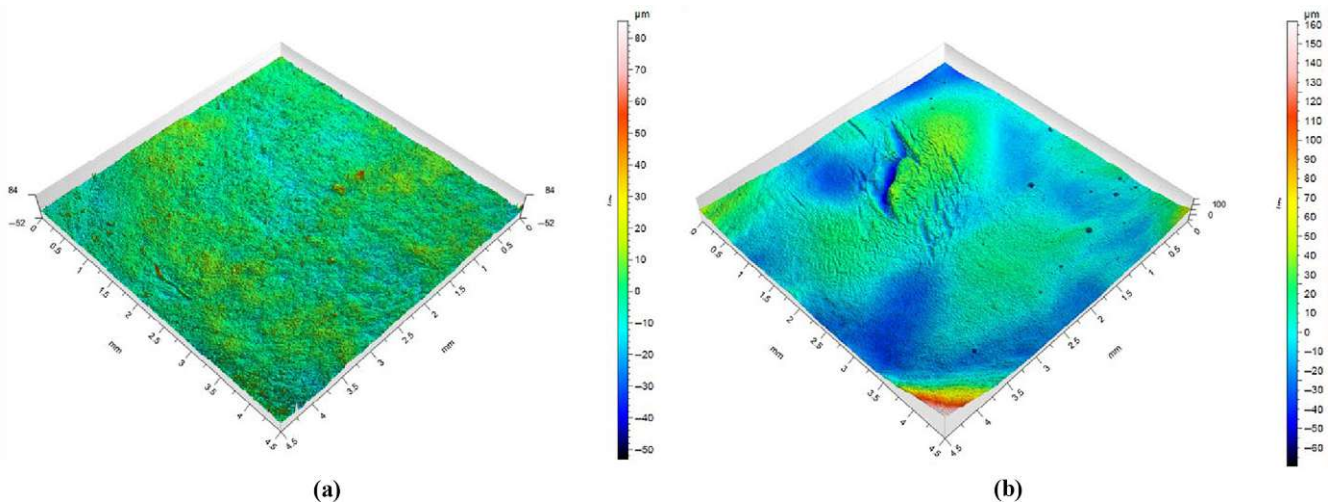
Figure 4 Comparison of the COF values for H$_2$O and SF at 39°C and at RT

Figure 5 (a) 3D topographic image of the surface before the test; (b) 3D topographic image of the surface after the test

(a)

(b)

reduction but considering that an individual takes 1-4 million steps each year (Seedom and Wallbridge, 1985), its importance to a sensitive biological environment can be foreseen.

Temperature effect was even more obvious in the SF. The ACOF reduction of 25.4 per cent (0.0114-0.0084) is remarkable considering that the initial values were already low. On the other hand, this tendency would also be expected because the SF was derived directly from the bovine sample. It would perform better under the natural working conditions of the bovine body. A decrease in the relative viscosity is expected due to the alterations in temperature from RT to body temperature (Reimann *et al.*, 1975) and assumed to be one of the reasons for the decrease in ACOF.

Even though the main scope of this paper is the investigation of lubricating capabilities of different biological media, the surface of the cartilage samples has been investigated to validate the potential of the designed tribotest system mimicking the natural progress. With the aim to observe wear of the cartilage samples, the test duration with H_2O as a lubricant was increased to 24 h (leading to 86,400 cycles). Here, it should be underlined that as the cartilage samples punched out from the condyles, continuity of the cartilage matrix already was disturbed. So what is here modelled is not cartilage going through the expected lifecycle from the beginning but cartilage with an already initiated adverse health condition.

The pattern of wear is visible to the eye when the images acquired before the tribotest (Figure 5(a)) and taken after the test (Figure 5(b)) are compared. Changes in the topography can be quantified using 3D optical microscopy. Various areas of rupture were observed reaching a depth of 62.60 μm. The shape of the ruptures and the formation of surface fissures match the ones encountered in the literature (Fick and Espino, 2011). During the image processing, only the central area of samples (4.5×4.5 mm) were taken into consideration to avoid artefacts created during the punching process. The form component was removed prior to any other metrological operation according to the ISO 3274 standard because the primary profile should not contain the nominal form of the workpiece (ISO, 1998).

4. Conclusions

We conducted tribological tests using a specimen holder designed for *ex vivo* cartilage samples derived from bovine donors, with the samples submerged in H_2O and SF at room and body temperatures. The developed system proved the capability of differentiating the selected media by means of the COF, even though the obtained values were notably low as expected from a cartilage-against-cartilage installation. Furthermore, changes in the COF values due to a change of temperature between RT and 39°C were seen. Best performance by means of repeatability (within 10 per cent) and level of COF (minimum 0.0052 at 39°C) was measured for H_2O. However, to get repeatable results, nutritious particles in the SF must be considered more accurately.

The results support the assumption of the impact of water in the friction behaviour of the cartilage-against-cartilage contact. Increasing the temperature to body temperature of the bovine, the SF shows a decrease in ACOF with similar rheological behaviour as H_2O. A remarkably low COF value for distilled water constitutes more evidence to support the assumption. As the fluid in articular cartilage effectively serves as an SF reserve and 70-80 per cent of its composition is H_2O, it can be stated that the tribotest system mimics the natural working conditions of an actual knee joint adequately.

References

Accardi, M.A., Dini, D. and Cann, P. (2011), "Experimental and numerical investigation of the behaviour of articular cartilage under shear loading-Interstitial fluid pressurisation and lubrication mechanism", *Tribology International*, Vol. 44 No. 5, pp. 565-578.

Accardi, M.A., McCullen, S.D., Callanan, A., Chung, S., Cann, P.M., Stevens, M.M. and Dini, D. (2013), "Effects of fiber orientation on the frictional properties and damage of regenerative articular cartilage surfaces", *Tissue Engineering: Part A*, Vol. 19 Nos 19/20.

Arno, S., Walker, P.S., Bell, C., Krasnokutsky, S., Samuels, J., Abramson, S.B., Regatte, R. and Recht, M. (2012),

"Relation between cartilage volume and meniscal contact in medial osteoarthritis of the knee", *The Knee*, Vol. 19 No. 6, pp. 896-901.

Athanasiou, K.A., Rosenwasser, M.P., Buckwalter, J.A., Malinin, T.I. and Mow, V.C. (1991), "Interspecies comparisons of in situ intrinsic mechanical properties of distal femoral cartilage", *Journal of Orthopaedic Research*, Vol. 9 No. 3, pp. 330-340.

Basalo, M.I., Chahine, N.O., Kaplun, M., Chen, F.H., Hung, C.T. and Ateshian, G.A. (2007), "Chondroitin sulfate reduces the friction coefficient of articular cartilage", *Journal of Biomechanics*, Vol. 40 No. 8, pp. 1847-1854.

Bauer, C., Göçerler, H., Niculescu-Morzsa, E., Jeyakumar, V., Stotter, C., Tóth, I., Klestil, T., Franek, F. and Nehrer, S. (2019), "Effect of osteochondral graft orientation in a biotribological test system", *Journal of Orthopaedic Research*, Vol. 37 No. 3.

Cetinkaya, G., Hatipoglu, I. and Arat, S. (2014), "The value of frozen cartilage tissues without cryoprotection for genetic conservation", *Cryobiology*, Vol. 68 No. 1, pp. 65-70.

Chan, S.M.T., Neu, C.P. and Komvopoulos, K. (2011), "The role of lubricant entrapment at biological interfaces: reduction of friction and adhesion in articular cartilage", *Journal of Biomechanics*, Vol. 44 No. 11, pp. 2015-2020.

Cohen, Z.A., McCarthy, D.M., Kwak, S.D., Legrand, P., Fogarasi, F., Ciaccio, E.J. and Ateshian, G.A. (1999), "Knee cartilage topography, thickness, and contact areas from MRI: in-vitro calibration and in-vivo measurements", *Osteoarthritis and Cartilage*, Vol. 7 No. 1, pp. 95-109.

DIN 51834-1 (2010), "Tribological test in the translatory oscillation apparatus part 1: general working principles".

Dowson, D. and Jin, Z.M. (1992), "Micro-elastohydrodynamic lubrication of Low-Elastic modulus solids on rigid substrates", *Journal of Physics D – Applied Physics*, Vol. 25 No. 1A, pp. 116-123.

Escobar Ivirico, J.L., Bhattacharjee, M., Emmanuel Kuyinu, E., Naira, L.S. and Laurencin, C.T. (2017), "Regenerative engineering for knee osteoarthritis treatment: biomaterials and Cell-Based technologies", *Engineering*, Vol. 3 No. 1, pp. 16-27.

Fick, J.M. and Espino, D.M. (2011), "Articular cartilage surface rupture during compression: investigating the effects of tissue hydration in relation to matrix health" *The Journal of the Mechanical Behavior of Biomedical Materials*, Vol. 4 No. 7, pp. 1311-1317.

Harris, M.L., Morberg, P., Bruce, W.J. and Walsh, W.R. (1999), "An improved method for measuring tibiofemoral contact areas in total knee arthroplasty: a comparison of K-scan sensor and Fuji film", *Journal of Biomechanics*, Vol. 32 No. 9, pp. 951-958.

Hutson, P.R., Crawford M.E. and Sorkness L.R. (2003), "Liquid chromatographic determination of hydroxiproline in tissue samples", *The Journal of Chromatography B*, Vol. 791 Nos 1/2, pp. 427-430.

ISO (1998), ISO 3274, geometrical products specifications (GPS) – Surface texture: profile Method – Nominal characteristics of contact (stylus) instruments".

ISO 14243-1 (2009), "Implants for surgery – wear of total knee joint prostheses", Zurich.

Jin, Z.M. and Dowson, D. (2005), "Elastohydrodynamic lubrication in biological systems", *Proceedings of the Institution of Mechanical Engineers Part J – Journal of Engineering Tribology*, Vol. 219 No. 5, pp. 367-380.

Kawano, T., Miura, H., Mawatari, T., Moro-Oka, T., Nakanishi, Y., Higaki, H. and Iwamoto, Y. (2013), "Mechanical effects of the intraarticular administration of high molecular weight hyaluronic acid plus phospholipid on synovial joint lubrication and prevention of articular cartilage degeneration in experimental osteoarthritis", *Arthritis & Rheumatism*, Vol. 48 No. 7, pp. 1923-1929.

Krishnan, R., Kopacz, M. and Ateshian, G.A. (2004), "Experimental verification of the role of interstitial fluid pressurization in cartilage lubrication", *Journal of Orthopaedic Research*, Vol. 22 No. 3, pp. 565-570.

Krishnan, R., Mariner, E.N. and Ateshian, G.A. (2005), "Effect of dynamic loading on the frictional response of bovine articular cartilage", *Journal of Biomechanics*, Vol. 38 No. 8, pp. 1665-1773.

Linn, F.C. (1968), "Lubrication of animal joints: II", *Journal of Biomechanics*, Vol. 1 No. 3, pp. 193-205.

Lum, Z.C., Shieh, A.K. and Dorr, L.D. (2018), "Why total knees fail-A modern perspective review", *World Journal of Orthopedics*, Vol. 9 No. 4, pp. 60-64.

Mabuchi, K., Ujihira, M. and Sasadab, T. (1998), "Relationship between the conformity and the lubricating ability of synovial fluid", *Clinical Biomechanics*, Vol. 13 Nos 4/5, pp. 250-255.

Mace, T.A., Zhong, L., Kilpatrick, C., Zynda, E., Lee, C.T., Capitano, M., Minderman, H. and Repasky, E.A. (2011), "Differentiation of CD8$^+$ T cells into effector cells is enhanced by physiological range hyperthermia", *Journal of Leukocyte Biology*, Vol. 90 No. 5, pp. 951-962.

Malekipour, F., Whitton, C., Oetomo, D. and Lee, P.V. (2013), "Shock absorbing ability of articular cartilage and subchondral bone under impact compression", *Journal of the Mechanical Behavior of Biomedical Materials*, Vol. 26, pp. 127-135.

Martin, R.B., Burr, D.B. and Sharkey, N.A. (1998), *Skeletal Tissue Mechanics*, Springer Science & Business Media: New York, NY, pp. 291-304.

MDPI (2016), "Biosafety level criteria centers for disease control and prevention", available at: www.cdc.gov/labs/pdf/CDC-BiosafetyMicrobiologicalBiomedicalLaboratories-2009-P.PDF (accessed 1 February 2016).

Meireles, S., Wesseling, M., Smith, C.R., Thelen, D.G., Verschueren, S. and Jonkers, I. (2017), "Medial knee loading is altered in subjects with early osteoarthritis during gait but not during step-up-and-over task", *PLoS One*, Vol. 12 No. 11, p. e0187583.

Merkher, Y., Sivan, S., Etsion, I., Maroudas, A., Halperin, G. and Yosef, A. (2006), "A rational human joint friction test using a human cartilage-on-cartilage arrangement", *Tribology Letters*, Vol. 22 No. 1, pp. 29-38.

Milner, P.E., Parkes, M., Puetzer, J.L., Chapman, R., Molly Stevens, M.M., Cann, P. and Jeffers, J.R.T. (2018), "A low friction, biphasic and boundary lubricating hydrogel for cartilage replacement", *Acta Biomaterialia*, Vol. 65, pp. 102-111.

Moore, A.C. and Burris, D.L. (2017), "Tribological rehydration of cartilage and its potential role in preserving joint health", *Osteoarthritis and Cartilage*, Vol. 25 No. 1, pp. 99-107.

Patil, S., Steklov, N., Song, L., Bae, W.C. and D'Lima, D.D. (2014), "Comparative biomechanical analysis of human and caprine knee articular cartilage", *The Knee*, Vol. 23, pp. 119-125.

Qian, S. and Ge, S. (2012), "Investigation of contact and friction behavior of natural cartilage by glass slope configuration", *Physics Procedia*, Vol. 33, pp. 85-95.

Rahimizadeh, A., Nourmohammadi, Z., Arabnejad, S., Tanzer, M. and Pasini, D. (2018), "Porous architected biomaterial for a tibial-knee implant with minimum bone resorption and bone-implant interface micromotion", *Journal of the Mechanical Behavior of Biomedical Materials*, Vol. 78, pp. 465-479.

Reimann, I., Stougaard, J. and Northeved, A. (1975), "Measurement of the viscosity of", *Scandinavian Journal of Rheumatology*, Vol. 4 No. 1, pp. 43-48.

Seedom, B.B. and Wallbridge, N.C. (1985), "Walking activities and wear of prostheses", *Annals of the Rheumatic Diseases*, Vol. 44 No. 12, pp. 838-843.

Shiomi, T., Nishii, T., Tamura, S., Tanaka, H., Murase, K., Yoshikawa, H. and Sugano, N. (2012), "Influence of medial meniscectomy on stress distribution of the femoral cartilage in porcine knees: a 3D reconstructed T2 mapping study", *Osteoarthritis and Cartilage*, Vol. 20 No. 11, pp. 1383-1390.

Song, Y., Greve, J.M., Carter, D.R., Koo, S. and Giori, N.J. (2006), "Articular cartilage MR imaging and thickness mapping of a loaded knee joint before and after meniscectomy", *Osteoarthritis and Cartilage*, Vol. 14 No. 8, pp. 728-737.

Su, C., Chen, C., Huang, Y., Chen, S. and Fang, H. (2017), "Optimization of biomolecular additives for a reduction of friction in the artificial joint system", *Tribology International*, Vol. 111, pp. 220-225.

Sugiyama, S., McGowan, M., Phillips, N., Kafi, M. and Young, M. (2007), "Effects of increased ambient temperature during IVM and/or IVF on the in vitro development of bovine zygotes", *Reproduction in Domestic Animals = Zuchthygiene*, Vol. 42 No. 3, pp. 271-274.

Suzuki, T., Hosseini, A., Li, J.S., Gill, T.J. 4th. and Li, G. (2012), "In vivo patellar tracking and patellofemoral cartilage contacts during dynamic stair ascending", *Journal of Biomechanics*, Vol. 45 No. 14, pp. 2432-2437.

Takahashi, Y., Sugano, N., Takao, M., Sakai, T., Nishii, T. and Pezzotti, G. (2014), "Raman spectroscopy investigation of load-assisted microstructural alterations in human knee cartilage: preliminary study into diagnostic potential for osteoarthritis", *Journal of the Mechanical Behavior of Biomedical Materials*, Vol. 31, pp. 77-85.

Unsworth, A. (1995), "Recent developments in the tribology of artificial joints", *Tribology International*, Vol. 28 No. 7, pp. 485-495.

Willing, R., Lapner, M., Lalone, E.A., King, G.J. and Johnson, J.A. (2014), "Development of a computational technique to measure cartilage contact area", *Journal of Biomechanics*, Vol. 47 No. 5, pp. 1193-1197.

Wilusz, R.E., Zauscher, S. and Guilak, F. (2013), "Micromechanical mapping of early osteoarthritic changes in the pericellular matrix of human articular cartilage", *Osteoarthritis and Cartilage*, Vol. 21 No. 12, pp. 1895-1903.

Corresponding author

Hakan Göçerler can be contacted at: Hakan.Gocerler@ac2t.at

177

PAPER IV

Biotribological Tests of Osteochondral Grafts after Treatment with Pro-Inflammatory Cytokines

Christoph Bauer[1] iD **, Hakan Göçerler[2], Eugenia Niculescu-Morzsa[1], Vivek Jeyakumar[1], Christoph Stotter[1,3], Thomas Klestil[3,4], Friedrich Franek[2], and Stefan Nehrer[1]** iD

Abstract

Objective. During osteoarthritis progression, cartilage degrades in a manner that influences its biomechanical and biotribological properties, while chondrocytes reduce the synthesis of extracellular matrix components and become apoptotic. This study investigates the effects of inflammation on cartilage under biomechanical stress using biotribological tests. *Methods.* Bovine osteochondral grafts from five animals were punched out from the medial condyle and treated with or without pro-inflammatory cytokines (interleukin-1β [IL-1β], tumor necrosis factor-α [TNF-α], IL-6) for 2 weeks. After incubation, biotribological tests were performed for 2 hours (alternating 10 minutes test and pause respectively at 39°C, 180 N, 1 Hz, and 2 mm stroke). Before and after testing, the cartilage surface was imaged with a 3-dimensional microscope. During testing, the coefficient of friction (COF) was measured, while gene expression analysis and investigation of metabolic activity of chondrocytes were carried out after testing. Histological sections of the tissue and wear debris from the test fluid were also analyzed. *Results.* After biotribological tests, surface cracks were found in both treated and untreated osteochondral grafts. In treated grafts, the COF increased, and the proteoglycan content in the cartilage tissue decreased, leading to structural changes. Chondrocytes from treated grafts showed increased expression of genes encoding for degradative enzymes, while cartilage-specific gene expression and metabolic activity exhibited no significant differences between treated and untreated groups. No measurable difference in the wear debris in the test fluid was found. *Conclusions.* Treatment of osteochondral grafts with cytokines results in a significantly increased COF, while also leading to significant changes in cartilage proteoglycan content and cartilage matrix compression during biotribological tests.

Keywords

osteoarthritis, cytokines, biotribology, friction, histology

Introduction

Osteoarthritis (OA) is one of the most common degenerative joint diseases worldwide, and frequently affects the hands and weightbearing joints of the body.[1,2] Etiological causes of the disease are diverse. Most common are biochemical imbalances between anabolic and catabolic factors as well as progressive surface degradation caused by mechanical stress.[3] The pathogenesis of OA also leads to the formation of osteophytes, remodeling of the subchondral bone, and inflammation in the joint.[4,5] This inflammation is characterized by the release of pro-inflammatory cytokines such as interleukin-1β (IL-1β), tumor necrosis factor-α (TNF-α), and IL-6 as well as proteolytic mediators like matrix metalloproteinases (MMPs).[6-8] All these factors lead to an imbalance in metabolic homeostasis of the cartilage tissue followed by degradation and alteration of the synovial fluid. As a consequence, the biomechanical and biotribological properties of the joint are influenced,[9,10] which can lead to

chondrocyte apoptosis and reduced synthesis of important components of the extracellular matrix (ECM).

The lubrication of synovial joints involves a complex interaction between different factors such as tissue composition, structure, and mechanics. The excellent friction and wear properties of articular cartilage are achieved by

[1]Department for Health Sciences, Medicine and Research, Center for Regenerative Medicine, Danube University Krems, Krems, Austria
[2]AC2T research GmbH, Wiener Neustadt, Austria
[3]LK Baden-Mödling-Hainburg, Department of Orthopedics and Traumatology, Baden, Austria
[4]Center for Medical Specializations, Department for Health Sciences, Medicine and Research, Danube University Krems, Krems, Austria

Corresponding Author:
Christoph Bauer, Center for Regenerative Medicine, Department for Health Sciences, Medicine and Research, Danube University Krems, Dr. Karl Dorrek Straße 30, Krems, 3500, Austria.
Email: christoph.bauer@donau-uni.ac.at

179

a mixed lubrication regime that includes fluid-film lubrication by synovial fluid and boundary lubrication by thin films on the cartilage surfaces.[11] These properties can be disturbed and negatively affected by inflammation processes such as those occurring in OA. Increased friction in osteoarthritic joints is attributed to decreasing load support of interstitial fluid, which can be squeezed out with the progression of OA, and the altered rheological properties of the synovial fluid.[12-14] In the latter case, the reduced capacity for boundary lubrication, which is associated with a decreased level of lubricin, plays an essential role.[15,16] This further increases the risk of joint damage and the progression of OA.[16,17]

Various studies have used degradative enzymes to examine the biomechanical and biotribological properties of cartilage, investigating changes in the mechanism of fluid support as well as depletion of glycosaminoglycans from the cartilage matrix.[13,18] Both led to an increased coefficient of friction.[13,19] Most tests involved the use of a pin-on-disc tribometer, where the cartilage was not moved against cartilage tissue; instead, other materials—such as metal, ceramic, or glass—were used. However, the natural response of the tissue due to movement and stress on other soft tissue such as cartilage has typically been neglected.[20-22] Understanding the change in the frictional properties of cartilage as well as the role of inflammation in this process may lead to new means of suppressing joint degradation.

The aim of this study was to investigate the influence of pro-inflammatory cytokines on osteochondral grafts in a well-established *ex vivo* test system with biotribological and biological outcome measures. In our experimental setup, both untreated and treated surfaces of osteochondral grafts were slid over one another. Our hypothesis was that treatment with pro-inflammatory cytokines would result in increased surface damage, a higher coefficient of friction, and reduced cartilage-specific parameters (e.g., gene expression, metabolic activity) compared to untreated osteochondral grafts in a cartilage-on-cartilage biotribological test system.

Methods

Specimen Preparation

Five bovine knees were obtained from cows slaughtered between the ages of 18 and 20 months. Under aseptic conditions, osteochondral grafts were harvested from the medial femoral condyle using a Single-Use OATS punch (Arthrex Inc., Naples, FL, USA). Each knee yielded 12 to 16 osteochondral grafts (8 mm diameter, 15 mm height). The osteochondral grafts were washed for 2 hours in phosphate-buffered saline (PBS, Sigma-Aldrich Chemie GmbH, Steinheim, Germany) at 37°C to remove loose bone particles and fatty tissue. The samples were then cut to 8 mm height with a custom-made cartilage holder.

Table 1. Classification of the Test Groups.

		Untested	Biotribologically Tested
Untreated	Group 1	×	
	Group 2		×
Cytokine-treated	Group 3	×	
	Group 4		×

Grouping of the Cartilage Grafts

In total, 4 groups of osteochondral grafts (**Table 1**) were used in this study with 3 osteochondral grafts in each group (2 grafts for metabolic activity and gene expression; 1 graft for histology).

Treatment with Pro-Inflammatory Mediators

Each osteochondral sample of the control and treatment group were cultivated for 2 weeks in 3 mL growth medium (GIBCO DMEM/F12 GlutaMAX-I, Life Technologies, Carlsbad, CA, USA) supplemented with 5% fetal calf serum (FCS; GIBCO, Life Technologies), antibiotics (penicillin 200 U/mL; streptomycin 0.2 mg/mL), amphotericin B 2.5 µg/mL (Sigma-Aldrich Chemie GmbH, Steinheim, Germany), and 0.05 mg/mL ascorbic acid (Sigma-Aldrich Chemie GmbH, Steinheim, Germany). Culture medium was changed every 3 days. In the treatment group, the medium was additionally supplemented with the pro-inflammatory cytokines IL-1β, IL-6 and TNF-α (all 3 were used in a concentration of 10 ng/mL) (Sigma-Aldrich). After 2 weeks of incubation, biotribological tests for each animal were performed within the next 2 days at 39°C. During the testing time (2 hours), the untested group was also kept at 39°C. Before and after testing, the samples were stored at 4°C until both tested and untested osteochondral grafts were analyzed on day 17.

Biotribological Test System

A test system with a specially designed sample holder, which was already applied in previous studies,[23,24] was used and is shown in **Fig. 1**. It performs a reciprocal sliding movement between the osteochondral grafts. These grafts are submerged in a test fluid (in this case PBS) to mimic conditions in the knee joint. The test setup itself encloses a sample holder to ensure sterile conditions throughout the testing process. This is necessary as biological samples should not be exposed to external influences, which may introduce artefacts and interfere in the process of further analysis.

The applied load was 180 N and, considering the contact area of 50.26 mm^2 for 8 mm diameter cartilage samples, an initial estimated average pressure value of 3.57 MPa was
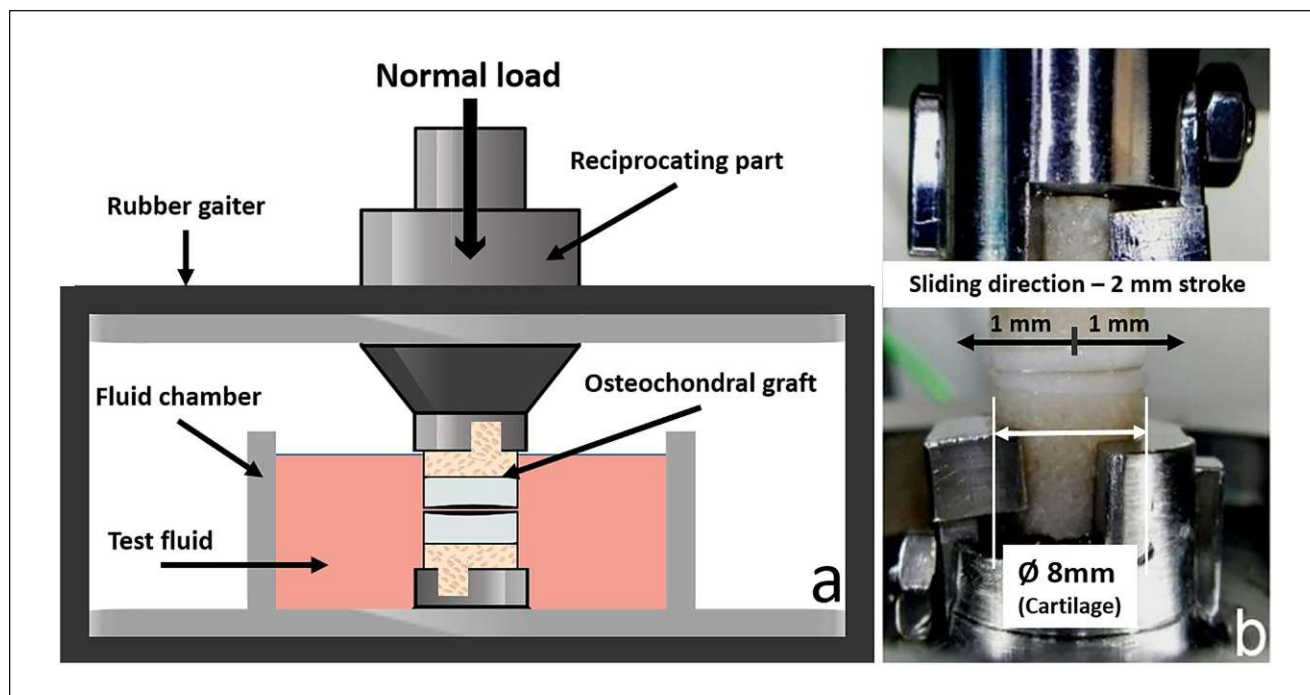
Figure 1. Biotribological test system. (**a**) Schematic of the designed biotribological installation, which was a pin-on-pin setup. (**b**) Image of the cartilage-against-cartilage contact in the biotribo-test system; upper graft holder is reciprocating during the tests with cytokine-treated or untreated osteochondral grafts.

achieved. The plane was assumed flat for all tested cartilage samples. The created tribo-model was a match in terms of contact pressure measurements for the tibiofemoral compartment of a human knee under the normal load of body weight with 0° of flexion.[25] To mimic loading and unloading conditions of the knee during walking, the system was loaded for 10 minutes and then unloaded for another 10 minutes for a total test period of 2 hours (6 cycles) with a stroke of 2 mm and a frequency of 1 Hz.

For transportation purposes, samples that were initially stored at 4°C were equilibrated to room temperature for half an hour, followed by another half an hour in the specimen holder, and then submerged in PBS at a temperature of 39°C (internal bovine body temperature).

Metabolic Activity

Metabolic activity of chondrocytes within the tissue was measured using an XTT-based *ex vivo* toxicology assay kit according to the manufacturer's instructions (Cell Proliferation Kit II, Roche Diagnostics, Basel, Switzerland). Cartilage was cut from the osteochondral grafts with a scalpel and divided longitudinally into two parts for XTT assay and RNA isolation. The cartilage was minced into smaller fragments on a 24-well plate. After tissue weight for each sample was determined, the tissue was incubated in the XTT solution (1 mL medium, 490 μL XTT reagent,

and 10 μL activation reagent) for 4 hours at 37°C; the surrounding air contained 5% (v/v) CO_2. After incubation, the XTT solution was removed and retained. Remaining tetrazolium product in the tissue was extracted by incubation with 0.5 mL dimethyl sulfoxide (DMSO) for 1 hour at room temperature under continual agitation. Then the XTT and DMSO solutions were pooled, and the absorbance was measured at 492 nm and 690 nm (background wavelength) in triplicates in a 96-well plate using a multimode microplate reader (Synergy 2, Winooski, VT, USA) with Gen 5 software. Absorbance was normalized to the wet weight of the tissue.

RNA Isolation

The other half of the cartilage tissue retrieved from the osteochondral grafts was stored in RNAlater (Qiagen, Hilden, Germany) at 4°C for up to 1 week. After storage, the cartilage was minced into smaller fragments and transferred into tubes containing ceramic beads (MagNA Lyser Green Beads, Roche Diagnostics, Basel, Switzerland) with a 300 μL lysis buffer (10 μL β-mercaptoethanol + 290 μL RLT [from Fibrous Tissue Kit, Qiagen, Hilden, Germany]). Until RNA isolation, the tube was stored in liquid nitrogen. For RNA isolation, the tube was thawed and transferred to the MagNA Lyser (Roche Diagnostics, Basel, Switzerland) for homogenization of the cartilage

Table 2. Sequences of Primers and Conditions Used in Quantitative Polymerase Chain Reaction.

Primer	Abbreviation	Sequence (3′–5′)
Glyceraldehyde-3-phophate dehydrogenase	GAPDH	
Forward		ATGTTCCAGTATGATTCCACCC
Probe		AGCTTCCCGTTCTCTGCCTTGAC
Reverse		ATACTCAGCACCAGCATCAC
Aggrecan core protein 1	ACAN	
Forward		ACCTACGATGTCTACTGCTACG
Probe		AGAAGGTGAACTGCTCCAGGCG
Reverse		AGAGTGGCGTTTTGGGATTC
Collagen, type II, alpha 1	COL2A1	
Forward		GTGCAACTGGTCCTCTGG
Probe		CCTTGTTCGCCTTTGAAGCCAGC
Reverse		ACCTCTTTTCCCTTCTTCACC
Matrix metalloproteinase 1	MMP1	
Forward		TTCAACCAGGTGCAGGTATC
Probe		AAATTCATGCGCTGCCACCCG
Reverse		AGCCCCAATGTCAGTAGAATG
Matrix metalloproteinase 13	MMP13	
Forward		CTAAACATCCCAAAACGCCAG
Probe		CCCTTGATGCCATAACCAGTCTCCG
Reverse		ACAGCTCTGCTTCAACCTG

tissue. The homogenization step (6,500 rpm, 20 seconds) was repeated 4 times with a 2-minute cooling phase after each step. According to the manufacturer's instruction, every sample was then incubated with 20 μL proteinase K (from Fibrous Tissue Kit) for 30 minutes for a higher yield. RNA was eluted in 30 μL and stored at −80°C until cDNA synthesis.

Gene Expression Analysis

Gene expression analysis was carried out as previously described.[26] Briefly, cDNA synthesis was performed using Transcriptor First Strand cDNA Synthesis Kit (Roche, Basel, Switzerland). Additionally, RNA from bacteriophage MS2 was added to stabilize the isolated RNA during cDNA synthesis. Real-time quantitative polymerase chain reaction (RT-qPCR) was performed in triplicate using the LightCycler 96 from Roche (Basel, Switzerland). In total, 4 genes—collagen type 2 (COL2A1), aggrecan (ACAN), matrix metalloproteinase-1 (MMP1), and matrix metalloproteinase-13 (MMP13)—were analyzed, while glyceraldehyde-3-phosphate dehydrogenase (GAPDH) was used as housekeeping gene (**Table 2**).

Histology

For histological analysis, osteochondral grafts were fixed in 4% buffered formaldehyde solution (VWR, Radnor, PA, USA) for up to 1 week and decalcified under constant agitation using Osteosoft solution (Merck, Burlington, MA,

USA). After decalcification (duration of 4-6 weeks), the osteochondral grafts were embedded in Tissue-Tek OCT (optimal cutting temperature, VWR, Radnor, PA, USA) and stored at −80°C. Sectioning was done using the CryoStar NX70 Cryostat (Thermo Fischer Scientific, Waltham, MA, USA), with −25°C for the knife temperature and −20°C for the chamber temperature. Six-micrometer sections were obtained and processed for safranin O/light green staining. Images were taken with a Leica DM-1000 microscope and processed using the Leica Manager software (Leica, Wetzlar, Germany). To quantify changes within the cartilage sections stained with safranin O/light green, a modified Mankin scoring system was used (**Table 3**).[27] The assessment was done by 5 independent observers with a maximum score of 15.

Microscopic Images

The InfiniteFocus G5 3D microscope (Alicona Imaging GmbH, Graz, Austria) was used to optically analyze the cartilage surface before and after the test to reveal determinant surface roughness parameters for the biotribological performance of cartilage tissues. PBS was added every 5 minutes to prevent the cartilage surface from drying out. The InfiniteFocus G5 uses Focus Variation technology, combining the small depth of focus of an optical system with vertical scanning to provide topographical and color information from the variation of focus. Due to the vertical movement of the precision optics along the optical axis with continuously capturing data from the surface, each region of the object

Table 3. Components of the Modified Mankin Scoring System.

Structure	Cellularity	Matrix Staining	Tidemark Integrity	Score
Smooth surface/normal	Normal arrangement	Normal staining	Normal and intact	0
Roughened surface/single crack or area of delamination	Clustering in superficial layer or loss of cells up to 10%	Slight loss of stain	Disrupted	1
Multiple cracks/moderate delamination	Disorganization or loss up to 25%	Moderate loss of stain	×	2
Fragmentation in cartilage or severe delamination	Cell rows absent or loss up to 50%	Severe loss of stain	×	3
Loss of fragments	Very few cells present	No stain present	×	4
Complete erosion to tidemark	×	×	×	5
Erosion beyond tidemark	×	×	×	6

can be sharply focused. Algorithms convert the acquired sensor data into 3-dimensional information and a true color image with full depth of field. This is achieved by analyzing the variation of focus along the vertical axis. The initial image of the cartilage was further processed to obtain a surface profile. This method was described in our previous study in detail.[23]

Sulfated Glycosaminoglycans (sGAG)

The quantification of sGAG was performed according to Barbosa *et al.*[28] In brief, fluid (PBS) used during biotribological tests was treated overnight with 25 U/mL proteinase K (Sigma-Aldrich, St. Louis, MO, USA) at 56°C. After inactivation of the enzyme (90°C, 10 minutes), the fluid was collected in ultra-free filter reaction tubes of 0.1 µm pore size (Millipore, Burlington, MA, USA) and centrifuged (12,000g, 4 minutes, room temperature). One milliliter of a 1,9-dimethyl-methylene blue solution (DMMB) was added to 100 µL filtrate and vigorously mixed to allow the formation of complexes of DMMB and sGAG in the sample. The complexes were pelleted via centrifugation (12,000g, 10 minutes, room temperature) and subsequently dissolved in a decomplexation solution. After 30 minutes of shaking, the absorbance was measured at 656 nm photometrically using an Ultrospec 3300 pro spectrophotometer (Amersham Bioscience plc, Amersham, UK). The sGAG amount was calculated from a standard curve with shark chondroitin sulphate (Sigma-Aldrich, St. Louis, MO, USA). The measurement for both treated and untreated posttesting osteochondral grafts was performed in duplicate.

Hydroxyproline (HYP) Assay

Total collagen content was determined by quantifying the hydroxyproline content. Test fluid, after biotribological tests, was hydrolysed in 6 M HCl at 110°C for 18 hours and the hydroxyproline content from the hydrolyzed solution was measured with a chloramine-T/Ehrlich spectrophotometry-based assay at a wavelength of 560 nm.

Statistical Analysis

All statistical analysis was performed using GraphPad Prism Software (GraphPad Prism Software Inc., San Diego, CA, USA). The statistical analysis was carried out using a 1-way analysis of variance. Multiple comparisons were performed via a nonparametric Kruskal-Wallis test followed by Dunn's post hoc test. Data from the metabolic activity and gene expression are shown in a box plot to represent median, first quartile, and third quartile, with error bars indicating maximum and minimum values. Where outliers were present, dots above or below are shown. The values for the coefficient of friction are reported as means ± standard error of the mean (means ± SEM). Statistical significance was set at $P < 0.05$.

Results

Osteochondral Grafts

Punched out osteochondral grafts for biotribological tests had a symmetrical flat surface in almost every sample used for the experiments. Asymmetric grafts, which were not possible to avoid, were used for the untested control and treatment group as flatness was not a critical factor as it was for grafts used in biotribological tests.

Metabolic Activity of the Cells

The metabolic activity of chondrocytes in osteochondral grafts showed no differences between the untested (control and cytokine-treated) groups. Metabolic activity of the tested control group was significantly lower (4-fold of the median value) than the untested control group (**Fig. 2**). Cytokine treatment of osteochondral grafts showed similar results (2-fold decrease of the median value) with some
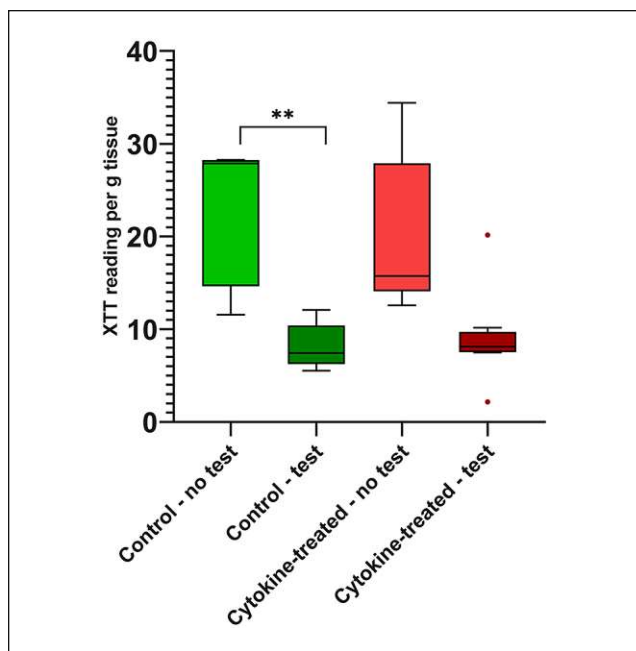
Figure 2. Measurement of the metabolic activity. Chondrocytes from tested and untested osteochondral grafts after treatment with and without pro-inflammatory cytokines were analyzed concerning their metabolic activity using XTT assay. $n = 5$ animals/group; $**P < 0.01$. Data are expressed as median and range with Tukey box-and-whisker plot: lower box = 75 percentile, upper box = 25 percentile, whisker = nonoutlier range, dot = outlier (>1.5-fold above/below the box).

outliers in the tested group, resulting in a nonsignificant difference.

Expression of Anabolic and Catabolic Cartilage-Specific Genes

For the analysis of gene expression, specific bovine primers were designed and tested successfully regarding optimal temperature values for primer annealing. After 17 days, the anabolic marker COL2A1 showed a nonsignificant difference in the untested groups, whereas the expression of osteochondral grafts treated with pro-inflammatory cytokines tended to be decreased (**Fig. 3a**). After the biotribological tests, an approximately 2-fold increase in median value could be observed in both groups when compared to the untested groups, but this was not statistically significant. The analysis of ACAN (**Fig. 3b**), another anabolic marker, showed a very similar expression pattern. Here, the treatment with cytokines led to a reduction of ACAN gene expression in the untested group and tended to be increased in a nonsignificant manner after the test. Gene expression values of the control groups were on the same level before and after testing with no statistical significance in comparison to the treatment groups.

In addition, **Figure 3** shows the expression of the catabolic genes MMP1 (**Fig. 3c**) and MMP13 (**Fig. 3d**), 2 genes involved in the breakdown of interstitial collagens (e.g., types I, II, and III). The occurrence of pro-inflammatory cytokines led to a significantly increased expression of MMP1 in the untested and tested group compared with both control groups (tested and untested), where levels were near the detection limit. The gene MMP13 was also highly expressed with cytokine treatment, to the degree that a significant difference could not be shown between treated and untreated groups. After biotribological tests, the expression of MMP13 remained on a constant level when comparing tested versus untested groups.

Microscope Images

Prior to biotribological tests, microscopic images of the surfaces of untreated and treated osteochondral grafts showed no cracks and fissures (**Fig. 4**) or other microscopically visible damages. Only height differences of up to 90 μm in the starting material were observed. However, our focus was on the formation of superficial cracks and fissures, which are caused by the applied load under physiological conditions (3.57 MPa). **Fig. 4** also shows that the specifically applied load causes cracks and fissures in cartilage tissue, but without differences between cytokine-treated and untreated osteochondral grafts. The extent of surface changes ranged from deep trenches (up to 250 μm) to small superficial cracks (up to 20 μm). Since all grafts examined showed similar damage after biotribological tests, it was impossible to define a difference in cartilage surface between untreated and treated groups.

Histology

For histological analysis, safranin O/light green staining was performed as shown in **Fig. 5** and used as an additional means of finding any differences (e.g., cracks or fissures) between untreated and treated osteochondral grafts in a biotribologically tested and untested state.

Osteochondral grafts in the control group retained a higher amount of proteoglycans in the untested state, which could slightly differ from graft to graft as a result of different harvesting locations. In comparison, proteoglycan content in the untested treatment group was highly reduced. Here, safranin O only stained proteoglycans in deeper layers of the cartilage, which are rich in proteoglycans. As a result, much higher differences between the control and treatment group were shown after the biotribological tests. In both biotribologically tested groups, cracks and fissures appeared on the cartilage surface as observed in microscopic images. In the control group, proteoglycan content was not influenced as the detected staining intensity was similar to the untested samples. Osteochondral grafts of the treatment group
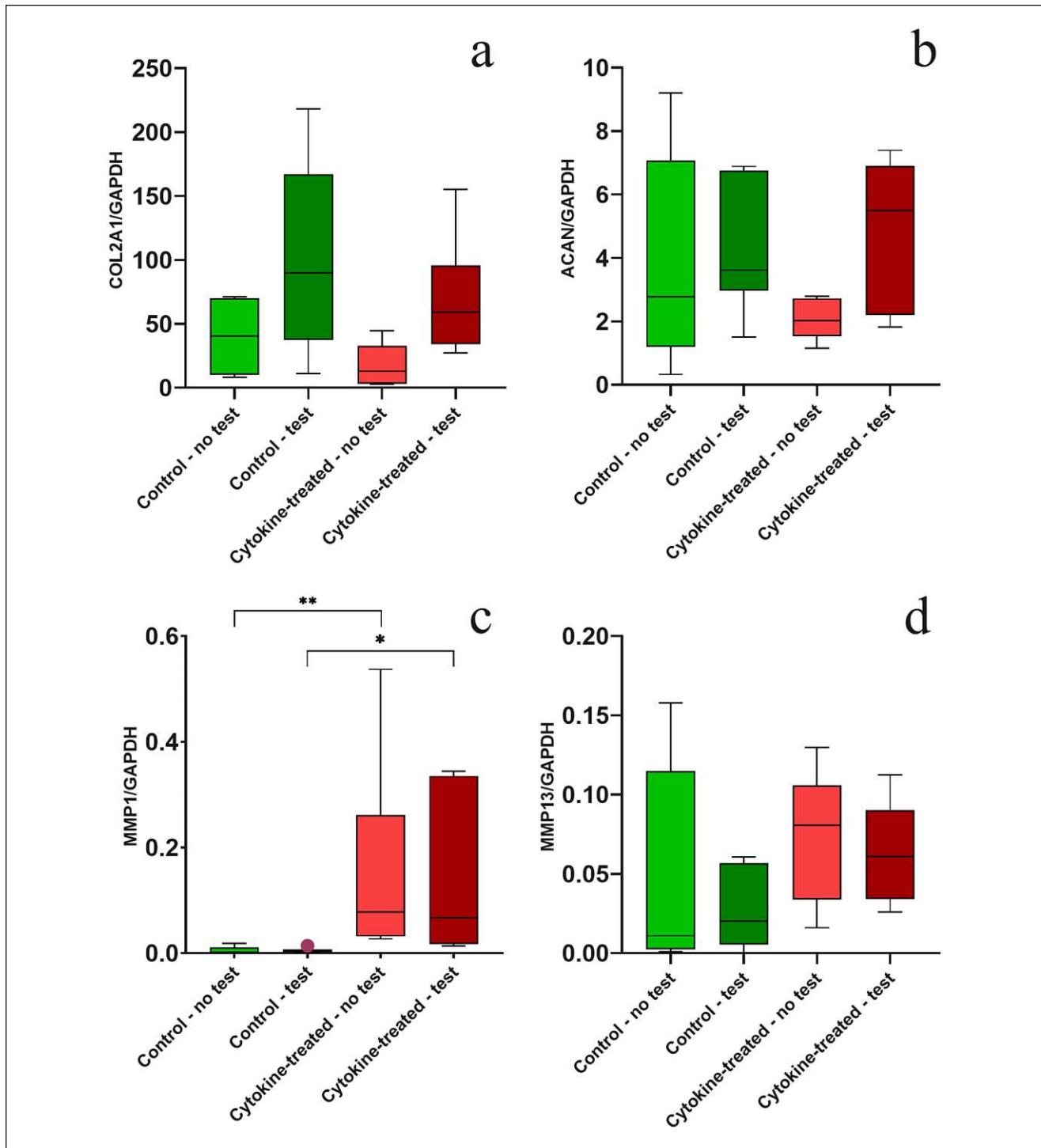
Figure 3. Gene expression analysis of (**a**) COL2A1, (**b**) ACAN, (**c**) MMP1, and (**d**) MMP13 in biotribologically tested and untested osteochondral grafts with and without pro-inflammatory cytokine treatment. $n = 5$ animals/group; *$P < 0.05$, **$P < 0.001$. Data are expressed as median and range with Tukey box-and-whisker plot: lower box = 75 percentile, upper box = 25 percentile, whisker = nonoutlier range, dot = outlier ($>$1.5-fold above/below the box).

demonstrated a further reduced proteoglycan content in the tested state in comparison with the untested samples, indicating an influence by biotribological tests. Furthermore,

histological sections not only exhibited superficial changes with cracks and fissures, but also a compression of the cartilage tissue itself. Here, pro-inflammatory cytokine treatment
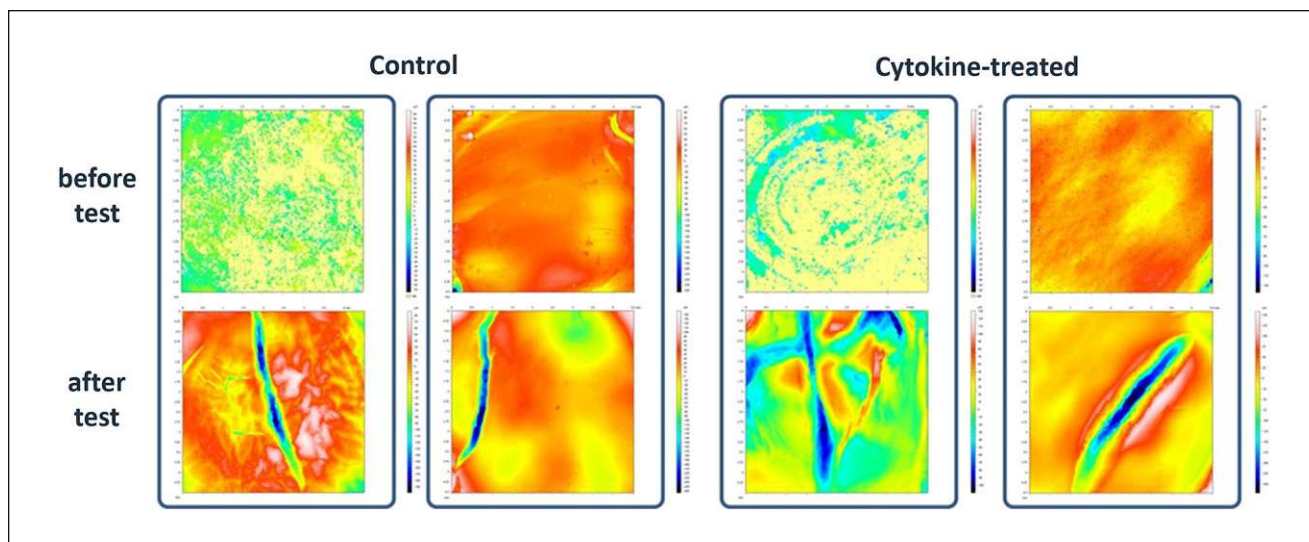
Figure 4. Alicona 3-dimensional microscope images. Representing images of major changes on the cartilage surface structure before and after biotribological tests for untreated and cytokine-treated osteochondral grafts.
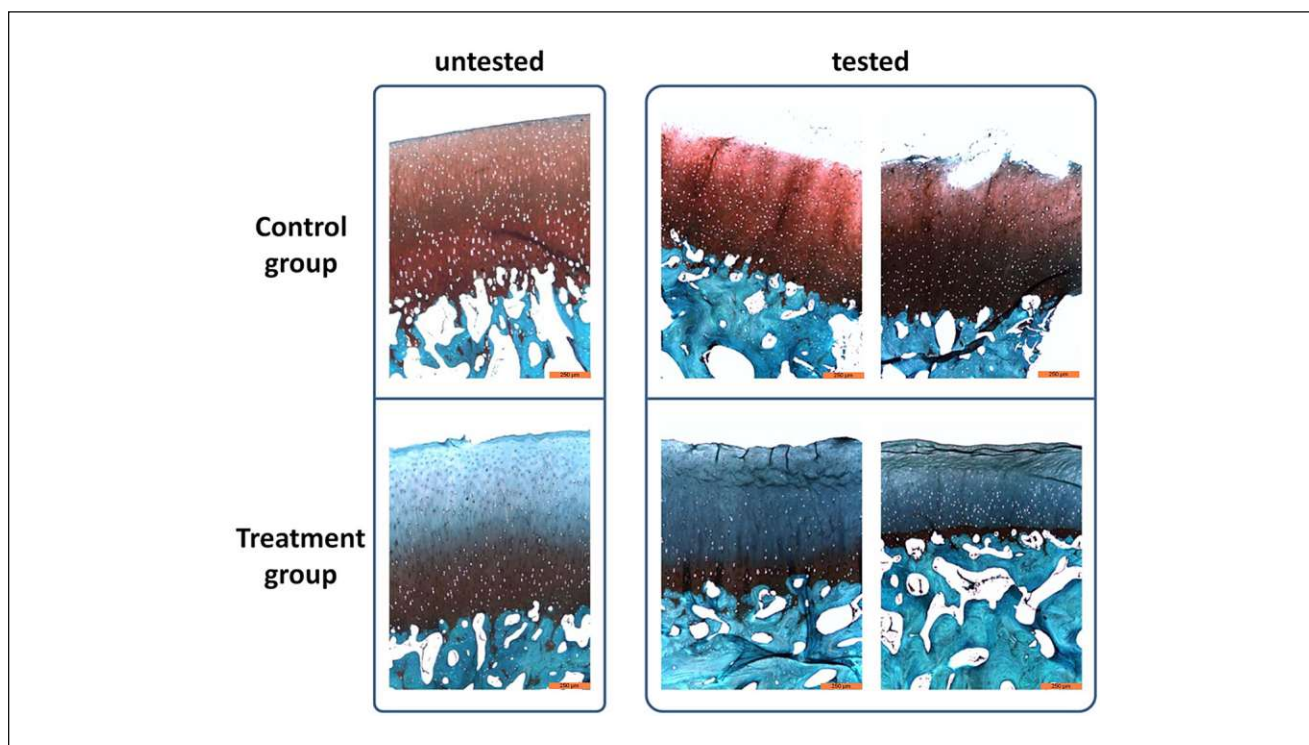

Figure 5. Histological assessment of osteochondral grafts. Exemplary histological images of cytokine-treated and untreated grafts in a biotribologically tested and untested state stained with safranin O/light green. Scale bar 250 µm.

of osteochondral grafts aggravates the extrusion of interstitial fluid during mechanical loading. In addition to the vertical cracks, horizontal cracks appeared within the cartilage tissue. The evaluation of the histological sections using a modified Mankin Scoring System showed the qualitative differences quantitatively. In the untested control, the 5 observers agreed and rated it with 0 points. In comparison, the samples in an untested state and treated with cytokines achieved a mean value of 4.4 points. The biotribologically tested osteochondral grafts received a mean score of 3.2
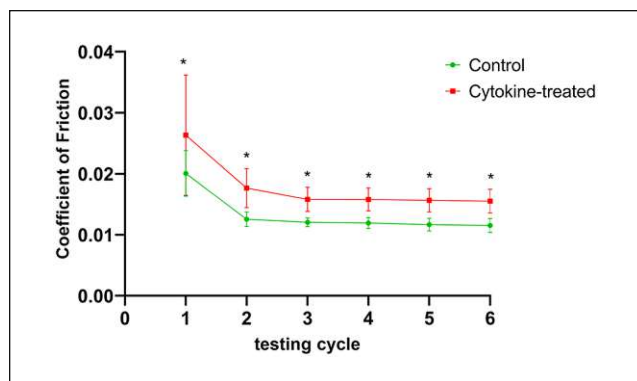
Figure 6. Coefficient of friction. During biotribological tests, the coefficient of friction was measured continuously; Calculation of mean values of untreated (green) and cytokine-treated (red) osteochondral grafts was performed from each test cycle (10 minutes of testing) of a total test period of 2 hours. $n = 5$ animals/group; $*P < 0.05$.

points in the untreated state, while the cytokine-treated and -tested samples achieved a mean score of 8.

Coefficient of Friction

During biotribological tests, the coefficient of friction (COF) was recorded in each of the 6 cycles with significantly higher values measured in the first cycle in both the control (0.0200) and treatment group (0.0263) compared with subsequent cycles (**Fig. 6**). During the course of two-hour testing, the COF values for both groups reached a corresponding level from the second test cycle on. The control group values ranged between 0.0115 and 0.0125, while treatment group values were within a range of 0.0155 to 0.0176. Comparison of both groups showed a significant difference in COF for each test cycle.

sGAG and HYP in the Supernatant after Testing

After biotribological testing of osteochondral grafts (control and treatment group), the test fluids (PBS) were collected and measured for their content of released or abraded sulfated glycosaminoglycans (sGAG), as well as for their hydroxyproline (HYP) content. There was no significant difference in sGAG content between treated and untreated osteochondral grafts in our test setup. Both groups in **Fig. 7** showed similar values for the respective test fluids after biotribological tests. In addition, hydroxyproline could not be detected in the test fluids of either group (no figure is shown).

Discussion

The aim of this study was to identify possible differences between biotribologically tested and untested osteochondral
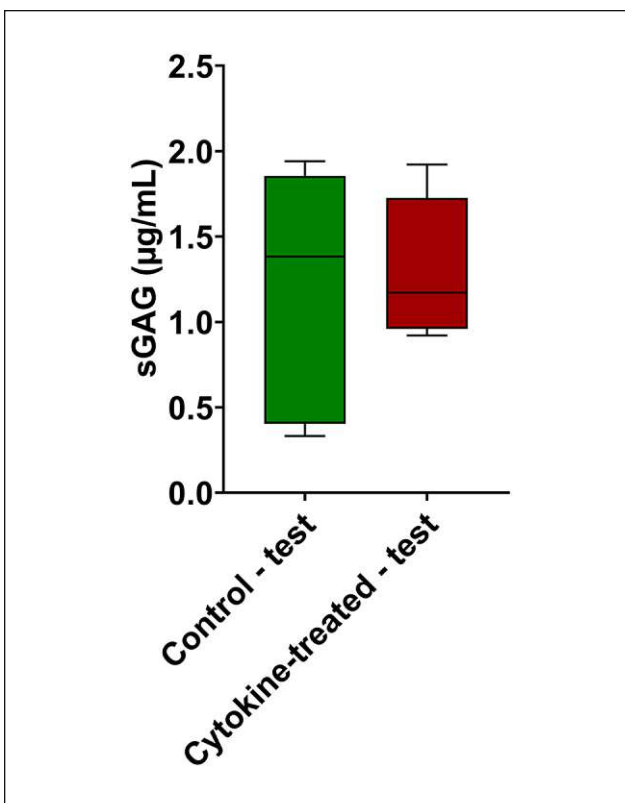

Figure 7. Quantification of sulfated glycosaminoglycans (sGAG). sGAG concentrations measured in the collected test fluids of cytokine-treated and untreated osteochondral grafts after biotribological tests. $n = 5$ animals/group. Data are expressed as median and range with Tukey box-and-whisker plot: lower box = 75 percentile, upper box = 25 percentile, whisker = nonoutlier range.

grafts pretreated with and without pro-inflammatory cytokines. The grafts were taken from bovine cartilage of the medial-femoral condyle for reproducibility and availability, treated with cytokines and tested in an established cartilage-on-cartilage biotribological test system. In our experiments, we were able to show that treatment with pro-inflammatory cytokines leads to changes in the proteoglycan content of the cartilage, which is an already known phenomenon.[29] Additionally, the applied force during biotribological tests leads to a compression of the cartilage matrix of treated osteochondral grafts. This compression could be the reason for the higher coefficient of friction measured in treated osteochondral grafts. The metabolic activity of the cells was only influenced by the biotribological test itself, while the gene expression of cartilage-specific and catabolic markers showed only small differences between the treated and untreated groups. No differences were observed in microscopic images of the cartilage surface after testing, except for cracks appearing in both test groups.

As shown in our previous study,[23] the use of a cartilage-on-cartilage test system reflects native physiological conditions more accurately than testing against a metal or glass counterpart. This test setup is particularly advantageous when imitating inflammatory reactions, as this approach not only depends on the test fluid but also on how the cartilage matrix of both osteochondral grafts changes during treatment. The fact that the test system used here has a normal force of 180 N and thus exerts a pressure of 3.57 MPa on the cartilage surface of the osteochondral grafts ensures constant contact between the cartilage surfaces. The pressure achieved is comparable to pressure measurements of the tibial-femoral compartment in a human knee joint under normal physical load.[25]

The choice of cytokines in our study was limited to IL-1β, TNF-α, and IL-6, which are the most studied cytokines in relation to OA.[30] IL-1β and TNF-α are the most important pro-inflammatory cytokines in this context, playing an important role in the pathogenesis and progression of the disease, while IL-6, which is secreted by chondrocytes especially when exposed to a stimulus like IL-1β,[31,32] is considered a potential biomarker for early OA. These cytokines are first produced in the tissue and then released into the synovial fluid, resulting in the promotion of catabolic processes and enzymatic cartilage degradation.[33] This is in accordance with findings in patients suffering from knee OA, where pro-inflammatory cytokines were detected in synovial fluid, cartilage and synovial membranes.[34-36] The cytokine concentrations of 10 ng/mL used in this study are much higher than those found in synovial fluids taken from OA patients.[37,38] However, these high concentrations were used to achieve a rapid effect on the cartilage tissue, which was reached after a two week period of incubation of the osteochondral grafts. This effect was confirmed by the strongly reduced proteoglycan content of the cartilage tissue shown in histological observations. Although this study only focused on this limited array of cytokines, it should be mentioned that there are other pro-inflammatory factors in the synovial fluid of patients. Though they are typically present in smaller quantities, their effect on osteochondral grafts could still be of relevance.

During biotribological tests, the coefficient of friction was measured as an indicator of mechanical stress. In the healthy knee joint, this unitless number is around 0.005.[39] In our tests, this value could not be achieved, probably due to PBS test fluid being used as a substitute for synovial fluid. The values for the untreated osteochondral grafts varied between 0.0115 and 0.0125, which is comparable to lower levels measured in untreated grafts in our previous study.[23] However, treatment with pro-inflammatory cytokines increased the coefficient of friction, with values measured between 0.0155 and 0.0176. This increase can probably be explained by the fact that the biotribological tests compressed the cartilage of the treated grafts and caused unevenness on the surface.

The surface of the osteochondral grafts was examined both before and after biotribological tests using an optical microscope. Prior to the tests, the surface of the untreated and treated group exhibited no damage, which indicates that the cartilage surface is not damaged during harvesting of the osteochondral grafts. After biotribological tests, cracks with a depth of up to 250 μm appeared in both treated and untreated groups. The shape and appearance of these surface cracks are comparable to other studies,[40,41] including our previous study.[23] For an additional assessment of the surface and extracellular matrix components of the cartilage tissue, histological sections of the osteochondral grafts were stained with safranin O/light green. These tests revealed that the proteoglycan content was significantly decreased in osteochondral grafts treated with pro-inflammatory cytokines. Similar results were shown by Gitelis *et al.*,[42] when the cartilage tissue was incubated in a pro-inflammatory environment. Furthermore, histological images from treated grafts showed a level of proteoglycans comparable to Mankin Osteoarthritis Score 2 or OARSI (Osteoarthritis Research Society International) grade 2 to 3.[43,44] This indicates that our treatment with cytokines had an effect comparable to a grade of degenerative OA. Subsequent biotribological tests in treated osteochondral grafts led to compression of the cartilage matrix with vertical tears in the tissue. In untreated samples, these changes did not occur. The altered biomechanical properties of the tested cartilage can thus be attributed to the loss of proteoglycans, as there was a decrease in compressive modulus of cartilage while the tissue was exposed to higher loads while being subjected to mechanical stress.[29]

Adding pro-inflammatory cytokines to the culture medium of osteochondral grafts reduced the expression of cartilage-specific genes such as collagen type 2 and aggrecan. It is well established that the cytokines used in this study reduce or inhibit the synthesis of these genes.[37,45,46] The mechanical stress applied during biotribological tests reversed this reduction and also led to an increased expression in the untreated samples, especially the expression of collagen type 2. That mechanical stimulus can have such an effect has been demonstrated by several studies.[47,48] Similarly, the expression of degradative enzymes was increased by pro-inflammatory cytokines, which further confirms that the culture conditions created for this study were similar to those found in OA. An increase of MMPs gene expression in bovine chondrocytes was also shown by Lv *et al.*[49] when using IL-1β for the treatment of cartilage. In addition, this study was able to show that a dynamic mechanical stress in the physiological range does not lead to a difference in gene expression of MMPs.[49] This was also confirmed by Fehrenbacher *et al.*,[50] where a change in MMPs gene expression only occurs from about 12 MPa

upward. The pressure of 3.57 MPa used in our study is within the physiological range and consequently had no effect on the gene expression of MMPs.

However, there are also some limitations to the current study that have to be taken into account. The experimental setup is an *ex vivo* model, which is difficult to compare with physiological conditions as there may occur abnormal loading conditions due to the fact that surrounding tissue is lacking. In addition, no strong conclusions regarding the biological and biomechanical properties of human cartilage can be made based on experiments with bovine cartilage. A further limitation is the use of 3 cytokines, while the synovial fluid of an OA patient contains many other pro-inflammatory and anti-inflammatory mediators. Additionally, under real-world conditions, damage to cartilage would usually occur over a longer duration. Here, only short-term effects on cartilage tissue are shown. Another limitation lies in the fact that the PBS test fluid used in this study is not comparable to synovial fluid, which also contains nutrients and lubricants (e.g., hyaluronic acid). Consequently, only a limited evaluation of cartilage metabolism based on the tested conditions is possible.

In conclusion, the present study shows that the treatment of osteochondral grafts with pro-inflammatory cytokines leads to a decrease in proteoglycan levels in the treated cartilage, which is comparable to progressive degenerative OA. Under a physiological load the decrease leads to changes in the biomechanical and biotribological properties of the cartilage with significant changes in tissue structure. These observations could provide new insights into how cartilage and chondrocytes behave under the similar conditions found in OA.

Authors' Note

Acknowledgments and Funding

Declaration of Conflicting Interests

Ethical Approval

Ethical approval for this study was obtained from the Regional Ethical Committee (GS4-EK-4/199-2016).

ORCID iDs

Christoph Bauer (iD) https://orcid.org/0000-0002-5142-3834

Stefan Nehrer (iD) https://orcid.org/0000-0001-8008-2226

References

1. Berenbaum F. Osteoarthritis as an inflammatory disease (osteoarthritis is not osteoarthrosis!). Osteoarthritis Cartilage. 2013;21(1):16-21.

2. Lawrence RC, Helmick CG, Arnett FC, Deyo RA, Felson DT, Giannini EH, *et al*. Estimates of the prevalence of arthritis and selected musculoskeletal disorders in the United States. Arthritis Rheum. 1998;41(5):778-99.

3. Neu CP, Khalafi A, Komvopoulos K, Schmid TM, Reddi AH. Mechanotransduction of bovine articular cartilage superficial zone protein by transforming growth factor β signaling. Arthritis Rheum. 2007;56(11):3706-14.

4. Martel-Pelletier J, Boileau C, Pelletier JP, Roughley PJ. Cartilage in normal and osteoarthritis conditions. Best Pract Res. 2008;22(2):351-84.

5. Ayhan E, Kesmezacar H, Akgun I. Intraarticular injections (corticosteroid, hyaluronic acid, platelet rich plasma) for the knee osteoarthritis. World J Orthop. 2014;5(3):351-61.

6. Wolk K, Witte K, Witte E, Raftery M, Kokolakis G, Philipp S, *et al*. IL-29 is produced by TH17 cells and mediates the cutaneous antiviral competence in psoriasis. Sci Transl Med. 2013;5(204):204ra129.

7. Steenvoorden MMC, Bank RA, Ronday HK, Toes REM, Huizinga TWJ, DeGroot J. Fibroblast-like synoviocyte-chondrocyte interaction in cartilage degradation. Clin Exp Rheumatol. 2007;25(2):239-45.

8. Arend WP. The balance between IL-1 and IL-1Ra in disease. Cytokine Growth Factor Rev. 2002;13(4-5):323-40.

9. Bowland P, Ingham E, Jennings L, Fisher J. Review of the biomechanics and biotribology of osteochondral grafts used for surgical interventions in the knee. Proc Inst Mech Eng H. 2015;229(12):879-88.

10. Musumeci G, Trovato FM, Pichler K, Weinberg AM, Loreto C, Castrogiovanni P. Extra-virgin olive oil diet and mild physical activity prevent cartilage degeneration in an osteoarthritis model: an in vivo and in vitro study on lubricin expression. J Nutr Biochem. 2013;24(12):2064-75.

11. Jahn S, Seror J, Klein J. Lubrication of articular cartilage. Annu Rev Biomed Eng. 2016; 18:235-258.

12. Basalo IM, Mauck RL, Kelly TAN, Nicoll SB, Chen FH, Hung CT, *et al*. Cartilage interstitial fluid load support in unconfined compression following enzymatic digestion. J Biomech Eng. 2004;126(6):779-86.

13. Basalo IM, Raj D, Krishnan R, Chen FH, Hung CT, Ateshian GA. Effects of enzymatic degradation on the frictional response of articular cartilage in stress relaxation. J Biomech. 2005;38(6):1343-9.

14. Wright V, Dowson D. Lubrication and cartilage. J Anat. 1976;121(Pt 1):107-18.

15. Teeple E, Elsaid KA, Fleming BC, Jay GD, Aslani K, Crisco JJ, *et al*. Coefficients of friction, lubricin, and cartilage damage in the anterior cruciate ligament-deficient guinea pig knee. J rthop Res. 2008;26(2):231-7.

16. Elsaid KA, Fleming BC, Oksendahl HL, Machan JT, Fadale PD, Hulstyn MJ, *et al*. Decreased lubricin concentrations and markers of joint inflammation in the synovial fluid of patients with anterior cruciate ligament injury. Arthritis Rheum. 2008;58(6):1707-15.

17. Rhee DK, Marcelino J, Baker M, Gong Y, Smits P, Lefebvre V, *et al*. The secreted glycoprotein lubricin protects cartilage surfaces and inhibits synovial cell overgrowth. J Clin Invest. 2005;115(3):622-31.

18. Pastrama MI, Ortiz AC, Zevenbergen L, Famaey N, Gsell W, Neu CP, *et al*. Combined enzymatic degradation of proteoglycans and collagen significantly alters intratissue strains in articular cartilage during cyclic compression. J Mech Behav Biomed Mater. 2019;98:383-94.

19. Kumar P, Oka M, Toguchida J, Kobayashi M, Uchida E, Nakamura T, *et al*. Role of uppermost superficial surface layer of articular cartilage in the lubrication mechanism of joints. J Anat. 2001;199(Pt 3):241-50.

20. Moore AC, Burris DL. Tribological and material properties for cartilage of and throughout the bovine stifle: Support for the altered joint kinematics hypothesis of osteoarthritis. Osteoarthritis Cartilage. 2015;23(1):161-9.

21. Zhou ZR, Jin ZM. Biotribology: recent progresses and future perspectives. Biosurface Biotribol. 2015;1(1):3-24.

22. Trevino RL, Stoia J, Laurent MP, Pacione CA, Chubinskaya S, Wimmer MA. Establishing a live cartilage-on-cartilage interface for tribological testing. Biotribology (Oxf). 2017;9:1-11.

23. Bauer C, Göçerler H, Niculescu-Morzsa E, Jeyakumar V, Stotter C, Tóth I, *et al*. Effect of osteochondral graft orientation in a biotribological test system. J Orthop Res. 2019;37(3):583-92.

24. Göçerler H, Pfeil B, Franek F, Bauer C, Niculescu-Morzsa E, Nehrer S. The dominance of water on lubrication properties of articular joints. Ind Lubr Tribol. 2020;72(1):31-7.

25. Patil S, Steklov N, Song L, Bae WC, D'Lima DD. Comparative biomechanical analysis of human and caprine knee articular cartilage. Knee. 2014;21(1):119-25.

26. Bauer C, Niculescu-Morzsa E, Nehrer S. A protocol for gene expression analysis of chondrocytes from bovine osteochondral plugs used for biotribological applications. MethodsX. 2017;4:423-8.

27. Henson FMD, Vincent TA. Alterations in the vimentin cytoskeleton in response to single impact load in an in vitro model of cartilage damage in the rat. BMC Musculoskelet Disord. 2008;9:94.

28. Barbosa I, Garcia S, Barbier-Chassefière V, Caruelle JP, Martelly I, Papy-García D. Improved and simple micro assay for sulfated glycosaminoglycans quantification in biological extracts and its use in skin and muscle tissue studies. Glycobiology. 2003;13(9):647-53.

29. Maldonado M, Nam J. The role of changes in extracellular matrix of cartilage in the presence of inflammation on the pathology of osteoarthritis. Biomed Res Int. 2013;2013:284873.

30. Nees TA, Rosshirt N, Zhang JA, Reiner T, Sorbi R, Tripel E, *et al*. Synovial cytokines significantly correlate with osteoarthritis-related knee pain and disability: inflammatory mediators of potential clinical relevance. J Clin Med. 2019;8(9):1343.

31. Stannus O, Jones G, Cicuttini F, Parameswaran V, Quinn S, Burgess J, *et al*. Circulating levels of IL-6 and TNF-α are associated with knee radiographic osteoarthritis and knee cartilage loss in older adults. Osteoarthritis Cartilage. 2010;18(11):1441-7.

32. Kapoor M, Martel-Pelletier J, Lajeunesse D, Pelletier JP, Fahmi H. Role of proinflammatory cytokines in the pathophysiology of osteoarthritis. Nat Rev Rheumatol. 2011;7:33-42.

33. Schaible HG. Mechanisms of chronic pain in osteoarthritis. Curr Rheumatol Rep. 2012;14:549-56.

34. Schlaak JF, Pfers I, Meyer Zum Büschenfelde KH, Märker-Hermann E. Different cytokine profiles in the synovial fluid of patients with osteoarthritis, rheumatoid arthritis and seronegative spondylarthropathies. Clin Exp Rheumatol. 1996;14(2):155-62.

35. Ning L, Ishijima M, Kaneko H, Kurihara H, Arikawa-Hirasawa E, Kubota M, *et al*. Correlations between both the expression levels of inflammatory mediators and growth factor in medial perimeniscal synovial tissue and the severity of medial knee osteoarthritis. Int Orthop. 2011;35(6):831–8.

36. Moos V, Fickert S, Müller B, Weber U, Sieper J. Immunohistological analysis of cytokine expression in human osteoarthritic and healthy cartilage. J Rheumatol. 1999;26(4):870-9.

37. Chadjichristos C, Ghayor C, Kypriotou M, Martin G, Renard E, Ala-Kokko L, *et al*. Sp1 and Sp3 transcription factors mediate interleukin-1β down-regulation of human type II collagen gene expression in articular chondrocytes. J Biol Chem. 2003;278(41):39762-72.

38. Mabey T, Honsawek S, Tanavalee A, Yuktanandana P, Wilairatana V, Poovorawan Y. Plasma and synovial fluid inflammatory cytokine profiles in primary knee osteoarthritis. Biomarkers. 2016;21(7):639-44.

39. Majd SE, Rizqy AI, Kaper HJ, Schmidt TA, Kuijer R, Sharma PK. An in vitro study of cartilage–meniscus tribology to understand the changes caused by a meniscus implant. Colloids Surfaces B Biointerfaces. 2017;155:294-303.

40. Fick JM, Espino DM. Articular cartilage surface rupture during compression: Investigating the effects of tissue hydration in relation to matrix health. J Mech Behav Biomed Mater. 2011;4(7):1311-7.

41. Malekipour F, Whitton C, Oetomo D, Lee PVS. Shock absorbing ability of articular cartilage and subchondral bone under impact compression. J Mech Behav Biomed Mater. 2013;26:127-35.

42. Gitelis SL, Bodker A, Laurent MP, Kirk SS, Filardo G, Meyer MA, *et al*. The effect of surgical insertion and proinflammatory cytokines on osteochondral allograft survival and metabolism. Cartilage. 2018;9(3):284-92.

43. Pauli C, Whiteside R, Heras FL, Nesic D, Koziol J, Grogan SP, *et al*. Comparison of cartilage histopathology assessment systems on human knee joints at all stages of osteoarthritis development. Osteoarthritis Cartilage. 2012;20(6):476-85.

44. Pritzker KPH, Gay S, Jimenez SA, Ostergaard K, Pelletier JP, Revell K, *et al*. Osteoarthritis cartilage histopathology: grading and staging. Osteoarthritis Cartilage. 2006;14(1):13-29.

45. Porée B, Kypriotou M, Chadjichristos C, Beauchef G, Renard E, Legendre F, *et al*. Interleukin-6 (IL-6) and/or soluble IL-6 receptor down-regulation of human type II collagen gene expression in articular chondrocytes requires a decrease of Sp1·Sp3 ratio and of the binding activity of both factors to the COL2A1 promoter. J Biol Chem. 2008;283(8):4850-65.

46. Lefebvre V, Peeters-Joris C, Vaes G. Modulation by interleukin 1 and tumor necrosis factor α of production of collagenase, tissue inhibitor of metalloproteinases and collagen types in differentiated and dedifferentiated articular chondrocytes. Biochim Biophys Acta. 1990;1052(3):366-78.

47. Correro-Shahgaldian MR, Colombo V, Spencer ND, Weber FE, Imfeld T, Gallo LM. Coupling plowing of cartilage explants with gene expression in models for synovial joints. J Biomech. 2011;44(13):2472-6.

48. Schätti OR, Gallo LM, Torzilli PA. A model to study articular cartilage mechanical and biological responses to sliding loads. Ann Biomed Eng. 2016;44(8):2577-88.

49. Lv M, Zhou Y, Polson SW, Wan LQ, Wang M, Han L, *et al*. Identification of chondrocyte genes and signaling pathways in response to acute joint inflammation. Sci Rep. 2019;9(1):93.

50. Fehrenbacher A, Steck E, Rickert M, Roth W, Richter W. Rapid regulation of collagen but not metalloproteinase 1, 3, 13, 14 and tissue inhibitor of metalloproteinase 1, 2, 3 expression in response to mechanical loading of cartilage explants in vitro. Arch Biochem Biophys. 2003;410(1):39-47.

191

PAPER V

Effect of Osteochondral Graft Orientation in a Biotribological Test System

Christoph Bauer,[1] Hakan Göçerler,[2] Eugenia Niculescu-Morzsa,[1] Vivek Jeyakumar,[1] Christoph Stotter,[1,3] Ivana Tóth,[2] Thomas Klestil,[3,4] Friedrich Franek,[2] Stefan Nehrer[1]

[1]Danube University Krems, Department for Health Sciences, Medicine and Research, Center for Regenerative Medicine and Orthopedics, Dr.-Karl-Dorrek-Strasse 30, 3500 Krems, Austria, [2]AC2T Research GmbH, Wr. Neustadt, Austria, [3]LK Baden-Mödling-Hainburg, Department of Orthopedics and Traumatology, Baden, Austria, [4]Danube University Krems, Department for Health Sciences, Medicine and Research, Center for Health Sciences and Medicine, Krems, Austria

ABSTRACT: Autologous osteochondral transplantation (AOT) utilizing autografts is a widely used technique for the treatment of small-to-medium cartilage defects occurring in knee and ankle joints. The application of viable cartilage and bone ensures proper integration, early weight bearing, as well as restoration of biomechanical and biotribological properties. However, alignment of the autografts onto the defect site remains a pivotal aspect of reinstating the properties of the joint toward successful autograft integration. This is the first study to perform tests with different orientations of osteochondral grafts in a cartilage-on-cartilage test system. The objective was to estimate if there are differences between aligned and 90°-rotated grafts concerning molecular biological and biomechanical parameters. Tissue viability, assessed by XTT assay indicated lower metabolic activity in tested osteochondral grafts (aligned, $p = 0.0148$ and 90°-rotated, $p = 0.0760$) in favor of a higher anabolic gene expression (aligned, $p = 0.0030$ and 90°-rotated, 0.0027). Tissue structure was evaluated by Safranin O histology and microscopic images of the surface. Aligned and 90°-rotated grafts revealed no apparent differences between proteoglycan content or cracks and fissures on the cartilage surface. Test medium analyzed after tribological tests for their sulfated glycosaminoglycan content revealed no differences ($p = 0.3282$). During the tests, both the friction coefficient and the relative displacement between the two cartilage surfaces were measured, with no significant difference in both parameters (COF, $p = 0.2232$ and relative displacement, $p = 0.3185$). From the methods we deployed, this study can infer that there are no differences between aligned and 90°-rotated osteochondral grafts after tribological tests in the used ex vivo tissue model. © 2019 The Authors. *Journal of Orthopaedic Research*® Published by Wiley Periodicals, Inc. on behalf of Orthopaedic Research Society. J Orthop Res 37:583–592, 2019.

Keywords: mechanobiology; cartilage; synovium & osteoarthritis

Focal articular cartilage defects of the knee are a challenging condition that requires a surgical intervention to minimize further casualties. Defects on the articulating surfaces of the knee joint mainly occur due to traumatic injuries, avascular necrosis, or a joint deformity.[1–3] Here, different strategies are available for the treatment of full-thickness defects. Among them, currently used techniques include bone marrow stimulating methods (e.g., microfracture, drilling, abrasion arthroplasty, or spongialization), chondrocyte implantation directly (autologous chondrocyte implantation [ACI]) or in combination with biomaterials (matrix-associated chondrocyte implantation [MACI]). Also, intra-articular injection of lubricants (e.g., hyaluronan), as well as the implantation of single or multiple autologous grafts (mosaicplasty), are used as treatment options.[1,4–6]

The latter being predominantly used for small-to-medium defects, wherein the number of autologous grafts, which can be isolated from a non-weight bearing zone of the femoral condyle, draws its limitation along donor-site morbidity. Nevertheless, osteochondral autologous transplantation is a single-step procedure in which a vital hyaline cartilaginous tissue and subchondral bone are transplanted to a primed defect.[3] Also, allografts yielded 12–24 h after a donor's death can be stored fresh or cryopreserved and transplanted later. In this procedure, one of the main advantages of implying osteochondral allografts is the presence of chondrocytes, which are still metabolically active.[7] Furthermore, osteochondral transplantation, either autologous or allogeneic, has the benefit of providing both viable hyaline cartilage and underlying bone, allowing good bony integration and early weight bearing to the joint.[8] Consequently, a congruent articular cartilage surface similar to that of the natural joint can be obtained which subsequently restores the biomechanical and tribological properties of the joint.[2,9]

In this context, tribological principles play a significant role and have gained attention over the last decade in elucidating how natural synovial joints function or fail and provide insights into different design principle criteria.[10] The moving contacts between the surfaces are mandatory to produce high fluid pressurization, as well as a low coefficient of friction from a tribological point of view.[11] Important aspects which can affect measurements are friction, wear, and lubrication. Additional aspects include debridement products of implants or from the cartilage

itself, which subsequently can lead to inflammatory responses.[10] Numerous studies have used pin-on-disc or flat-on-flat tribometers for distinctive basic tribological models. In the latter cases, the biological cartilage–cartilage interface of a joint is replaced by an interface of cartilage against glass, metal, ceramic, or another biomaterial. However, this setup neglects the natural response of the tissue to movement and load against a soft tissue surface.[10,12–14] Other in vitro studies investigating tribological characteristics of different hydrogels were limited due to relative usage of small sample size with articulation against articular cartilage.[13] Other systems involving cartilage-on-cartilage systems compared only friction and lubrication of the chondroplastic materials.[15]

Considering the three-dimensional structure of articular cartilage and the direction of collagen fibrils responsible for its unique mechanical properties, it likely seems that the orientation of the osteochondral grafts plays a decisive role. However, the orientation of osteochondral grafts and its influence on contact pressure and chondrocyte viability has not been studied yet in a biological cartilage-on-cartilage test system. Here, in vitro models should represent the anatomical and physiological conditions tangibly, wherein tribological test systems could support to understand better and mimic these conditions. They can serve as a strategic preclinical test platform to evaluate treatment options and provide relevant information on the performance and suitability of implant materials.[13]

This study aimed to investigate the effects of orientation of osteochondral grafts in a well-established test system concerning tribological and biological outcome measures ex vivo. In our experimental setup, two cartilaginous surfaces were moved against each other. We hypothesized that 90°-rotated grafts could have increased surface damage, higher coefficient of friction and decreased cartilage-specific parameters (e.g., metabolic activity, gene expression) in comparison to aligned osteochondral grafts in a cartilage-on-cartilage tribological test system.

METHODS

Specimen Preparation

Eight bovine knees were obtained from 18- to 20-months-old slaughtered cows. Under aseptic conditions, osteochondral grafts were harvested from the medial femoral condyle using a Single-Use OATS punch (Arthrex Inc., Naples). Osteochondral grafts were marked in order to describe their orientation within the joint surface. A sterile pen was used to mark them on the anterior side of the osteochondral grafts (see Figure 2). Each knee yielded 12–16 osteochondral grafts (8 mm diameter; 15 mm height). The osteochondral grafts were washed for 2 h in phosphate buffered saline (PBS, Sigma–Aldrich Chemie GmbH, Steinheim, Germany) at 37°C to remove loose bone particles and fatty tissue. The samples were then cut to 8 mm height with a custom-made cartilage holder. Subsequently, the osteochondral samples were cultivated in a growth medium (GIBCO DMEM/F12 GlutaMAX-I,

Invitrogen, LifeTech Austria, Vienna, Austria) with antibiotics (penicillin 200 U/ml; streptomycin 0.2 mg/ml) and Amphotericin B 2.5 μg/ml (Sigma–Aldrich Chemie GmbH) for 7 days. This step was introduced to overcome a decrease in metabolic activity and equilibrate the ex vivo environment after the harvesting procedure.[6] After seven days of incubation, tribological tests for each animal were performed within the next two days at 39°C. During the testing time (2 h), the untested group was also kept at 39°C. Before and after testing samples were held at 4°C until both tested and untested osteochondral grafts were analyzed on Day 10.

Biotribological Test System

A test system with a specially designed sample holder for this study is shown in Figure 1. It performs a reciprocal sliding movement between the osteochondral grafts. These grafts are submerged in a test fluid (in this case PBS) to mimic the conditions in the knee joint. The test setup itself encloses the sample holder to ensure sterile conditions throughout the testing process that the biological samples are not exposed to external influences and may cause artifacts which may interfere in the process of further analysis.

The applied load was 180 N and, considering the contact area of 50.26 mm^2 for ø8 mm cartilage samples, an initial estimated average pressure value of 3.57 MPa was achieved. The plane was assumed flat for all tested cartilage samples. The created tribo-model matches with contact pressure measurements for the tibiofemoral compartment of a human knee under the normal load of body weight with 0° flexion.[16] To mimic loading-unloading conditions of the knee during walking, the system was loaded for 10 min and then unloaded for another 10 min for a total test period of two hours with a stroke of 2 mm and a frequency of 1 Hz.

Samples stored for transportation purposes at 4°C were equilibrated to room temperature for half an hour, followed by another half an hour in the specimen holder, and were submerged in PBS at a temperature of 39°C (internal bovine body temperature).

The tribological installation was a pin-on-pin setting with two different arrangements. In one group, the samples were aligned in the same orientation as they were in the joint. The orientation was anterior to posterior in both the upper and the lower osteochondral grafts (group "aligned," see Figure 2a). In the second group of samples, the upper osteochondral graft was rotated 90° in a clockwise direction ("90°-rotated," see Figure 2b), whereby the orientation relative to the lower osteochondral graft changed. This arrangement should simulate implantation of an osteochondral graft during osteochondral transfer perpendicular to the anterior-posterior axis of the joint.

Metabolic Activity

For the measurement of the metabolic activity of chondrocytes within the tissue, an XTT based ex vivo toxicology assay kit (Sigma–Aldrich Chemie GmbH) was used according to the manufacturer's instructions. Cartilage was cut from the osteochondral grafts with a scalpel and divided longitudinally into two parts for XTT assay and RNA isolation. The cartilage was minced into smaller fragments onto a 24-well plate. Tissue weight for each sample was determined, and then the tissue was incubated in the XTT solution (1 ml medium, 490 μl XTT reagent, and 10 μl activation reagent) for 4 h at 37°C in 5% (v/v) CO_2 in the air. After incubation,
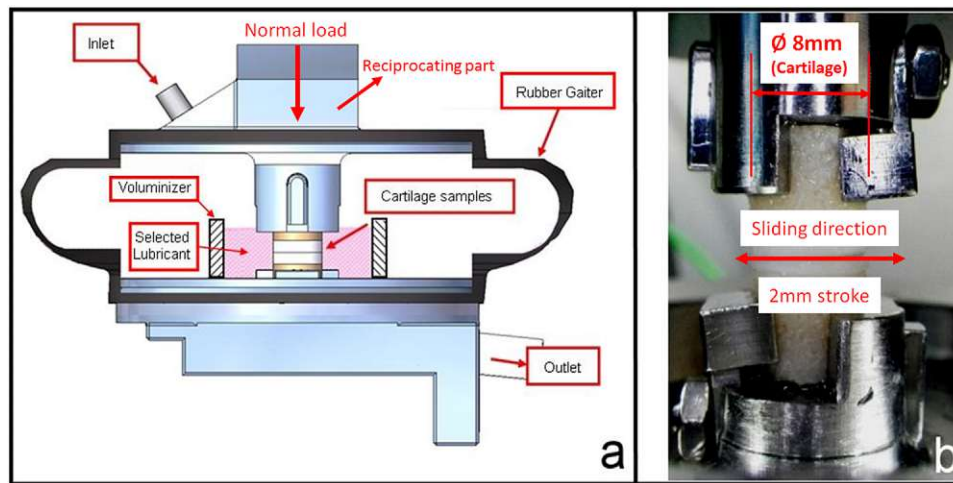
194

Figure 1. (a) Schematic of the designed test setup with specimen holder; in- and outlet could be used for a continuous medium exchange or to introduce additives to the system and observe their effects online, but it is not relevant for this experimental setup; (b) image of cartilage-against-cartilage contact in the tribo-test; the upper part of the tribometer is reciprocating during the tests.

the XTT solution was removed and retained. Tetrazolium product was extracted from the tissue using 0.5 ml dimethyl sulfoxide (DMSO), and the remaining tissue was incubated for 1 h at room temperature under continual agitation. Then the XTT and DMSO solutions were pooled, and the absorbance was measured at 492 nm and background wavelength at 690 nm as triplicates in a 96-well plate using a multi-mode microplate reader (Synergy^{TM} 2, Winooski, Vermont) with the software Gen 5. Absorbance was normalized to the wet weight of the tissue.

RNA Isolation
The other half of the cartilage tissue retrieved from the osteochondral grafts was stored in RNAlater^{TM} (Sigma–Aldrich, St. Louis, MI) at 4°C up to one week. After storage, the cartilage was minced into smaller fragments and transferred in tubes containing ceramic beads (MagNA Lyser Green Beads, Roche Diagnostics, Basel, Switzerland) with 300 µl lysis buffer (10 µl ß-mercaptoethanol + 290 µl RLT [from Fibrous Tissue Kit, Qiagen, Hilden, Germany]). Until RNA isolation, the tube was stored in liquid nitrogen. For RNA isolation, the tube was thawed and transferred to the

MagNA Lyser (Roche Diagnostics) for homogenization of the cartilage tissue. The homogenization step (6,500 rpm, 20 s) was repeated four times with a 2-min cooling phase after each step. According to the manufacturer's instruction, every sample was then incubated with 20 µl Proteinase K (from Fibrous Tissue Kit) for 30 min for a higher yield. RNA was eluted in 30 µl and stored at −80°C until cDNA synthesis.

Gene Expression Analysis
Gene expression analysis was carried out as previously described.[17] Briefly, cDNA synthesis was performed using Transcriptor First Strand cDNA Synthesis Kit (Roche, Basel, Switzerland). Additionally, RNA from bacteriophage MS2 was added to stabilize the isolated RNA during cDNA synthesis. Real-time quantitative polymerase chain reaction (RTqPCR) was performed in triplicate using the LightCycler$^{®}$ 96 from Roche. In total, four genes—Collagen type 2 (COL2A1), Aggrecan (ACAN), Matrix Metalloproteinase-1 (MMP1), and Matrix Metalloproteinase-13 (MMP13)—were analyzed, while Glyceraldehyde-3-phosphate dehydrogenase (GAPDH) was used as housekeeping gene.

Histology
For histological analysis, osteochondral grafts were fixed in 4% buffered formaldehyde solution (VWR, Radnor, PA) for up to 1 week and decalcified under constant agitation using Osteosoft solution (Merck, Burlington, MA). After decalcification (duration of 4–6 weeks), the osteochondral grafts were embedded in Tissue-Tek$^{®}$ OCT (Optimal Cutting Temperature, VWR, Radnor, PA) and stored at −80°C. Sectioning was done using the CryoStar^{TM} NX70 Cryostat (Thermo Fischer Scientific, Waltham, MA), with −25°C for the knife temperature and −20°C for the chamber temperature. A 6 µm sections were obtained and processed for Safranin O staining. Images were taken with a Leica microscope DM-1000 and processed using the Leica Manager software (Leica, Wetzlar, Germany).

Figure 2. (a) Visualization of osteochondral graft sample where the x-axis is aligned with walking direction; (b) 90°-rotated (around z-axis) specimen on top.

Alicone 3D Microscope
Alicona 3D microscope was used to optically analyze cartilage surface before and after the test to reveal determinant surface roughness parameters for the tribological performance of cartilage tissues. PBS was frequently added every
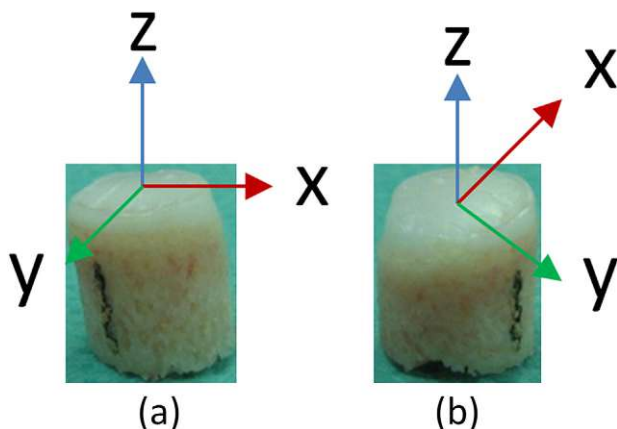
195

5 min to prevent the cartilage surface from drying out. First, widely applied roughness parameters, such as the average (Ra), root mean square roughness (Rq), skewness (Rsk), and kurtosis (Rku) are considered. The initial image of the cartilage (Figure 3a) has been cropped to center 4 mm diameter zone to avoid impaction effects on the cartilage surface analysis (Figure 3b). Then, the image was leveled (Figure 3c) and form removed (Figure 3d) to reduce location related inconsistency of the surface profile. This means that a form component must be removed before any other metrological operation. When the form is just a line segment or a plane, this operation is called leveling. In a nonplanar form, it is called form removal. As surface texture parameters depend on a reference (mean line or mean plane) used in the detection of peaks and valleys, or on the calculation of mean values and moments, form removal and leveling make it possible to define this reference. In our case, due to the location of the sample derived or the punching process, the surface could be tilted or concave. In order to remove the tilt, the leveling process is applied to the outcome of the 3D microscope image, as the tilt refers to a line or plane adjustment. To further remove the concave geometry, 2nd-degree polynomial or spherical for the removal process was applied.

Sulfated Glycosaminoglycans (sGAG)

The quantification of sGAG was performed according to Barbosa et al.[18] In brief, fluid (PBS) used during tribological tests was treated overnight with 25 U/ml proteinase K (Sigma–Aldrich) at 56°C. After inactivation of the enzyme (90°C, 10 min), the fluid was collected in ultra-free filter reaction tubes of 0.1 μm pore size (Millipore, Burlington,

MA) and centrifuged (12,000g, 4 min, room temperature). One milliliter of a 1.9-dimethyl-methylene blue solution (DMMB) was added to 100 μl filtrate and vigorously mixed to allow the formation of complexes of DMMB and sGAG in the sample. The complexes were pelleted via centrifugation (12,000g, 10 min, room temperature) and subsequently dissolved in decomplexation solution. After 30 min of shaking, the absorbance was measured at 656 nm photometrically using an Ultrospec 3300 pro photometer (Amersham Bioscience plc, Amersham, UK). The sGAG amount was calculated from a standard curve with shark chondroitin sulfate (Sigma–Aldrich). The measurement for each aligned or 90°-rotated test of osteochondral grafts was performed in duplicate.

Statistical Analysis

All data are expressed as means ± standard deviations (S.D.) in a box plot. Non-parametric Mann–Whitney U-test was used to make comparisons between paired data, and multiple comparisons were performed by non-parametric Kruskal–Wallis test followed by Dunn's posthoc test. Statistical significance was set at $p < 0.05$. All statistical analysis was performed using GraphPad Prism Software (Graphpad Prism Software Inc., San Diego, CA).

RESULTS

Osteochondral Grafts

Punched out osteochondral grafts for tribological tests had a symmetrical flat surface in almost every sample used for the experiments (Figure 4a). Asymmetric grafts (Figure 4b), which were not possible to circumvent, were
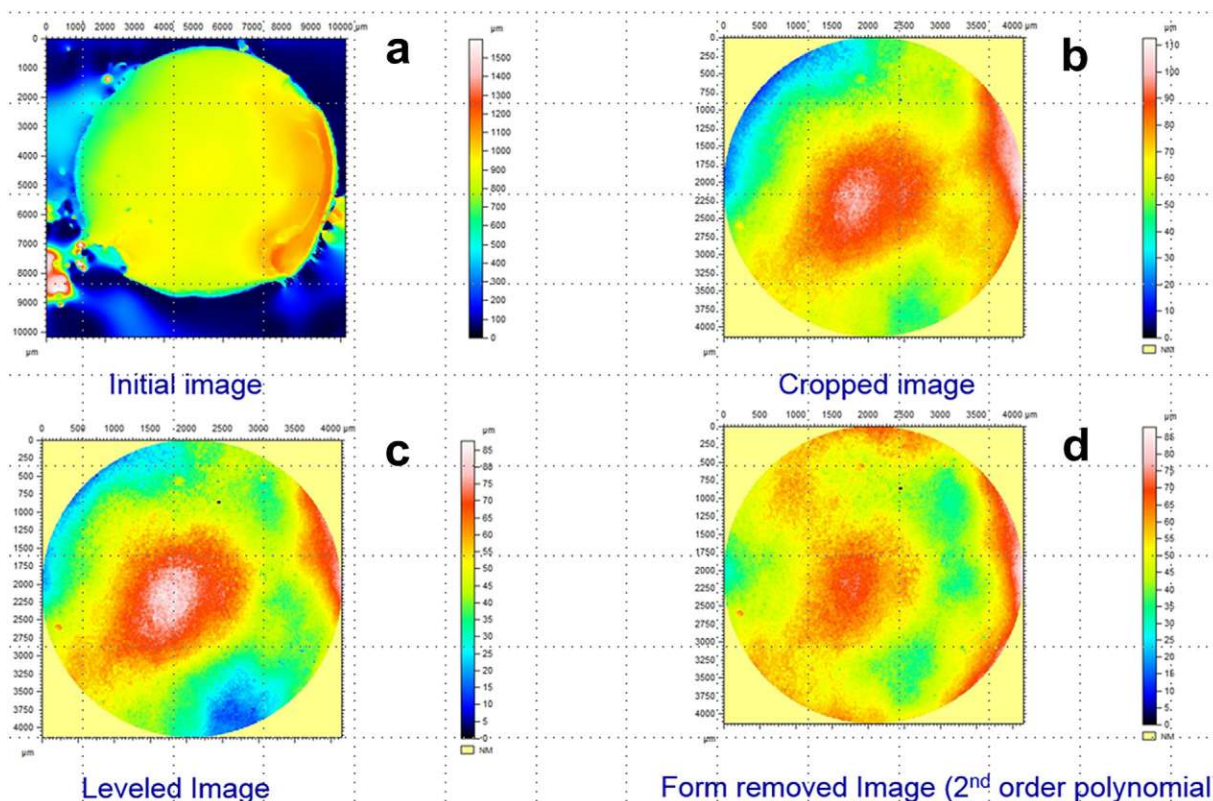

Figure 3. (a) Initial image of cartilage surface; (b) surface after cropping to center location; (c) leveled surface image; (d) form removed final version of surface to be analyzed.
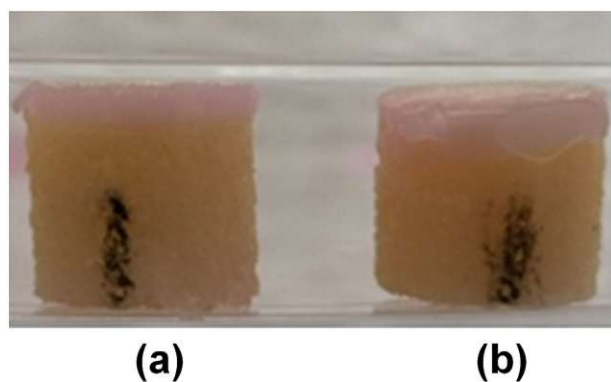
Figure 4. (a) Example for a used osteochondral graft for testing showing a symmetrical flat surface; (b) asymetric graft used for control (Day 0) and untested groups.

Figure 5. Metabolic activity of osteochondral grafts in untested and tested (aligned, 90°-rotated) conditions after 10 days of incubation with a comparison to day 0 (dotted line).

used for control (Day 0) and the untested group as the flatness is not a critical factor as for the ones used within the tribological test system.

Metabolic Activity of the Cells

The metabolic activity of chondrocytes in osteochondral grafts showed a constant value on Day 0 (dotted line) within all animals (Figure 5), but on Day 10 the metabolic activity exhibited a significant difference ($p < 0.05$) between untested osteochondral grafts and the two test groups (aligned, $p = 0.0148$ and 90°-rotated, $p = 0.0076$). Comparisons for metabolic activity between tested osteochondral grafts in aligned versus 90°-rotated orientation indicated no significant differences ($p > 0.9999$). Nevertheless, in both groups, the absorption per gram of tissue was on a much lower level compared to Day 0 or on Day 10 in the untested group.

Expression of Anabolic and Catabolic Cartilage-Specific Genes

For the analysis of gene expression, specific bovine primers were designed and tested successfully regarding optimal temperature values for primer annealing. After 10 days, the anabolic marker COL2A1 of the untested group decreased by fourfolds from Day 0 after harvesting of the osteochondral grafts.

In comparison, the results of the tested osteochondral grafts were significantly higher (aligned, $p = 0.0030$ and 90°-rotated, $p = 0.0027$) than the
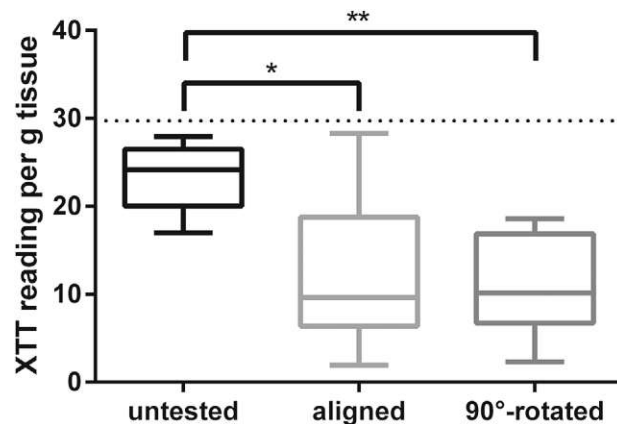
untested group on day 10 but showed no differences ($p = 0.9314$) concerning aligned or 90°-rotated orientation of the grafts during testing (Figure 6a). ACAN, another anabolic marker for gene expression, did not show this dramatic reduction from Day 0 to 10 in the untested group compared to COL2A1, but also had a slightly higher (aligned, $p = 0.4807$)) and significant difference (90°-rotated, $p = 0.0274$) value. Between the two tested groups within the tribological test system, no significant difference ($p = 0.1615$) was shown (Figure 6b).

However, osteochondral grafts which were tested in a 90°-rotated orientation had a slightly higher expression for the gene ACAN. In Figure 7, the catabolic genes MMP1 and MMP13, both of which are essential in the breakdown of interstitial collagens; for example, types I, II, and III were less expressed on day 10 in the untested group compared to Day 0. MMP1 gene expression increased significantly ($p = 0.0104$) between untested and 90°-rotated grafts (Figure 7a) and showed no significance between untested and aligned ($p = 0.1206$) or aligned and 90°-rotated ($p = 0.2319$) groups. MMP13 showed a significant difference in both aligned and 90°-rotated osteochondral grafts (aligned, $p = 0.0070$ and 90°-rotated, $p = 0.0205$) compared to the untested group, but no significance ($p = 0.1520$) within the tested groups (Figure 7b).
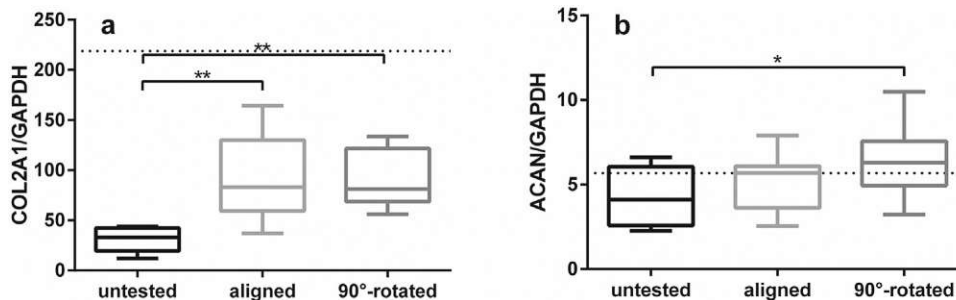

Figure 6. Gene expression of anabolic cartilage-specific genes. (a) COL2A1; and (b) ACAN expression in untested and tested osteochondral grafts after 10 days of incubation. In both graphs, Day 0 is shown as a dotted line.
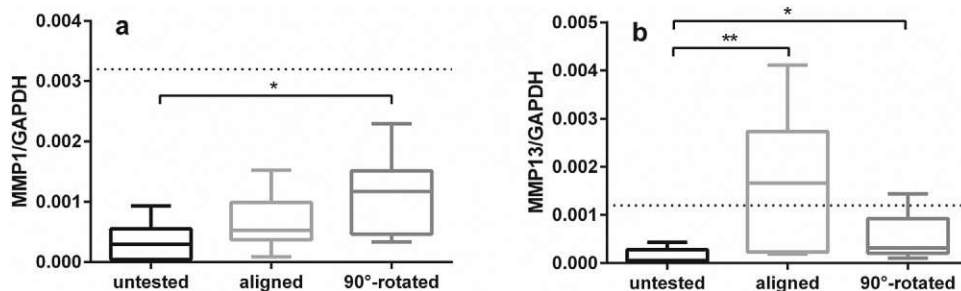
Figure 7. Gene expression of catabolic cartilage-specific genes. (a) MMP1 and (b) MMP13 expression in untested and tested osteochondral grafts after 10 days of incubation. In both graphs, Day 0 is shown as a dotted line.

Histology

For histological analysis, Safranin O staining was performed as shown in Figure 8. As an additional statement to microscope images of the surface, the histological evaluation was also used to find any differences (e.g., cracks or fissures) between the aligned and 90°-rotated osteochondral grafts.

Images of the untested control tissue sections stained with Safranin O revealed different strengths in the intensity of the staining for grafts from different points of withdrawal of the used medial cartilage. This was also shown in the osteochondral grafts tested in the tribological test system. So, no inference concerning proteoglycan content between the untested, aligned, and 90°-rotated group was detected.

Microscope Images

Before tribological tests, the microscopic images of the surfaces of the aligned and the 90°-rotated groups showed no cracks or fissures, but height differences in the starting material could be visualized by the used method (Figure 9). In these samples, there was a deviation of up to 100 microns. However, this was not included in our observations, because we focused more on cracks and fissures on the surface. which were achieved from the applied strain under physiological conditions (3.57 MPa). Our results demonstrate that from the specified applied strain, cracks and fissures occurred but no differences in depletion of the proteoglycan content between loaded (aligned and 90°-rotated) and untested grafts were seen. The severity of these damages ranges from deep trenches (more than

200 μm deep) to small superficial cracks (up to 50 μm). Also, there were osteochondral grafts that did not show any damage in aligned and 90°-rotated orientation. This finding makes it impossible to define a difference in cartilage surface area concerning aligned and 90°-rotated osteochondral grafts tested in the tribological test system.

Coefficient of Friction (COF) and Relative Displacement

During tribological tests, COF values in aligned osteochondral grafts varied between 0.012 and 0.016 during each test cycle (Figure 10). In comparison, 90°-rotated grafts showed similar results at the end of each cycle with no significant difference ($p = 0.2232$). The range was from 0.012 to 0.018 (Figure 11). Also, increasing relative displacement between the top and bottom holders, during the 10-min stimulation phase, was observed in both test groups. The values in aligned orientated osteochondral grafts were around 900 μm (Figure 10) and so much lower than in 90°-rotated grafts, where the values reached up to 1300 μm (Figure 11).

sGAG in the Supernatant After Testing

In the aligned and the 90°-rotated osteochondral grafts, the test fluids (PBS) after tribological tests were collected and measured for their content of released or abraded sulfated glycosaminoglycans. There was no significant effect in sGAG content between the orientations of osteochondral grafts in our test setup as both groups in Figure 12 showed similar values in the fluid after tribological tests.

Figure 8. Sections of cartilage tissue from untested and tested (aligned, 90°-rotated) osteochondral grafts on Day 10 stained with Safranin O; scale bar 250 μm.
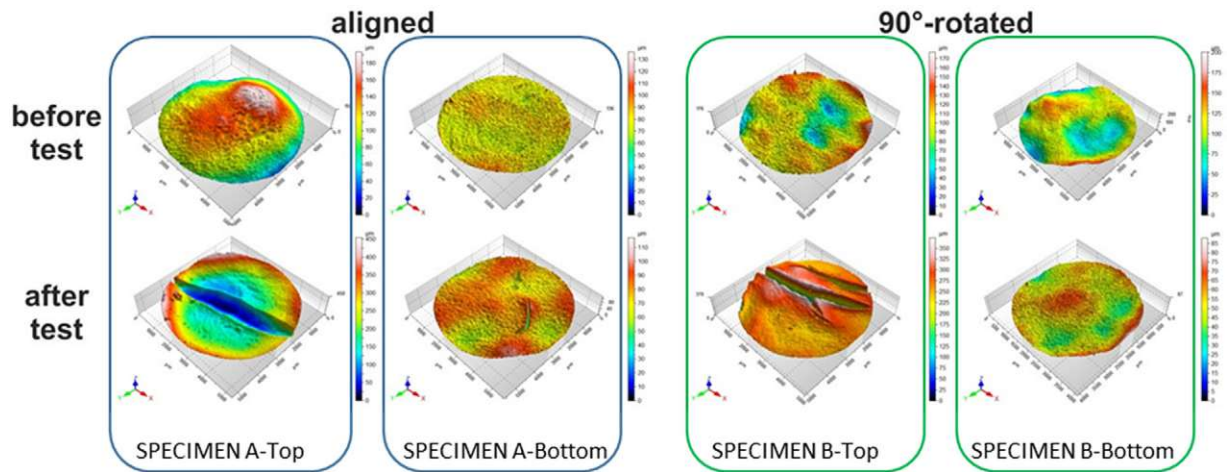
Figure 9. Output of 3D microscope representing major changes on the surface structure following tribological tests for aligned and 90°-rotated samples.

DISCUSSION

The objective of the current study was to investigate possible differences between aligned and 90°-rotated bovine osteochondral grafts in an established cartilage-on-cartilage (COC) biotribological test system. Bovine osteochondral grafts from the medial femoral condyle were investigated due to experimental reproducibility and availability. We could demonstrate that both aligned and 90°-rotated grafts showed higher expression of anabolic makers and decreased metabolic activity compared to controls. There were no differences between the two treatment groups for the coefficient of friction, proteoglycan content, and sulfated glycosaminoglycan (sGAG) release in the test fluid. Our results suggest that the orientation of osteochondral grafts regarding rotation relative to the joint axis might not have an impact on cartilage wear and metabolic outcome measures. While alignment of the graft and proper restoration of the articular surface have been shown to be crucial during autologous osteochondral transplantation, our findings indicate that there are no differences in the osteochondral graft orientation in the used ex vivo tissue model.

The use of a COC biotribological test system has been used as it more closely reflects physiological conditions compared to other counterpart materials like metal or glass. Similarly, metal-on-cartilage test systems led to an increase in apoptotic chondrocytes compared to the COC test systems. However, these differences can occur due to different loading magnitudes and loading rates, which in turn result in differences between structural damage of the articular cartilage.[19] To ensure stable contact between cartilage surfaces, a normal pressure of 180 N exerting a pressure of 3.57 MPa on the cartilage surface of the osteochondral grafts was deployed in our experimental setup. Consequently, the tribological test system is very similar to the pressure measurements of the tibial-femoral compartment of a human knee joint under normal body pressure.[16]

Additionally, during the testing period of 2 hours, the coefficient of friction (COF) and relative displacement was also recorded as indicators of mechanical
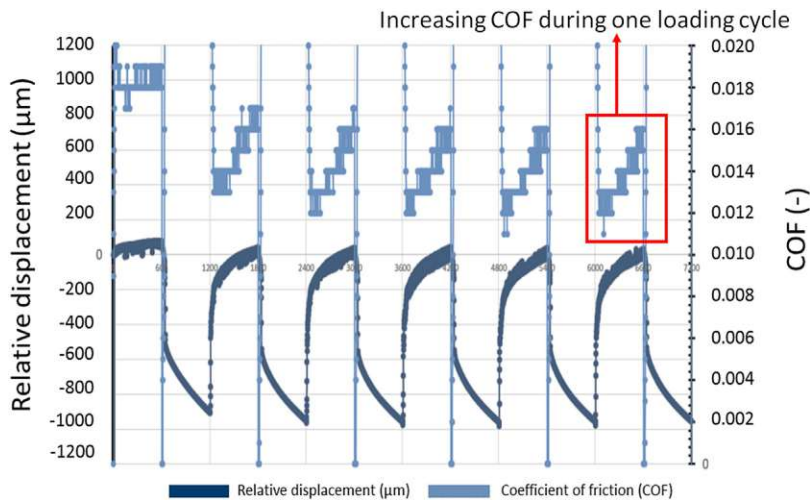

Figure 10. Coefficient of friction and relative displacement values versus time for aligned samples.
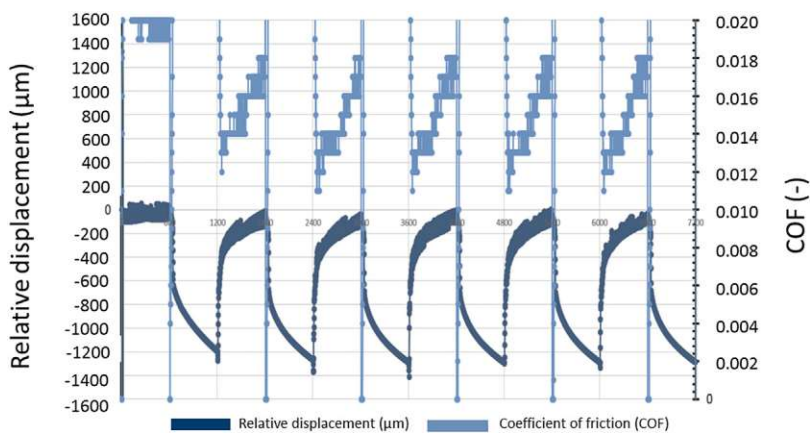
Figure 11. Coefficient of friction and relative displacement values versus time for 90°-rotated samples.

stress. In healthy synovial joints, the COF values are approximately around 0.005.[20] This low value could not be reached during the tests in our biotribological test system, as PBS was used instead of synovial fluid as a cartilage-surrounding fluid. The COF values during the tests varied between 0.012 and 0.018, whereas the aligned grafts reported slightly lower values. The increase from 0.012 to 0.016 (aligned) or 0.018 (90°-rotated) during a test cycle could occur from abnormal loading conditions that lead to extensive creep and exudation of the tissue. Here, increasing relative displacement values from 900m to 1300 μm during the loading cycle may hint at the conformity of cartilage.

For the harvesting of osteochondral grafts, different methods being used in clinics were available. In our study, however, we used single-Use OATS as it is the most common harvesting device. Besides, it was shown that cell viability around the edges of osteochondral grafts is best conserved by this method compared to the other punching or rotating techniques.[1] Before and after the tribological tests, microscopic images were taken and additionally processed to obtain a 3D topographical image of the cartilage surface. Various areas on the cartilage surface showed ruptures which had a depth of up to 200 μm in both tested groups. The shape of the ruptures and the formation of surface

fissures show similar properties to those reported by other studies.[21,22] Concerning the evaluation of the cartilage surface, histology was additionally used to show modifications of the surface and the proteoglycan content of the cartilage itself. Tested osteochondral grafts were compared with a control group after a total incubation time of 10 days. Differences between the groups could not be assessed, as also indicated by Tekari et al., as over the whole cartilage surface proteoglycan content, but not gene expression patterns, were varying.[23] After harvesting osteochondral grafts, the locations within the donor site were numbered on taken pictures to always use grafts from more or less the exact location in all the animals used. This repetitive process was not always possible as cuts and osteochondral defects occurred on the donor site and grafts had to be taken out from different areas on the medial condyle.

The release of sulfated glycosaminoglycans (sGAGs) into the culture medium in organ cultures with full-depth articular cartilage is used to detect or quantify tissue degradation.[6,14] In our study, the release of the sGAGs was used as a parameter to determine the breakdown of the cartilage concerning different orientations of the OC grafts. Since the measurements of the sGAGs for aligned and 90°-rotated grafts reached nearly identical levels, it was not possible to make any statements regarding differences in the release of the two test conditions. However, since damages in the form of cracks and fissures occurred under both conditions, the result was not unexpected. Another possibility that could have influenced the sGAG value is the washing out of proteoglycans from the peripheral areas of the extracellular matrix as a result of the missing lateral constraint as well as the disruption of non-covalent interactions between aggrecan and long chains of hyaluronic acid molecules in cartilage.[6]

Besides the analysis of tissue parameters, the chondrocytes within the cartilage were also considered. As the mitochondrial activity of chondrocytes within osteochondral grafts decreases after harvesting procedure and stabilizes after approximately 6 days,[6] the grafts were first incubated in culture medium for 7 days to ensure stabilized mitochondrial activity,
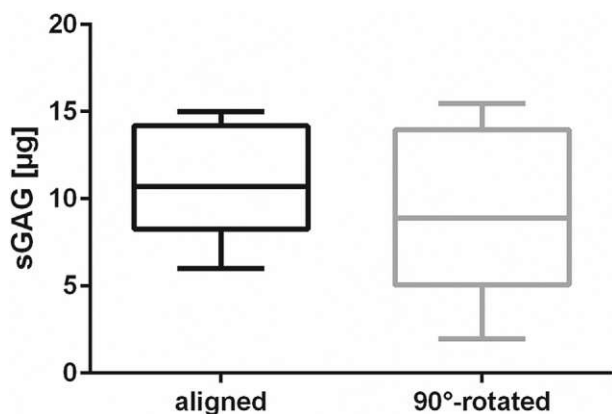

Figure 12. Release of sulfated glycosaminoglycans into the test fluid by osteochondral grafts after tribological tests on Day 10.

200

before tribological tests were performed. After these tests, both groups (aligned and 90°-rotated) showed the same level of activity, which is much lower compared to the untested group. This phenomenon could be the result of testing itself, as chondrocytes were possibly detached from the superficial layer[24] due to applied surface strain and hence a reduced cell count occurs in the cartilage tissue. Also, it could be possible that cells reduce metabolic activity in favor of performing more synthesis of, for example, collagen 2 or aggrecan. The latter case seems sensible, primarily because gene expression of collagen 2 in tested osteochondral grafts significantly increased. Aggrecan tends to increase in aligned grafts, but only the comparison between the untested group and 90°-rotated grafts is significant. However, no significant difference between the two test groups is noted. Additionally, to the two cartilage-specific genes collagen 2 and aggrecan, the matrix metalloproteinases MMP1 and MMP13 were analyzed for their gene expression. The significant increase in both genes could be due to inflammatory processes or tissue remodeling. As no inflammation mediators were used or introduced in this model, it is apparent that tissue remodeling initiated due to mechanical stress is happening.[24,25]

However, there are several limitations in this experimental setup. First, it must be considered that ex vivo culture often limits oxygen and nutrient supply, usually occurring under physiological conditions. Second, osteochondral grafts were harvested from 18 to 24-month-old animals. At this age, cattle are considered young but are expected to reach skeletal maturity.[26] Anyway, no direct link to mature human tissue concerning biological and biomechanical properties can be done.

Furthermore, our model only shows short-term effects on cartilage tissue and does not include other components of a joint. Influences of synovium, synovial fluid, meniscus, or subchondral bone are not considered. As the last point, the analysis of sGAG in the test medium is an important marker of wear and is associated with histology and metabolism.

Nevertheless, other clinically relevant markers such as Hydroxyproline (HYP) or cartilage oligomeric matrix protein (COMP) could be investigated. In particular, COMP is sensitive to mechanical stress, while HYP is used to detect collagen fragments as a structural marker of injury.[27] Overall, it has to be considered that all these experiments were performed ex vivo. The levels of different parameters analyzed could look different in vivo.

The alignment of osteochondral grafts in a cartilage-on-cartilage biotribological test system has not been studied extensively yet. Only a simulation study on osteochondral grafting was done, which showed effects between differently aligned osteochondral grafts after removal from an unloaded area and implantation in a loaded zone. However, this was only shown in computer simulation models and not in vivo.[28] Therefore, our biotribological system could

provide further insights, as biological samples are used, and the system uses pressure loads similar to those in the human knee joint. Nevertheless, no definite tendency or effect was found in molecular biological and biomechanical parameters with the used methods, so we can conclude that no differences could be shown in this ex vivo tissue model.

AUTHOR CONTRIBUTIONS

All authors contributed extensively to the work presented in this paper. C.B. contributed in study plan, harvesting grafts, biological analysis, data analysis, and wrote the manuscript. H.G. contributed in study plan, tribological tests, microscopic images, and wrote the manuscript. E.N.M. contributed in harvesting grafts, biological analysis, and discussed the results. V.J. contributed in discussing the results, data analysis, proofreading, and commented on the manuscript. I.T. and T.K. discussed the results and commented on the manuscript. C.S. contributed in harvesting grafts, biological analysis, discussion of the results, and commented on the manuscript. F.F. supervised tribological tests and acquired funding. S.N. supervised biological evaluations, acquired funding, came up with the idea for this study, discussed results, and commented on the manuscript.

ACKNOWLEDGMENTS

REFERENCES

1. Hafke B, Petri M, Suero E, et al. 2016. Chondrocyte survival in osteochondral transplant cylinders depends on the harvesting technique. Int Orthop 40:1553–1558.
2. Bowland P, Ingham E, Jennings L, et al. 2015. Review of the biomechanics and biotribology of osteochondral grafts used for surgical interventions in the knee. Proc Inst Mech Eng H 229:879–888. Available from: http://www.ncbi.nlm.nih.gov/pubmed/26614801%5Cn.
3. Andrade R, Vasta S, Pereira R, et al. 2016. Knee donor-site morbidity after mosaicplasty—a systematic review Journal of Experimental Orthopaedics. J Exp Orthop 3:1–17.
4. Fermor HL, Russell SL, Williams S, et al. 2015. Development and characterisation of a decellularised bovine osteochondral biomaterial for cartilage repair. J Mater Sci Mater Med 26:1–11.
5. Bauer C, Berger M, Baumgartner R, et al. 2016. A novel cross-Linked hyaluronic acid porous scaffold for cartilage repair: an in vitro study with osteoarthritic chondrocytes. Cartilage 7:265–273. Available from: http://ovidsp.ovid.com/ovidweb.cgi?T=JS&PAGE=reference&D=ovftr&NEWS=N&AN=01555168- 201607000-00007.

6. Elson KM, Fox N, Tipper JL, et al. 2015. Non-destructive monitoring of viability in an ex vivo organ culture model of osteochondral tissue. Eur Cells Mater 29:356–369.

7. Williams SK, Amiel D, Ball ST, et al. 2003. Prolonged storage effects on the articular cartilage of fresh human osteochondral allografts. J Bone Jt Surg—Ser A 85:2111–2120.

8. Patil S, Tapasvi SR. 2015. Osteochondral autografts. Curr Rev Musculoskelet Med 8:423–428.

9. Robert H. 2011. Chondral repair of the knee joint using mosaicplasty. Orthop Traumatol Surg Res 97:418–429.

10. Zhou ZR, Jin ZM. 2015. Biotribology: recent progresses and future perspectives. Biosurf Biotribol 1:3–24. Available from: http://www.sciencedirect.com/science/article/pii/S2405451815000082.

11. Schätti OR, Gallo LM, Torzilli PA. 2016. A model to study articular cartilage mechanical and biological responses to sliding loads. Ann Biomed Eng 44:2577–2588.

12. Moore AC, Burris DL. 2015. Tribological and material properties for cartilage of and throughout the bovine stifle: support for the altered joint kinematics hypothesis of osteoarthritis. Osteoarthr Cartil 23:161–169.

13. Katta J, Jin Z, Ingham E, et al. 2008. Biotribology of articular cartilage—a review of the recent advances. Med Eng Phys 30:1349–1363.

14. Trevino RL, Stoia J, Laurent MP, et al. 2017. Establishing a live cartilage-on-cartilage interface for tribological testing. Biotribology 9:1–11.

15. Northwood E, Fisher J, Kowalski R. 2007. Investigation of the friction and surface degradation of innovative chondroplasty materials against articular cartilage. Proc Inst Mech Eng Part H J Eng Med 221:263–279.

16. Patil S, Steklov N, Song L, et al. 2014. Comparative biomechanical analysis of human and caprine knee articular cartilage. Knee 21:119–125.

17. Bauer C, Niculescu-Morzsa E, Nehrer S. 2017. A protocol for gene expression analysis of chondrocytes from bovine osteochondral plugs used for biotribological applications. MethodsX 4:423–428.

18. Barbosa I, Garcia S, Barbier-Chassefière V, et al. 2003. Improved and simple micro assay for sulfated glycosamino-glycans quantification in biological extracts and its use in skin and muscle tissue studies. Glycobiology 13:647–653.

19. Heiner AD, Smith AD, Goetz JE, et al. 2013. Cartilage-on-cartilage versus metal-on-cartilage impact characteristics and responses. J Orthop Res 31:887–893.

20. Majd SE, Rizqy AI, Kaper HJ, et al. 2017. An in vitro study of cartilage–meniscus tribology to understand the changes caused by a meniscus implant. Colloids Surfaces B Biointerface 155:294–303.

21. Fick JM, Espino DM. 2011. Articular cartilage surface rupture during compression: investigating the effects of tissue hydration in relation to matrix health. J Mech Behav Biomed Mater 4:1311–1317.

22. Malekipour F, Whitton C, Oetomo D, et al. 2013. Shock absorbing ability of articular cartilage and subchondral bone under impact compression. J Mech Behav Biomed Mater 26:127–135.

23. Tekari A, Luginbuehl R, Hofstetter W, et al. 2015. Bovine osteochondral tissues: a questionable model to evaluate mechanical loading in vitro. IEEE Trans Nanobioscience 14:716–721.

24. Musumeci G. 2016. The effect of mechanical loading on articular cartilage. J Funct Morphol Kinesiol 1:154–161. Available from: http://www.mdpi.com/2411-5142/1/2/154.

25. Grodzinsky AJ, Levenston ME, Jin M, et al. 2000. Cartilage tissue remodeling in response to mechanical forces. Annu Rev Biomed Eng 2:691–713. Available from: http://www.annualreviews.org/doi/10.1146/annurev.bioeng.2.1.691.

26. Motavalli M, Akkus O, Mansour JM. 2014. Depth-dependent shear behavior of bovine articular cartilage: relationship to structure. J Anat 225:519–526.

27. Kumahashi N, Swärd P, Larsson S, et al. 2015. Type II collagen C2C epitope in human synovial fluid and serum after knee injury—associations with molecular and structural markers of injury. Osteoarthr Cartil 23:1506–1512.

28. D'Lima DD, Chen PC, Colwell CW, Jr. 2009. Osteochondral grafting: effect of graft alignment, material properties, and articular geometry. Open Orthop J 3:61–68. Available from: http://benthamopen.com/ABSTRACT/TOORTHJ- 3-61.

List of publications

The enumeration provided herein comprises the publications conspicuously absent from the appendices of the thesis:

1) Katja Hölzl, Marian Fürsatz, Hakan Göcerler, Barbara Schädl, Sara Žigon-Branc, Marica Markovic, Claudia Gahleitner, Jasper Van Hoorick, Sandra Van Vlierberghe, Anne Kleiner, Stefan Baudis, Andreas Pauschitz, Heinz Redl, Aleksandr Ovsianikov, Sylvia Nürnberger, **Gelatin methacryloyl as environment for chondrocytes and cell delivery to superficial cartilage defects**, *Journal of Tissue Engineering and Regenerative Medicine*, Volume 16, Issue 2, (2022), 207-222
https://doi.org/10.1002/term.3273

2) Vladimir Totolin, Hakan Göcerler, Manel Rodríguez Ripoll, Martin Jech, **The role of ferric oxide nanoparticles in improving lubricity and tribo-electrochemical performance during chemical–mechanical polishing**, *Tribology Letters*, Volume 65, Article number: 20, (2017)
https://doi.org/10.1007/s11249-016-0806-4

3) Vladimir Totolin, Hakan Göcerler, Manel Rodríguez Ripoll, Martin Jech, **Tribo-electrochemical study of stainless steel surfaces during chemical–mechanical polishing** , *Lubrication Science*, (2016), 28, 363–380
https://doi.org/10.1002/ls.1336

4) Vladimir Pejaković, Vladimir Totolin, Hakan Göcerler, Josef Brenner, Manel Rodríguez Ripoll, **Friction and wear behaviour of selected titanium and zirconium based nitride coatings in Na2SO4 aqueous solution under low contact pressure**, *Tribology International*, 91, (2015), 267–273
https://doi.org/10.1016/j.triboint.2015.04.047